Technical Design Report for a Nosecone Calorimeter (NCC) for the PHENIX Experiment

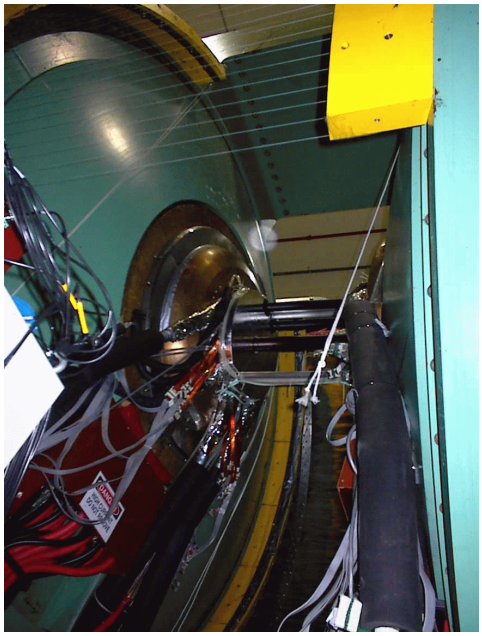

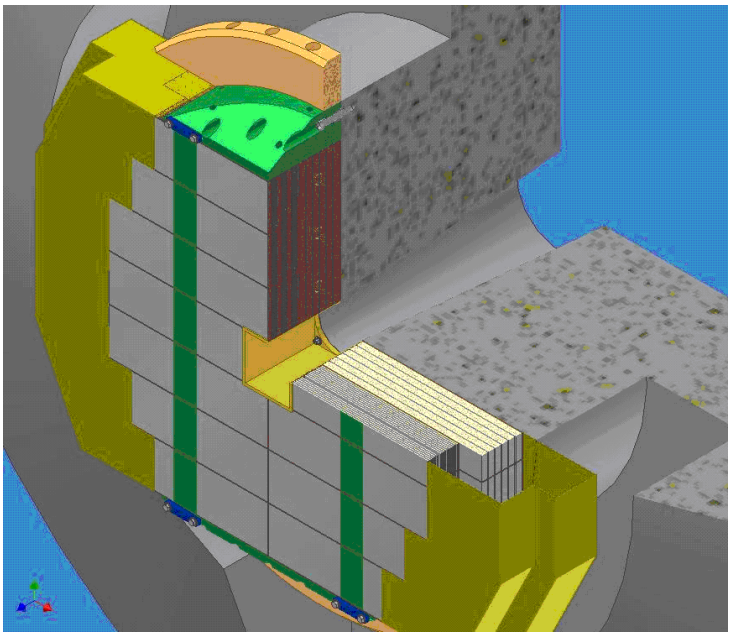

Relativistic Heavy Ion Collider
Brookhaven National Laboratory
April, 2007 update i.e. TDR - version 1.0

CVS history Last update by RKS 4/05/2007 4:20 PM BNL time

1. authors - need to update
2. intro - updated
3. Physics Overview - updated
4. Heavy Ion Physics - updated - needs figure caps/better figs and cites
5. pA - no change
6. spin - no change - need to shorten
7. design - updated
8. management - updated
9. budgetschedule - updated need new numbers
10. appendix A - check these numbers again
11. appendix B - updated - needs some more work
12. appendix C - added
13. appendix D - added
14. appendix E - added
15. appendix F - updated
16. appendix G - added

PHENIX Nosecone Calorimeter

Participants

February, 2006

University of California, *Riverside, CA 92521, USA*
K. Barish, S. Bathe, V. Dzordzhadze, O. Eyser, T. Hester, A. Moreale, Ken Sedgewick, R. Seto, Z. Yasin

Chemistry Dept., Brookhaven National Laboratory, *Upton, NY 11973-5000, USA*
R. Nouicer, R. Pak, A. Sukhanov

Instrumentation Dept., Brookhaven National Laboratory, *Upton, NY 11973-5000, USA*
Z. Li, V. Radeka, S. Rescia

Physics Dept., Brookhaven National Laboratory, *Upton, NY 11973-5000, USA*
S. Boose, B. Johnson, E.P. Kistenev, D. Lynch, S.P. Stoll, C.L. Woody

Charles University, *Ovocny trh 5, Praha 1, 116 36, Prague, Czech Republic*
Michael Finger, Miroslav Finger, P, Mikes,

University of Colorado, *Boulder, CO 80309, USA*
E. Kinney, J. Nagle

Columbia University and Nevis Laboratories, *Irvington, NY 10 533, USA*
C.Y. Chi

Institute of Physics, Academy of Sciences of Czech Republic, *Na Slovance 2, 182 21 Prague 8, Czech Republic*
J. Popule, L. Tomasek, M. Tomasek, V. Vrba

Czech Technical University, *Zikova 4, 166 36 Prague 6, Czech Republic*
M. Virius, J. Klaus, T. Liska

Ewha Women's University, *Seoul, Korea*
S. Nam, I. Park

FNAL - Fermi National Accelerator Laboratory, *Batavia, IL 60510, USA*
W. E. Cooper, M. Demarteau, M. Hrycyk, K. Krempetz, Y. Orlov

University of Illinois Urbana-Champaign, *Urbana, IL 61801, USA*
M. Chiu, M. Grosse-Perdekamp, J. Koster, J.C. Peng

Iowa State University, *Ames, IA 50011, USA*
J.C. Hill, J.L. Lajoie, F. Wei

Joint Institute for Nuclear Research- Dubna *Moscow Region, Russia*
S. Afanasiev, S. Basilev, A. Baskakov, A. Bychkov, A. Isupov, N. Kotsev, A. Litvinenko, A. Malakhov, V. Peresedov, P. Rukoyatkin, V. Slepnev, I. Slepnev, L. Zolin

Korea University, *Seoul, 136-701, Korea*
B. Hong, B.I. Kim, K.S. Sim

RIKEN, The Institute of Physical and Chemical Research, *Wako, Saitama 351-0198, Japan*
I. Nakagawa, A. Taketani

Skobeltsyn Institute of Nuclear Physics, Lomonosov Moscow State University, *Voro b'evy Gory, Moscow 119992, Russia*
G.A. Bogdanova, D. Karmanov, M. Merkin, V. Volkov, A. Voronin

Dept. of Physics and Astronomy, Stony Brook University, *SUNY, Stony Brook, NY 11794, USA*
A. Deshpande

Institute of Physics, University of Tsukuba, *Tsukuba, Ibaraki 305, Japan*
S. Esumi

Yonsei University, *IPAP, Seoul 120-749, Korea*
J.H. Kang, D.J. Kim, S. Kim

Contents

1 Introduction and Executive Summary **1–1**

2 Physics Overview **2–1**
2.1 Heavy Ion Physics . . . 2–2
2.1.1 Hard Scattering . . . 2–2
2.1.1.1 Photon-Tagged Jets . . . 2–4
2.1.1.2 Response of the Medium . . . 2–5
2.1.1.3 Contribution of the NCC . . . 2–8
2.1.2 Heavy Quarkonia . . . 2–8
2.1.2.1 Contribution of the NCC . . . 2–11
2.1.3 Charm via Electrons . . . 2–12
2.2 p+A Physics, Nucleon Structure and Saturation . . . 2–13
2.2.1 The Colored Glass Condensate . . . 2–13
2.2.1.1 Contribution of the NCC . . . 2–14
2.2.2 Other Physics Topics . . . 2–17
2.2.2.1 Antiquark distribution in nuclei at small x . . . 2–17
2.2.2.2 Cronin effect and x_F-scaling . . . 2–18
2.3 Spin Structure of the Nucleon . . . 2–18
2.3.1 Physics Motivation . . . 2–18
2.3.2 Nucleon Structure: Gluon Polarization . . . 2–20
2.3.3 Transverse Spin Physics . . . 2–23
2.3.4 Nucleon Structure: Quark Polarization . . . 2–28

3 Design of the NCC **3–1**
3.1 Overview . . . 3–1
3.2 Upgrade Layout and NCC Configuration . . . 3–3
3.3 NCC Design considerations . . . 3–4
3.4 The Performance of the NCC . . . 3–8
3.4.1 Simulations - the optimization procedure . . . 3–10
3.4.2 Containment, energy and position resolution . . . 3–10
3.4.3 Discrimination between hadronic and electromagnetic activities in NCC 3–11
3.4.4 Jet measurements . . . 3–15
3.4.5 Muons in NCC: reconstruction and rejection . . . 3–16
3.4.6 π^0 reconstruction . . . 3–18

3.5 NCC Occupancy and Dynamic Range Considerations . . . 3–22
3.6 NCC Mechanical Design . . . 3–24
3.7 NCC Readout . . . 3–26
3.7.1 Sensors . . . 3–26
3.7.2 Pad-Structured Readout Layers . . . 3–28
3.7.3 Stripixel readout layers . . . 3–30
3.8 NCC Electronics . . . 3–31
3.8.1 NCC analog signal processing . . . 3–32
3.9 NCC Based Event Triggering . . . 3–36
3.9.1 The NCC Level-1 Trigger System . . . 3–38
3.9.2 Ongoing R&D Program . . . 3–42

4 Project Management and Responsibilities 4–1
4.1 Project background . . . 4–1
4.2 The management plan for the NCC . . . 4–2
4.2.1 PHENIX management structure . . . 4–2
4.2.2 PHENIX subsystem leadership . . . 4–2
4.2.3 Role of BNL . . . 4–2
4.2.4 Specification of deliverables . . . 4–5
4.2.4.1 Calorimeter . . . 4–5
4.2.4.2 DAQ system . . . 4–6
4.2.4.3 Auxiliary Systems and Integration . . . 4–6
4.3 Institutional involvement . . . 4–6
4.3.1 US based Institutions . . . 4–6
4.3.2 International participation . . . 4–7
4.4 Acknowledgements . . . 4–8

5 Budgets and Schedule 5–1
5.1 Overview . . . 5–1
5.2 Contingency Analysis . . . 5–2
5.3 Overhead Estimate . . . 5–2
5.4 Tungsten-Si Calorimeter R&D . . . 5–2
5.5 NCC Construction . . . 5–3
5.6 Additional NCC to complement DOE Construction project . . . 5–5

A Event Rates A–1

B Physics Simulations B–1
B.1 Direct Photons . . . B–2
B.2 The χ_c . . . B–4
B.3 Spin Simulations . . . B–10
B.3.1 W isolation cuts: the quark structure of the nucleon. . . . B–12
B.4 Looking for a Colored Glass Condensate - a Simple Model . . . B–15
B.5 A Simulation Study of the Reaction Plane by the NCC . . . B–17

B.6 Muons and Background B–1

C Test Beam Results **C–1**
C.1 Data analysis C–1

D Sensor Research and Development **D–1**

E Pad Readout Chain **E–1**
E.1 SPICE Simulation Of The Pad Sensor Readout Chain. E–1
E.2 Simulation Model of the Pad Sensors Readout Chain E–2
E.3 Transmission Line Analysis E–3
E.4 Selection of Cut-Off Frequency of the Low-Pass Filter E–3
E.5 Transient Analysis E–5
E.5.1 Nonlinearity E–5
E.6 Noise Analysis. E–7
E.7 Summary Table E–7
E.8 Dynamic Range of Signal Measurement E–9
E.9 Summary E–10

F Silicon Strip Sensors and Readout **F–1**
F.1 Strip Sensors F–1
F.1.1 Design Principle F–1
F.1.2 SVX4 Readout Chip F–3
F.2 Stripixel Ladder F–3
F.3 Sensor Readout Module (SRM) F–5
F.3.1 Power consumption F–6
F.4 Front-End Module (FEM) F–6
F.4.1 FPGA Selection F–9
F.4.2 Number of LVDS pairs. F–9
F.4.3 FEM Ports F–10
F.5 Zero Suppression and Data Compression F–10
F.6 Program and Control Module (PCM) F–11
F.7 Readout Chain Development F–11
F.8 Production and Assembly of Silicon Readout Layers F–14
F.9 Radiation Tolerance of Front-End Electronics F–16
F.9.1 Inside calorimeter F–16
F.9.2 Outside calorimeter F–16
F.10 References F–18

G Power Proposal **G–1**
G.1 PHENIX NCC Bias Voltage Supply G–1
G.2 PHENIX NCC LV Supply G–2

List of Figures **F–1**

List of Tables **T–1**

References **R–1**

Chapter 1

Introduction and Executive Summary

Over the first five years of data taking at RHIC, numerous interesting measurements and discoveries have been made. In particular,

- The medium created in gold-gold reactions equilibrates very rapidly on times scales $\leq$2 fm/c as indicated by comparisons of the collective motion of created particles and hydrodynamic model calculations. In fact, these calculations indicate the medium after equilibration behaves like a nearly perfect liquid (low viscosity), demanding that the system be strongly interacting. In addition, the initial energy densities are extremely high - 2 orders of magnitude greater than an ordinary nucleus. The state of matter has been given the name Strongly Interacting Quark Gluon Plasma (sQGP)

- The cold nuclear matter viewed at large virtually may exhibit exciting features of gluon saturation - as described in the color glass condensate framework (CGC).

These conclusions have come from several experimental observations using the initial suite of PHENIX detector subsystems [1, 2].

1. The suppression of high energy particles in central heavy ion collisions at *mid-rapidity* together with the lack of suppression in deuteron nucleus collisions - jet quenching - indicating energy densities of 10-20 GeV/fm^3 - far above the critical energy density predicted by lattice calculations.

2. The large values of elliptic flow - indicating that the initial system thermalizes rapidly and has nearly zero viscosity.

3. The large baryon to meson ratio at moderate values of momentum (several GeV). This together with the scaling behavior of the elliptic flow indicates that the effective degrees of freedom at hadronization carry the quantum numbers of quarks.

4. The suppression of high energy particles at *forward rapidity* in deuteron nucleus collisions, consistent with the predictions of the CGC model.

In addition, the polarized p+p program has made initial steps in the measurement of the gluon contribution to the spin structure of the nucleon. It is important to note here that the measurements thus far have been at moderate x_{BJ}, and are consistent with the gluons carrying very little of the nucleon spin (albeit with very large error bars). Similar measurements at moderate x at SLAC in the early 1980's indicated that the quark contribution to the nucleon spin was consistent with the naive quark model. It was not until measurements at low x from CERN became available that it was realized that the quarks could only account for a quarter of the nucleon spin - and the "spin crisis" was born. Hence, measurements at low x are critical.

These observations, up to now, are currently rather qualitative particularly in the heavy ion program. Further understanding and discovery will require precision measurements. This will be made possible by an upgrade of the machine luminosity (RHIC II) and significant upgrades of the detectors. The demands of the program require that the unique capabilities of the PHENIX Experiment at RHIC - that is the ability to make precision measurements of leptons and photons - be extended to larger coverage.

We have designed a pair of PHENIX Nosecone Calorimeters (NCC) covering both positive and negative rapidity regions. Even one of the pair will significantly enhance the physics capabilities of the PHENIX detector by extending calorimetric coverage to forward rapidities and increasing the coverage by more than a factor of 10. A key advantage for the NCC is the presence of the muon spectrometer in the forward (and backward) regions. Together with the Forward Silicon vertex Detector, the NCC will make PHENIX a nearly 4π spectrometer, capable of detecting photons, electrons, muons, and hadrons. Our prime motivation is to provide precision measurements of direct photons, π^0s and dielectrons in A+A, p(d)+A, and polarized p+p collisions. The upgrade will provide access to the physics observables that are not currently accessible to PHENIX or are now available only indirectly with very limited accuracy. The primary measurements addressed by the NCC are:

1. The Strongly Interacting Quark Gluon Plasma - Heavy Ion Collisions
   (a) The opacity of the sQGP via studies of correlated high energy hadron-jet and γ-jet events
   (b) The suppression of the charmonium and bottomonium states due to screening via measurements of the χ_c and χ_b states
2. The structure of very high energy density cold nuclear matter and the fate of the gluon structure function over a large x-range as a precursor to the sQGP. These studies will be done in p(d)+A Collisions via measurements of
   (a) direct photons and jets
   (b) hadrons (particularly π^0s and ηs)
   (c) dielectrons
3. The spin structure of the nucleon, particularly at low x_{BJ} - polarized p+p collisions via

(a) Direct photons and jets

(b) hadrons (particularly π^0s and ηs)

(c) W isolation

Some of the strengths of the NCC are as follows. Firstly, by correctly identifying multiphoton showers in the high position resolution layers built into the calorimeters we will measure π^0 yields at large rapidities thus extending the PHENIX sensitivity to jet quenching studies. Secondly, by increasing acceptance for the direct photons we will make possible the study of correlated photon-jet production, which is a critical process for understanding the Color Glass Condensate and its relevance to initial state modifications in heavy ion collisions, as well as in understanding the opacity of the sQGP. The NCC will extend the measurement of the gluon structure function to low-x values $\approx 10^{-3}$, critical both to the understanding of a possible CGC phase, and the spin structure of the nucleon. Finally, by providing energy measurements within a cone around lepton or photons, the NCC will dramatically improve background conditions for the identification of leptons from W and charm decays, and direct photons, *i.e.* particles being emitted from the initial hard processes being studied.

The NCC replaces the present Copper Nosecones in front of the muon spectrometer. The NCC is a silicon-tungsten sandwich sampling calorimeter, which is longitudinally composed of 3 calorimeter sections read out by Si pads 1.5×1.5 cm^2. In addition there are two precision sections readout by strip-pixels at 468 μm pitch. These are located at a depth of 2 and 7 radiation lengths and enable us to identify, and measure π^0s to high energy even when there is an overlap of showers in the pads. This also allows the separation of direct photons and high energy π^0s.

To avoid cost intensive and time consuming R&D, we relied heavily on established technologies and expertise already available in collaborating laboratories. For the calorimeter we propose to use silicon sensors closely resembling those currently in use for prototyping future calorimeter for ILC and a number of cosmic ray experiments. For coordinate detectors we follow the lead of the PHENIX Silicon Vertex Tracker and use pixilated strips with 2-D sensitivity. As a backup to this latter solution we are working with the NUCLON experiment in Russia on implementing standard one-coordinate strip detectors with the identical strip width of 468 μm. We plan to use hybrid preamplifier chips developed at BNL for the ATLAS experiment at CERN as a base solution for signal conditioning in calorimeter and the SVX4 readout chip developed at FNAL to readout the strip detectors.

Over 70 NCC participants from 20 institutions are cooperating to design, construct, install, and operate the NCC. Among these participants are many experts with extensive experience in calorimetry, in silicon detector technology, the design, fabrication and operations of modern readout electronics, mechanical and integration issues, software experts as well as physicists who are well versed in the different aspects of analysis necessary to extract physics from this detector. With the help of institutional contributions, PHENIX was able to maintain a small but well focused effort over the past two years to aid in the design of the detector, and to establish expertise in the relevant technologies.

We propose to construct our NCC detector over a period of three years, U.S. FY08, FY09, and FY10. To carry out this project we seek funding of a total of $4M through the DOE Office of Nuclear Physics. While the plan is to eventually construct an NCC for both the North and South arms of the PHENIX spectrometer, we propose to initially build only one NCC using funds from the DOE. We are actively working to secure funding for a second NCC from our Japanese and European colleagues, in particular the RIKEN Institute of Japan which is already participating in the R&D effort. In addition, we expect smaller contributions from the Czech Republic and Russia. A majority of the physics topics discussed in this proposal will be addressed using just one NCC. However, there are significant advantages to having two NCC detectors available. These include (a) in p+A collisions - the ability to simultaneously study the proton and the heavy ion side of the collision, (b) in p+p collisions - the ability to provide isolation cuts for W boson physics for the measurement of anti-quark spin, and (c) a factor of 2 in rate for rare processes such as high momentum direct photons and the χ_c.

Considerable progress has been made in the past several months. In particular the design is a great deal more mature, particularly in the readout and assembly. Further prototype tests have been made of sensor design of both the pads and stripixels. We have also begun to identify collaborators with the capabilities to test and assemble the various parts of the detector.

The structure of this document is detailed in the Table of Contents on pages *iii* to *v*:

- Chapter 2 discusses the physics motivation.
- Chapter 3 presents a detailed description of the NCC and technical aspects of the project.
- Chapter 4 gives a preliminary management plan of the project, including the roles and responsibilities of the participating institutions.
- Chapter 5 shows the Budgets and Schedule.
- Appendix A presents event rate estimates
- Appendix B describes several simulation studies.
- Appendix C gives the results of analysis done on data taken from a prototype module in a test beam at Protvino. in a test beam. details on the Silicon Strip Sensors.
- Appendix D describes R and D done.
- Appendix E describes an analysis of the pad sensor readout chain.
- Appendix F gives details on the Silicon Strip Sensors.
- Appendix G gives details on the power.
- Lists of Figures, Tables, and References conclude the document.

Chapter 2

Physics Overview

The NCC increases the calorimetric coverage of the PHENIX detector to forward and backward rapidities so that the total coverage is increased by more than an order of magnitude. This impacts the entire PHENIX physics program in Å, p(d)+A, and polarized p+pcollisions. This section gives an overview of the physics program relevant to the NCC in each of these three areas. For the study of heavy-ion collisions, the essential questions revolve around our understanding of the sQGP state of matter. High $p_\perp$ photons opposite a high energy parton can be used as a calibrated probe to measure the energy loss of quarks or gluons in the plasma. It now appears that, at least in some energy regimes, the energy loss exhibits itself up as a bulk response of the system yielding a shock wave in the form of a Mach Cone or Cerenkov emission, as might be expected from a continuous medium. The yield of charmonium and bottomoniunm states - particularly the χ_c measured in conjunction with the muon spectrometer, will give information on the deconfinement temperatures. Finally, since the NCC can be used to find the reaction plane with great accuracy, all such signatures can be studied as a function of the geometry of the colliding system. This should lead to very accurate measurements of the energy loss of high momentum partons in the plasma.

As mentioned in the introduction the physics program at the Relativistic Heavy Ion Collider (RHIC) has given us a wealth of new information. The emerging picture is as follows: The initial state of the nucleus relevant to bulk system in AA collisions at RHIC energies is a state of saturated gluons - this has been given the name of a Colored Glass Condensate (CGC). This CGC state allows for a rapid thermalization of the colliding partons forming perfect fluid - that is - a system with viscosity near zero. This system - called the Strongly Interacting Quark Gluon Plasma (sQGP) is almost opaque to high momentum partons and has an energy density 50 times that of normal nuclear matter. These exciting results immediately lead to many questions which demand quantitative answers- among them: a)what is the energy loss mechanism of partons as they traverse this matter. Is the picture of energy loss by gluon radiation correct, or does the fact that the interactions seem to be so strong demand a different picture? How much energy is lost? b) What is the mechanism by which the CGC thermalizes so rapidly? c) Can we explicitly observe the deconfinement of quarks and gluons?

Direct photons, jets, and high momentum particles in polarized $p + p$ collisions are an effective way to make measurements of the gluon spin contribution. In addition transversely

polarized protons will give access to the transverse structure functions in of the nucleon. In conjunction with the muon spectrometer the NCC will allow us to make isolation cuts for the study of W bosons to measure anti-quark spin structure functions.

The electromagnetic calorimeter in the central region (EMC) has been a critical element in these discoveries - the strongest and cleanest understanding of the suppression of high momentum hadrons - i.e. "jet quenching" comes from $\pi^0 s$ measured by the EMC. The demands of the program require that the unique capabilities of the PHENIX Experiment at RHIC - that is the ability to make precision measurements of leptons and photons - be extended to larger coverage.

2.1 Heavy Ion Physics

2.1.1 Hard Scattering

Hard scattered partons are an important probe of the matter created in heavy-ion collisions. Because the hard scattering event occurs early in the evolution of the collisions ($\tau <$ 1 fm/c), the scattered partons can be affected by the evolution of the surrounding QCD matter, particularly if this matter passes through a deconfined phase. The scattered partons will be sensitive to the medium primarily through the mechanism of energy loss resulting in a reduction of the energy available to the parton when it fragments into hadrons. This phenomenon was predicted to lead to a suppression of particles with large transverse momentum in heavy-ion collisions at RHIC and this suppression has been quantified by excellent measurements from the first RHIC runs [3, 4, 5, 6]. Measurements in d+Au collisions have demonstrated that the suppression is not due to initial state effects [7].

The four RHIC experiments have measured charged particle spectra from Au+Au collisions at $\sqrt{s_{NN}} = 130$ and 200 GeV, with measurements for unidentified hadrons extending out to $p_T \sim 12$ GeV/c. All of these measurements show a suppression of high transverse momentum hadrons in central collisions when compared to data from p+p collisions (suitably scaled by the number of binary collisions and the energy difference). The PHENIX detector is also capable of reconstructing the decay of the π^0 meson to two photons using the electromagnetic calorimeter in both central arms. Using the measured production of π^0 mesons in both p+p and Au+Au collisions, we can construct a ratio known as the nuclear modification factor R_{AA}:

$$R_{AA} = \frac{dN_{AA}}{< N_{coll} > \times dN_{pp}} \tag{2.1}$$

where dN_{AA} is the differential yield for a point-like process in an AA collision, and dN_{pp} is the differential yield for the same process in nucleon-nucleon collisions. The number of binary collisions for a given centrality class N_{coll} is estimated using a Glauber model of the nuclear overlap. In the naive limit that a nucleus-nucleus collision can be though of as a superposition of independent nucleon-nucleon collisions, the nuclear modification faction at high p_T should be unity. The nuclear modification factor for charged hadrons and neutral pions as measured by the PHENIX collaboration is shown in Figure 2.1. There is a significant suppression of high transverse momentum hadrons observed in Au+Au collisions, consistent

with substantial energy loss of the scattered partons. A similar suppression was observed in data taken at $\sqrt{s_{NN}} = 130$ GeV [3]. Models of energy loss that incorporate the expansion of the system indicate the energy loss in the matter created in heavy-ion collisions at RHIC may be as much as fifteen times larger than the energy loss of a comparable parton in ordinary nuclear matter [8].

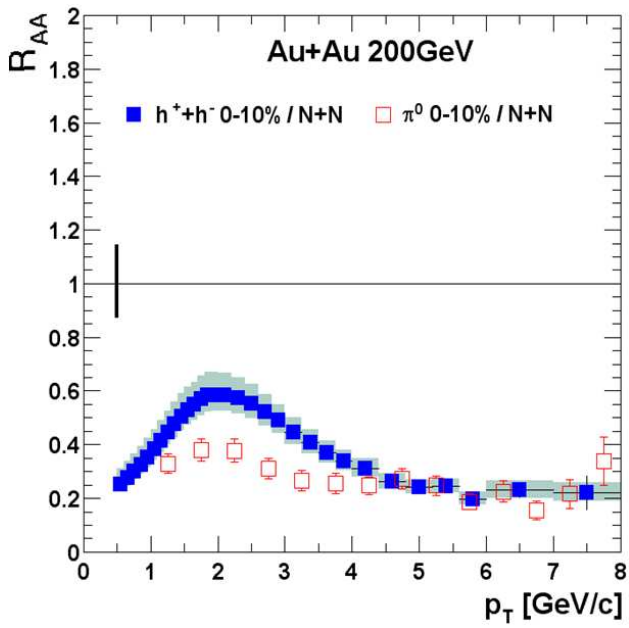

Figure 2.1: R_AA for π_0 mesons and inclusive charged particles from as measured by PHENIX. The difference in the observed suppression for charged hadrons and neutral pions between 1-4 GeV/c is due to the changing particle composition of the charged hadrons, highlighting the importance of the π^0 measurement.

In heavy-ion collisions at RHIC energies direct detection of jets is complicated by large backgrounds from particles in the underlying event. However, jets of hadrons can still be identified using two-particle correlation techniques, which take advantage of the fact that hadrons resulting from a parton cascade will be correlated in azimuthal angle and pseudorapidity. Such techniques make use of the "leading hadron" effect in jet fragmentation, where a single hadron often ends up with a large fraction of the parton momentum. Selecting high transverse momentum hadrons provides a good proxy for the jet direction and momentum. At high-p_T inclusive charged particles can often be subject to background processes that result in a low-p_T particle being reconstructed at high momentum. In contrast, the measurement of π^0 mesons becomes essentially background-free at high-p_T. In addition, at RHIC the particle composition of the inclusive charged measurements change dramatically for transverse momenta between 2 and 5 GeV/c [9], further complicating the physics interpretation.

The PHENIX experiment used the central arm electromagnetic calorimeters (EMCal) to measure π^0 production to very high transverse momentum in a variety of colliding systems.

These measurements demonstrated the power of exploiting the measurement of π^0 mesons with an electromagnetic calorimeter in relativistic heavy-ion collisions.

Originally the mechanism of energy loss was thought to be primarily through medium-induced gluon radiation [10, 11, 12, 13, 14, 15, 16, 17], however recent results from PHENIX looking at electrons from the decay of heavy quarks show suppression as strong as for light quarks Figure 2.2 [18]. Gluon radiation should be significantly reduced for heavy quarks, and one would expect that the suppression should be much weaker. In order to explain the data, models of energy loss via gluon radiation must invoke parameters - e.g. gluon density - which are far in excess of what is reasonable. This has led theorists to examine other mechanisms such as collisional energy loss.

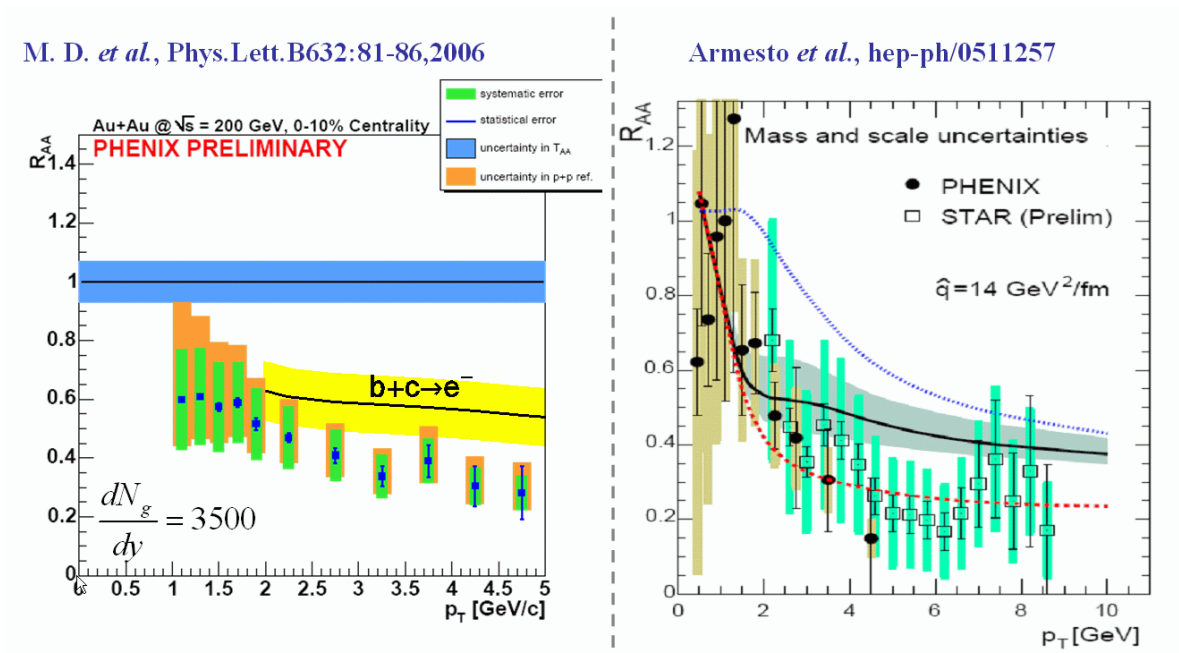

Figure 2.2: Data from PHENIX and STAR showing electrons from charm and bottom decay as compared to models theoretical models of Djordjevic et al (left) and Armesto et al (right) where values of dN/dy and $\hat{q}$ far in excess of reasonable values are required to fit the data. (Say this better) [19, 20]

2.1.1.1 Photon-Tagged Jets

The suppression of high-p_T hadrons seen at RHIC is a complicated interplay between the density and time evolution of the created matter, the collision geometry, and the transverse momentum of the probe. Disentangling these effects in such a way as to allow detailed comparisons between theoretical models of energy loss is complicated by the number of factors that affect the suppression observed in the final state. One way to simply the observables is to use jets that are produced in coincidence with photons via a QCD-Compton process (see Figure 2.3). The photon escapes the colored medium essentially unmodified and without

undergoing energy loss, and therefore provides a measure of the total energy of its partner jet. The cross-section for such a process is substantially smaller than the full dijet cross section, however, and the detection of direct photons in such an environment is difficult.

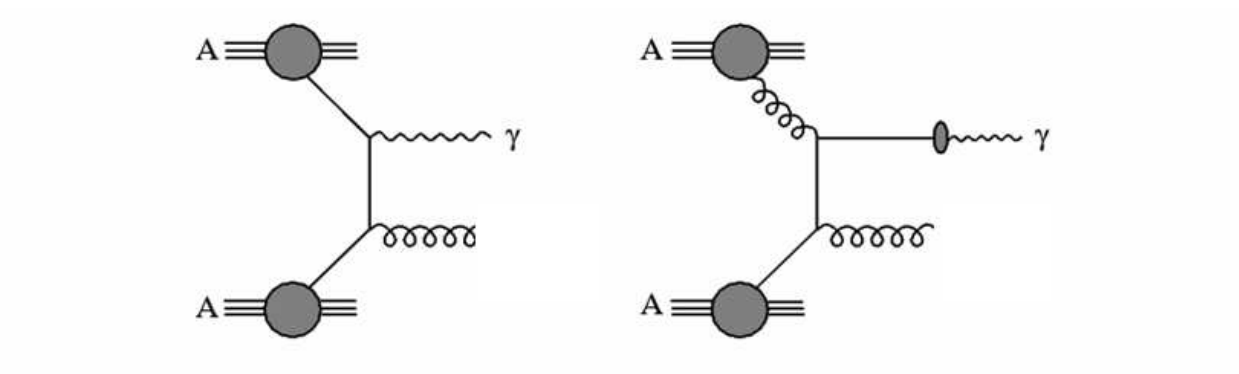

Figure 2.3: Tree level diagrams for the production of direct photons by QCD-Compton processes. The photon produced in the hard scattering only interacts electromagnetically and will escape the surrounding medium produced in nucleus-nucleus collisions without interacting. The jet produced by the partner parton in the interaction will, however, interact and suffer energy loss. Measuring both the photon and jet in the final state allows for a calibration of the energy loss.

Direct photons at mid-rapidity in AuAu collisions at $\sqrt{s_{NN}} = 200$ GeV have already been measured by the PHENIX collaboration, as shown in Figs. 2.4 and 2.5. These initial measurements demonstrate not only the feasibility of measuring direct photons in a heavy-ion environment but the observed scaling with the number of binary collisions indicates that the photons do indeed survive unmodified to the final state. Future studies with photon-tagged jets will allow a detailed, quantitative study of the energy loss suffered by the partner jet, further elucidating the nature of the matter created at RHIC.

2.1.1.2 Response of the Medium

Experiments have been able to study the response of the medium gaining understanding of the energy loss by selecting high momentum hadrons or direct photons and examining the recoil particles on the opposite side. One finds that the recoil particles show a behavior which may be indicative of a shock wave, such as a Mach cone Figure 2.6. [CITE-mach cone correlation data]. Instead of thinking of the process of energy loss as in a pQCD framework, it may be more be more enlightening to think of the system as a continuous medium - a fluid - and to calculate and measure transport coefficients such as the viscosity and diffusion coefficients and other quantities such as the speed of sound. Recently a powerful new theoretical technique has been used to calculate transport calculations directly using AdS/CFT correspondence from string theory. While the theory that is modeled is a super-symmetric conformal field theory - it has been shown to behave at high temperatures - particularly near the critical point, in a manner similar to QCD. [CITE-AdS/CFT similar

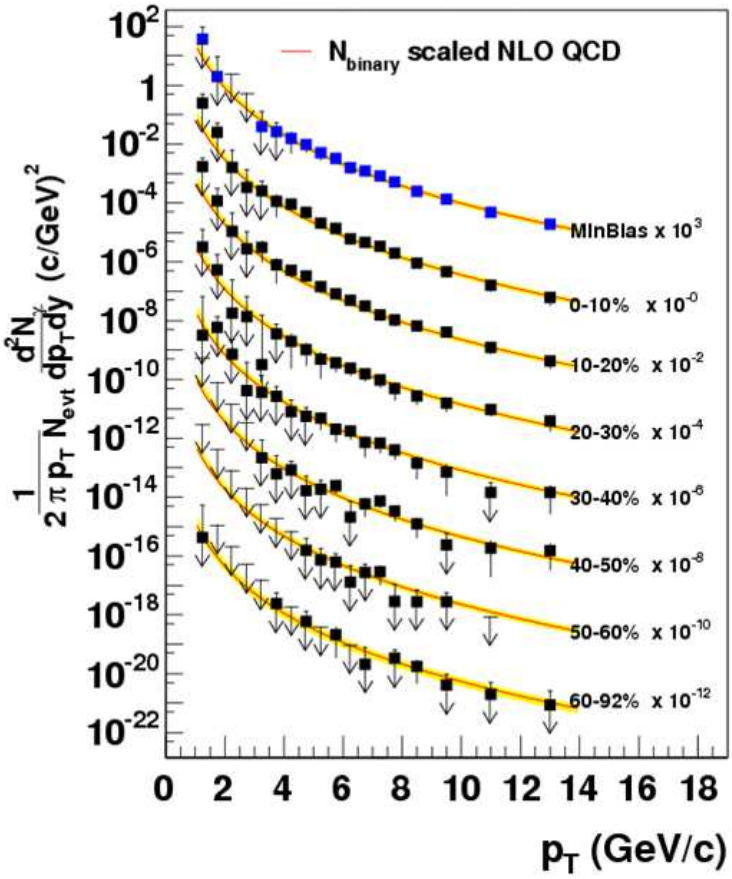

Figure 2.4: Measured direct photon invariant multiplicity at mid-rapidity as a function of centrality in AuAu collisions.

to QCD] This connection between a gravitational theory in 5 dimensional AdS and RHIC physics is clearly an exciting avenue that must be pursued. There have been many papers published on this subject in the past few years. The first of these calculations done by Son and his collaborators, calculated the viscosity in such a theory and found it to be very small - presumably exactly what we are seeing at RHIC [21]. Gubser and his colleagues have calculated the response of the to the loss of energy from high momentum partons, and find that the medium responds by producing a "Mach Cone" [22, 23]. It has been suggested by Shuryak and Antroini that the angular opening of such a cone should be dependent on the mass of outgoing parton [24, 25]. Whether one takes these ideas at face value, it is clear the characteristics of particles correlated with outgoing high momentum partons be carefully measured as a function of the energy or momentum, the mass of the outgoing parton, the rapidity and the centrality.

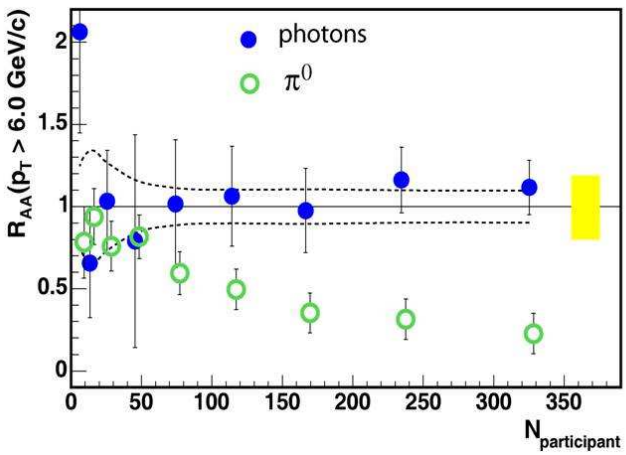

Figure 2.5: R_{AA} for direct photons as a function of transverse momentum as compared with that for $\pi^0 s$ showing that the direct photon suppression is consistent with zero.

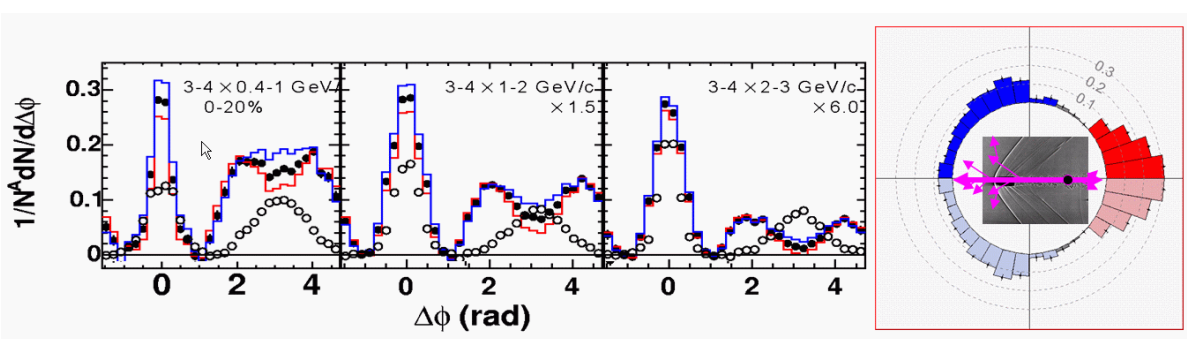

Figure 2.6: (left) jetcone (right) jetcone

2.1.1.3 Contribution of the NCC

The NCC would add substantial rapidity coverage to the PHENIX detector for the detection of photons and π_0 mesons, covering $1 < |\eta| < 3$, and increasing the overall coverage PHENIX acceptance about a factor of 10. Jet physics and energy loss studies using both photon-tagged jets as well as leading π_0 mesons will be possible with the NCC. This additional pseudorapidity coverage will allow for the study of physics observables away from central rapidity. Because the effective energy density of the created matter decreases as a function of pseudorapidity, when combined with measurements in the central arms, the NCC observables will provide a robust picture of the created matter for a variety of energy densities within a single colliding system.

For the measurement of the "Mach Cone" mentioned above, trigger particles can be hadrons (light quarks or gluons), heavy quarks or direct photons. Heavy quarks can be identified by the FVTX and the VTX detectors together with leptons measured in the EMCAL, the Muon Arms, and the NCC. Direct photons and hadrons)π^0s can be identified and measured in the NCC adding to the capabilities in the central arms. The NCC will then be capable of detecting particles correlated with these trigger particles (i.e. those particles forming the related "Mach Cone") over a large range of rapidity in the forward and backward directions.

2.1.2 Heavy Quarkonia

Heavy quarkonia states are amongst the best probes created in heavy ion collisions for understanding modifications of the interactions amongst partons in the medium - perhaps a quark gluon plasma. The formation of charm-anticharm $c\overline{c}$ and bottom-antibottom $b\overline{b}$ quark pairs occurs on very short time scales given the inverse mass ($t \approx 0.1$ fm/c). A small fraction of the time the pair evolves into a physical bound quarkonia state with a time scale given by the relative momentum of the heavy quarks in the bound state ($t \approx 1$ fm/c). Since charm and bottom quarks have a mass much larger than the expected temperature of the medium, they are only abundantly created in the earliest stage of the nuclear collision. Thus, we can unambiguously ascribe the final yield of heavy quarkonia to how the quarks and antiquarks interact with the surrounding cold and hot nuclear medium between their creation time and the final freeze-out of the system ($t \approx 10$ fm/c).

The original suggestion [26] that color screening in a deconfined medium should lead to a suppression of heavy quarkonia states has evolved significantly over the past 20 years. New evidence from studies of lattice QCD reveal that many of the quarkonia states continue to exist, in modified form, inside the deconfined medium of a quark gluon plasma up to temperatures well beyond the expected 170 MeV transition value [27]. The current state of the art in lattice QCD yields a somewhat ambiguous picture where considerations of free energy give a different melting point for quarkonia than studies of the spectral functions [28, 29]. However, it is common amongst the pictures that the more weakly bound ψ' and χ_c should be modified and melt at a lower temperature compared with the J/ψ and Υ states. This is shown from two different calculations in Table 2.1 [30]. The sequential suppression expected as one increases the temperature of the medium is shown in Figure 2.7 [31].

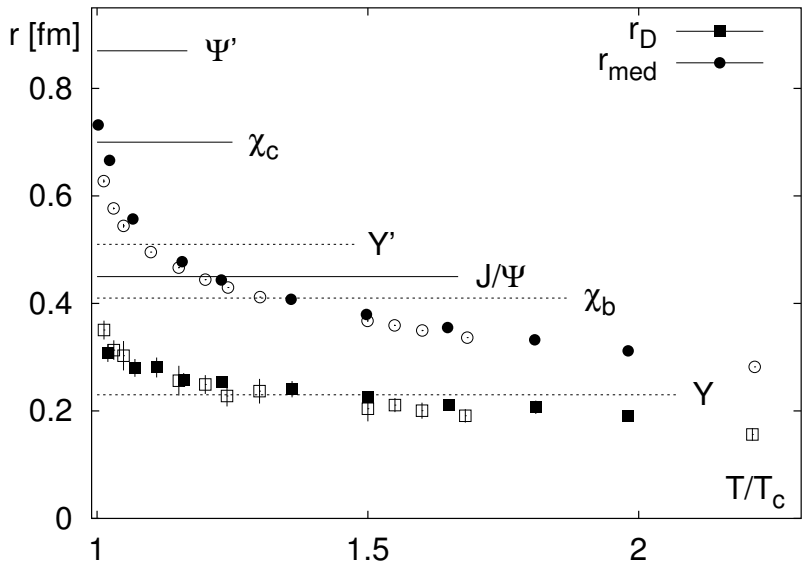

Figure 2.7: The scale r_{med} which gives an estimate for the distance beyond which the force between a static quark anti-quark pair is strongly modified by temperature effects and the Debye screening radius, $R_D = 1/m_D$. Open (closed) symbols correspond to SU(3) (2-flavor QCD) calculations. The horizontal lines give the mean squared charge radii of some charmonium and bottomonium states.

Table 2.1: Dissociation temperatures obtained from different analyses in quenched QCD.

Heavy Quarkonium	$U^{(1)}_{Q\bar{Q}}(\mathbf{r},T)$ Potential	$F_1(\mathbf{r},T)$ Potential	$U_1(\mathbf{r},T)$ Potential	Spectral Analysis
$J/\psi, \eta_c$	$1.62\,T_c$	$1.40\,T_c$	$2.60\,T_c$	$\sim 1.6\,T_c$
χ_c	unbound in QGP	unbound in QGP	$1.19\,T_c$	dissolved below $1.1\,T_c$
ψ', η_c'	unbound in QGP	unbound in QGP	$1.20\,T_c$	
Υ, η_b	$4.10\,T_c$	$3.50\,T_c$	$\sim 5.0\,T_c$	
χ_b	$1.18\,T_c$	$1.10\,T_c$	$1.73\,T_c$	
Υ', η_b'	$1.38\,T_c$	$1.19\,T_c$	$2.28\,T_c$	

Particular interest in the χ_c state, in addition to the J/ψ, is twofold. First, in the different lattice calculations is a likely that the χ_c and J/ψ states span the binding energy range where one of the states at least will have some color screening effects. Second, it is expects from hadron-hadron and hadron-nucleus measurements that of order 40% of the reconstructed J/ψ are from χ_c decay feeddown. Thus, the measurement of both states is likely necessary

to disentangle various effects and extract the fundamental physics from this probe.

There are three P wave quarkonia states $(\chi_{c1}, \chi_{c2}, \chi_{c3})$ all of which can decay via $\chi_c \longrightarrow \gamma J/\psi$, though only the first two have appreciable branching fractions, 0.27 and 0.17 respectively. The PHENIX experiment currently measures the J/ψ away from mid-rapidity via reconstruction of the two decay muons, and needs to add the capability to measure the associated photon. The photon from the radiative decay of the χ_c has a small relative momentum to that of its parent and therefore the proposed nosecone calorimeter has good acceptance (58%) for γ when the J/ψ is accepted into the existing PHENIX forward spectrometer. In addition, due to the forward rapidity of these χ_c, the photon is boosted and can have an appreciable momentum.

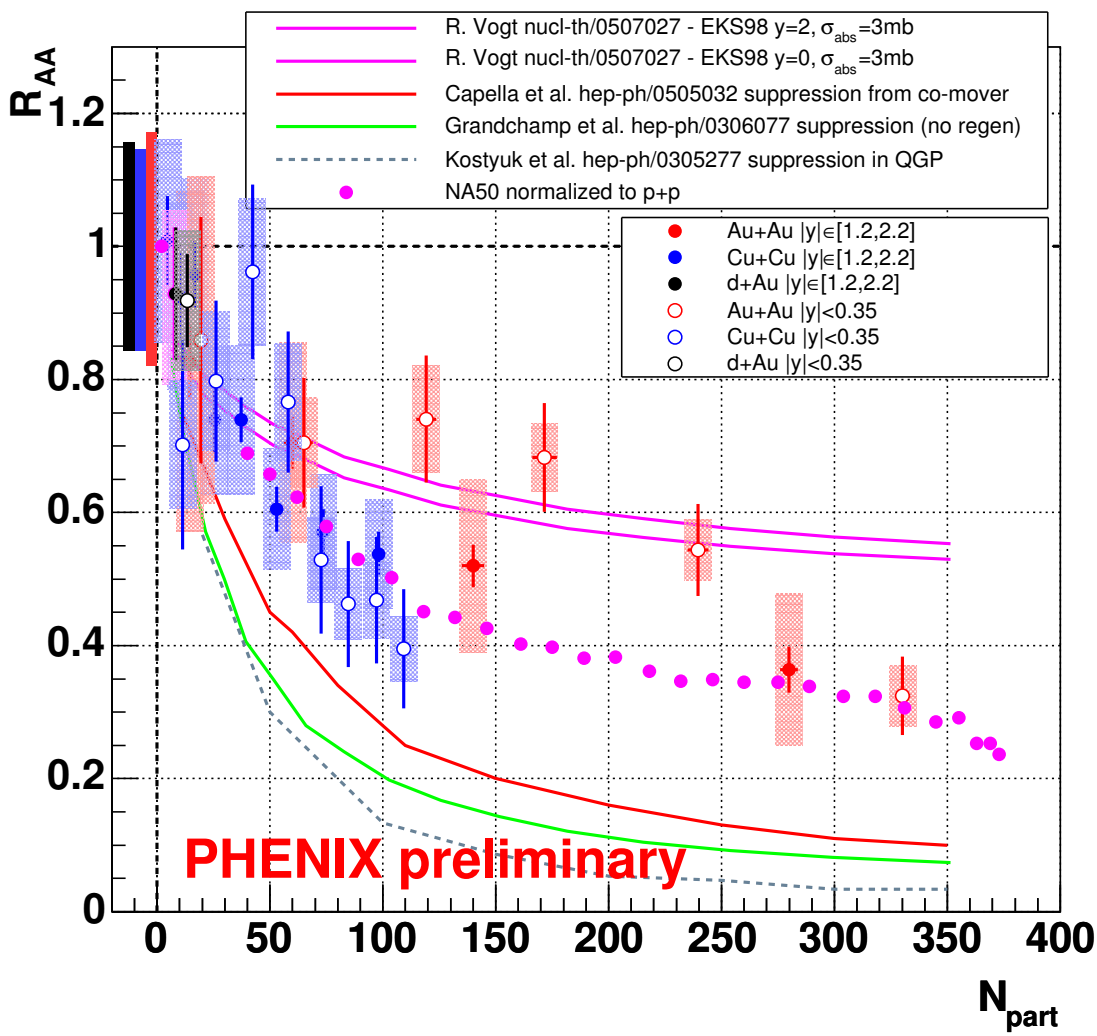

Figure 2.8: PHENIX Preliminary R_{AA} for J/ψ in $Au+Au$ and $Cu+Cu$ 200 GeV reactions.

The first statistically significant results on heavy quarkonia in heavy ion collisions at RHIC Fig. 2.8 come from the PHENIX experiment [32]. Although the results are currently in preliminary form, a very striking and perhaps surprising observation has been made. As shown in the figure below, the nuclear suppression factor is quite similar at RHIC energies as the results from the NA50 and NA60 experiments [33, 34] at the CERN-SPS, almost an order of magnitude lower in collision energy. Most model calculations of expected J/ψ production, whether via color screening or co-mover absorption, predicted a substantially larger suppression at RHIC due to the higher energy density and also higher temperature. In fact, there were many predictions that the J/ψ might be so suppressed as to make any observation difficult, and thus turning the focus to the more tightly bound and thus less suppression Υ(1s) state. However, this new experimental information, drives us to make precision measurements not just of the more tightly bound states, but the less tightly bound χ_c and ψ'.

2.1.2.1 Contribution of the NCC

In order to see the χ_c one reconstructs the $\mu^+\mu^-\gamma$ invariant mass and subtracts off the $\mu^+\mu^-$ invariant mass where the dimuon mass is required to be in the J/ψ peak. The χ_c should show up as a peak at the χ_c-J/ψ mass difference of about 400-500 MeV. PHENIX has made a proof of principle measurement of the χ_c in pp collisions using the central arms, where we have electromagnetic coverage. See Fig. 2.9. While it will be difficult to obtain enough statistics in the central arms to make a measurement of χ_c suppression in heavy ion collisions, the substantially larger acceptance of the NCC together with the muon arms will make this measurement possible.

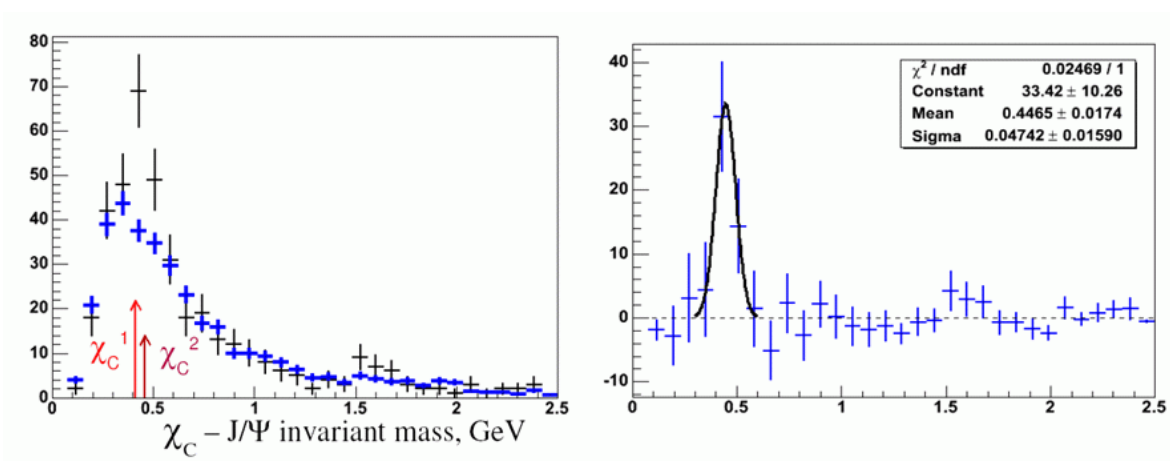

Figure 2.9:
$J\psi\gamma J\psi$ invariant mass spectrum showing the χ_c peak in pp collisions as seen by the PHENIx central arm in run-5. We see about 50 χ_c. Background subtracted spectrum is shown on the right. The resolution of the peak is about 50MeV consistent with the resolution of the EMCAL.

The expeced R_{AA} for the χ_C as measured by the NCC is shown in Fig. 2.10 where the

J/ψ is detected via its di-muon decay in the muon spectrometer. The photon detected by the NCC is in the rapidity range 1¡—y—¡1.5 (we need to show others later. This is compared to the R$_A A$ of the J/ψ measured by PHENIX in Run-4. Errors for the χ_C are statistical only. It is assumed that the pp measurement of the χ_C adds a negligible error to the ratio. The errors are of the order of 10% which simply comes from the fact that about 10K χ_C's are detected over a background of 600K. Since this is a S/B of less than 2%, systematic errors on the background subtraction must be evaluated carefully. This needs to be pursued. Ultimately we will need test beam data to understand how well we can the multi photon background to the signal photons, and a test where the prototype is put into PHENIX for a short while to measure the level of expected backgrounds.

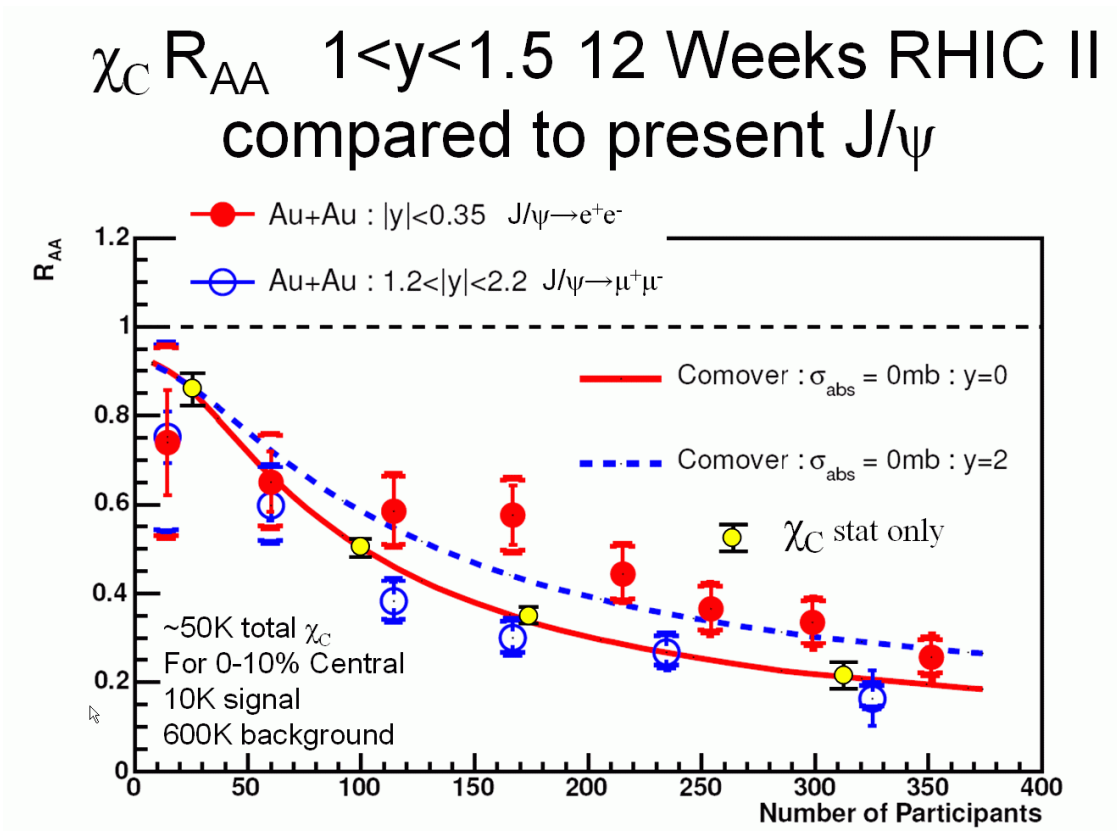

Figure 2.10: R$_{AA}$ for the χ_C in where the χ_C decays to a J/$\psi + \gamma$ and the J/ψ is detected via its di-muon decay in the muon spectrometer. The photon detected by the NCC in the rapidity range 1¡—y—¡1.5 (we need to show others later. This is compared to the R$_A A$ of the J/ψ measured by PHENIX in Run-4. Errors for the χ_C are statistical only. It is assumed that the pp measurement of the χ_C adds a negligible error to the ratio.

2.1.3 Charm via Electrons

Further PHENIX upgrades include a silicon vertex detector with coverage matching that of the forward muon spectrometer. With the additional capability to statistically tag displaced

vertices's, we greatly extend our ability to measure charm and bottom via single muon semi-leptonic decays by rejecting much longer lifetime muon backgrounds from pion and kaons decays. Additionally, one can then separate J/ψ contributions from B meson decay. Putting this information from the forward silicon detector with the nosecone calorimeter, may allow for the tagging of forward rapidity electrons which has a displaced vertex. In principle, one can then separate the charm and bottom semi-leptonic decay electrons from the very prompt Dalitz decays and conversions. This could be complementary to the single muon program. In reality the kinematic coverage for both is limited by the coverage of the silicon detector and both measure essentially the same thing with quite different kinematics.

We note that with a limited number of layers in the silicon detector, significant detailed studies on whether a clean electron sample can be obtained in proton-proton or heavy ion reactions must be completed.

2.2 p+A Physics, Nucleon Structure and Saturation

A system of very low viscosity is formed very early (t $\approx$ 1 fm/c) in the collisions of heavy ions. As mentioned above, pQCD calculations predict thermalization times longer than this. How then, can the system thermalize so quickly? An exciting new development has emerged, in that non-perturbative methods of calculating the early stages of such collisions are now available in a formulation often referred to as the Colored Glass Condensate. Such calculations indicate that the low-x partons in nuclear collisions are packed together such that their nuclear wavefunctions overlap and saturation occurs - thereby distorting the wave-functions. It is precisely these low-x partons which lead to the formations of most of the low momentum partons in a RHIC collisions which make up the dense sQGP. Various ideas have been formulated which allow for the thermalization of the system starting from the CGC. [35, 36, 37, 38]

The NCC upgrade will offer many exciting new opportunities for the study of this regime by studying p(d)+A collisions. It is important to note that the c.m. energy at RHIC is more than a factor of 5 greater than any existing fixed-target experiments. This fact, together with the forward rapidity acceptance of the NCC makes accessible kinematic regions not accessible before - in particular - the low-x region where CGC calculations are applicable.

In the following we briefly discuss the CGC model and measurements which have been made by the present PHENIX detector. It will be made clear why the measurement of the CGC must be made in the forward rapidity region. In addition, several other topics of interest in pA collisions will be discussed.

2.2.1 The Colored Glass Condensate

Recently, Mclerran and his collaborators [39, 40, 41] have used a classical approximation for the initial stage of a heavy ion collision, arguing that the occupation numbers at low x where much of the particle production occurs are rather high (see Fig. 2.11). This model - which they have named the "Colored Glass Condensate"- shows the phenomenon of gluon saturation and makes predictions which can be used to calculate the initial conditions in a heavy

ion collision which in turn can then be used as input to the hydrodynamical calculations. This calculation relies on the fact that very early in the collision, gluon saturation effects at low x set a value of Q$\sim$Q$_S$ where α_S can be considered small but the occupation numbers are high. The value of Q_S at RHIC is 1-2 GeV so $\alpha_S^2 \sim \frac{1}{10}$. Fig. 2.12 shows the region of of x and Q where this saturation should take place. The saturation assumed by these authors is present in the initial state before the nuclei collide. Hence the study of proton-nucleus collisions will be important in distinguishing these effects, from final state effects such as the formation of a quark-gluon plasma.

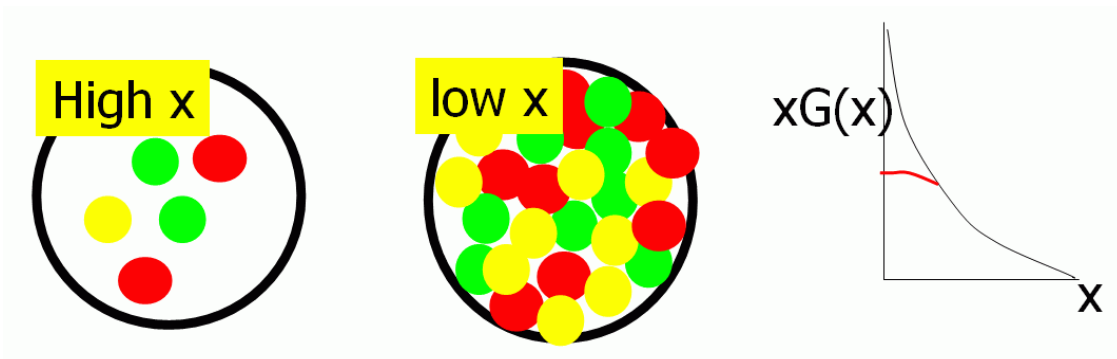

Figure 2.11: A schematic showing the saturation of the gluons at low-x. This has the effect of suppressing very low x gluons and pushing them to higher-x

Such an effect is consistent with electron-proton collisions at HERA [42]. In a heavy ion collision, the nucleus acts as an amplifier of the effect because of the the thickness of the nucleus. Saturation effects which in a proton would be at x 10^{-4} would show up in pA collisions at x 10^{-2}. Investigations of CGC signals use the fact that in going to forward rapidities, one begins to sample a lower range in x in the nucleus.

The ratio

$$R_{CP} = \frac{Yield(central)/N_{coll}(Central)}{Yield(peripheral)/N_{coll}(Peripheral)} \tag{2.2}$$

is a measure of the yield per collision from hard processes coming from central as compared to peripheral collisions, where the peripheral collisions are taken as a baseline. If pp data is available, it is often used as the baseline as will be done later in the definition of R$_{AA}$. Using punch-through hadrons identified in the muon spectrometer PHENIX looked at this ratio in deuteron-nucleus collisions. For a given p_T, a lower and lower value of x is sampled as one moves to higher rapidity. Since the gluon structure function increases at low x one would see a stronger suppression as one moves to higher rapidity. Fig. 2.13 shows just this effect, with the more central collisions showing a larger suppression. One interesting fact is that in the backward rapidity region, a strong enhancement is shown.

2.2.1.1 Contribution of the NCC

The NCC will be directly sensitive to the gluon structure function (or what is taken for a structure function in the CGC model) over a large region of x and Q^2 allowing measurements

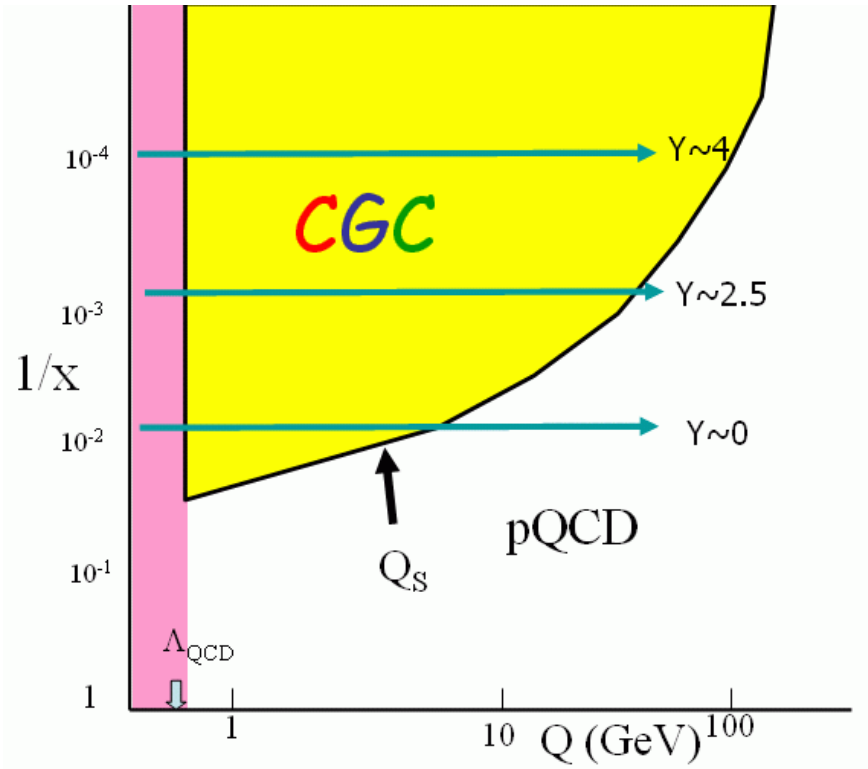

Figure 2.12: Regions of the nucleus showing the CGC region bordered by a line representing Q_S. As one goes forward in rapidity to regions covered by the NCC, one crosses into the CGC region.

both inside and outside the saturation regions shown in Fig. 2.12. At midrapidity in central heavy ion collisions, there is a clear difference between the suppression of direct photons and hadrons (see Figure B.1). This was clear sign that the suppression was due primarily to final state interactions - the sQGP; and not due to the initial state - the CGC. By contrast, for central pA collisions , neither hadrons nor direct photons, show suppression at midrapidity. As just mentioned, in the forward rapidity region, hadrons do show a suppression in pA collisions fig. 2.13. One important test is to look at direct photons. If the suppression is due to the initial state - that is the CGC - direct photons should also show a suppression. (See appendix C for a simulation of this effect.) By charting out the suppression vs centrality and rapidity the NCC will be able to map out the saturation regions shown in figure Fig. 2.12.

The following is a list of many interesting channels in the forward rapidity regions which are sensitive to gluon distributions which are accessible to the NCC. These channels include:

1. Single hadron production. Several hadrons can be readily detected by NCC via their decays to lepton/photon channels. The hadrons and their relevant decay channels include $\pi^0 \to \gamma\gamma$, $\eta \to \gamma\gamma$, $\omega \to \pi^0\gamma$, $\phi \to e^+e^-$, $J/\Psi \to e^+e^-$, $\Psi' \to e^+e^-$, $\chi_c \to \gamma J/\Psi$ followed by $J/\Psi \to e^+e^-$, and $\Upsilon \to e^+e^-$. The p-A data at forward rapidity region on the production of these particles would significantly enhance the physics reach of PHENIX which is currently limited to heavy quarkonium and punch-through hadrons.

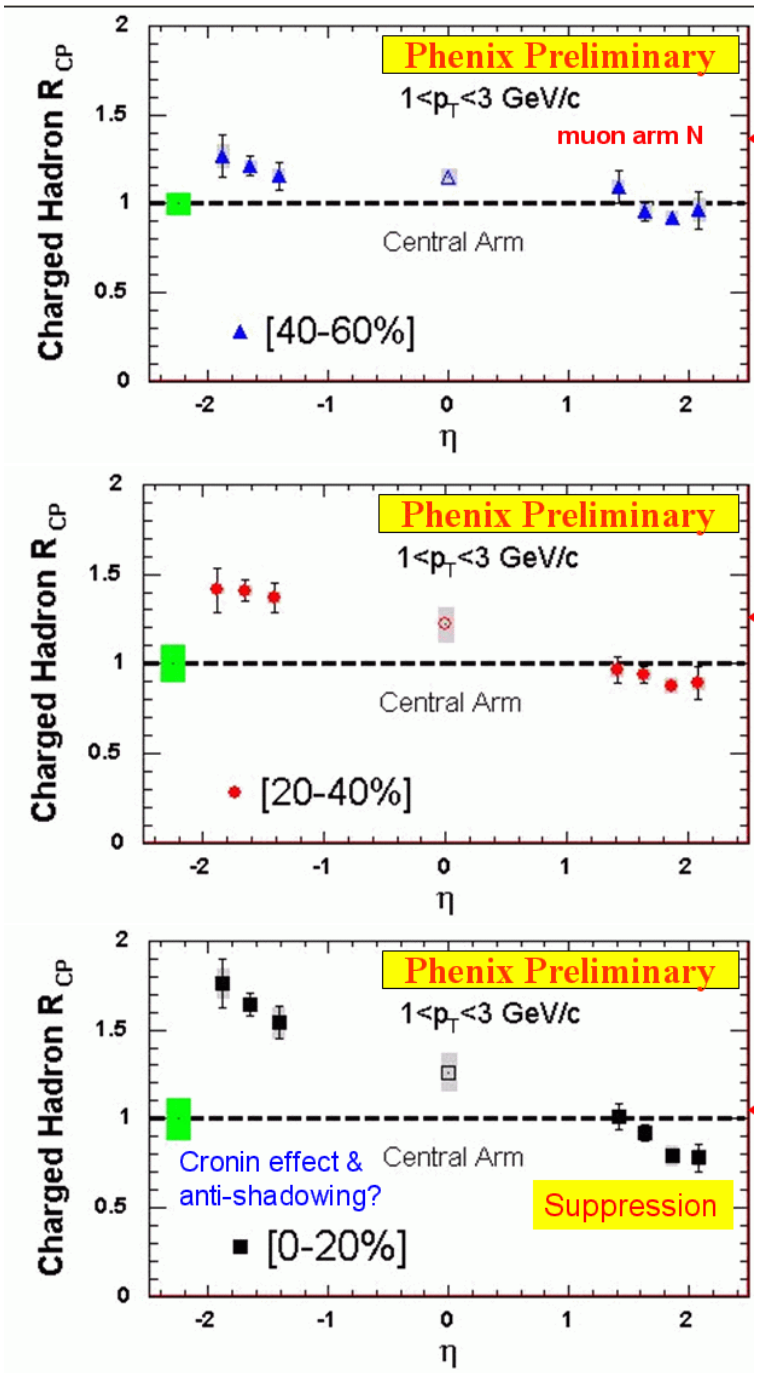

Figure 2.13: R_{CP} for charged hadrons as measured in by the PHENIX muon arms for different centralities.

2. Direct photon and jet production. The inclusive production of direct photons at forward rapidity is sensitive to the gluon distribution. Moreover, a measurement of direct photon in coincidence with a jet would be very valuable since the kinematic variables of the gluons can be readily reconstructed.

3. Dihadron production. The nosecone calorimeters will greatly extend the kinematic coverage for detecting dihadrons. A hadron such as π^0 or η could be detected in the NCC, while the other hadron could be measured by the barrel detectors. Energetic dihadrons would correspond largely to leading particles from dijet events, and can provide independent information on the gluon distributions in nuclei at small x.

4. Open charm and beauty production. In conjunction with the Forward Silicon Tracker, the NCC can be used to measure D and B meson productions via their semi-leptonic decays ($D \to eX$ and $B \to eX$). These heavy-quark productions are sensitive to gluon distributions. Furthermore, the acceptance for detecting a pair of charmed particle through their semileptonic decays is significantly enhanced when the NCC is combined with the muon spectrometers ($D \to eX$ in coincidence with $D \to \mu X$).

2.2.2 Other Physics Topics

2.2.2.1 Antiquark distribution in nuclei at small x

In addition to the study of the CGC, other topics can also be addressed in pA collisions in the forward rapidity region. In the past decade, nuclear shadowing at small x – has been very well characterized experimentally in DIS [43]. The experimental signature is that the DIS cross section ratio falls below unity for $x \leq 0.08$. Theoretically, shadowing has been studied extensively in the past 10 years [44].

Shadowing is also expected in hadronic processes. To date, the only experimental evidence for shadowing in hadronic reactions is the reduction in the nuclear dependence seen in the Drell-Yan experiments E772 [45] and E866 [46]. The lowest x covered in these experiments is $x = 0.04$, just below the onset of shadowing effect.

Shadowing in the $p + A$ Drell-Yan process is largely due to antiquarks in the nucleus, unlike in DIS, where quarks dominate for most of the explored region. Although shadowing effects are expected for antiquarks and gluons, there is no known requirement that they be identical [47] to those for quarks. There exists no experimental information on the antiquark shadowing at small x ($x < 0.04$). The coverage in x_2 will be significantly extended at RHIC. In particular, the lowest x_2 reachable at RHIC is around 10^{-3}, a factor of 40 lower than in E772. Therefore, nuclear shadowing effect of antiquarks can be well studied at PHENIX using the muon arms and the NCC to detect Drell-Yan events via the $\mu^+\mu^-$ and e^+e^- channels.

An important role of the NCC in the Drell-Yan measurement is that it will allow a realistic determination of the contribution of open-charm background to the dimuon (or di-electron) events. The $e\mu$ pair events from the NCC and muon arm would lead to a direct measurement of the charm background. This would enable a reliable Drell-Yan measurement down to the smallest possible x values.

2.2.2.2 Cronin effect and x_F-scaling

Finally, the Cronin effect, first observed in fixed-target experiments, has also been seen in d+Au data at mid-rapidity. The mechanisms for the nuclear enhancement of large p_T events are still poorly understood. In particular, the dependencies of the Cronin effect on the hadron species and on the hadron rapidity (particularly the negative rapidity region) remain to be measured at RHIC energies. A universal x_F-scaling behavior [48] has been noted for hadron productions in p-A collisions. The ability to measure a variety of hadrons at the forward and backward rapidity region with the NCC would shed much light on the origin of the Cronin effect, as well as the validity of the x_F-scaling.

2.3 Spin Structure of the Nucleon

2.3.1 Physics Motivation

The nucleon is the only stable state of quarks and gluons known, the constituent which gives the atomic nucleus its mass, and therefore the mass of the visible matter which surrounds and comprises humanity. Despite decades of study, a detailed understanding of this state has eluded us. QCD, born whole as a lagrangian, describes a force which is too strong and complicated for the calculational techniques we have developed so far. Only in high-energy collisions has one been able to apply a quite sophisticated perturbation theory, due to the small value of the strong coupling α_s at the high-energy scale, that is, asymptotic freedom. Recent advances in the computational power of lattice theorists imply that we are close to the beginning of a new era of non-perturbative QCD calculations which can be realistically compared to data.

Unpolarized deep inelastic lepton scattering and Drell-Yan experiments have provided most of the data from which we have formed our present understanding of nucleon structure at high energy, an understanding which is still primitive. The 1-dimensional momentum fraction of the quarks on the light cone has been mapped out from relatively low values up to roughly 85%, over a broad but unfortunately correlated range of resolution scales, i.e., Q^2. Already this has revealed a rich phenomenology of structure which can be understood, over many orders of magnitude in Q^2, as the rapid fluctuation of color field energy into matter. Given the empirical partonic structure at one resolution scale, we now can reliably calculate the structure at some other scale, even if we cannot predict the structure *ab initio.*

Nonetheless, we still have little understanding of the physics or even the empirical distributions at large momentum fraction. At very low momentum fraction, we are hampered by the experimental correlation with low Q^2 (large distance scale) resolution in order to test our understanding of the quark-gluon fluctuations which are observed. New, precise electron scattering experiments, using both the electromagnetic and weak force, give us the spatial charge and magnetization distributions of quarks in the nucleon, but are difficult to connect to the 1-dimensional light-cone momentum distributions. The newly recognized use of exclusive reactions to determine generalized parton distribution will allow us to empirically connect these two regimes.

At high energy, there remain two fundamental aspects of the nucleon partonic structure which are mostly poorly determined by experiment. One is the nature of the quark and gluon motion transverse to the light-cone momentum direction, in other words, the true 3-dimensional momentum distribution. The other is the nature of the nucleon spin. At present, we have a limited set of high-energy data which tell us the alignment of the quarks along the light-cone momentum direction, as a function of the momentum fraction. These distributions are unknown at both high and very low momentum fraction, and the resolution range in Q^2 explored is much narrower than in the unpolarized case. In fact, even these data are limited to the case where the nucleon spin is along the light-cone momentum direction. Until the advent of the RHIC polarized proton collider data, there was no precise and clearly interpretable data on the polarization of the gluons along the nucleon spin direction. The polarized lepton scattering experiments have made it clear that the quark spins only contribute about 30% to the nucleon spin. The gluons, which make up roughly 50% of the total (unpolarized) partonic momentum distribution, may be expected to carry a significant fraction of the nucleon spin, but this distribution is almost completely unknown at present. The RHIC spin program using longitudinally polarized protons promises to answer the question of the gluon spin contribution definitively. First measurements using the existing PHENIX spectrometer have already constrained the polarized gluon distribution. The NCC will allow PHENIX to make a significantly more detailed and precise investigation of the polarized gluon distribution over a much broader range of light-cone momentum fraction, and as a function of momentum fraction.

When one explores the polarization of quarks with the nucleon spin perpendicular to the light cone, our understanding of both transverse momentum and spin are strongly tested, and at least in experiment, intrinsically linked to each other. Ever since the observation of a large asymmetry in high-energy proton scattering, it has been clear that transverse effects would play an important role. These effects have been shown to persist even at RHIC energies, almost undiminished in size. Recent progress has been spurred by the observations of transverse asymmetries in lepton scattering from transversely polarized protons. First glimpses from these experiments have prompted intense theoretical activity, with new insight gained into the role of gauge links in calculating partonic field operators. We now have firm predictions relating the fragmentation process in lepton scattering to that in Drell-Yan. The possibility of a distribution arising from the correlation of spin and longitudinal momentum fraction is now widely accepted, and again there are early first glimpses from lepton scattering. A natural explanation for this correlation is the existence of significant quark orbital angular momentum. In fact, orbital angular momentum is essentially unexplored experimentally at the partonic level. Exclusive reaction experiments, if able to determine the generalized parton distributions sufficiently well, can give us information only about the total angular momentum. Theoretically, there is now a much more thoroughly developed formalism to describe transverse measurements. The distributions are functions not only of momentum fraction and Q^2, but now transverse parton momentum k_T as well. While the dependence can be modeled, there is evidence that one can develop the transverse momentum distribution directly from perturbative QCD (pQCD). Thus, using transversely polarized protons at RHIC, one should be able to explore these new distributions in a regime where

pQCD can be safely applied, for example using spin-dependent two-hadron correlation functions [49]. The addition of the NCC will clearly increase the PHENIX hadron acceptance at forward rapidity where the transverse effects are large. While extracting this new distributions is indeed more difficult, it is clear that this is a very active and developing area in high energy spin physics, and forward acceptance is required in order for PHENIX to be a major player in this area. If the longitudinal program finds that the gluon contribution to the nucleon spin is small, the transverse physics will be the only effective avenue at RHIC to study the partonic nature of orbital angular momentum.

Below we give a more detailed description of what we hope to learn from this program. In addition, we touch upon the role that the NCC may be able to play at 500 GeV in the study of the anti-quark production via W boson production.

2.3.2 Nucleon Structure: Gluon Polarization

Our present knowledge of the partonic structure of the nucleon is encoded in the so-called parton distribution functions (PDF) which depend on Bjorken x, the light-cone momentum fraction, and the momentum scale Q^2. Since the quarks are spin-1/2 particles, we can actually define two quark distributions, so-called helicity distributions, which describe the partons with the same or opposite helicity of that of a proton with helicity along the light cone direction. We will denote the polarized PDFs by $q_f^{\rightarrow}(x, Q^2)$ and $q_f^{\leftarrow}(x, Q^2)$, where f is the flavor of the quark or a gluon, however we will typically denote the unpolarized gluon distribution as $g(x, Q^2)$. In general, the unpolarized PDFs are then the sum of the helicity distributions: $q_f(x, Q^2) = q_f^{\rightarrow}(x, Q^2) + q_f^{\leftarrow}(x, Q^2)$. It is common to also define $\Delta q_f(x, Q^2) = q_f^{\rightarrow}(x, Q^2) - q_f^{\leftarrow}(x, Q^2)$.

The distributions for charged partons can be extracted directly from inclusive deep inelastic lepton scattering (DIS) experiments (in which only the scattered lepton is detected) if the Q^2 and energy ν of the photon are sufficiently high. Deep inelastic neutrino scattering allows one to separate quark and antiquark distributions, which the charged lepton scattering cannot distinguish. One can attempt to isolate the charged partons by flavor using so-called flavor tagging, where the known valence quark content of of hadrons is correlated with the flavor of the quark which absorbed the virtual photon. The detection of DIS lepton and a leading hadron, known as semi-inclusive DIS (SIDIS), necessarily depends on modeling of the fragmentation process. Lepton scattering from the gluon distribution is complicated, as the gluon has no electromagnetic or weak charge, thus extraction is more model dependent. To date the most successful DIS program has been the analysis of di-jets [50], which primarily (but not exclusively) derive from the photon-gluon fusion diagram. If there is insufficient energy to produce jets, one may attempt to substitute leading hadrons, but again, one is now more model dependent. In fact, global fits are regularly made by a number groups around the world, using not only the DIS data, but also data from hadron colliders and theoretical constraints derived from QCD sum rules [51, 52, 53].

The dependence on these functions on Q^2 can be directly related to the fluctuation of the gluons into quark-antiquark pairs and the radiation of gluons by quarks through the DGLAP equations, and this provides an means in principle to determine the polarized gluon

distribution from the Q^2 evolution of the polarized quark distributions measured in DIS. The results of a recent analysis [54] of the available polarized DIS data (from SLAC, CERN, and DESY) are displayed in Fig. 2.14 (left panel) and show that the present uncertainties on ΔG are so large that even the sign of the gluon polarization is barely constrained; much more precise polarized DIS data, over a broader range in x and Q^2, would be necessary to provide better limits. The fact that the photon-quark asymmetry A_1 itself has only very small Q^2 dependence gives this type of analysis only a small "lever arm."

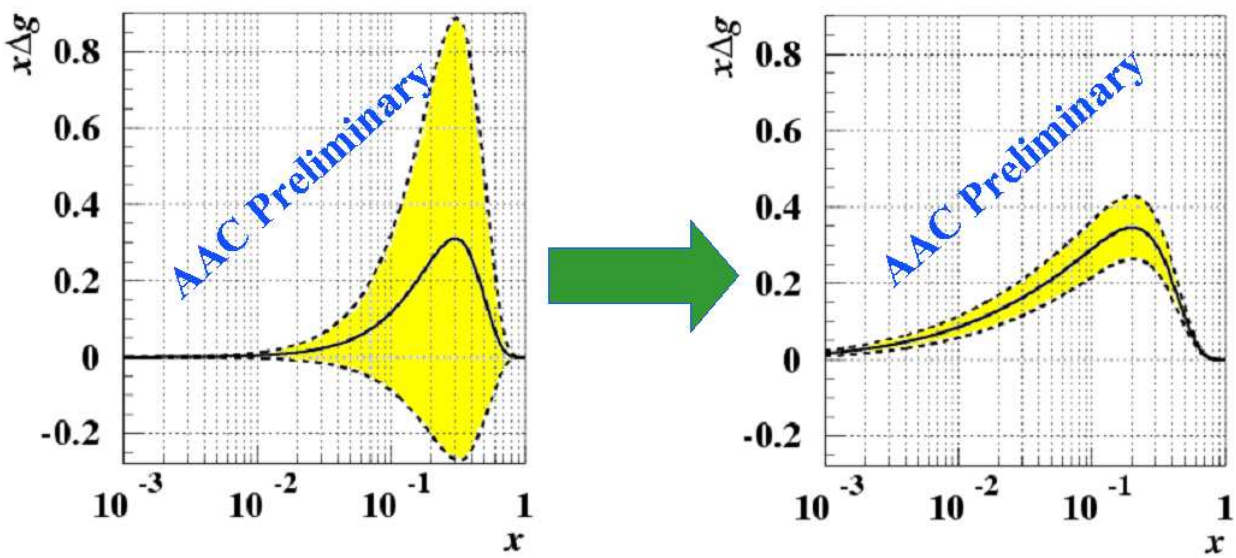

Figure 2.14: Polarized gluon distribution derived from NLO-QCD analysis of existing DIS data. The ranged limited by the dashed curves shows the range of gluon polarizations allowed by the data. The effect of including the direct photon results anticipated from PHENIX data from one year at design luminosity in the same NLO-QCD global analysis are shown in the right panel.

The RHIC spin program will provide the first precise measurement of the x-dependence of polarized gluon distribution $\Delta g(x)$. The PHENIX experiment, which has excellent particle identification and high rate capabilities, is well suited to this measurement as we are sensitive to Δg through multiple channels and each of these channels has independent experimental and theoretical uncertainties. Our main sensitivity is through inclusive hadron production, direct photon production, and heavy quark production.

In unpolarized $p+p$ experiments the gluon distribution function has been measured using single- and di-jet events as well as from direct photon events. In both cases, jets or high p_t photons carry information directly from the underlying hard scattering process which can be calculated using pQCD. As the cross sections factorize into a hard scattering and a proton structure part a measurement determines the parton distribution functions connected to the processes, schematically

$$\sigma \sim q\left(x_A\right) \otimes G\left(x_B\right) \otimes \left|\mathcal{M}_{\mathrm{pQCD}}\right|^2$$

where x_A and x_B are the fraction of proton momentum carried by the partons entering the

hard scattering process. The theoretical problems present in the interpretation of fixed-target data have been largely resolved for the collider environment [55, 56]. PHENIX's first direct γ cross-section measurement indicates that these calculations are valid at RHIC.

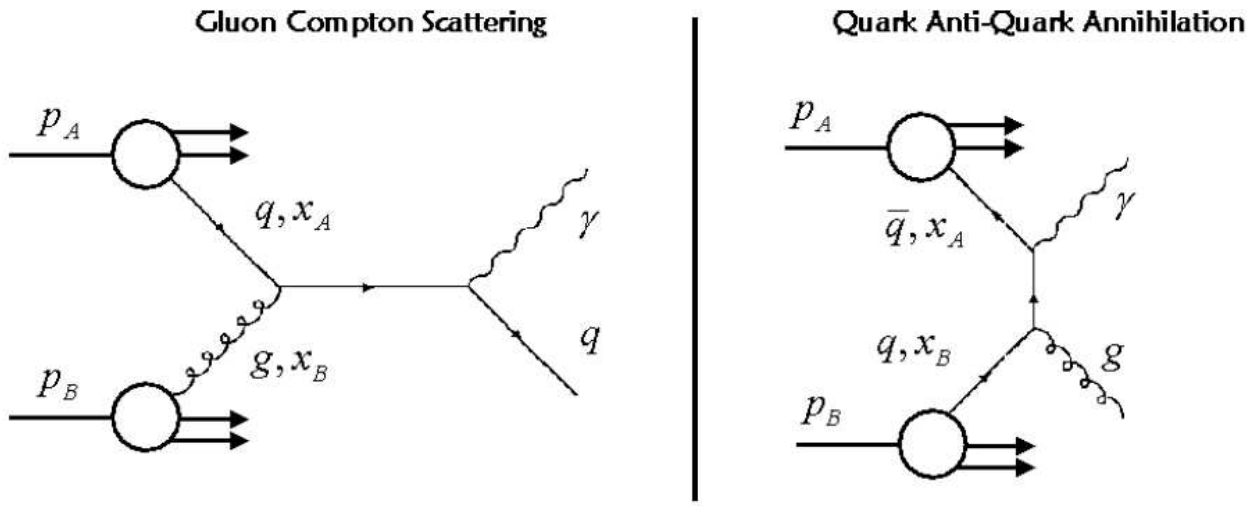

Figure 2.15: Direct photon production in the gluon compton and quark anti-quark annihilation processes. The ratio of the two processes has been studied using PYTHIA and was found to be about 9:1.

At RHIC, direct photon production is dominated by quark-gluon Compton scattering (see Fig. 2.15), which ensures that the double spin asymmetries from direct photon production provide the cleanest theoretical access to the gluon polarization $\Delta g/g$.

Helicity conservation at the quark-gluon vertex gives rise to a double spin asymmetry

$$A_{LL} \sim \frac{\Delta q_f\left(x_A\right)}{q_f\left(x_A\right)} \otimes \frac{\Delta g\left(x_B\right)}{g\left(x_B\right)} \otimes a_{LL}^{qg \to q\gamma}$$

from which $\Delta g/g$ can be extracted. The hard scattering asymmetry is denoted by $a_{LL}^{qg \to q\gamma}$ is calculated for the underlying quark-gluon Compton diagram with perturbative QCD. Background from the quark anti-quark annihilation process has been studied using the event generator PYTHIA and was found to be small.

The measurement of a double spin asymmetry for the case of detecting only the direct photon, typically as a function of p_T necessarily involves a convolution of over the momentum fractions of the colliding partons; one compares the measurements to QCD predictions based on different models of the gluon distribution. If one can also detect the opposing quark jet, then one may extract the the shape of the distribution more directly, as the initial momentums fractions x_A and x_B are now known (though the flavors and gluon combinations remain unknown and are summed over). This essentially allows a much more direct determination of the polarized gluon distribution. Unfortunately, the limited acceptance, $\eta \leq |0.35|$, of the current PHENIX detector and the absence of hadronic calorimetry presently make it impossible for us to reconstruct jets.

The NCC allows us to greatly extend the x-range of PHENIX's measurement. as well as provide information on the x dependence. The right panel of Fig. 2.14 displays the impact of PHENIX direct photon (inclusive) data on the range of allowed polarized gluon distributions. Despite the fact that the gluon polarization appears best constrained and falls off with decreasing x, the integral, ΔG, is dominated by contributions from $x < 0.1$ since this is the region where the gluons are most abundant [note that Δg is multiplied by x]. It is thus important to measure Δg to values of x as far below 0.1 as feasible. Historically it is interesting to note that the quark spin crisis only arose when EMC [57] extended the measurement of quark spin contributions to low x. Extrapolations of the SLAC [58] data alone led to results for the quark spin contribution consistent with expectations from naive quark models. The additional geometric acceptance in the forward direction provided by the NCC extends the measurement of the gluon polarization from $0.01 < x < 0.3$ down to about $x = 0.001$. Further, in combination with the new PHENIX inner tracker detectors, which will allow crude jet-reconstruction in the PHENIX central arm, the calorimeter makes it possible to obtain a rough measurement of x on an event-by-event basis by detecting the away-side jet associated with the recoiling quark. The x measurement allows for a leading-order determination of Δg as described above; this will be particularly valuable in constraining Δg at low x and complimenting the NLO determination that will utilize the inclusive measurements. A rough jet measurement can also be made with the NCC, making possible a full range of measurements.

Overall, PHENIX is sensitive to Δg through multiple channels. The kinematic coverage for these various channels within PHENIX are shown in Fig. 2.16. The complementary measurements cover slightly different kinematic ranges, and most importantly provide alternative ways to the gluon polarization with different systematic and theoretical uncertainties. Figure 2.17 compares the x-Q^2 footprint of these channels to that of the DIS experiments. Note that the HERA range denotes the collider experiments H1 and Zeus, which cannot measure the required double spin asymmetries.

2.3.3 Transverse Spin Physics

It is fair to say the much of the interest in high-energy spin physics can be traced to two surprising results: the observations of large lambda hyperon polarizations [59] and large single spin asymmetries in pion production from polarized nucleon-nucleon collisions [60]. The general expectation from pQCD at leading twist was that these asymmetries would be vanishingly small, due to the chiral dynamics of QCD It was therefore startling when E704 discovered very large asymmetries in pion production from polarized $p+p$ collisions at $\sqrt{(s)}$ = 20 GeV. The expectation that yet higher energy would cause these asymmetries to vanish, was again invalidated by the STAR discovery that these effects persisted to the much higher $\sqrt{(s)}$ of 200 GeV [61], since it was thought that any power corrections should be suppressed at higher energies, despite the fact that the predictions of unpolarized cross-sections agree very well with the data. The single spin asymmetries for π^0 mesons detected at STAR, as a function of Feynman x, are shown in Fig. 2.18. Given that the magnitude of asymmetries at high energies are typically only a few percent, these forward asymmetries are quite large.

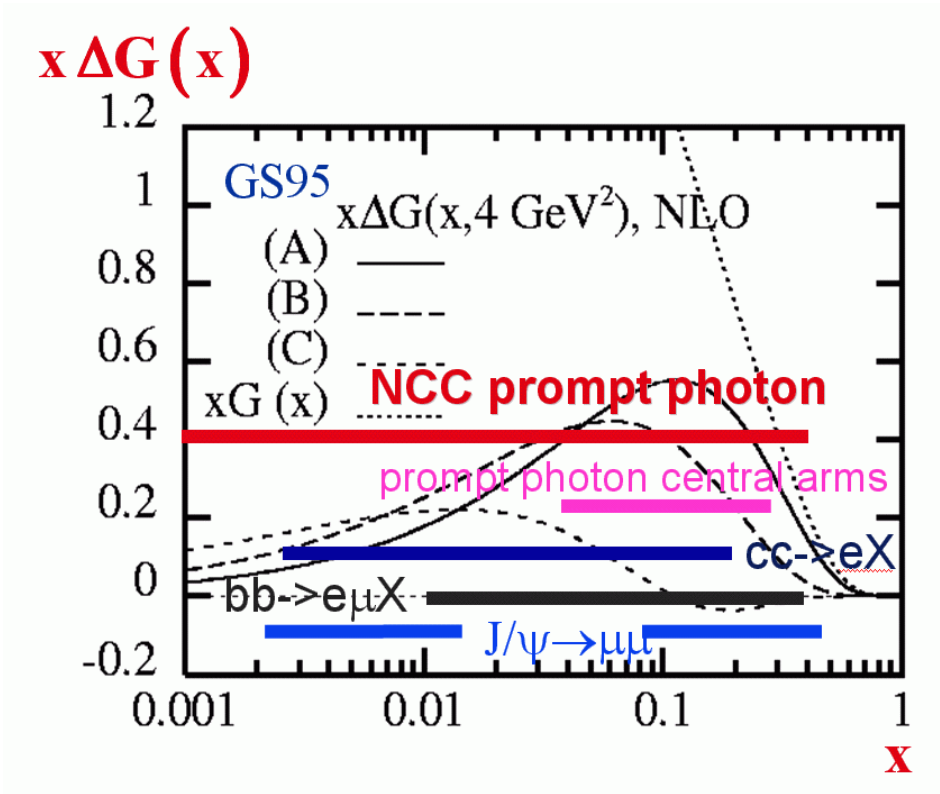

Figure 2.16: Kinematic coverage for PHENIX measurements that are sensitive to Δg. x_{Bj} range shown on-top parameterization of ΔG.

One might questions whether the forward reactions are too soft to apply perturbative QCD, but as shown in Fig. 2.19 the cross sections are well described by NLO pQCD [62] as well as by PYTHIA [63]. The existence of large single spin asymmetries at RHIC, along with the good theoretical understanding of the unpolarized cross-sections gives hope that transverse spin effects can be used as a tool to probe the transverse structure of protons.

There are three basic sources for the single spin asymmetries observed so far:

1. the existence of the Sivers function [64] which describes the correlation between the spin direction of the proton and the transverse momentum of the parton. Partons from the Sivers distribution fragment with the normal well-known fragmentation functions.

2. the existence of Collins fragmentation functions [65] which provide a correlation between the momentum of the final state particles with the direction of the initial parton spin. The initially transversely polarized quark are described by the transversity distribution [66]

3. Higher twist mechanisms in the initial and/or final state [67]

The recent observation of azimuthal asymmetries in semi-inclusive pion electroproduction at HERMES, from both longitudinally [68] and transversely polarized nucleon targets [69]

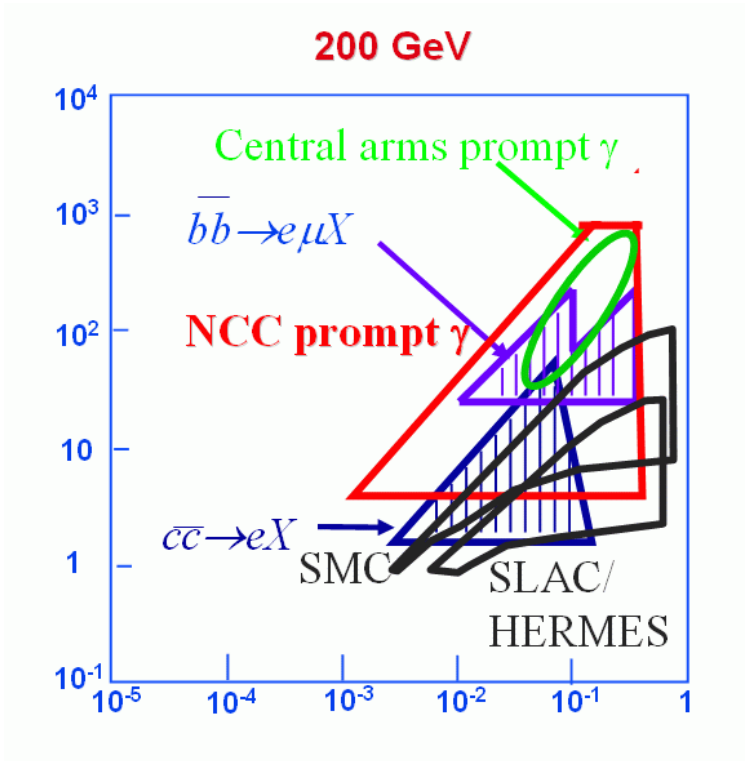

Figure 2.17: Range of x and Q^2 accessible by various DIS experiments compared to those accessible at PHENIX. Note that the HERA range denotes the collider experiments H1 and Zeus, which cannot measure the required double spin asymmetries.

along with the STAR results has sparked renewed and intense theoretical study of this physics. Using the transversely polarized target data, HERMES has made a preliminary extraction of the separate asymmetries arising from the Sivers mechanism and the Collins mechanism. Additional efforts at BELLE have made the first extraction [70] of a Collins fragmentation function for e^+e^- annihiliation. Collins fragmentation functions of two pion states have also been proposed [71], and there is a preliminary observation once again at HERMES [72].

The existence of sizeable Collins fragmentation functions will allow the extraction of the transversity distribution of the nucleon $\delta q_f(x)$. Just as in the case of Δq_f, the transversity is a measure of the alignment of quarks along or opposite the nucleon spin; the critical difference is that in the longitudinal case, the nucleon spin is along the light-cone direction, while in the transverse case, it is perpendicular to this direction. Non-relativistically, this is a trivially different distribution, but once on the light-cone these are "independent" distributions, of the same leading order (A common (correct) model of the of the quark-gluon structure could predict both distributions, but you cannot determine one distribution from the other). The transversity is interesting for a number of reasons. Besides completing our knowledge of the nucleon at leading order, it is notable for being mainly sensitive to the valence quark spin structure, and furthermore, its Q^2 evolution is quite different due to the lack of coupling

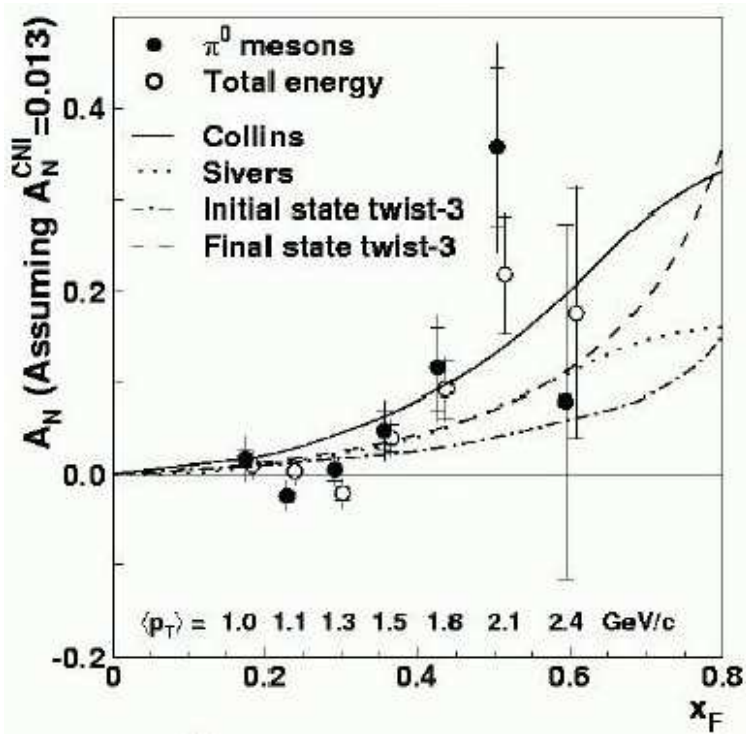

Figure 2.18: Single spin asymmetry from π^0 mesons at forward rapidity ($\langle\eta\rangle = 3.8$) as a function of Feynman x, measured at the STAR experiment from transversely polarized pp collisions at $\sqrt{s} = 200$ GeV [61].

between gluon transversity functions and quark transversity functions. These attributes provide an important test of our understanding of the longitudinal antiquark and gluon spin structure functions, especially with regard to relativisitic effects.

The existence of Sivers distributions also provides an interesting window into the structure of the nucleon. This function accounts for the possibility that a parton's transverse momentum depends on the orientation of the nucleon spin. Orbital angular momentum of the quarks about the spin axis would naturally provide just such a correlation. At present, this connection is still not understood theoretically at the partonic level, but the distribution function itself is now generally accepted and well defined.

Effects in forward hadron production from transversely polarized pp collisions are somewhat more complicated than in polarized SIDIS, but as usual, the effects are typically larger and easier to study. Formally, there has been considerable progress in working out a formalism of possible distributions and fragmentation functions, for example as given in Refs. [73, 74, 75]. Predictions based on models of the nucleon are now being constrained by the data, but there is still much more data needed. As an example, the calculation of the asymmetry in pion production for the E704 experiment is shown in Fig. 2.20, taken from Ref. [75]. These models explore maximal bounds for the various distribution, but the point here is that the distributions in x_F are quite different, and they do not change much as a function of energy.

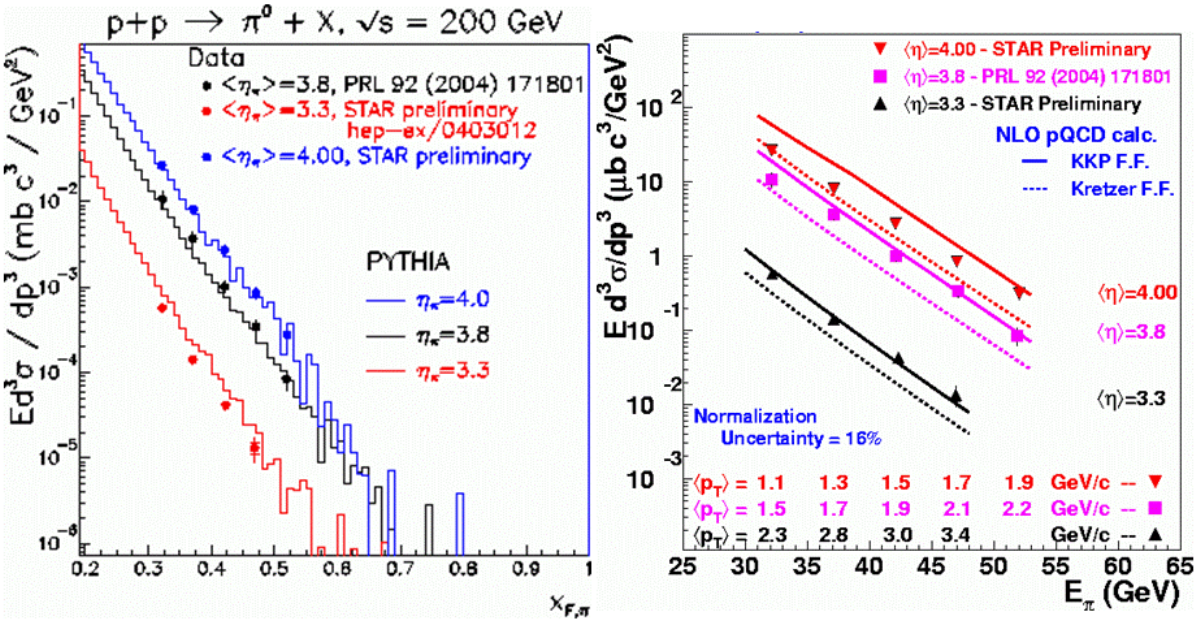

Figure 2.19: Forward inclusive π^0 cross sections measured at the STAR experiment from transversely polarized pp collisions at $\sqrt{s} = 200$ GeV [61]; the average pseudorapidity is $\langle\eta\rangle = 3.8$. In the left panel, these results are compared to predictions using PYTHIA [63] as a function of feynman x; in the right panel they are compared to NLO pQCD [62] calculations as a function of the pion energy.

The NCC along with the recently installed Muon Piston Calorimeter(MPC) and the standard PHENIX central detectors will allow an important series of transverse spin measurements to be carried out at PHENIX. These should us to separate out the mechanisms contributing to the forward inclusive asymmetry. Specifically, the Sivers distribution can be measured in the azimuthal asymmetry of back-to-back di-hadrons or di-jets, where one of the hadrons is the forward π^0 or jet. The Collins fragmentation function can be measured in the hadron distribution around a jet axis. The two hadron Collins function can be measured by di-hadron correlations in the near side of a jet. Whatever is left can be use to test calculations of higher twist effects.

In general the exploration of transverse spin asymmetries in SIDIS and pp collisions requires one to investigate the dependence of the asymmetries on the p_T of the hadrons. This raises serious questions about the universality of the distribution and fragmentation

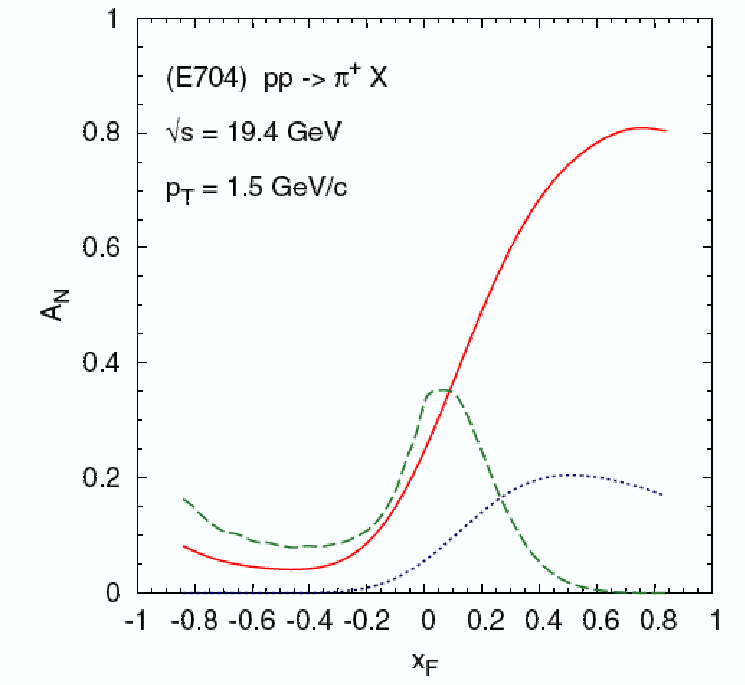

Figure 2.20: Different contributions to A_N, plotted as a function of x_F, for $p^{\uparrow}p \rightarrow \pi^+X$ processes and E704 kinematics. The different lines correspond to solid line: quark Sivers mechanism alone; dashed line: gluon Sivers mechanism alone; dotted line: transversity $\otimes$ Collins. All other contributions are much smaller. Taken from Ref. [75].

functions which can be investigated in both experiment and theory. It has as well forced modelers to include the intrinsic k_T of the partons in some fashion. These issues are being addressed aggressively by the theoretical community. In fact, if we hope to start developing a true 3-dimensional understanding of the nucleon structure, this physics must be confronted and understood.

2.3.4 Nucleon Structure: Quark Polarization

While Δq has been fairly well measured, the anti-quark's contribution to Δq is not well-known. Some information has come recently from the polarized SIDIS measurement from the HERMES collaboration [76], using a flavor tagging analysis of the identified hadron asymmetries. The HERMES results on the sea polarization are accompanied by a substantial systematic error due to the observed small size of the asymmetry, and the weakness of the correlation from the flavor tagging. As usual, the weak interaction is of critical use in determining the sea quark distributions, allowing the PHENIX measurement to provide an important independent measurement of high precision and much higher Q^2, using an experimental approach completely different from that of HERMES.

The high-energy polarized proton beams at RHIC provide copious yields of W bosons, and the parity-violating nature of the weak interaction permits the extraction of light quark

and anti-quark polarizations through measurements of longitudinal single spin asymmetries in W^+ and W^- production. Bourrely and Soffer first discussed this idea using QCD at leading order perturbation theory [77]. Recently Yuan and Nadolsky presented a using modern resummation techniques in addition to an NLO calculation [78]. This work leads to a robust interpretation of the PHENIX quark polarization measurement in W production. In PHENIX, W production is characterized either by detecting high-energy electrons (or positrons) in the two central spectrometer arms or by reconstructing high-p_T muons in the two muon spectrometers. Due to their eight–times-larger acceptances, the PHENIX muon spectrometers will dominate the measurement statistically. The anticipated integrated luminosity of 800 pb^{-1} will yield approximately 10^4 detected W^+ and W^- events. However, before a successful measurement can be carried out, the event selection electronics must be improved significantly. The muon trigger was designed for heavy ion running and low-luminosity proton collisions; an upgrade is required to record selectively energetic muons from W decay during the high-rate spin running. Recently, the NSF has awarded a collaboration within PHENIX funds of almost \$2M to carry out this upgrade using resistive plate chambers to be installed in each muon spectrometer.

Figure 2.21 shows the projected precision of PHENIX on the light quark polarizations in the proton. Superimposed on the plot are projections of the accuracy achieved in preliminary results from HERMES (the figure has not yet been updated with the actual published final results). The anticipated measurements are highly complementary in nature. The HERMES results feature more complete kinematic coverage, while the PHENIX results are of greater precision. The PHENIX technique distinguishes cleanly between the light quark flavors in a model-independent way, while the HERMES kaon asymmetries are able to probe the strange quark polarization. Finally, the systematic uncertainties in the two experiments are of completely different origin.

The measurement of the anti-quark spin contribution to the spin of the proton will be via the measurement of high p_T leptons coming from W's – a rather rare process. The NCC upgrade will extend this measurement both by allowing the detection of electrons and positrons in the forward region (though without charge determination) – in addition to the muons, and in reducing potential backgrounds. One of the potentially large backgrounds is the decay of low momentum pions and kaons within the magnet muon tracker volume, resulting in an apparently straight line (high momentum) trajectory. Such background events can be studied and, if necessary, reduced by requiring a separation between the lepton-detected by either the muon spectrometer (muons) or the calorimeter (electrons) and the jet, as detected by the calorimeter.

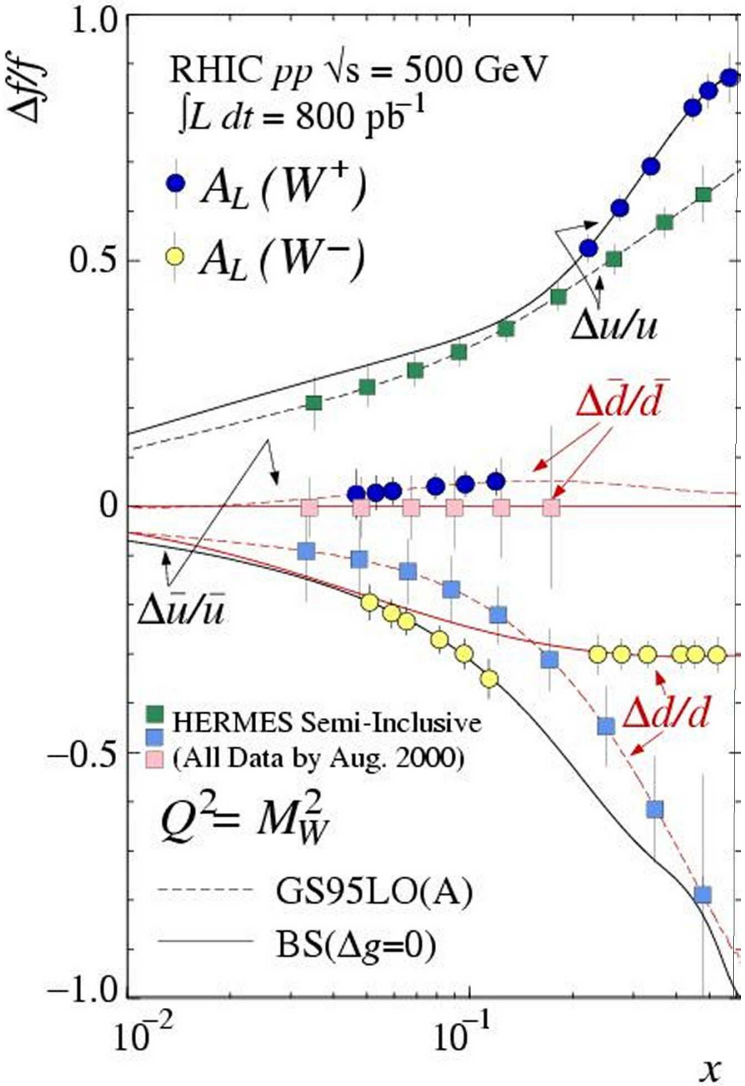

Figure 2.21: Simulation of measurements of light quark polarizations from W boson production at RHIC, compared with preliminary data from the HERMES experiment.

Chapter 3

Design of the NCC

3.1 Overview

The PHENIX[1, 79] detector introduced in Fig. 3.1, is designed to perform a broad study of nucleus-nucleus (A+A), proton- or deuteron-nucleus (p+A or d+A), and proton-proton (p+p) collisions to investigate nuclear matter under extreme conditions and to measure spin dependent structure functions. PHENIX collaboration built for the needs of the heavy-ion and polarized-proton programs the detector with unparalleled capabilities. Global detectors characterize the collisions, a pair of central spectrometers at mid rapidity measure electrons, hadrons, and photons, and a pair of forward spectrometers measure muons. Each central spectrometer is limited in geometric acceptance to about one steradian partially compensated by excellent particle identification. All currently existing subsystems have proven excellent energy and momentum resolution.

The proposed Nosecone calorimeter subsystem will increase PHENIX geometric acceptance at midrapidities tenfold, will introduce new quality to PHENIX: direct access to jets and photons produced in forward direction and will improve running conditions in the Forward muon spectrometer. Physics with upgraded PHENIX will benefit of observables that are to date not accessible to PHENIX or available only indirectly with very limited accuracy. Forward production of inclusive jets, direct photons or Drell-Yan pairs at large xF in proton-proton and nucleon-ion collisions at RHIC will provide a new window for the observation of saturation phenomena expected at high parton number densities [3, 4]. Nose cone calorimeters will also become a critical component to the measurement of the spin dependent structure fencings by providing independent measurement for the total (charge combined) yield of gauge bosons in pp interactions and assisting muon system in removing background to high transverse momentum muon candidates. Calorimetry upgrade to the forward spectrometer will open the possibility to measure photons from decays of the charmonium states such as the $\chi_c \rightarrow \mathrm{J}/\psi + \gamma$ for the study of charmonium suppression in heavy ion collisions.

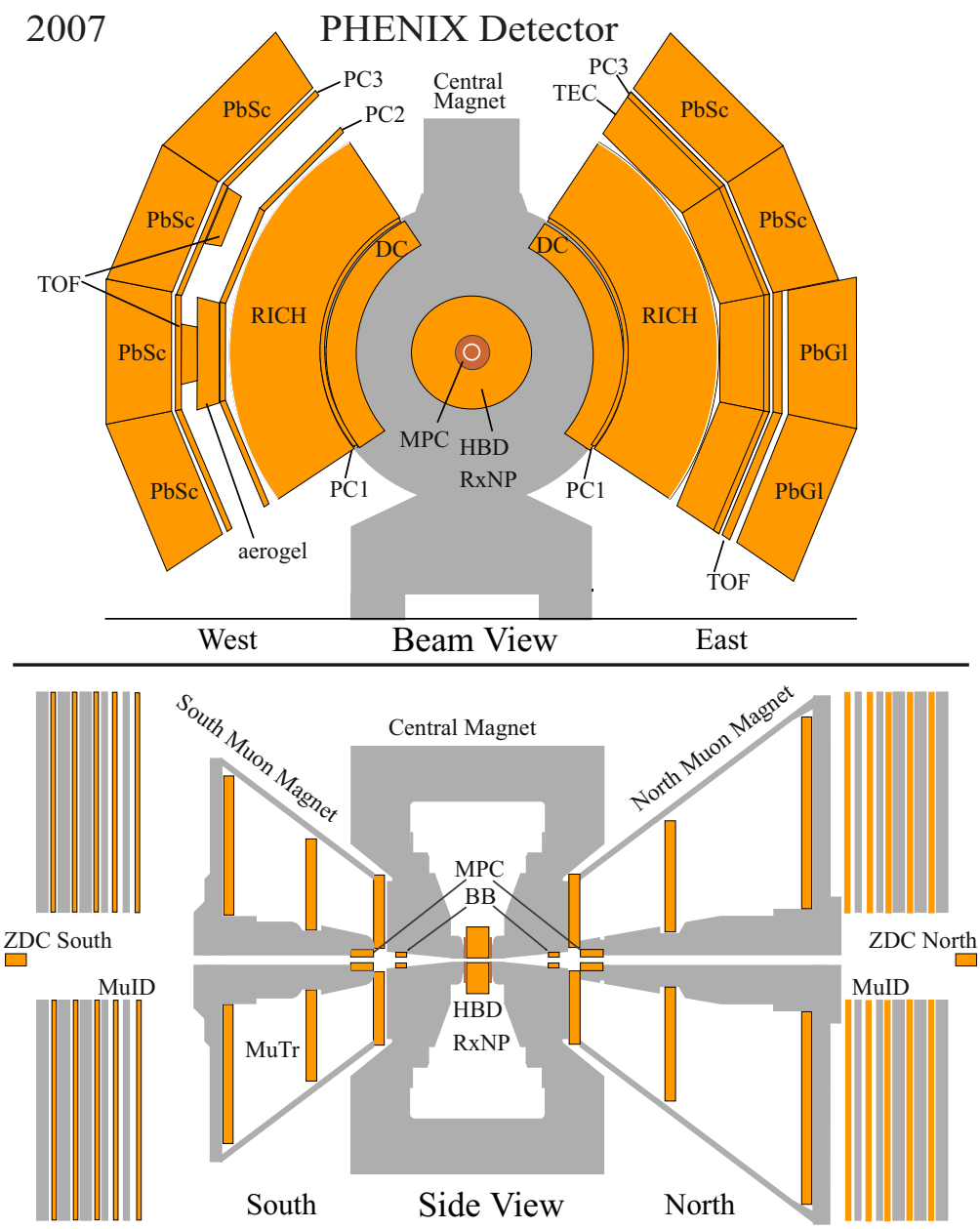

Figure 3.1: A beam view (top) and side view (bottom) of the PHENIX detector in its most recent configuration. BB-Beam-Beam trigger counters, DC-Drift Chambers, RICH - ring imaging Cerenkov counters, aerogel - Aerogel Cherenkov counters, PC-Pad Chambers, TEC - Time Expansion Chambers, PbSc/PbGl – Electromagnetic Calorimeters, MPC- Muon Piston Calorimeters, MuTr/MuId -Muon Tracking and Muon Identification, and ZDC - Zero Degree Calorimeters. Magnetic field is axial in the central region, the muon magnets generate a radial magnetic field.

3.2 Upgrade Layout and NCC Configuration

The PHENIX Forward (Muon) spectrometers (illustrated in bottom panel of Fig. 3.1) was built to identify muons in the muon filter(identifier) MuID and measure their momenta via the muon tracker MuTr. and the muon identifier (MuID).

The ongoing upgrade to the PHENIX Forward Spectrometers includes an enhanced muon trigger able to recognize muons and impose cutoffs on the muon pointing and muon momenta in the muon system at a RHIC rate of 10 MHz, a forward Si vertex detectors (FVTX) measuring track impact parameters in the forward direction and Nose Cone Calorimeters for measuring and identifying particles producing electromagnetic and hadronic showers and measuring jet vectors. The proposed upgrade to the forward spectrometers is shown diagrammatically in Fig. 3.2.

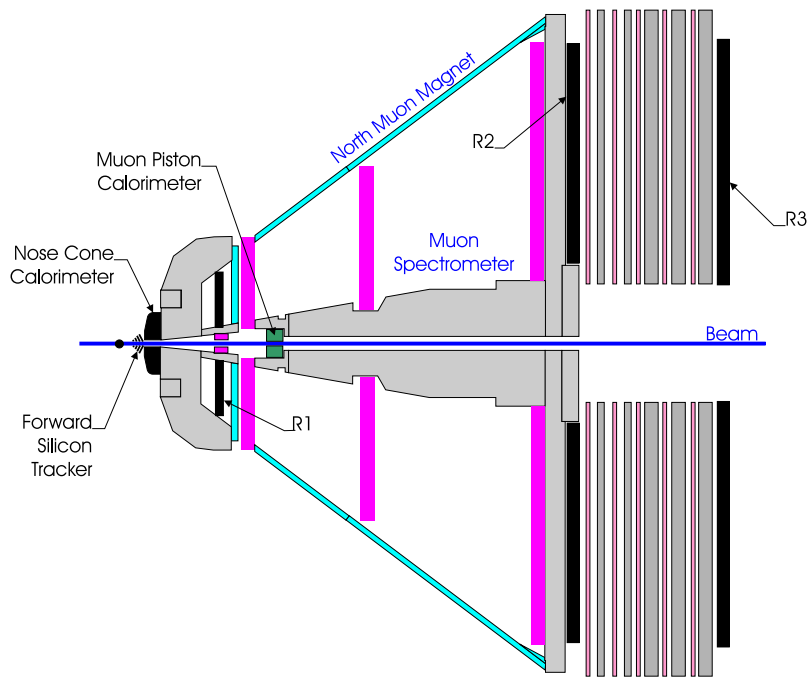

Figure 3.2: Schematic rendering of the new PHENIX Forward Spectrometer. R1-R3 – new resistive plate chambers built for triggering on muons. All other upgrade components are identified in the figure.

The PHENIX central region is constrained by the magnet poles to ±60 cm along the beam line shared between NCC and Forward and Central Silicon Vertex Trackers (VTX). Two identical NCC will be installed on the North and South magnet poles each occupying 19.5 cm of available real estate..

The along-the-beam-axis space allocated to calorimeters is currently used by supplementary muon filters (NoseCones, one for each magnet pole, brass disks 19 cm deep and $\sim$ 1m in diameter). The depth and geometry of new calorimeters is chosen to fit within the envelope

of the existing Cu Nose Cones. Fig. 3.3 is a 3-d rendering of one of the PHENIX central magnet poles with NCC installed. Shadowed regions indicate the PHENIX central arms acceptance which is unaffected by the presence of this new device.

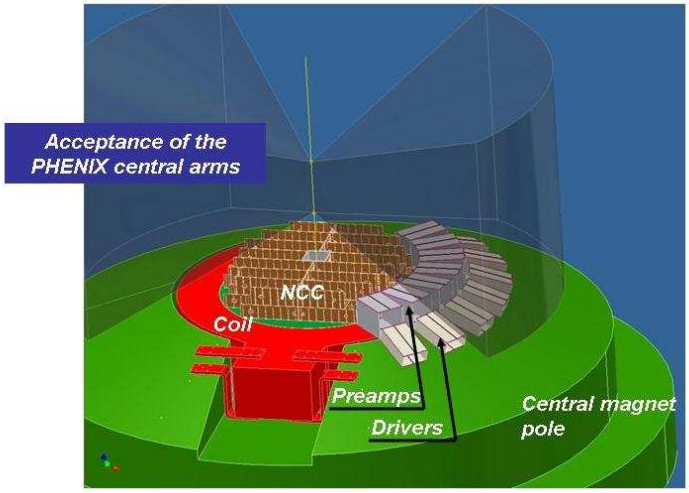

Figure 3.3: NCC assembled on the PHENIX Central Magnet pole. Shadowed is the acceptance of the Cental Arms.

As a component of the PHENIX Forward Spectrometer the NCC will add the following functionality:

1) precision measurements of individual electromagnetic showers;

2) $\gamma/\pi 0$ discrimination similar to the central PHENIX electromagnetic calorimeters;

3) photon(electron)/hadron discrimination comparable to that in the central arms;

4) jet finding, jet energy and impact position measurements. Jet vector measurements. Isolation cone energy measurements;

5) fast trigger on local total energy deposition (jet), fast trigger on electromagnetic energy (direct photons and $\pi 0$'s), qualifying primitives for fake muon rejection.

It will also assist in matching muon trajectories identified in the forward muon spectrometer to tracks in the central vertexing system.

3.3 NCC Design considerations

The design requirements imposed on the detector by physics considerations are:

- the ability to measure electromagnetic showers with a precision comparable to the sum of all systematic uncertainties characteristic of similar measurements with PHENIX central electromagnetic calorimeters (π^0 effective mass resolution better then 20 MeV in the p_T range above 5 GeV/c),

- the ability to discriminate between electromagnetic and hadronic showers in the calorimeter allowing extraction of the direct photon signal down to ∼5% of the π^0 yield,
- the ability to reconstruct π^0's via effective mass measurements and shower shape analysis to the p_T extent allowed by the calorimeter acceptance and RHIC luminosity,
- the ability to measure shower impact vectors with resolution sufficient for efficient matching to charged tracks reconstructed by Forward Silicon Tracking,
- the ability to measure the total jet energy and jet angle with precision sufficient to reconstruct kinematics of the g-q hard scattering resulting in γ-jet events with jets in the forward direction,
- ability to measure energies inside the jet cone around high p_T lepton candidates for isolation testing.

To satisfy these specifications we design calorimeters which are a combination of highly segmented electromagnetic (EM1 and EM2) and hadronic (HAD) components supplemented by high resolution preshower detector(PS) at a depth of $\sim 2X_0$ and a shower maximum detector (SM) at a depth of $\sim 9X_0$. Role of PS is to count photon hits and measure hit-to-hit separation, role of SM is to measure decay asymmetry whenever the π^0 candidate is found in PS detector.

The longitudinal structure of the calorimeter tower is sketched in Fig. 3.4.

The NCC's are located 40.5 cm from the nominal collision point on the north and south poles of the PHENIX central magnet and limited to a depth of 19.5 cm each. Building the instrumentation capable of attaining the required performance under the constrains of PHENIX geometry requires the densest absorber material (tungsten) and the most versatile active media known to instrumentation in physics (silicon). Silicon provides for versatility of segmentation, tungsten has a small Moliere radius (9.3 mm) so the showers are very compact. Tungsten also has an excellent ratio of radiation and absorption lengths which is important for electromagnetic energy measurements in the presence of heavy hadronic background.

The compromises are required in order to achieve the goals of this proposal using available technology and limited funding. Based upon physics expectations priorities are given to particle identification (including resolving close showers), electromagnetic energy measurements and triggering capabilities.

The design of the NCC relies heavily on past experience in Si-W calorimetry[80, 6, 7]. Since even upgraded PHENIX will have no means to measure particle momenta in the forward direction the NCC must be capable of discriminating between hadronic and electromagnetic activities as a stand alone device.

Such a calorimeter covering an area ∼0.7 m^2 with towers comparable in size to the Moliere radius will have ∼2500 silicon pixels per readout layer. A number of ongoing R&D projects aimed at building similar calorimeters for the experiments at a future electron-positron linear collider considering the option to digitize signals from every pixel in all sampling layers. The proposed solutions are mostly on the drawing board and prohibitively

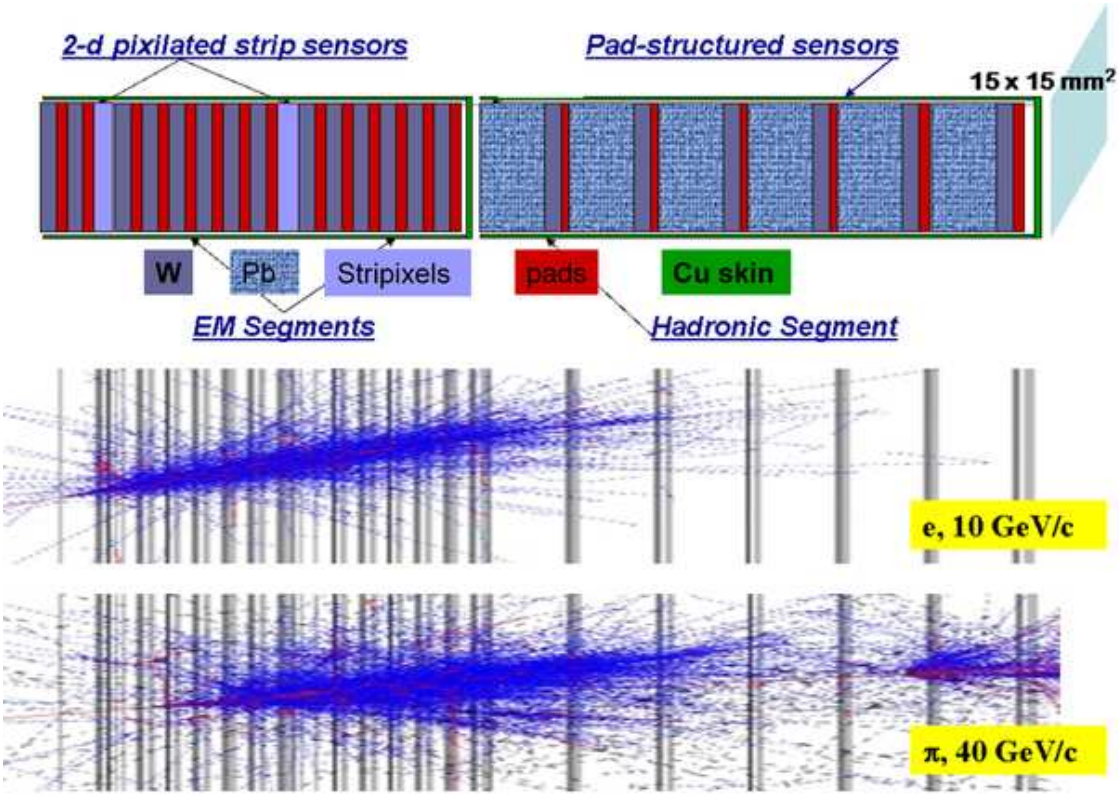

Figure 3.4: Longitudinal structure of a single calorimeter tower showing the locations of the three calorimetric segments, EM1, EM2, and HAD, and the high resolution position detectors- preshower(PS) and shower-max(SM). Bottom panel are electomagnetic and hadronic showers due to 10 GeV/c electron and 40 GeV/c charged pion

expensive. To reduce cost and complexity we decided on an option with pixels from a number of sequential silicon sampling layers ganged together and connected to the input of a single amplification/digitization circuit. An extensive SPICE simulation efforts were made to simulate minuscule details of ganged readout so the electronics noise will never reach the level comparable with intrinsic stochastic resolution of the device (see Appendix). The system prototype fully implementing all solutions presented in this document is currently under construction and will be tested in the test beam later this year.

The decision to gang the pixels allows to reduce the number of channels in the detector by a factor of 6−7 (see below), and to use signal amplification solutions developed by the BNL Instrumentation Department for earlier projects[14]. This option also allows to solve the problem of compatibility between a new detector and existing mechanical infrastructure in efficient manner.

Calorimeter built to discriminate between electromagnetic and hadronic showers using shower shape measurements only must have hadronic (or leakage) segment to measure energies beyond the total absorption depth for electromagnetic showers. We propose to build

relatively shallow electromagnetic segments leaving as much space for the leakage section as available. The hadronic segment (HAD) is structured following the pattern used in EM1 and EM2 (except for the total absorber plate thickness which is ∼13 mm) will (1) assist the energy measurements of photons at the extreme upper end of the spectrum, (2) serve as an effective electromagnetic/hadronic discriminator tool, and (3) guarantee the low-grade hadronic energy measurements in calorimeter. Thick hadronic plates will certainly degrade the calorimeter energy resolution for electromagnetic shower measurements beyond estimate given above but the compromise seems unavoidable to compensate for missing charged particle momentum measurements. The relative shallowness of the electromagnetic segments also serves to suppress the hadronic pile-up contribution to electromagnetic energy mostly contained in EM1 and EM2.

The W absorber plate thickness and the total depth of absorber in the calorimeter are also constrained by readout which is about 2.5 mm per layer divided up into 0.5 mm silicon, 1.6 mm of support components, and clearance gaps. The optimization process converged on the design with 20 pad-structured sampling layers and two layers of 2-d position sensitive pixelated strips (preshower-PS and shower max-SM) which will serve as a very efficient photon-π^0 identifier able to discriminate between individual electromagnetic showers and overlapping photons from high momentum π^0's. Both longitudinal and lateral shower profiles can be measured in the device and used in the particle identification.

Because of the limited total depth of a calorimeter we have chosen to apply the same lateral granularity throughout the whole depth of the calorimeter. We have chosen 4 mm W plates for the first two fine segments (EM1 and EM2) based upon the following simple considerations later tested in simulation.

The radial shower profile, which is used to discriminate between single and multiple showers, has a pronounced central core surrounded by halo. GEANT simulated profiles integrated over the shower depth in different materials are shown in the Fig. 3.5 function of the distance from shower axis is in Moliere units (9.3 mm for pure W). W and Pb show nearly identical behavior with W being the material of choice if resolving showers is the primary goal. 50% of the shower energy is contained within a radius of 0.25 $R_{Moliere}$ which can be used as a back-of-the-envelope estimate for intrinsic limit for two-shower separation. Further improvements are hampered by fluctuations in the number of particles in the shower. Symmetrically decaying 30 GeV/c π^0's will have two photons in the calorimeter at a distance of the order of 5 mm (depending on the production kinematics) thus suggesting the Moliere radius no larger then 20 mm for NCC. Technology sets a lower limit to the thickness of readout layers (carrier boards, silicon sensors, interconnects, protection) close to 2.5 mm. To keep the Moliere radius below 20 mm the thickness of W plates in the fine sections of calorimeter must be equal or above this value. The electromagnetic segments built of 4mm W + 2.5 mm readout sampling cells have Moliere radius of 14mm fully conforming to the specifications derived from expected two-shower resolving power. An infinitely deep calorimeter built of 4 mm W plates and 2.5 mm readout layers (525 mm Si sensors) will sample approximately 1.4% of energy left in the calorimeter by minimum ionizing particles

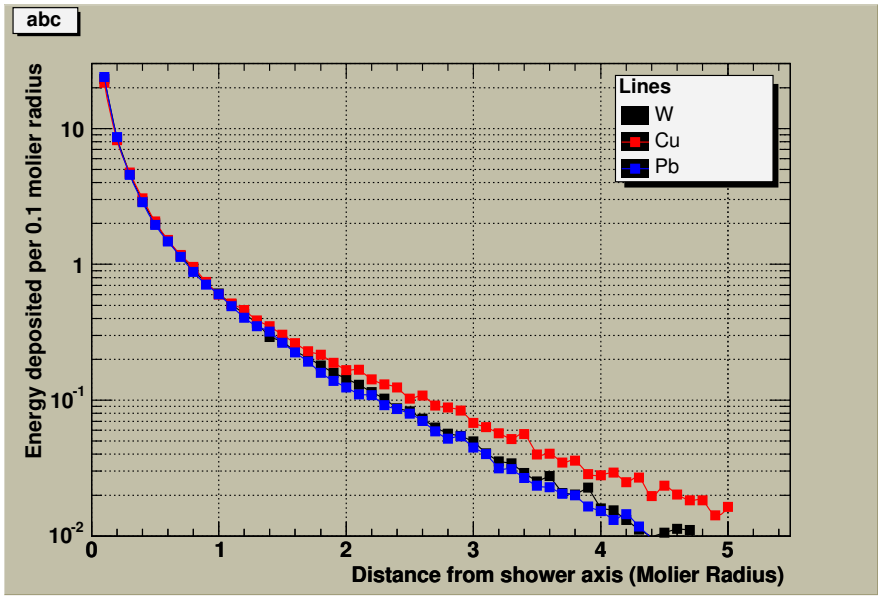

Figure 3.5: Radial profile of the electromagnetic showers in different materials(from simulation)

resulting in the intrinsic limit to the energy resolution (sampling fluctuations only) of

$$\frac{\sigma}{E} \simeq \frac{20\%}{\sqrt{E}}.$$

A short summary of the calorimeter design features is in the Table 3.1 (all counts are for a single calorimeter unit). The calorimeter will have a total depth seen by particles at normal incidence of $\sim$42 X_0 or 1.6 L_{abs}.

The remaining issue of concern for direct photons physics is the background of charged electrons impinging on NCC. The addition of the FVTX will bring solution to the large ($\eta >$ 2) rapidity range in NCC while only statistical tools are available (for example the difference in shower development between photons and electrons) at the low ($\eta < 2$) rapidities.

3.4 The Performance of the NCC

An extensive study of the present design including Monte-Carlo simulation and hardware R&D culminated in the construction and beam testing of a small proof-of-principle detector prototype to be described later in this document. In our simulation effort the calorimeter as described above was simulated using GEANT to produce libraries of electromagnetic and hadronic showers and PYTHIA simulated events. The calorimeter was located 40.5 cm from the production vertex. The whole active area of the calorimeter was illuminated. The simulated data presented below are integrated over impact angles 0 to 45 degrees.

Table 3.1: Nose Cone Calorimeter design features. All counts are for a single unit

Parameter		Value	Comment
Distance from collision vertex		40.5 cm	
Radial coverage		50 cm	
Geometrical depth		$\sim$ 19.5 cm	
Absorber		W	42 X_0 or 1.6 Labs
Readout		Si pads (15x15 mm2) and pixilated strips (.0.5x0.5 mm pixels grouped into 60 mm long strips)	
Calorimeter		EM1 and EM2 (14 sampling cells: 4mm W + 2.5 mm readout) longitudinally structured into two identical non-projective sections. HAD (6 sampling cells: 13 mm W + 2.5 mm readout)	
Preshower detector (PS)		Stripixel layer downstream of the first two EM sampling cells	
Shower max detector (SM)		Stripixel layer downstream of the first 9 EM sampling cells	
Sensors		calorimeter	3320 (14 x 160 + 6 x 180)
		PS and SM detectors	320 (2 x 160)
Channel count		calorimeter	8000
		PS and SM detectors	81920 (672 SVX4 chips)
Multiple scattering in NCC combined with Fe magnet pole		133 MeV	To compare with 106 MeV in the existing configuration with Cu NoseCone
Expected EM energy resolution		$23\%/\sqrt{E}$	
Expected jet energy resolution		$45\%/\sqrt{E}$	
Two showers resolved at	in calorimeter	3 cm	
	in preshower	2 mm	
	in shower max.	4 mm	

3.4.1 Simulations - the optimization procedure

For the purposes of optimization the NCC 3D-model implemented in ACAD was converted into GEANT3 model which is now part of a standalone and PISA based simulations chains. Unless explicitly specified the results presented in this chapter are based upon standalone GEANT simulation.

3.4.2 Containment, energy and position resolution

The depth and positions of calorimeter segments were optimized with respect to the shower profile to insure approximately equal energy sharing betweem EM1 and EM2 and a linear dependence of the energy deposited in the EM2 vs energy of the photon (see Fig. 3.6).

Most of the electromagnetic energy stays in the electromagnetic segments (EM1 and EM2) with relatively low energy dependent leakage to hadronic segment. The calibration coefficients used to convert energy in silicon into energies deposited in individual segments (sampling fractions) extracted from single electron simulation differ between segments and depend on energy of impinging electron.

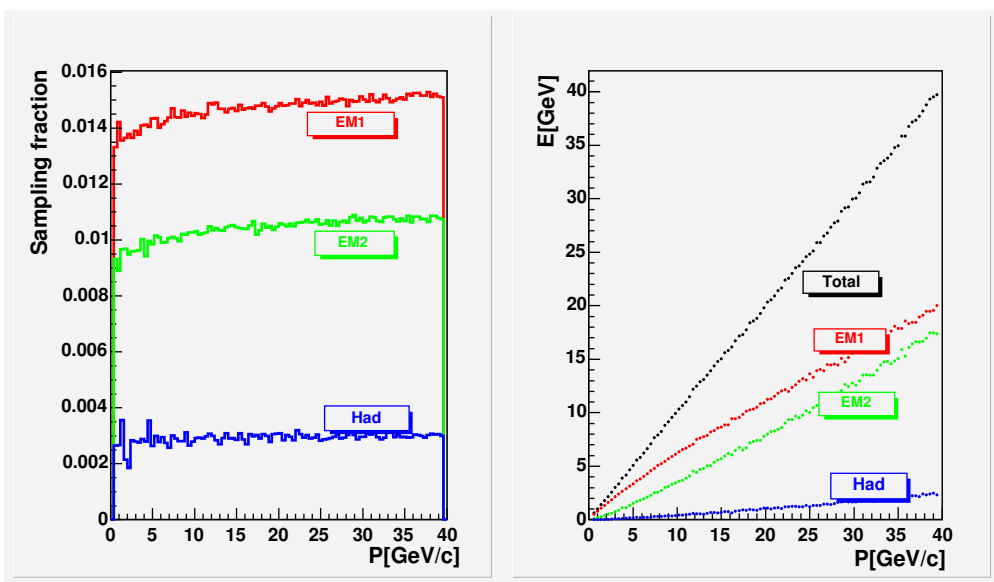

Figure 3.6: Left: Momentum dependence of the sampling faction in NCC segments; Right - energy measured in NCC segments and total energy in NCC vs impact electron momentum.

A simple functional form was used to describe the behavior observed in the simulated data. When energy dependent calibration coefficients were applied, the calorimeter response was found to be linear to better then 1% (Fig. 3.6, right panel). The energy resolution for electrons averaged over NCC phase space is shown in Fig. 3.7.

The coarse structure of the hadronic segment contributes to degradation of stochastic term (23% compared to 20% prediction based upon Wigmans compilation). It also results in a $\sim 1\%$ constant term - an important issue in statistical treatment of the data.

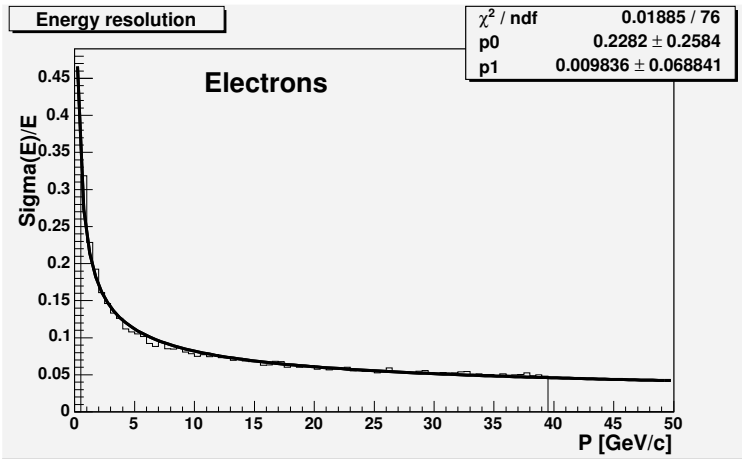

Figure 3.7: The momentum dependence of the intrinsic NCC electromagnetic energy resolution deduced from simulations.

The very preliminary estimates for NCC position resolution based only upon energy measurements in calorimeter towers are presented in Fig. 3.8. Resolution is defined as the RMS of the distribution of the deviations of the particle impact point from the line connecting showers in calorimeter segments. Comparable lateral and longitudinal dimensions of the individual sub towers in electromagnetic and hadronic segments allow for independent position measurements in every segment and provide some degree of pointing capabilities. A very preliminary estimate of the calorimeter pointing resolution (will be improved when proper treatment of the data from PS and SM detectors is established) is shown in the right panel in Fig. 3.8.

As seen from this figure the position and pointing resolution computed applying currently implemented reconstruction algorithms to energy measurements only is ∼2.5 mm and ∼6 mrad and nearly independent of electron momenta. It is interesting to note that similar values computed for hadronic hits are not much different - a feature of predominantly large impact angles resulting in particle trajectory passing through at least two towers in a segment in most of the cases. Both position and angular resolution degrades by nearly ×2 for muons which never interact in the calorimeter.

3.4.3 Discrimination between hadronic and electromagnetic activities in NCC

At present, the rejection procedure used to test the NCC performance is entirely based upon shower shape measurements with calorimeter towers. Lateral shower shape analysis in position sensitive layers (PreShower and ShowerMax) will be added at a later stage and is expected to improve results to some extent. Electron events were used to compute average energy and variance in every segment. The results were parametrized using simple polynomial functions. Analysis algorithm implemented for the purposes of this proposal combines the objects (tower clusters and strip clusters) reconstructed in NCC components into entities

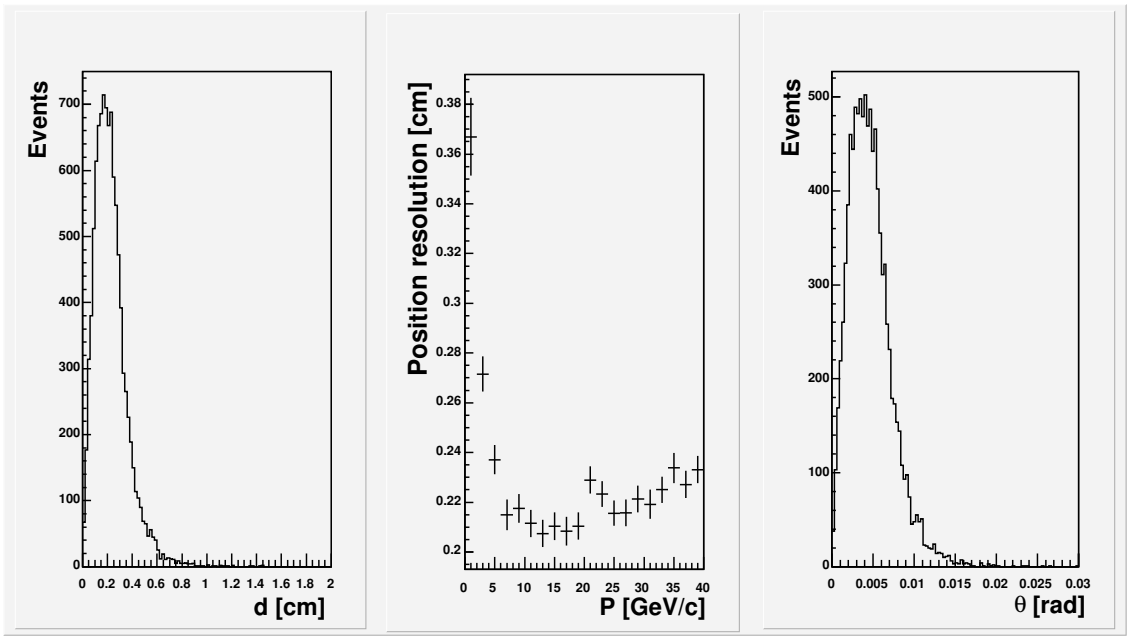

Figure 3.8: Left: radial distance between electron impact point and measured object; Center: the momentum dependence of the NCC position resolution (based upon energy sharing between towers only); Right: angule between impact vector and track vector measured in calorimeter.

named tracks. The energy of the track is equal to the sum of calibrated energies of contributing clusters, its geometrical parameters are defined as an energy weighted average of vectors pointing from primary vertex to individual contributing objects. A χ^2 estimator qualifying the difference between track parameters and predictions based upon energy pattern parametrization was used to separate electromagnetic from non-electromagnetic activities. The χ^2 distributions for electron and pion (treated as electrons) tracks in the calorimeter is shown in Fig. 3.9.

Nice feature of the data presented in this figure is a nearly identical behaviour of the electron χ^2 distributions based on longitudinal and transverse shower measurements what confirms statistical validity of underlying assumptions. A cut of $\chi^2 < 9$ was applied to the statistics of tracks due to charged hadrons impinging on the calorimeter to select those resulting in pattern of energy in calorimeter segments consistent with electron hypothesis. In the absence of independent momentum measurements for E/P matching, hadron rejection will depend on the momentum distributions of the particles we want to retain and particles we want to reject. We used PYTHIA to predict momentum spectrum of charged particles in calorimeter. (black line in Fig. 3.10). Red line in the same figure is the energy spectrum of fake-electromagnetic showers due to calorimeter exposure to properly weighted charged pions. The ratio of two histograms is the hadron suppression factor which must be applied to the spectrum of charged particles impinging on NCC to compute its contribution to the inclusive spectrum of electromagnetic activities as seen in NCC.

Further insight into NCC discrimination capabilities will certainly require much more

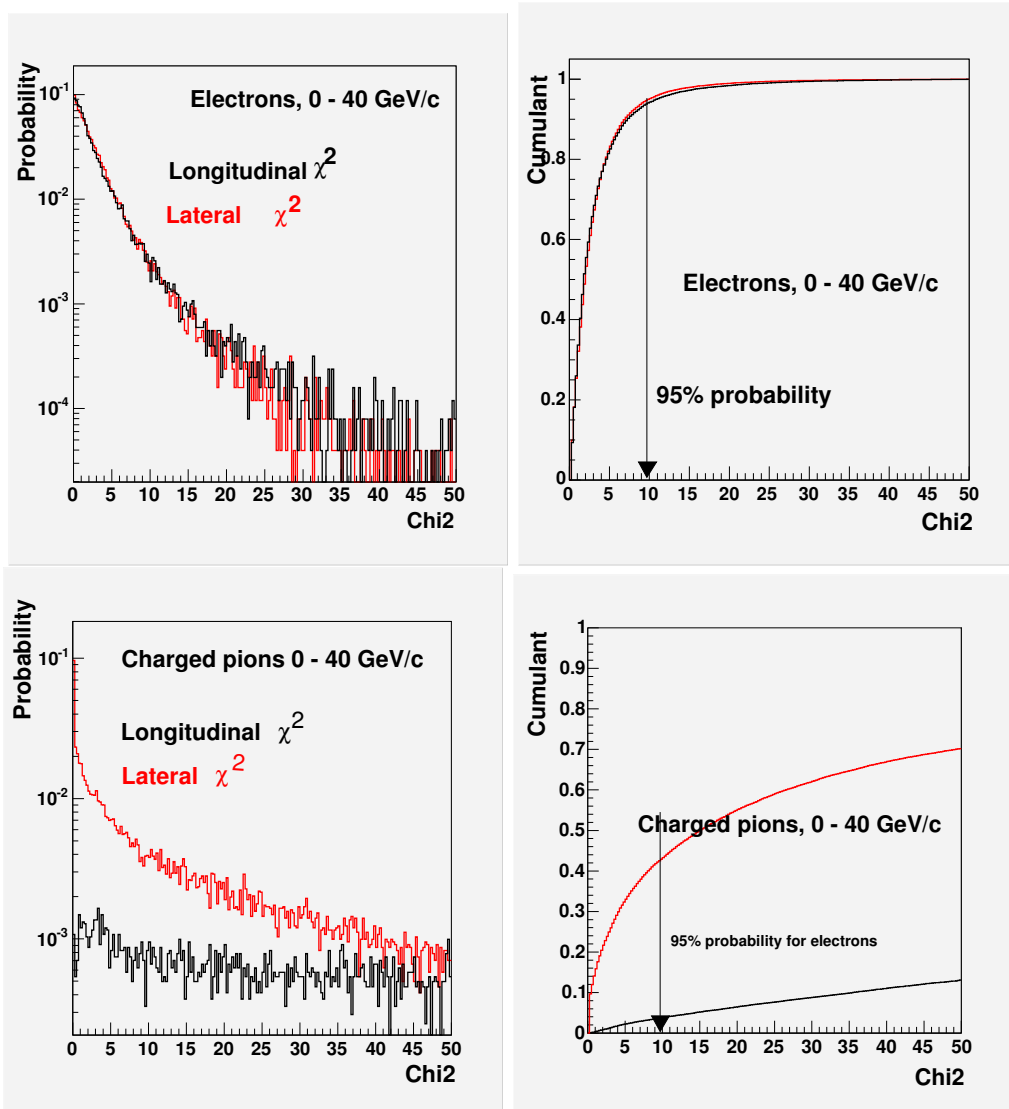

Figure 3.9: The χ^2 distributions for electrons (top) and pions (bottom) in the momentum range 0.5-40 GeV/c in NCC. The corresponding cumulative distributions are in the panels on the right . Currently is based upon energy measurements only.

involved simulation compared to what we were able to produce in time available. In particular it will be premature to consider the data presented in this section as final, lateral shower development measured in the tower structured segments of calorimeter and in PS and SM detectors is currently ignored by rejection algorithms.

Fig. 3.11 illustrates the efficiency of this rejection algorithm when applied for extraction of inclusive photon spectrum in minimum bias events simulated with PYTHIA.

The figure is selfexplanatory. The black and blue histograms are for all particles hitting NCC (all hit energies and all track energies), the other two histogramms are for the photons only (all photon energies and energies of the photon tracks selected by χ^2 criteria). While

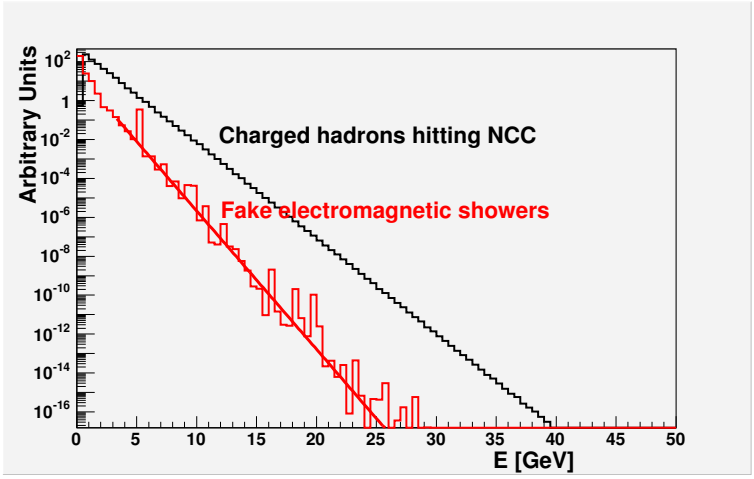

Figure 3.10: Top: Momentum distribution of hadrons impingin on NCC and energy distribution of residual (after χ^2 testing) tracks consistent with electromagnetic pattern. Currently is based upon longitudinally segmented energy measurements only.

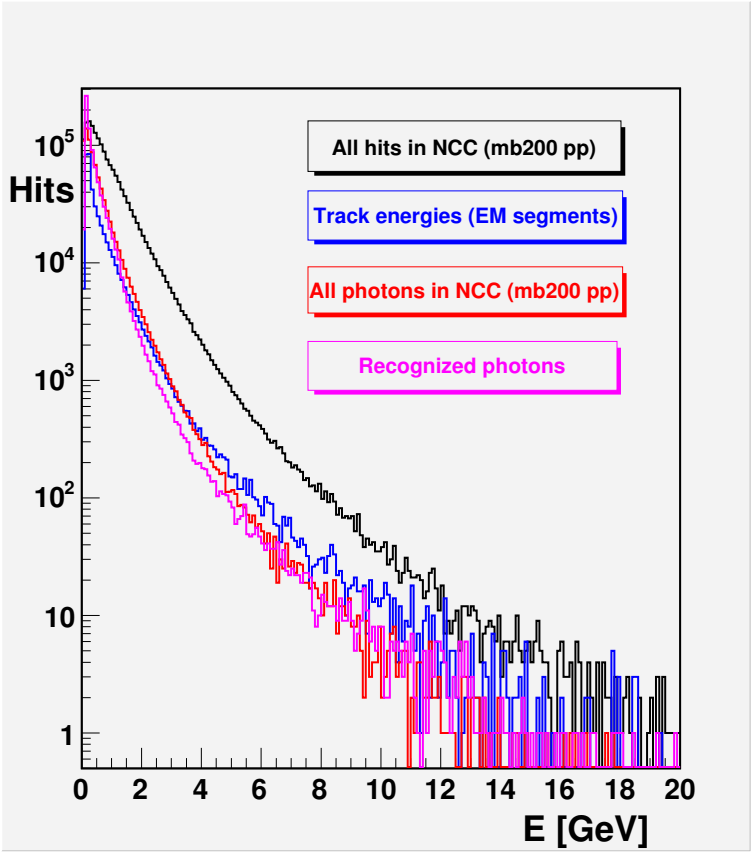

Figure 3.11: Energy distribution for all (black and blue) and photon (red and magenta) hits in minimum bias events in NCC. Black - energies from PYTHIA; blue - track energies in NCC; red - photons from PYTHIA; magenta - identified photons.

ratio of the first two histograms follow the general tendency observed in Fig. 3.10 the two figures for the photons are nearly identical what confirms that NCC can actually be used to measure the forward inclusive production of photons.

The residual tracks due to hadrons will contribute up to 0.1% of inclusive hadronic cross section to the photon spectra which must be processed through subtraction procedure usually applied to extract direct photon production. The latter value is to be compared to the corresponding numbers for direct photons which can be estimated from PHENIX published data on π^0's and direct photon production in p+p interactions at 200 GeV [8,9]. In the p_T range above 6 GeV/c where direct photon yield exceeds 10% of the π^0 yield ($\sim$5% of the charge hadron yield) fake electromagnetic showers in the proposed NCC are less then 1% of the total hadronic yield corresponding to a direct photon to fake electromagnetic showers ratio better then 10%.

3.4.4 Jet measurements

Jets in NCC are an important signature for the hard scattering process and a source of information on the kinematics of the underlying 2$\rightarrow$2 scattering. PHENIX is currently studying physics involving jets in the final state mainly through inclusive measurements of high transverse momentum hadrons. Extracting the information characterizing initial hard scattering and properties of the partons involved in 2$\rightarrow$2 hard process can't be done without external data on parton fragmentation properties which are modified by QGP and are subject to large theoretical uncertainties. Detailed jet measurements would require total absorption of hadrons in calorimeter what is certainly well above the NCC capabilities (precluded by space constrains). To estimate the NCC performance relevant to jet physics a library of PYTHIA jets was simulated (stripping off all particles which could not be traced to the fragmenting hard scattered parton) and processed trough GEANT. Only jets due to fragmenting parton pointing towards NCC were retained. In Fig. 3.12 the total energy of jet particles hitting NCC is shown vs the energy of fragmenting parton (left panel), energy measured in NCC function of jet energy delivered to NCC (central panel) and measured width of the jets (in units of NCC towers, right panel) are shown. Jet width is peaked around 2 towers what means that 4-towers radii cone around peak shower will on average contain more then 90% of measured jet energy (characteristic width of electomagnetic shower is $\sim$0.8 in the same units).

The percentage of the total jet energy measured in NCC (in elecron calibration) is $\sim$50% of the actual delivered jet energy (see Fig. 3.12). Jet energy fluctuation normalized to the total measured energy is shown in Fig. 3.13 function of total energy of all fragments hitting NCC. NCC measures jet energies with nearly constant rms$\sim$40% dominated by fluctuations in the number of fragments and hadronic leakage. Resolution defined as an RMS of the energy seen in EM segments (where the role of hadronic fluctuations is reduced) is shown in the same figure for comparison. Based upon already available data limiting measurements to EM-segments only is unlikely to improve energy resolution for jet-related measurements.

In general measurements of the total jet energy (or 4-momentum) are not required to reconstruct hard scattering kinematics if direct photon parameters are measured. What is

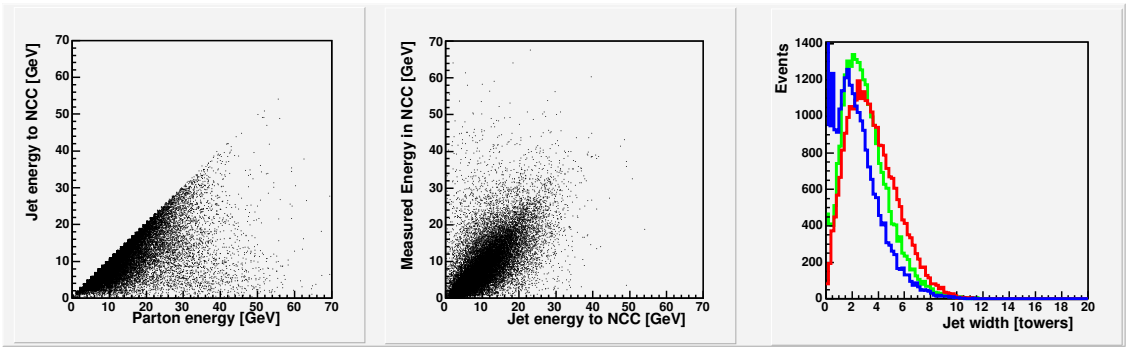

Figure 3.12: Left: Total enegry of jet fragments hitting NCC vs jet energy (PYTHIA); Center: Measured jet energy vs energy of fragments in NCC; Right: Jet width measured in NCC.

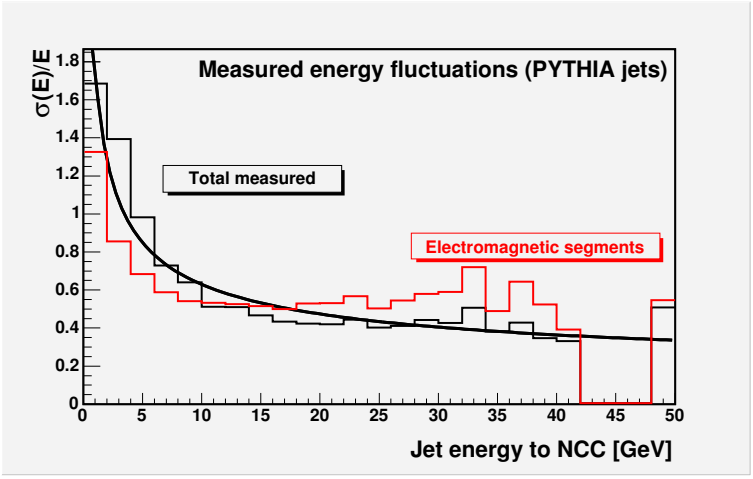

Figure 3.13: The relative RMS of the measured total and electromagnetic jet energies

of importance is an ability to trigger on jet, find the jet and measure its directional vector. The distribution of the angular differences between jet 3-vector as per PYTHIA, sum of fragment vectors and that measured in NCC (ignoring effects of underlying event) is shown in Fig. 3.14.

It is peaked around 20 mrad but has a large tail related to fluctuations in energies deposited by stable hadrons from jet core. The effect of limited angular resolution on reconstructed parton kinematics will be further investigated.

3.4.5 Muons in NCC: reconstruction and rejection

The distribution of energies left in NCC by mips of up to 50 GeV/c momenta is shown in the left top corner in Fig. 3.15. It peaks at ∼.6 GeV with contributions from individual segments peaking at 0.14 GeV, 0.12 GeV and 0.34 GeV respectively. NCC readout (see below and Appendix E) is designed to measure energies per tower up to 50 GeV in electron calibration with ∼13.5 bit resolution (least bit of ∼5 MeV) and a noise contribution well

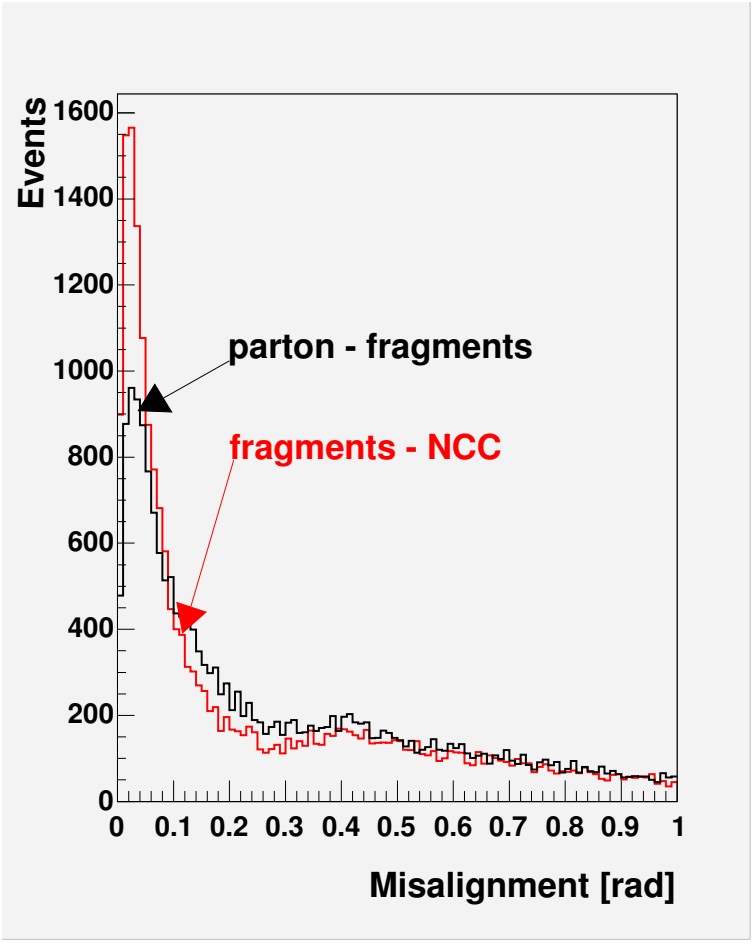

Figure 3.14: Jet angulare resolution (with respect to the vector sum of jet particles). Currently is based upon energy measurements only.

below a single bit width. A tipical MIP signal will be seen around channel 30 in every calorimeter segment what assures an effective peak to noise sepaparation for MIP signals. Muon energy pattern in calorimeter is different from both electromagnetic and hadronic showers. It typically shows smaller number of towers and a very simple longitudinal profile. A library of muons in NCC was used to define χ^2 estimator based upon values and rms of energies in segments, tower multiplicities in muon clusters and estimated position resolution (see Fig. 3.15 top right). A very preliminary χ^2 distribution is shown in Fig. 3.15 lower left panel, its cumulants computed for samples of muon and pion tracks are in the lower right panel. It is very encouraging to see that in segmented calorimeter even a very coarse implementation of χ^2 estimator for muons already allows to substantially reduce hadronic background.

The elimination procedure based upon χ^2 estimator as described above was applied to test NCC efficiency for suppressing fake muon background generated by muon spectrometer misinterpreting decays of low momentum punch-through hadrons. In general hits from fake muons will be distributed over NCC apperture following the anguar distribution of particles

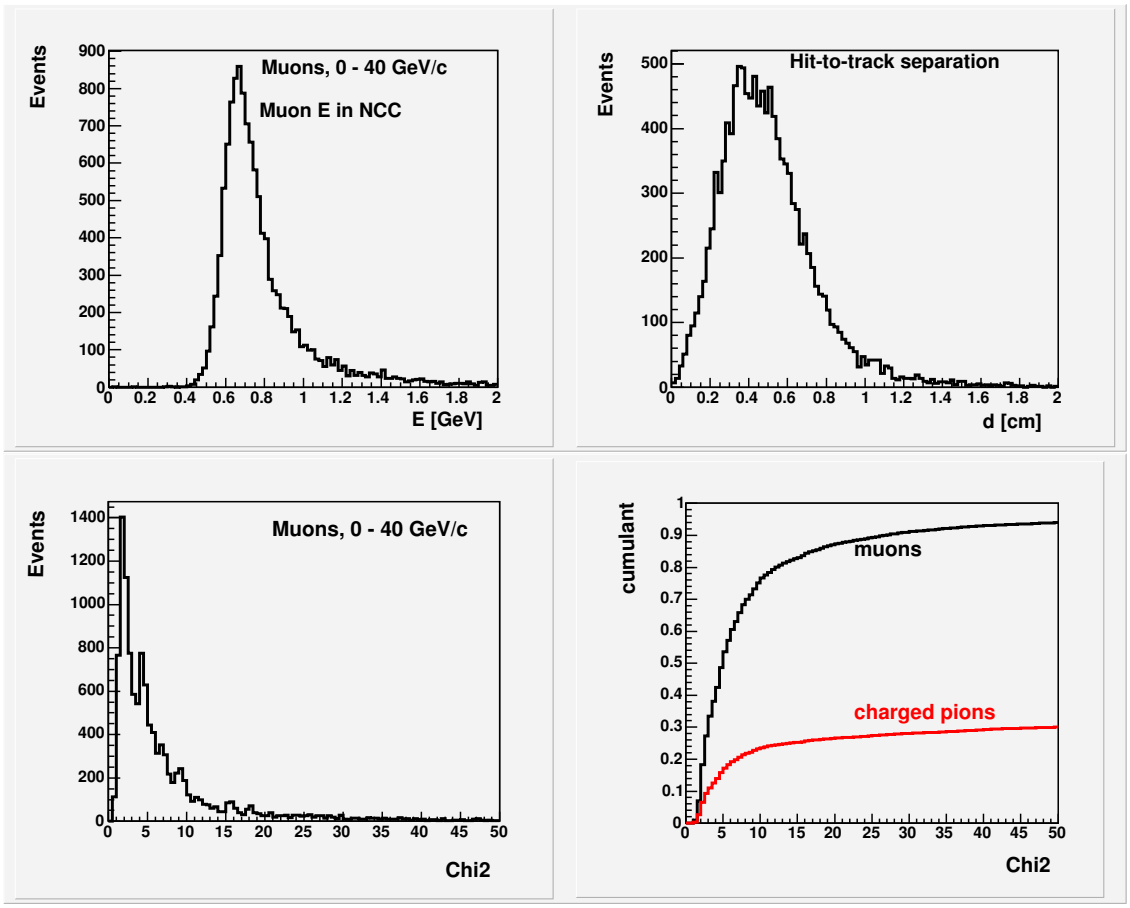

Figure 3.15: Base data used to extract fitting primitives for muons passing through NCC

in minimum bias events. Testing the probability for random hit in NCC to find an associated track with characteristics resembling MIP was done flipping momentum vectors of hadrons in minimum bias PYTHIA events and comparing them to the pattern seen in NCC in the opposite hemisphere. The radial distributions for all tested hits and for those passing the filter are shown in Fig. 3.16.

As expected algorithm works best on the periphery where unfortunately PHENIX does not have a muon coverage but even in the area close to the beam pipe it delivers the suppression factor ∼50.

3.4.6 π^0 reconstruction

Most of NCC physics is intrinsically related to the photon/π^0 measurements. Critical test of NCC performance are events with a correlated photon-jet in the final state resulting from Compton scattering of a low-x gluon on a quark, where the photon gives us a calibration of the energy and the transverse momentum of the gluon. The background to this process is the double-jet final state with one jet fragmenting into a leading π^0 faking a single photon due to shower overlaps. Given the characteristic slope of the shower core ∼0.2 $R_{Moliere}$, the

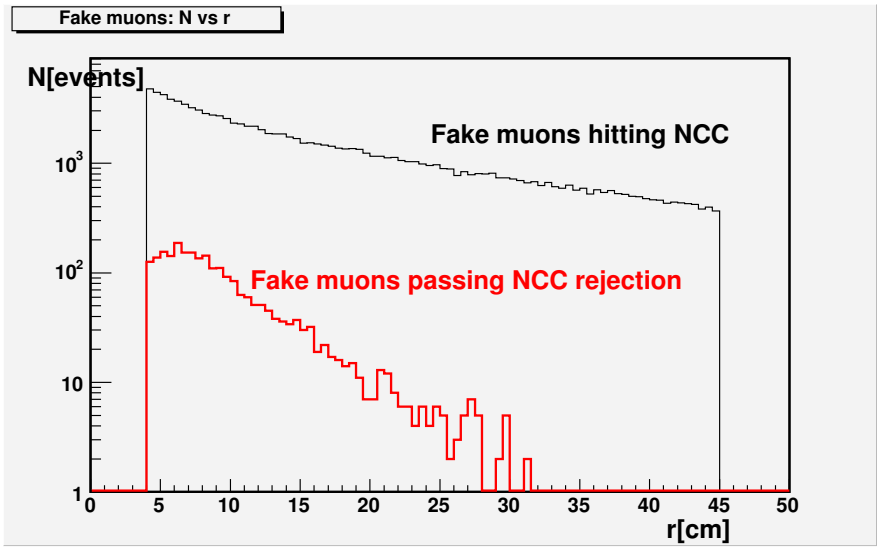

Figure 3.16: Fake muon rejection in NCC. NCC occupancy per PYTHIA minimum bias. Fake muons were simulated refleting momentum vectors of simulated particles hitting opposing NCC

clear separation of the maxima due to two photons with close energies in a detector built of composite material with Moliere radius $R_{Moliere}$ ∼18 mm should be possible down to a similar value of $\Delta \sim 0.2R_{Moliere}$.

The problem arises when attempting to prove that observed maxima are due to independent showers and not to the shower fluctuations. The separation is too small compared to the average shower radius at the same energy to make meaningful quantitative tests based on lateral shower shape measurements. The following strategy is adopted for the NCC to deal with fluctuations. We are installing two layers of identical 2-d position sensitive detectors (0.5 mm pitch) in the calorimeter at two depths: 2 X_0 and 7 X_0. The first layer (PreShower), installed downstream of the first two sampling layers in the first EM segment, is a hit counting layer where position resolution is limited by the strip width to ∼150 μm. The second (ShowerMax) layer will serve to measure the decay asymmetry through shower shape analysis at a depth where the shower expands to 1 $R_{Moliere}$ radius. The algorithm will first find all showers in the calorimeter. For every shower it will identify the regions of interest in PS and SM detectors and look for hits in the PS layer to find those which may contain overlapping candidates. These overlap candidates will be checked for consistency with the hits in the SM layer where the deconvolution will finally be made assuming that the contribution of individual photons is proportional to the peak energy values as measured in the SM detector. Simulations have shown that this approach works well to energies close to 30 GeV (effectively to the limit set by integrated luminosity).

This section shows the proof-of-principal for the algorithm as described above and will be further updated when test beam data will become available. The π^0 events were simulated with a uniform momentum distribution between 1 and 30 GeV/c. Checks were made that only those events with both photons inside NCC aperture are retained. The pattern

recognition algorithm used was simple and intended to answer whether the data actually posesses the features required to separate single showers from overlapping showers using this technique. In the detector with Moliere radius ∼14 mm and tower size 15×15 mm^2 decay kinematics implies that a substantial fraction of π^0 decays will yield clearly separated photons. As in the central calorimeter, we consider two showers distinct if their maxima are separated by at least one counter i.e. there is a visible valley between the showers.

A clustering algorithm was applied to the hits seen in the longitudinal segments of the calorimeter. The clustering was done separately in all segments. Showers ordered by energies were combined into "tracks" originating from the collision vertex. Whenever the algorithm produced more then one track in the NCC, an attempt was made to compute an effective mass. The comparison of the effective mass distributions for e- and π^0's events producing multitrack configurations is shown in the left panel in Fig. 3.17. A scatterplot of the effective mass vs π^0 momentum in "multitrack" π^0-events is shown in the right panel.

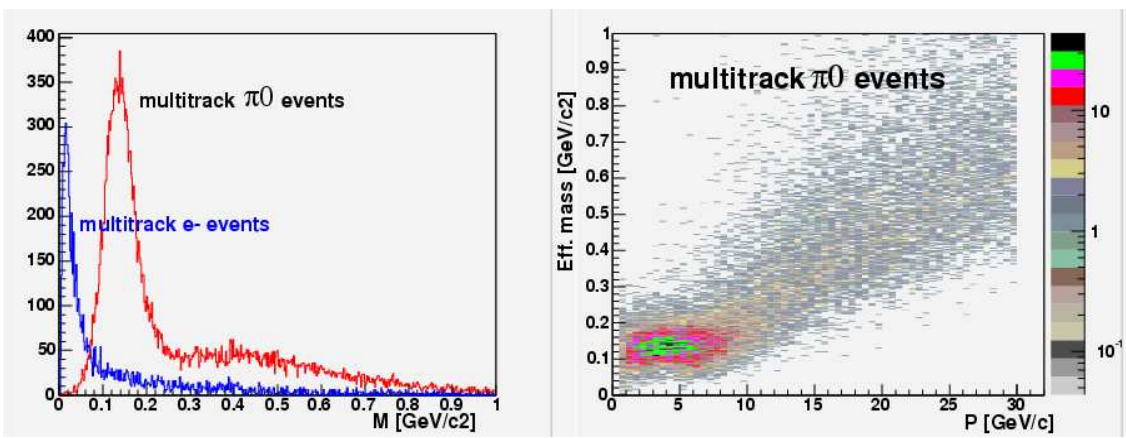

Figure 3.17: Two-shower effective mass distribution in the events with two distinct maxima found in the pattern of deposited energy in NCC.

A clear π_0 signal with a width of $\sim$ 25 MeV/c^2 is seen in π^0 events. The distribution for electron events is totally consistent with background. This approach works reasonably well for π^0 momenta below 7 GeV/c and fails at higher momenta where the showers begin to merge.

Thus computed probability to find two distinct showers in the event with both photons from π^0 decay in the detector aperture is shown in Fig. 3.18.

The events with effective mass outside the two standard deviation window around the π^0 mass as well as single "track" events were further subjected to a reconstruction procedure relying on the pre-shower (PS) detector for shower separation measurements and on the shower-max (SM) detector for decay asymmetry measurements.

All fired strips in the PS and SM detectors were subjected to a simple clustering algorithm which assumed all strips around a local amplitude maxima being part of a single cluster. For illustration in Fig. 3.19 the hit pattern produced by 12 GeV/c π^0 is shown in the PS and SM detectors.

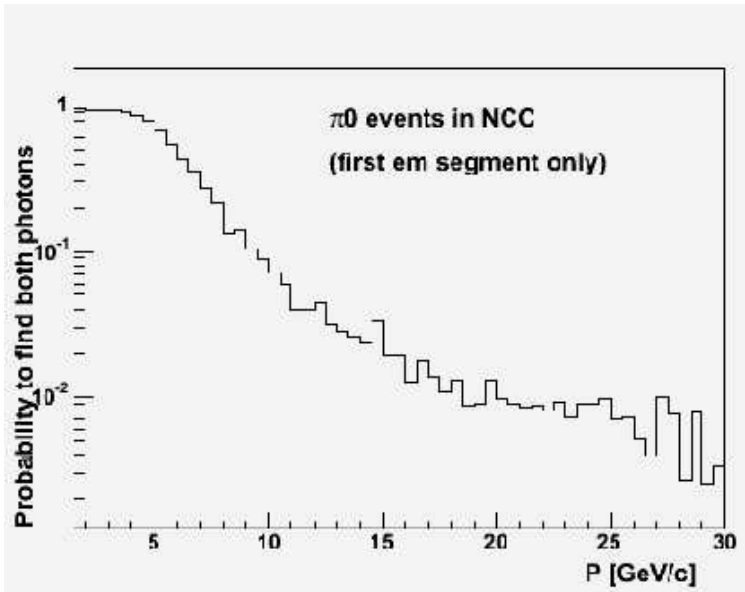

Figure 3.18: Probability to find both showers from π^0 decay as two distinct maxima in NCC vs momentum of π^0.

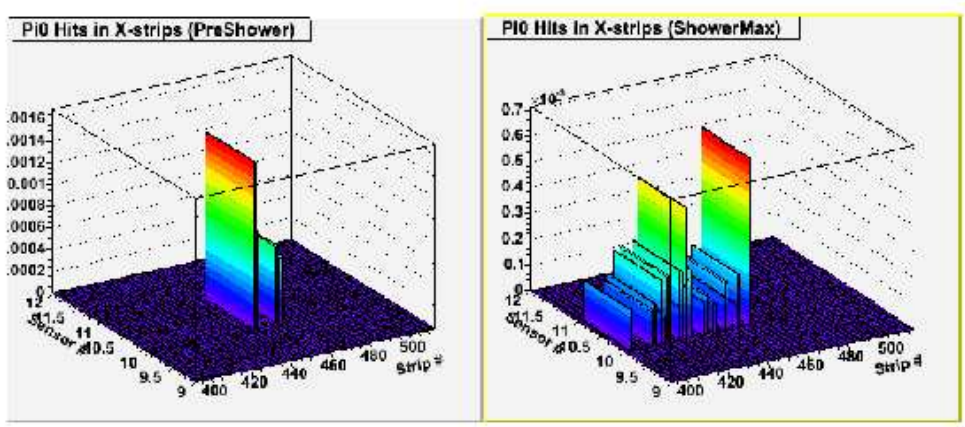

Figure 3.19: Energy patterns in the PreShowr and ShowerMax detectors due to two overlapping photons from 12 GeV/c π^0 decay. (The vertical axis is an energy per strip in GeV).

The multiplicities of fired strips in two detectors are grossly different. The clusters are obviously separated in both detectors but fluctuations are certainly the limiting factor adversely affecting the resolving power for any simple tests based on cluster multiplicities.

The total energy is obtained from the sum of energies in EM1, EM2 and HAD. The decay opening angle is obtained using hits in the PS detector. The decay asymmetry is obtained from the shower profiles in the SM detector. Once these three factors are known, the effective mass can be computed using formulas based upon trivial decay kinematics. The comparison of the distributions of effective masses reconstructed using this procedure in electron events

and π^0- events is shown in Fig. 3.20.

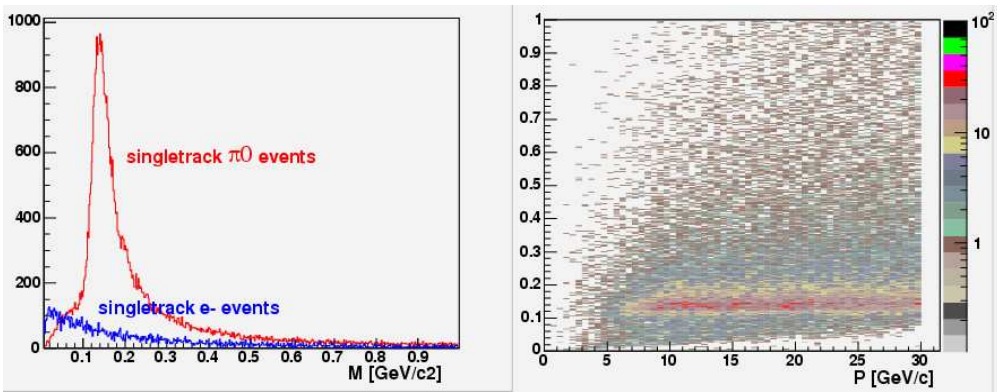

Figure 3.20: Reconstructed effective mass distribution in the events with a single distinct maximum found in the pattern of deposited energy in NCC.

The π^0 peak is present in π^0 events only, whereas the distribution for e-events is totally consistent with background. The shape of the π^0 peak as it is reconstructed by this procedure is a subject for further improvements. Currently it has a central peak characterized by $\sigma \sim$ 20 MeV/c2 consistent with detector energy resolution on top of a wide distribution which would usually be considered as a background. The real composition of the peak reflects correlations between the decay asymmetry and the effective mass resolution intrinsic to this approach. While asymmetric decays result in better separated showers, asymmetry measurements in the SM detector get less and less precise when energy in one of the showers decreases. There are also flaws and shortcuts in the current implementation of this procedure resulting in a complete failure to properly reconstruct very asymmetric decays. Addressing such issues will require further development. The losses and failures to reconstruct π^0's by the currently available algorithm are summarized in Fig. 3.21. We expect to make considerable improvements in the algorithm using data collected with prototype in a test beam.

Mass cuts 2 standard deviations around the central peak applied to π^0 masses reconstructed in "single track" events result in loosing 50% of π^0's from the peak region. All other losses are within 15% combined. If events producing reconstruction failures are excluded the estimated efficiency of algorithm to reconstruct π^0 both via multitrack and singletrack algorithm in the NCC is shown in Fig. 3.22.

Even at this early stage in the development the efficiency stays above 40% to 30 GeV. For comparison the π^0 reconstruction efficiency in the PHENIX central calorimeters drops to zero around 15 GeV/c.

3.5 NCC Occupancy and Dynamic Range Considerations

In the NCC the energies of showering particles are shared between three segments of the calorimeter. This sharing is uneven, with most of the electromagnetic energy deposited in

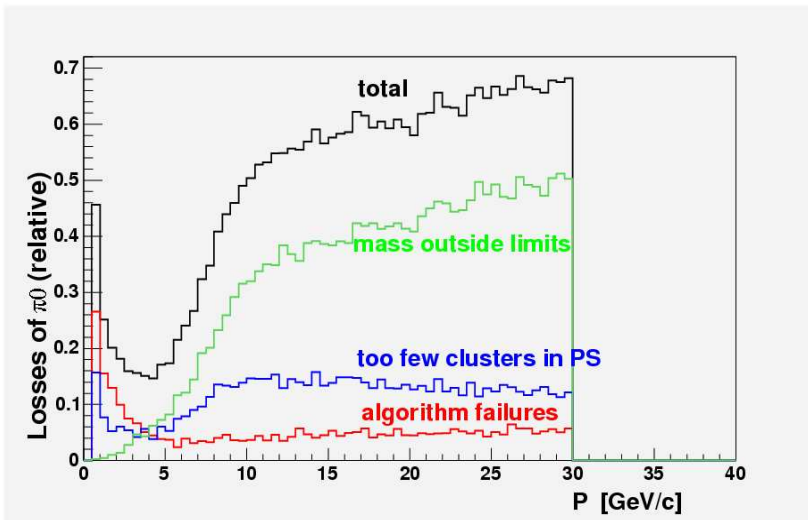

Figure 3.21: Probability for π^0 in NCC to fail in reconstruction or to end up outside 2σ mass window.

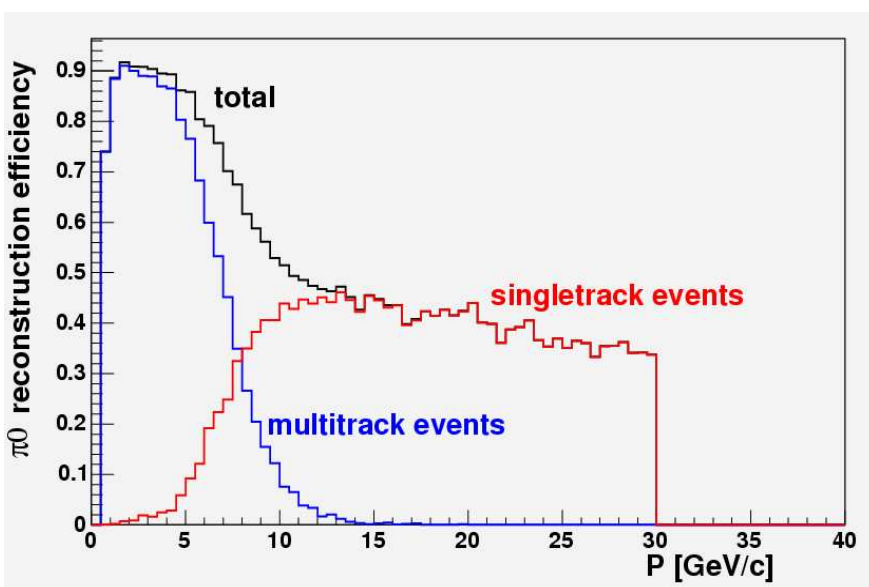

Figure 3.22: Probability for π^0 in NCC to be reconstructed within 2σ mass window.

EM segments, and most of hadronic energy in HAD. In p+p interactions it is sufficient to set the upper limit of the dynamic range per tower per section to $\sim 60\%$ of the W mass to cover the whole range of physics topics we are planning to study at a 500 GeV collision energy.

In heavy ion collisions, the calorimeter located at 40 cm from collision vertex will see a high occupancy environment resulting from hits due to different particles piling up. The potential impact on calorimeter dynamic range was estimated merging contributions from individual minimum bias events to simulate the environment typically observed in the central heavy ion collisions. The 50 GeV dynamic range was found equally fitting the needs of both physics programs.

The question of NCC performance in heavy ion collisions is in general vary complicated. To illustrate the problem an event with few 100 particles hitting each NCC (merged min bias events) is shown in Fig. 3.21.

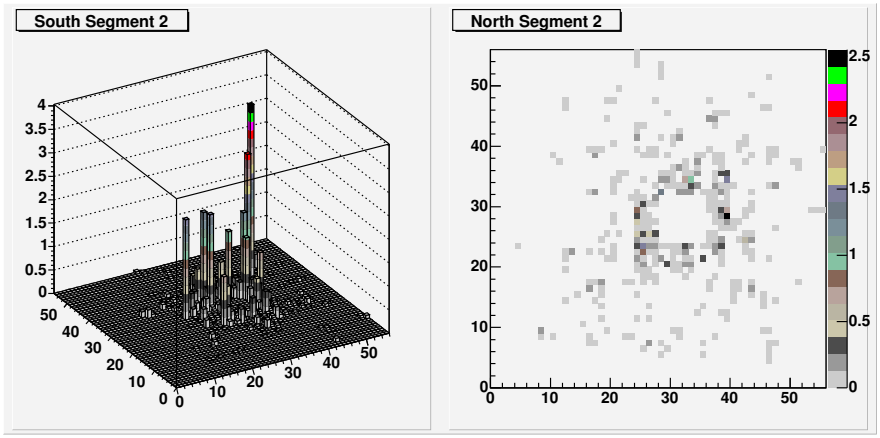

Figure 3.23: Something about dynamic range

Different data representation is chosen for North and South detectors. Most central region in the calorimeter is certainly overpopulated for meaninful low energy shower reconstruction. With increased centrality this region will extend towards smaller rapidities, correlations between event centrality and extent of the saturated regions are subject for further studies.

3.6 NCC Mechanical Design

A modular design illustrated in Fig. 3.24 was developed for NCC to allow for a relatively easy industrialization of the construction project.The NCC mechanical design is implemented in the form of Autodest Inventor 3D-model and transfered to the responsibility of the PHENIX engineering group so any potential modifications could be easily handled. The calorimeter is built of "bricks". Two kinds of bricks (see Fig. 3.25) are used to build two quasi-independent calorimeters: the electromagnetic (EM1 and EM2) and hadronic (HAD). All bricks are double silicon sensor wide. There are three standards for the brick length in the electromagnetic and hadronic segments (7/6/5 sensors in HAD, 6/5/4 sensors in EM1 and EM2). The

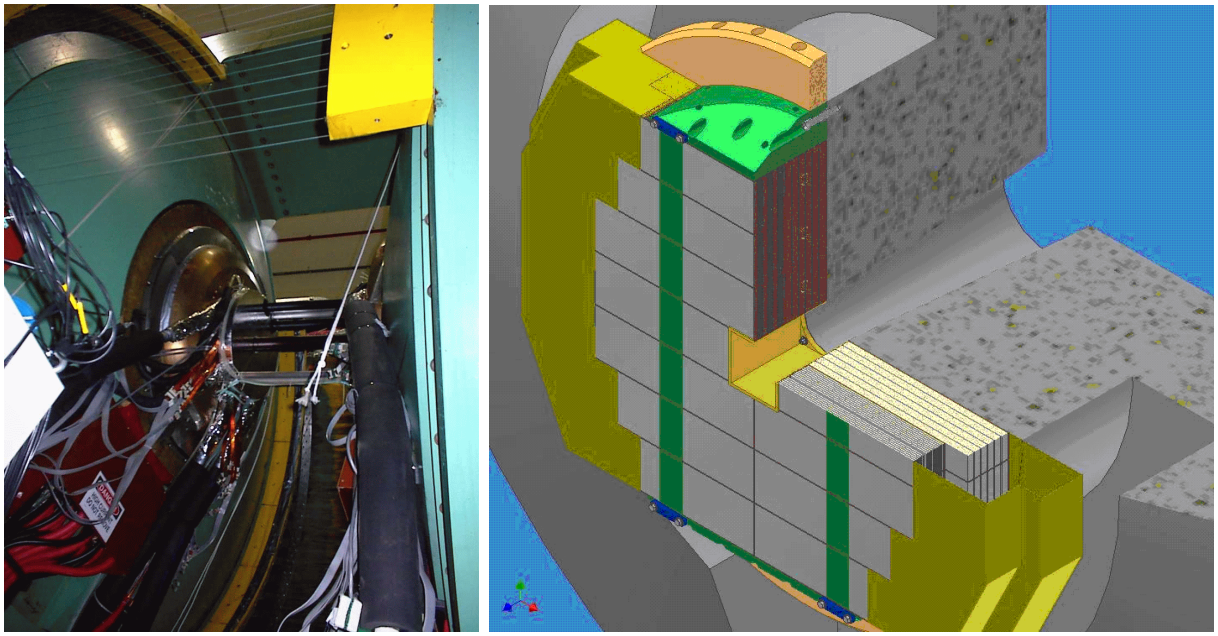

Figure 3.24: PHENIX Nose Cone (left panel). Nose Cone Calorimeter (right panel). Boxes upstream are electromagnetic segments (EM1 and EM2), downstream boxes are HAD.Crates with preamplifiers and cable drivers are also shown

electromagnetic bricks are much more demanding in terms of the readout as compared to the hadronic bricks. Electromagnetic bricks are composed of two electromagnetic segments (EM1 and EM2) built out of fine calorimeter sampling cells, preshower detector (PS) and shower max detector (SM). A hadronic brick consists of a single hadronic segment built out of coarse sampling cells. Each brick has a W plate facing upstream and Cu skin enclosing it on all other sides save one for connections to external electronics.

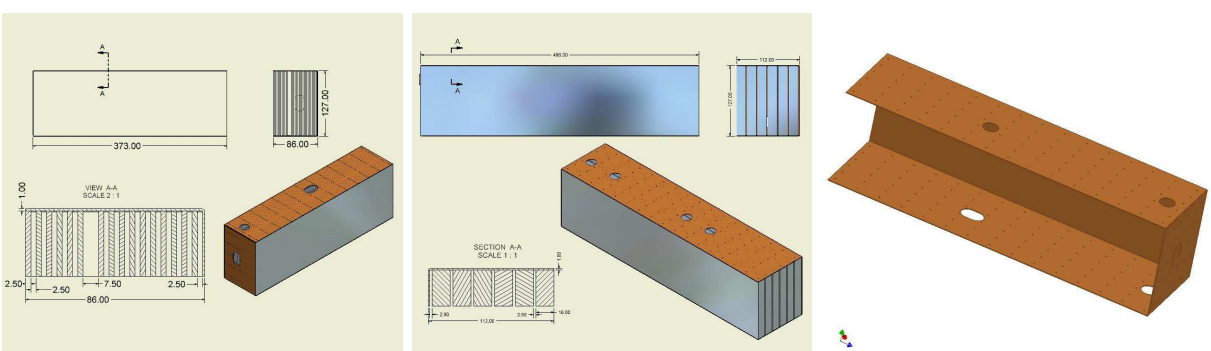

Figure 3.25: NCC building bricks. (left) electromagnetic [preshower and shower max detectors are shown partially extracted], (center) hadronic, (right) Cu skin for the electromagnetic brick.

When assembled, the bricks form two vertical walls. Small locking pins are used to maintain the geometry. For mechanical reasons the two walls have the same size vertically,

giving up some of the acceptance in hadronic segment. Horizontally the hadronic wall is two sensors wider compared to electromagnetic wall. This geometry allows us to minimize the cost while still measuring all particles originating in the area ±30cm with respect to the nominal collision point. The calorimeter walls are supported by two shelves above and below, and thin pretensioned front braces (strips of stainless steel or Kevlar) preventing the walls from buckling outward.

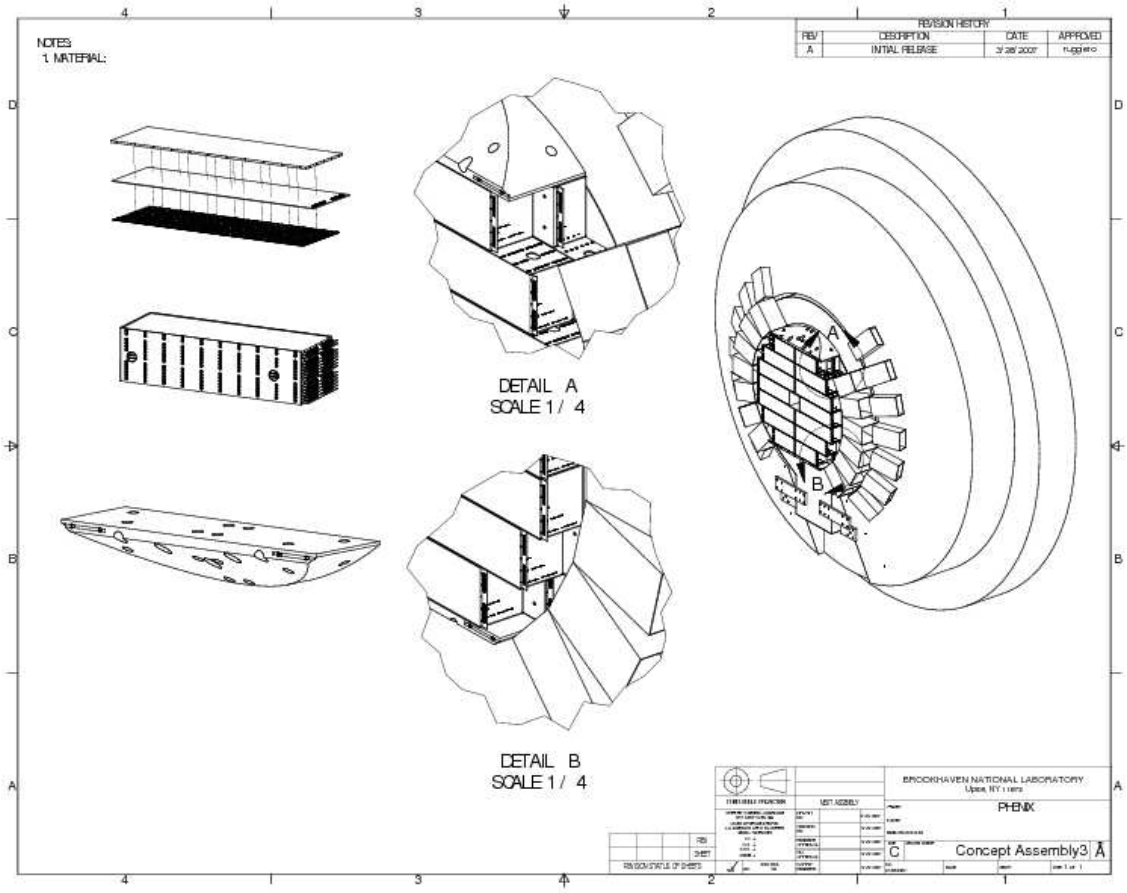

Figure 3.26: Main components of NCC design: sampling cell, brick, cutofs showing different pats of assembled calorimeter, assemblled calorimeter with analog readout electronics on magnet pole.

3.7 NCC Readout

3.7.1 Sensors

Two kinds of silicon sensors are used in NCC readout: pad structured and pixelated strips. They both will be described in more detail below and in Appendix D. The main require-

ments for the silicon detectors in the calorimeter are reliability, precise shower energy measurements via charge measurements in silicon, precise tracking measurements, and radiation hardness. The pad size chosen for the NCC is ∼1.55x1.55 cm^2. The strip size for PS and SM is ∼0.5x60 mm^2. All silicon detectors in the NCC are 6.2x6.2 cm^2 diced from 4" wafers 525 mm thick. Critical to the success of the experiment will be reliable operation of these sensors in a radiation environment. The estimates based upon total energy flow simulation predict the total fluence of 100 kRad (in Si) or about 3×10^{12} equivalent neutrons per cm^2 over the period of 10 years (assuming p+p interactions at 200 GeV with luminosity $\sim 2x10^{32}s^{-1}cm^{-2}$). For a pad size of the order of a few cm^2 and 300 mkm sensor thickness, published data predict the leakage current of the order of 5-10 mkA per pad. Handling this value of current requires decoupling capacitances between pads and preamplifiers.

For the operation of the detectors the control of leakage current is important because of the increased noise. Leakage current may also result in increased bulk heat production in silicon which may lead to thermal breakdown if the silicon detector is not cooled. In our design of sensors and selection of raw material we were guided by the experience and work done within the scope of the D0 (FNAL) and ALICE (LHC) projects and recent published data from the research and development in radiation hard silicon technology. In particular we followed few simple rules:

- Single sided sensors from established vendors to insure higher yields and less trouble due to the simplicity of the design. It is also well known that double sided sensors suffer more radiation damage,
- A minimal number of different sensor designs (only two in the NCC case). Design to successful completion of the project using a single vendor. Transfer the design to additional vendors when ready. This will speed production,
- Use short strips to reduce the number of ghosts hits to avoid creating pattern recognition problems. We use 4" wafers only,
- Specially designed guard ring structures. Such guard rings are important in order to keep breakdown voltage before and after irradiation as high as possible.

Following these recommendations the pad layers in the Nose Cone Calorimeters are built using single-sided single-metal p+ on n- bulk silicon devices. The technology of pad structured sensors is well tested. We have three established vendors ready to manufacture the 6.2x6.2 cm^2 pad-structured sensors using nearly identical design files, corrected for specifics of technology. The pixelated strips (stripixels) are novel detectors developed at BNL and currently selected as a base design for the silicon sensors in another of PHENIX upgrades - the central silicon tracker. The design chosen by PHENIX are interleaved stripixel detectors where each pixel is divided into two parts: X-cell (or pixel) and Y-cell. X-strips and Y-strips connect X-cells and Y-cells, respectively, in a strip detector readout scheme. In this detector two dimensional (2D) position sensitivity is achieved with single-sided processing. A short summary of sensor parameters is given in Table 3.2.

Both pad sensors and stripixels have been prototyped at ELMA (Russia), ON Semiconductors in Czech Republic and by the SENS Company in Korea. The R&D program to develop

Specifications	Pad-structured sensors	Stripixel sensors
Wafer thickness	525 mm	525 mm
Depletion voltage	100-120 V	100-120 V
Diod capacitance	25 pF	3 pF
Bias voltage	Full dep. V + 20V	Full dep. V + 20V
Leakage current	< 300nA total, <20nA/pad	< 1nA total
Junction breakdown	> 300V	> 300V
Implant area	15 x 15 mm2	
Al area	15.02 x 15.02 mm2	15-60 mkm prototyped. Decision pending.
Polysilicon bias resistor		1 m?
Interpad (strip) capacitance	< 2pF (pad-pad) or < 8 pF (pad-all neighbors)	TBD
Maximum heat dissipation from the bulk material	< 50 mW	< 50 mW
Heat dissipation from on-the-sensor electronics	-	o.5 Wt

Table 3.2: NCC Silicon Sensor parameters

pad-structured sensors is now completed. We are currently in the last stage of developing and prototyping stripixel sensors (the delivery of sensors of the final design manufactured following double-metal technology is expected in spring 2007).

We briefly review the design of the sensors and related infrastructure in this section. R&D results are presented in Appendix D.

3.7.2 Pad-Structured Readout Layers

The pad structured Si layers (20 in total) are built of 6x6 cm^2 silicon detectors subdivided into 16 identical square cross section pads (diodes).

The individual pad-structured sensors will be assembled into stacks consisting of silicon crystal, single layer interconnect board and ceramic substrate glued together using cilicon-based adhesive. Assembled and exploded stacks are shown in Fig. 3.27.

Sensors when glued to the dielectic side of interconnect board are wire bonded (pad center) through the 3 mm diameter vias to the bonding pads on the opposite side of the interconnect board. Area around bonding ring is also used for low-profile rc-network placement (not shown in the figure). Two 20 pin low profile (0.9 mm total height) connectors installed close to the edges of the interconnect board are used to connect the sensor stack to traces on a carrier board conductively glued to the tungsten plate (see Fig. 3.28).

Everywhere else the 0.9 mm gap between interconnect and carrier boards is filled with alumina ceramic spacer 0.8 mm thick glued to the inteconnect. The spacer will provide for rigidity of the sensor subassembly and prevent the sensor-interconnect laminate from

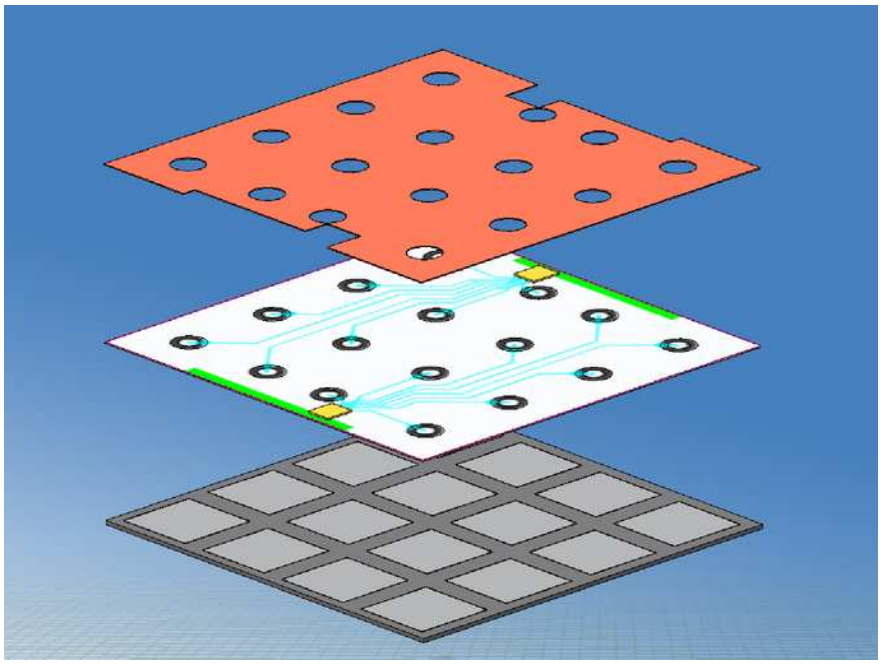

Figure 3.27: Pad-sensor stack. Explode view of the sensor stack in the right panel of the picture.

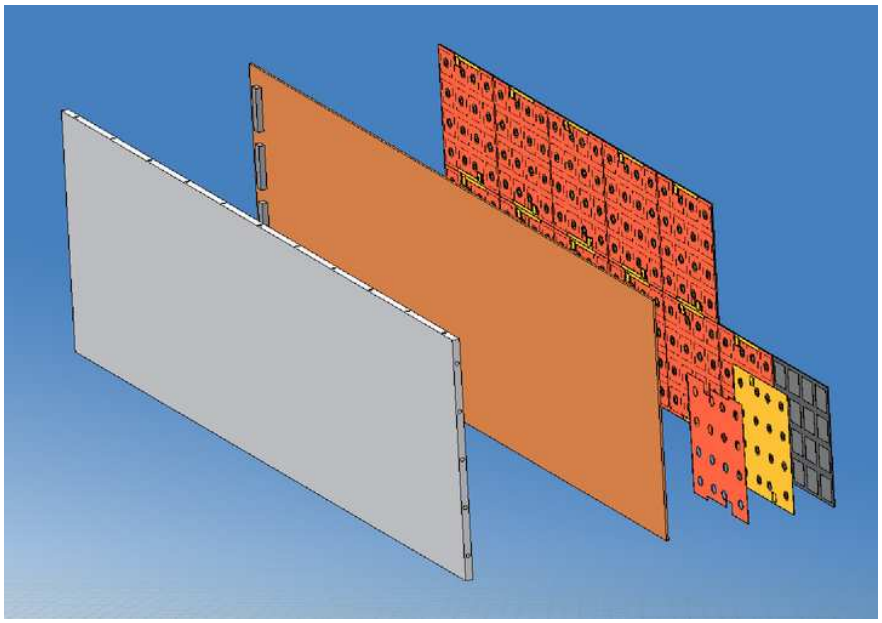

Figure 3.28: Exploded NCC pad-readout unit. Details of the sensor installation scheme are also included.

warping. Laminate of 4 mm W plate and carrier board with installed sensors form readout unit (sampling cell) which is used throuout the whole calorimeter depth. To increase amount of absorber in hadronic segment an additional 9mm W plates screwed to the 4 mm plates prior to assembly of the brick.

The interplate gap reserved for readout unit is 2.5 mm thick. 0.5 mm of this space is silicon, ∼0.2 mm is FR4 (motherboard), 0.2 mm is the FR4 interconnect and 0.9 mm partially filled with ceramic spacer are used to accomodate connectors and rc-network distributing bias voltage to individual diods. The remaining ∼0.2 mm gap is to insure that no pressure is applied to the surface of Si sensors. Such pressure may result in increased noise due to the piezoelectric effect.

This particular design is developed to insure (we are still working on testing different implementations) an easy repair of the assembled readout unit. If sensor fails the sensor stack can be removed from the carrier board and a new stack can then be installed.

The NCC will use five different readout units: all double sensor wide with the number of sensors varying between 8 and 14.

3.7.3 Stripixel readout layers

We have chosen a novel detector of interleaved pixelated strips ("stripixel") developed at BNL and already in use for the Central VTX in PHENIX. This novel detector generates X-Y two dimensional position sensitivity with a single-sided processing and readout. Fig. 3.29 is an illustration of the concept. It consists of a comb shaped structure with 250 μm prongs to cover a pixel area of 500x500 mm^2. Prongs are interleaved with similar prongs from two overlapping pixels on the right and on the left.

Alternate combs are connected either in the X direction (for measurement of the Y coordinate) or in the Y direction (for measurement of the X coordinate). The pitch between prongs belonging to different strips is chosen comparable to charge diffusion to insure uniform charge sharing. While it is easy to predict that an optimal pitch for a 525 μm wafer must be in the range of 15 mm, it may still be affected by the comb geometry and needs prototyping to optimize the pitch. Other critical issues are interpixel connections and crosstalk, the latter depends on the total length of the strip edge and strip implant which in turn is correlated to the pitch. While the PHENIX central VTX employs double metal technology for interpixel interconnects, forthe NCC we began with attempt to use n+ implants to create conductive regions in the bulk silicon separated from Al with a layer of SiO2. This technology have in principle better promise for radiation hardness. Unfortunately the first prototypes produvrd at ELMA have shown very asymmetric vharge collection and produced some hints of a large crosstalk between orthogonal strips (see Appendix D). Our next prototype will have double metal readout and will be available for testing in late spring this year.

The readout system for the stripixel silicon detectors is based on the SVX4 chip developed at FNAL for the D0-detector Upgrade and the existing PHENIX data acquisition system. Strips are connected to Data Collection Modules (part of the PHENIX DAQ system) through hybrids with an RC network and SVX4 chips daisy chained and followed by an interface board with a sequencer which are in turn connected to DCM's. The hybrids will be glued directly

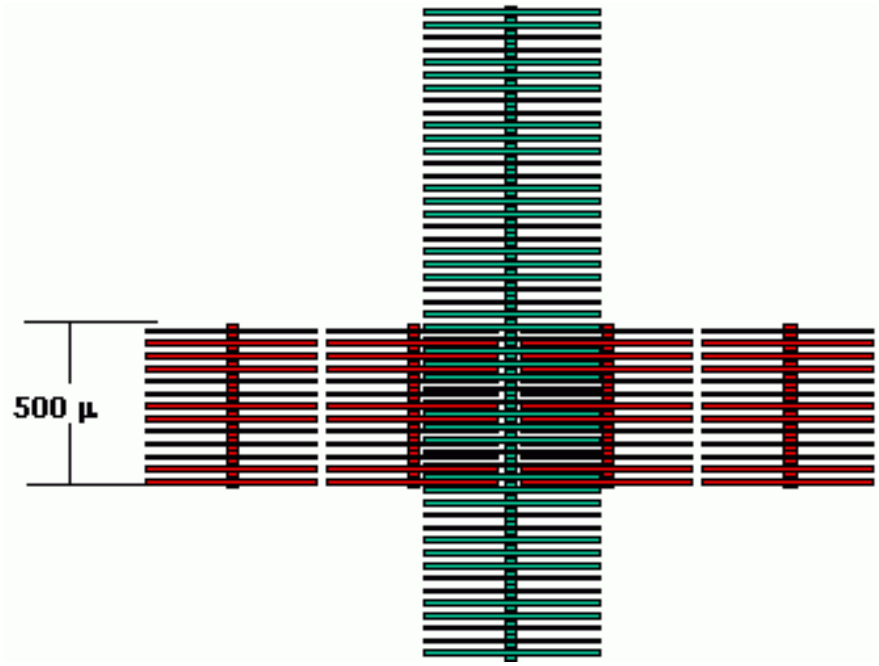

Figure 3.29: Design of the detector with interleaved pixilated strips with 2-d position sensitivity. Ionization charge produced by charged particles in Si is shared between X and Y oriented strips.

onto the sensors with the common of the sensor glued to seramic substrate and then to the carrier board.

Preliminary results of R&D work on StriPixel structures and a detailed proposal for readout electronics for StriPixel NCC layers developed in collaboration between the BNL NCC group, the BNL Instrumentation Department and the JINR LHE (Dubna) group can be found in Appendix D to this TDR.

If further tests of stripixel design with double metal technology will show that cross-talk between adjacent strips is unacceptable we will cancel further development of the stripixel sensor and will use the well established **silicon strip detectors**, designed and tested for NUCLEON experiment in cosmic ray physics (Moscow State University). These detectors have the same pitch and compatible with SRC boards. Figure 3.31 shows the two strip readout ladders (X and Y orientation) that will be mounted on both sides of the single ladder ceramic substrate.

3.8 NCC Electronics

For readout purposes the calorimeter is longitudinally segmented into two fine and one coarse segments and two 2-D sensitive coordinate layers. In total the silicon tungsten calorimeter as it was described above will have close to 60 000 silicon pixels and 80 000 strips. This calls for a compact, economical readout.

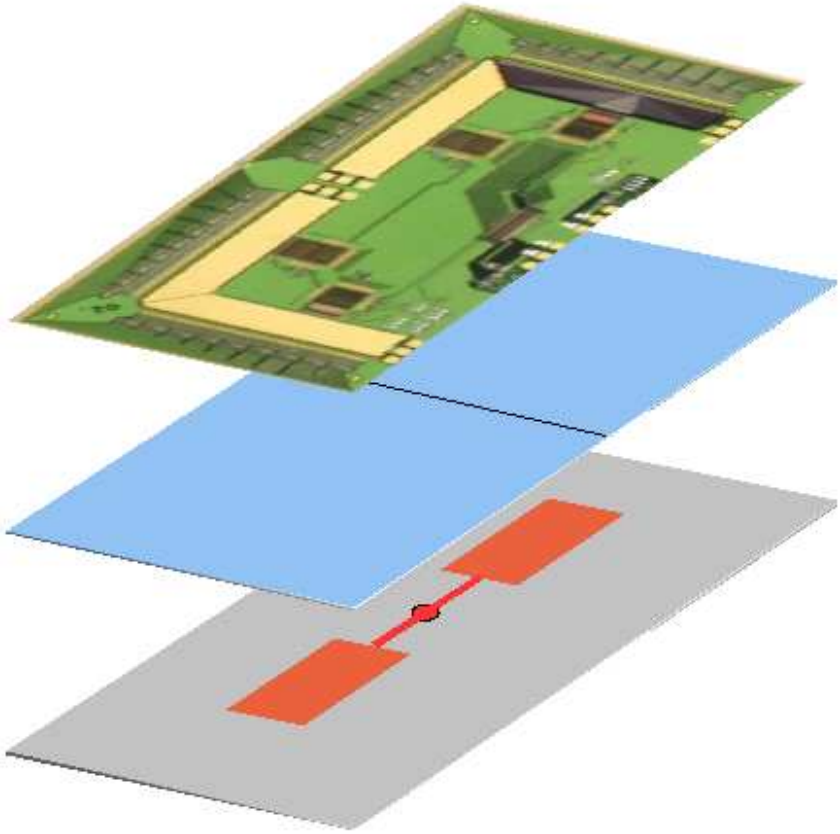

Figure 3.30: Expanded view of stripixel stack

3.8.1 NCC analog signal processing

The block diagram of the NCC analog signal processing plant is shown in Fig. 3.32.

As previously mentioned we will sum up signals from pixels in each longitudinal segment of the calorimeter. A simple passive (on the cable) summation scheme will be implemented on the outskirts of the detector. Signals from individual pixels are carried over the traces on the carrier boards to the low profile connectors daysy chained using custom designed FPC cable which is further plugged into the input connector in the preamplifier crate (see Fig. 3.33).

Rather modest goals for the electromagnetic energy resolution allow us to disregard the potential contribution to resolution due to the spread in the gains between individual pixels. Summed signals are amplified using hybrid line terminating amplifiers developed at BNL for the ATLAS liquid argon calorimeter. Modifications to the existing design will include polarity change for all transistors (to work for positive swing signals) and the addition of differential drivers to drive the signals over twisted pairs to the digital signal processing plant.

Depending on the location in the calorimeter the readout unit will deliver between 64

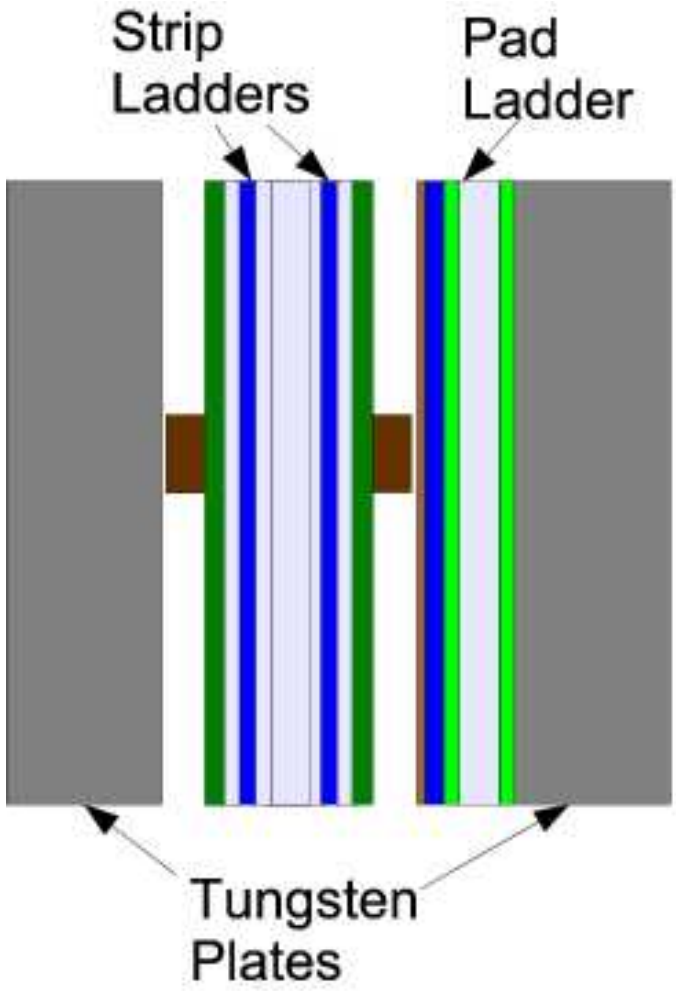

Figure 3.31: Arrangement of strip ladders between pad sensor assemblies on tungsten plates.

and 112 signal lines to the preamplifier board. In order to minimize the number of individually designed components in the detector, we are planning to use the same design of the preamp crate everywhere with only live channels populated. The motherboards host preamps, shapers and differential drivers arranged as in a row of fourteen daughter boards 16 channes (corresponding to sensor wide area in NCC segment) each.

Details of the signal processing chain for NCC towers were simulated using full component model built within LT SPICE electronics simulation framework. All related information can be found in Appendix E. Our main concern and reasoning for implementing the simulation with this degree of sophystication was related to the necessity to measure signals due to minimum ionizing particles in NCC towers. The simulation concluded that using the transresistance preamplifier developed at BNL complemented by the optimal low frequency bandpass filter an electonics noise can be reduced down to ENC$\sim$2000. This allows to reach dynamic range of the $\sim$10000 (close to 14 bits) in signal processing with ENC equivalent of LC/4.

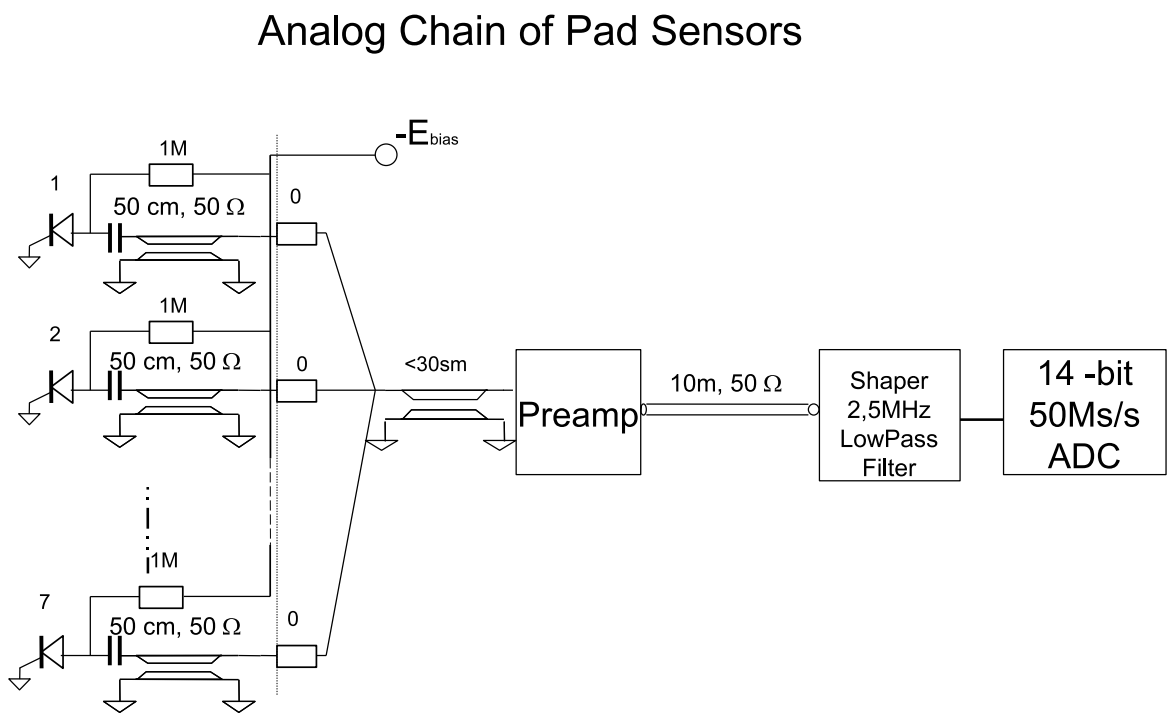

Figure 3.32: Signal processing block-diagram for NCC towers

The amplified differential signals will be driven from the detector to the FEM through 2mm Hard Metric (HM) cables. This cable is made from 2 isolated 26 gauge parallel wires with overall shield and 100 ohms impedance. The 2mm HM connector has 5 pins per row and can host 2 signal pairs plus central ground pin per row. Block-diagram of the digital signal processing plan including low level triggering is shown in Fig. 3.34.

The NCC Front-end Module (FEM) has the function of receiving the NCC preamp signals, digitizing the signals and sending them to Data Collection Module (DCM) and NCC local level 1 modules (LL1). The FEM will be hosted in the 6U VME crates located on the platform above the central magnet. Each FEM station will receive 64 channels of signals. A custom dataway will be used as a bus for the serial data and chain FEM data between adjacent modules. A crate interface module will serve to interface with the PHENIX granule timing module (GTM) as well as to the PHENIX slowdownload interface. The level 0 (L0) and level 1 (L1) timing signals and serial data will be generated from the interface module and sent to the FEM.

The cable receiver, as shown in Fig. 3.34, will receive, shape and drive the signal differentially to the ADC. Final gain adjustment can be done by changing the feedback resistors. An

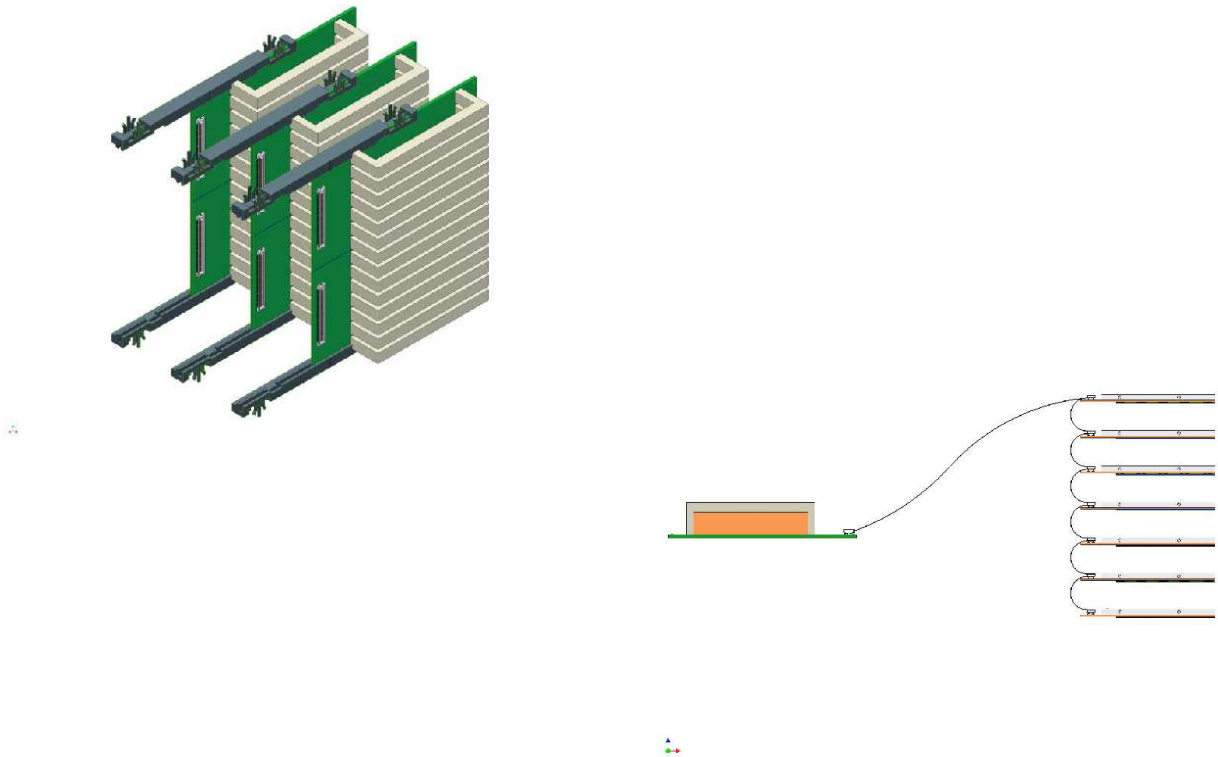

Figure 3.33: NCC custom built crate with preamplifiers and differential drivers for analog conditioning of signals from calorimeter towers

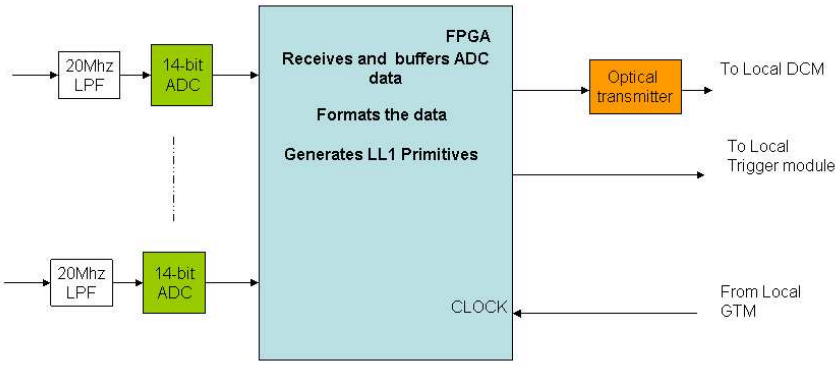

Figure 3.34: Digital signal processing in NCC

8 channel 50MHz 14-bit ADC running at 40 mhz (see Appendix C) will be used to digitize the signal. The ADC will sample the signal 4 times per RHIC beam crossing. Ignoring the voltage shift of the ADC, the full range the ADC is +1V to -1V. The amplifier and receiver arrangement can only swing the voltage from 0V in a positive direction. We will get 13 of 14 bits ADC. The ADC data is serialized using a 12 times sampling clock, 720MHz. An FPGA will be used to receive the serial data. The same FPGA will provide the 40 beam crossing L1 delay buffers, 5 L1 trigger event buffers and data format. Upon receive L1 trigger, 12 samples of data per channel will output to the DCM with a 6 times beam crossing clock. The data output of FEMs will be connected through a token passing dataway. An optical output will generate every 4 module to DCM.

A similar ADC boards were recently developed in PHENIX for Hadron Blind Detector Project and are already in use. An example board is shown in Fig. 3.35

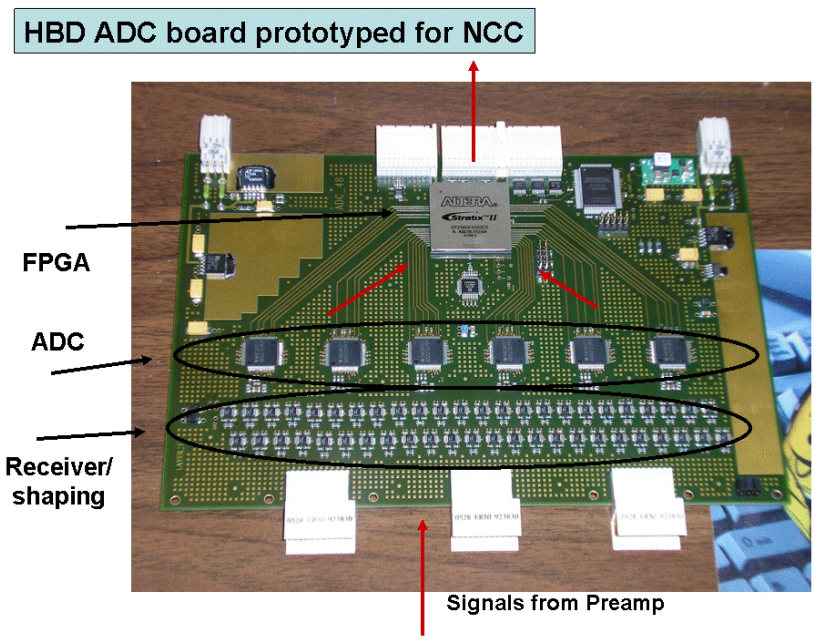

Figure 3.35: HBD ADC board considered to be a prototype for the NCC pad FEM

3.9 NCC Based Event Triggering

In order to pursue it's rare-event physics program the PHENIX experiment requires high luminosity from the RHIC accelerator and highly selective Level-1 and Level-2 trigger systems. In particular, the Level-1 trigger system is limited to a maximum rate of 12.5kHz by the readout rate of the detector front-end electronics. This will require an overall event rejection of up to ∼1000 when RHIC reaches its goal of ten times design luminosity for protons in future run. Since we anticipate the parallel acquisition of several rare event channels, the rejection for an individual trigger channel must be larger by a factor 5-10.

The PHENIX Level-1 trigger is fully pipelined and provides an event decision in less than 4.2μs (40 RHIC clock ticks). The Level-1 Trigger consists of two separate subsystems. The Local Level-1 (LL1) systems communicate directly with the participating detector systems. The input data from these detector systems is processed by the LL1 algorithms to produce a set of reduced-bit input primitive data for each RHIC beam crossing. The Global Level-1 system receives and combines this data to provide a trigger decision. In addition, busy signals (both global and trigger) are managed by GL1. The PHENIX detector system readout is divided into two sets of elements: granules and partitions. A granule is the smallest detector element that communicates with the PHENIX timing and control system via a Granule Timing Module (GTM). The GTMs distribute the local 9.4Mhz RHIC beam clock as well as control bits and event accepts to the granule. A partition is an administrative configuration of granules that share both busy signals and Level-1 triggers.

In this PHENIX upgrade the NCC LL1 primitive system will generate primitive information on the jet axes, as well as single and multiple high energy clusters. An upgraded muon LL1 trigger system will generate primitive information on the momentum of high p_T tracks, while a potential upgrade to provide the Si tracking coverage over the acceptance of the PHENIX muon arms will allow identification tracks with displaced vertices. In order to maximize the trigger rejection at Level-1 it will be necessary to combine trigger information from all of the forward Level-1 systems. To accomplish this, a new regional trigger processor will then take the complex trigger primitive information from the nosecone calorimeters, muon tracking system and muon identifiers, combine the individual detector LL1 primitives, make trigger decisions and send them to GL-1. A block diagram of the data flow is shown in Fig. 3.36.

The existing MuID LL1 system is based on a generic, configurable LL1 trigger board designed and built by Iowa State University, and is a prototype for the development of the NCC Level-1 trigger. The Generic Local Level-1 hardware (GenLL1) was designed to address a number of difficulties faced in extending the original design concepts for LL1 systems to address the full range of PHENIX trigger needs. First, the hardware had to be reprogrammable to allow not only quick corrections to the trigger logic, but modifications of the trigger system as the PHENIX physics program evolved. This also had the added advantage of lowering development costs and allowing quicker prototyping of new trigger systems. Second, the new hardware had to be able to manage a data throughput of $\sim$20Gb/s in order to be able to handle large data volume detectors (such as the Muon Identifier) without prohibitive cross-stitching between multiple boards (and crates of boards). Finally, in order to keep power consumption and heat load on the board within reasonable limits the GenLL1 design was required to use the next generation of HP GLINK receiver/transmitter logic (the HDMP 1032/1034), which runs at 3.3V. Smaller format transceivers (Agilent HFBR 5912) were also required in order to be able to handle up to twenty fiber inputs on a single 9U VME board.

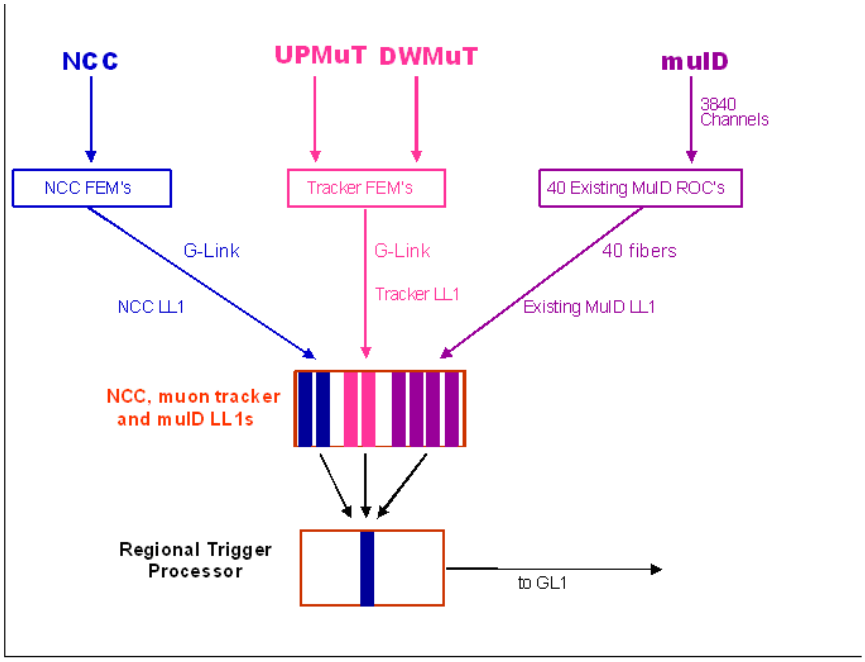

Figure 3.36: Block diagram of the combined forward PHENIX Level-1 trigger system showing the nosecone calorimeter, NCC, trigger muon tracker stations and the existing MuID LL1 system for a single PHENIX muon arm. In order to combine the primitives of the various trigger systems a regional trigger processor will combine the trigger information before sending primitives to Global Level-1.

3.9.1 The NCC Level-1 Trigger System

The nosecone calorimeter will use a Local Level-1 (LL1) trigger to select events via with a high p_T photon or jet in the calorimeter acceptance. As is typical of PHENIX LL1 systems the processing will consist of a set of pipelined stages. First, a set of primitive data will be digitized on the front-end modules (FEMs). Second, this data will be transferred to an LL1 system, and finally the bit-reduced trigger information is sent from the LL1 system to the PHENIX Global Level-1 trigger system, possibly via a new regional trigger processor to combine Level-1 information from the different forward detector systems as described in the previous section.

The NCC system consists of over 10k channels of analog data per nosecone spread over three layers in depth. The FEMs digitize the analog pad output, and pass the LL1 system an 8-bit ADC value per pad. The 8 bits per channel will allow a ∼100 MeV least count with a full range of 100 GeV, and will result in an aggregate bandwidth of 1,200Gbit/s per nosecone into the LL1 system, roughly a factor of 15x larger than the data processing capacity of the existing MuID LL1 trigger system. Simulations have shown that sufficient resolution can be obtained at LL1 with eight bit digitization per pad. In addition, we are considering the possibility that the FEMs could digitize data in 2x2 granularities to further reduce the data transfer into LL1.

Because of the large data volume and tight space constraints on the detector FEMs we are considering the possibility of transferring the data over high-speed serial links into an LL1 system located in the detector hall, as opposed to other LL1 systems that transmit their data over optical fiber links to LL1 electronics in the PHENIX rack room. The advantage of this approach would be that with serial links we could concentrate the entire NCC LL1 data stream into a smaller number of LL1 modules, simplifying the data cross-stitching required for trigger tile algorithms. This would only be possible by using high-speed copper serial links between the detector FEMs and the LL1 electronics which are inherently short-range, requiring the LL1 electronics to be located in the detector hall.

The LL1 system will aggregate the NCC pad data and form two types of tile for trigger processing. The first, a set of 2x2 tower non-overlapping trigger tiles will be available for prescaled triggering at very low p_T. The second set will be a collection of overlapping 8x8 tower overlapping trigger tiles. The 8x8 overlapping size was chosen to fully contain high p_T electromagnetic showers as well as a good match the the η width of a jet of hadrons. For both the 2x2 and 8x8 triggers the algorithm will begin by examining the relevant trigger tile in the EM2 section of the calorimeter. If energy is found in the EM2 tile, a corresponding tile is constructed in the EM1 and HAD calorimeter sections based on the center of the trigger tile in EM2 and the assumption that the incident energy came from a vertex location at $z = 0$. This "steering" in theta angle accounts for the fact that particles do not enter the NCC at normal incidence.

A sum is formed from the trigger tile energies in the EM1, EM2 and HAD sections, and this energy sum is compared to a threshold based on the desired E_T trigger threshold and the theta angle of the trigger tile in the EM2 section. In this way the total energy threshold varies as a function of theta in such a way as to keep the E_T threshold approximately constant. If the energy is above threshold, a trigger bit is set in the reduced bit output to Global Level-1. The reduced bit output of the NCC LL1 trigger, in the form of a set of bits indicating satisfied algorithms, would be transmitted to the GL1 system over optical fiber.

In order to separate electromagnetic from hadronic showers using the 8x8 trigger tiles, and additional selection is made based on the fraction of the total shower energy that is in the HAD calorimeter section, HAD/(EM1 + EM2). If this ratio is less than one, the trigger tile is tagged as an 8x8EM trigger. Simulation studies show that this separation in 99% efficient for high energy photon showers. Note that the 8x8 trigger is inclusive of the 8x8EM trigger.

Studies of the anticipated rejection from the NCC LL1 have been done using the simulated events and the PHENIX detector simulation application (pisa). For proton-proton collisions at $\sqrt{s}$ = 500GeV, approximately one million minimum bias events were generated and simulated in the PHENIX apparatus. Rejection factors for the 8x8 and 8x8EM trigger tiles were calculated, and are shown in Fig. 3.37. A table of the rejection factors is available in Table 3.9.1. We note that rejections in the range of 10000 for the 8x8EM trigger can be obtained with an E_T threshold between 10-12.5 GeV.

In order to examine the expected event rejection in heavy ion collisions, the event generator Hijing was used. To cover the full range of potential colliding species at RHIC we chose to simulate AuAu, CuCu and SiSi collisions. The expected rejection factors for the 8x8EM

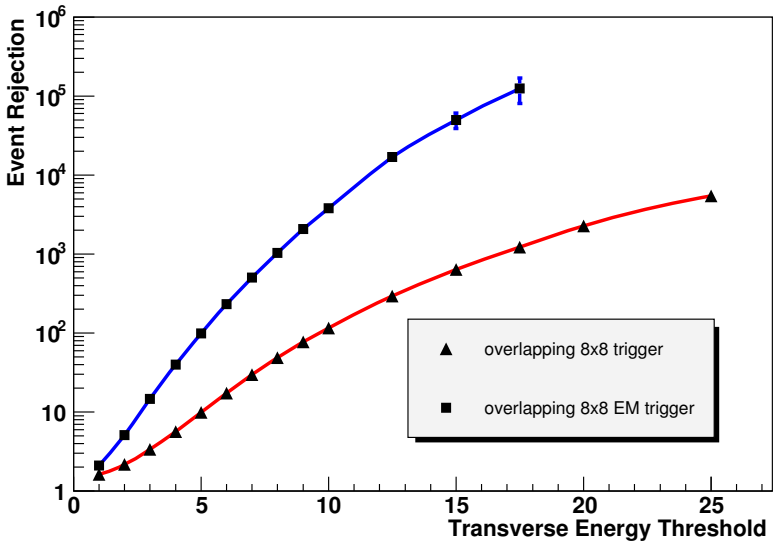

Figure 3.37: Anticipated NCC LL1 rejection factors of minimum bias proton-proton collisions at $\sqrt{s} = 500$GeV for the 8x8EM and 8x8 trigger tiles, as described in the text.

E_T Threshold (GeV)	8x8EM	8x8
1.0	2	1.6
2.0	5	2.0
3.0	15	3.5
4.0	40	5.7
5.0	99	10.0
6.0	233	17
7.0	505	30
8.0	1032	49
9.0	2083	77
10.0	3808	116
12.5	16910	295
15.0	49900	636
17.5	125000	1230
20.0	-	2300
25.0	-	5500

Table 3.3: Anticipated NCC LL1 rejection factors of minimum bias proton-proton collisions at $\sqrt{s} = 500$GeV for the 8x8EM and 8x8 trigger tiles.

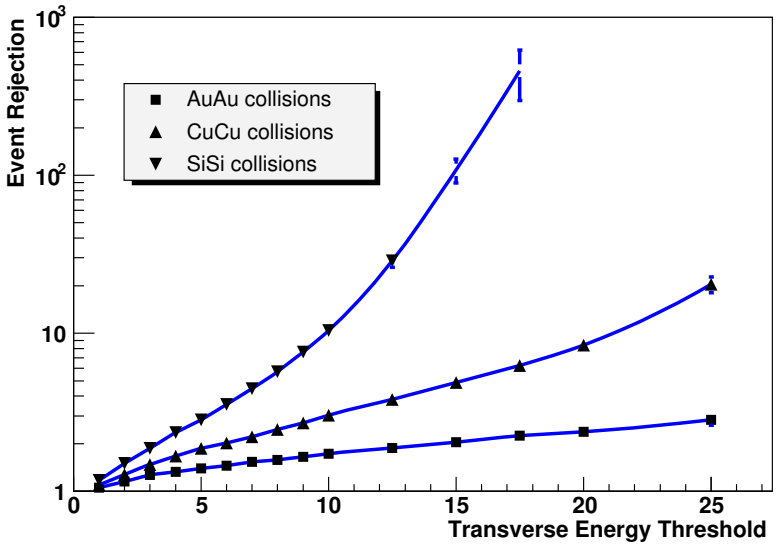

Figure 3.38: Anticipated NCC LL1 rejection factors of minimum bias heavy ion collisions at $\sqrt{s} = 200$GeV for the 8x8EM trigger tile, as described in the text.

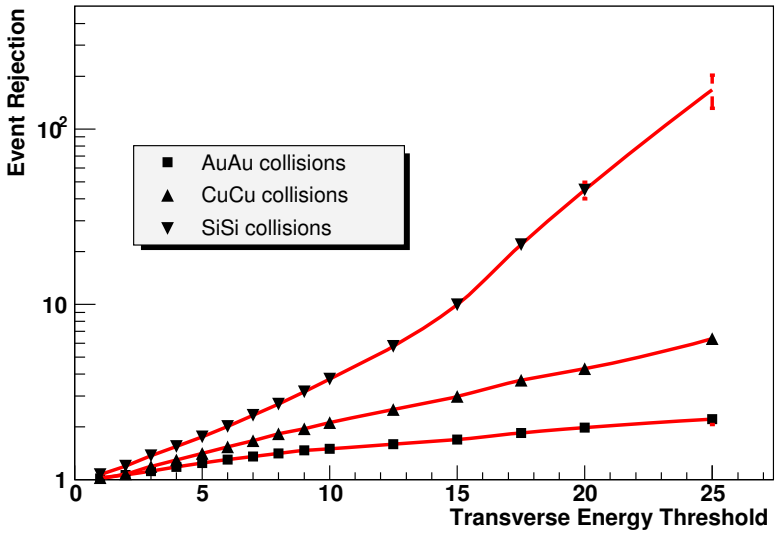

Figure 3.39: Anticipated NCC LL1 rejection factors of minimum bias heavy ion collisions at $\sqrt{s} = 200$GeV for the 8x8 trigger tile, as described in the text.

and 8x8 trigger tiles are shown in Fig. 3.38 and Fig. 3.39. As expected, substantial event selectivity can be obtained for collisions of light ions, but the very high overall multiplicity in Au+Au collisions limits the overall rejection that can be achieved. The rejection factors are shown in tabular form in Table 3.9.1. These results are based on simulations of 500 events for AuAu, 1600 events for CuCu, and 3700 events for SiSi.

	Si+Si		Cu+Cu		Au+Au	
E_T Threshold (GeV)	8x8EM	8x8	8x8EM	8x8	8x8EM	8x8
1.0	1.2	1.1	1.1	1.0	1.1	1.0
2.0	1.5	1.2	1.3	1.1	1.2	1.1
3.0	1.9	1.4	1.5	1.2	1.3	1.1
4.0	2.4	1.5	1.7	1.3	1.3	1.2
5.0	2.8	1.8	1.9	1.4	1.4	1.2
6.0	3.5	2.0	2.0	1.5	1.5	1.3
7.0	4.5	2.3	2.2	1.7	1.5	1.4
8.0	5.7	2.7	2.5	1.8	1.6	1.4
9.0	7.6	3.2	2.7	2.0	1.7	1.5
10.0	10.4	3.7	3.0	2.1	1.7	1.5
12.5	29	5.8	3.8	2.5	1.9	1.6
15.0	108	10	4.9	3.0	2.0	1.7
17.5	459	22	6.3	3.7	2.3	1.8
20.0	1225	45	8.4	4.3	2.4	2.0
25.0	-	167	20	6.4	2.8	2.2

Table 3.4: Anticipated NCC LL1 rejection factors of minimum bias heavy ion collisions at $\sqrt{s} = 200$GeV for the 8x8EM and 8x8 trigger tiles.

Finally, we examined the expected event rejection in d+Au collisions (again using the event generator Hijing). The expected rejection factors for the 8x8EM and 8x8 trigger tiles are shown in Fig. 3.40 and Fig. 3.41, with the rejection for each arm of the NCC identified separately due to the nature of the asymmetric colliding species. The rejection factors are shown in tabular form in Table 3.9.1. These results are based on simulations of 5000 d+Au events.

3.9.2 Ongoing R&D Program

With the help of institutional contributions it was possible to maintain a small, but well focused, effort over the past three years to explore technologies for silicon detectors suitable for the PHENIX NCC. The Collaborating groups in US, Japan, Russia, Korea, Finland and Czech Republic were able to design, manufacture, and test batches of DC-coupled pad-structured Si sensors, AC-coupled pad-structured sensors and first ever samples of StriPixel sensors with effective strip width of 0.5 mm. Their were enough DC coupled sensors for the proof-of-principle prototype calorimeter which was completed and beam-tested in November

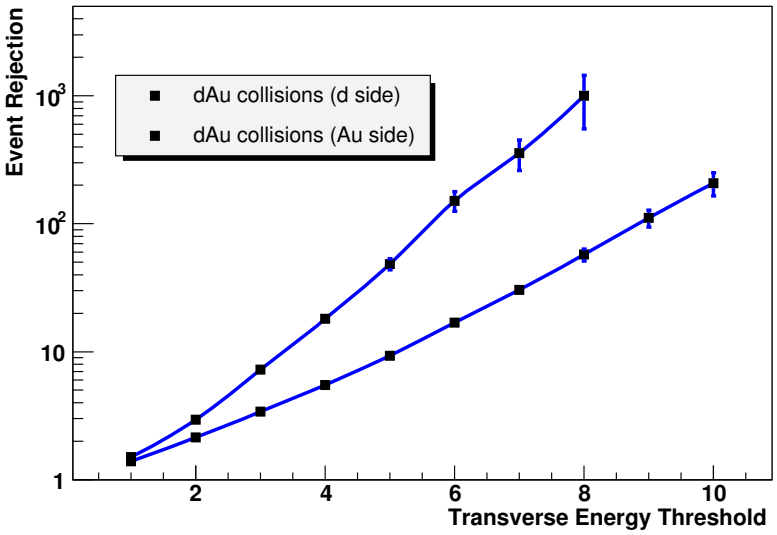

Figure 3.40: Anticipated NCC LL1 rejection factors of minimum bias d+Au collisions at $\sqrt{s}$ = 200GeV for the 8x8EM trigger tile, as described in the text. Note that the trigger rejections depend on whether the NCC arm in in the d-going or Au-going side of PHENIX.

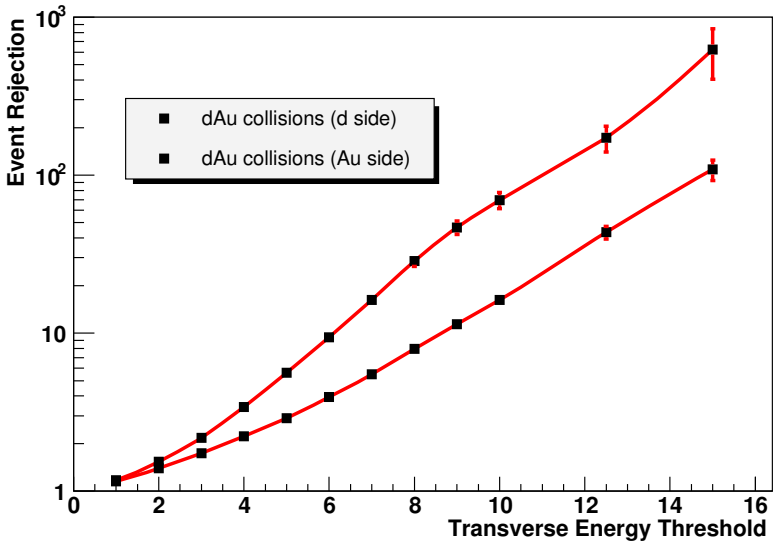

Figure 3.41: Anticipated NCC LL1 rejection factors of minimum bias d+Au collisions at $\sqrt{s}$ = 200GeV for the 8x8 trigger tile, as described in the text.Note that the trigger rejections depend on whether the NCC arm in in the d-going or Au-going side of PHENIX.

	d side		Au side	
E_T Threshold (GeV)	8x8EM	8x8	8x8EM	8x8
1.0	1.5	1.2	1.4	1.2
2.0	2.9	1.5	2.1	1.4
3.0	7.2	2.1	3.4	1.7
4.0	18	3.4	5.5	2.2
5.0	48	5.6	9.3	2.9
6.0	151	9.4	17	3.9
7.0	357	16	30	5.5
8.0	1000	29	57	7.9
9.0	-	47	111	11.4
10.0	-	69	208	16.2
12.5	-	172	1666	43
15.0	-	625	-	109

Table 3.5: Anticipated NCC LL1 rejection factors of minimum bias d+Au collisions at $\sqrt{s} = 200$GeV for the 8x8EM and 8x8 trigger tiles.

2005. The main results of completed R&D program are published in [IEEE, Breckenridge, QM] and presented in Appendicies to this chapter of TDR..

The ongoing R&D effort is aimed towrds finalizing technology choices as required by construction project We closely follow the development of the digital signal processing plant for HBD which is functionally identical to what is proposed for NCC and SVX4 based readout currently under development for the two outer layers of the PHENIX SVT.

The key issues still to be resolved are the noise (capacitative and pick-up) in the detector operating with ganged sequential pads and optimization of the stripixel sensor design. The solution to the noise issue requires extremely careful design with large care taken of grounding the detector components and readout electronics. We benefited from help from D0 silicon laboratory at FNAL in the detector design and will further rely on their expertise in large silicon systems and detector mechanics.

We continue stripixel sensor development. We retain the option of single sided stip detectors of a similar geometry as a backup solution. We plan to make the final technology choice in summer 2007.

For many parts of the NCC, the technology choices have been made, and R&D is focusing on prototyping the designs. The following topics will be pursued so the construction of the NCC could start in FY08:

- Production and testing of STriPixel test sensors to study the infuence of inter-pixel pitch on the charge sharing and crosstalk between strips;
- Finalizing the choice of the sensors for position sensitive layers;
- Finalizing design of the readout units for both kind of sensors;

- Testing heat dissipation in position sensitive layers. If required - designing and testing heat removal scheme for on the sensor SVX4 based readout electronix;
- Finalizing conversion of ATLAS preamps for PHENIX NCC application. Implementing new version of amplifier with 2-sided hybrid technology;
- Development of the readout electronics for NCC;
- Small scale production runs of pad-structured and StriPixel sensors to equip a fullscale brick-sized NCC prototype for on-the-bench and test beam measurements of the detector performance;
- Finalizing detector mechanical design;
- Constructing system prototype (single brick) and running test-beam experiment (likely at FNAL in 2007-2008).

References

[1] *PHENIX Conceptual Design Report*, PX20, BNL48922 internal report, 1993

[2] *The Relativistic Heavy Ion Collider Project: RHIC and its Detectors*, Edited by M. Harrison, T. Ludlam and S. Ozaki, NIMA499 , Issues 2-3, 235-880, 2003

[3] Seto, R., *Future measurements at RHIC*, Proceedings of Workshop on Nuclear Dynamics, Bahamas, January 2002, World Scientific 2002, nucl-ex/ 0204003.

[4] L. McLerran, R. Venugopalan, Phys. Rev. D49, 1994, 2233; L. McLerran, R. Venugopalan, Phys. Rev. D49, 1994, 3352; L. McLerran, R. Venugopalan, Phys. Rev. D50, 1994, 2225; see also E. Iancu, A. Leonidov, and L. McLerran hep-ph/0202270 and hep-ph/0202025 for a nice review of the saturation and RHIC physics.

[5] I. Golutvin et al.. *A Silicon Hadron Calorimeter module operated in a strong magnetic field with VLSI read out for LHC*, CERN-DRDC-91-54, CERN-DRDC-P-34, Jan 1992

[6] J.H. Adams et al., *The Silicon Matrix as a Charge Detector for the ATIC Experiment*, Instrum.Exp.Tech. 44, 455-461, 2001, Prib.Tekh.Eksp. 2001 N4, 38-44, 2001

[7] V. Bonvicini et al., *New concepts in silicon calorimetry for space experiments*, NIM.A518:186-187,2004

[8] R.Wigmans, *Calorimetry Energy Measurements in Particle Physics*, Oxford Science Publications, ISBN 0 19 850296 6, 2000

[9] S.S.Adler et al., *Midrapidity Neutral-Pion Production in Proton-Proton Collisions at* $\sqrt{s}$*=200 GeV*, Phys. Rev. Lett. 91, 241803, 2003

[10] S.S.Adler et al., *Mid-Rapidity Direct-Photon Production in p+p Collisions at sqrt(s) = 200 GeV*, hep-ex/0502006, 2005

[11] V.Bonvicini et al., *Silicon-Tungsten Calorimeter for the Forward Direction in the PHENIX Experiment at RHIC*, IEEE Transactions on Nuclear Science, v.52, 4, 874, 2005

[12] E.Kistenev, *Siliocon-Tungsten calorimeter for the forward direction in the PHENIX experiment at RHIC*, Czechoslovak Journal of Physics, v.55, 12, 2005

[13] V.Dzhordzhadze, *Extending Physics Capabilities of the PHENIX Detector with Calorimetry at Forward Rapidities*, Proc. 21st Winter Workshop on Nuclear Dynamics, 269-276, 2005

[14] S.Rescia, *A linear low power remote preamplifier for the ATLAS liquid argon EM calorimeter*, Nuclear Science Symposium, 1996. Conference Records., IEEE v.1, 659-661, 1996

Chapter 4

Project Management and Responsibilities

The organization and management of the proposed effort is embedded in the management structure of the PHENIX experiment, which is part of the BNL RHIC project. The new organization must satisfy a number of requirements including a clear interface to the existing RHIC and PHENIX management structure, clear roles and responsibilities within the existing PHENIX subsystem structure. Particular attention must be paid to the fact that a significant portion of the project efforts is carried by PHENIX groups which belong to the international component of PHENIX collaboration. Clear deliverables, responsibilities for deliverables and the accountabilities of the participating Institutions must be defined. These responsibilities will be formalized in memoranda of understanding (MOU's) between PHENIX and the participating Institutions. In this section, we outline our proposed management organization and delineate responsibilities within the project.

4.1 Project background

The proposed project is part of a detailed upgrades program to enhance the physics capabilities of PHENIX. The development of the PHENIX upgrade program started in response to the recent NSAC long-range plan, which was developed in 2000. The PHENIX Upgrade program spans the next 8 years. Realizing this plan will enable PHENIX to remain competitive well beyond the turn on of LHC expected for 2008, as well as advance our understanding of QCD by fully exploiting the unique spin physics capabilities of RHIC. The plan covers a broad range of measurements in A+A, p(d)+A, and p+p and its goal is to provide key measurements which currently can either not be addressed at RHIC or only with limited accuracy.

The calorimeter component of the PHENIX upgrade program was first proposed in the fall of 2004 when a Letter of Intent (LOI) for an upgrade of the forward region of PHENIX was written and presented to the PHENIX management. This LOI included the NCC, and a trigger for the muon spectrometer which is now being funded by the NSF. The forward LOI was reviewed at a joint meeting of the PHENIX detector council (DC) and executive

council (EC). Following their recommendations PHENIX management (PM) endorsed both projects and the group was charged with preparing NCC proposal for presentation to the DOE through BNL.

The NCC project was reviewed in December 2004 by a panel, including PHENIX Detector Council and Executive Council members as well as external members who are not PHENIX collaborators. The recommendations of the review panel have been very helpful to prepare the present proposal. All recommendations have been addressed and answers have been incorporated into the proposals. Subsequently, in March of 2006 a formal BNL review was undertaken and a recommendation was made by the review panel that the project begin funding in FY 2008. In addition technical recommendations were suggested to the NCC collaboration and again the recommendations of the review panel have been addressed.

4.2 The management plan for the NCC

4.2.1 PHENIX management structure

The NCC project is part of the PHENIX project and as such integrated into the PHENIX management structure as described by the PHENIX bylaws. The PHENIX Detector Council (DC) will advise PHENIX management on the design, construction, and integration of the NCC. The DC is co-chaired by the operations manager (Edward O'Brien) and the upgrades manager (Axel Drees). The NCC subsystem manager will serve as a member of the DC.

4.2.2 PHENIX subsystem leadership

We expect that the proposed NCC project will be funded through the DOE Office of Nuclear Physics (DOE-NP) beginning in 2008. The collaborating institutions will jointly fund remaining R&D efforts (2006-2007) resulting in construction and beam-testing of a W-Si prototype calorimeter serving as NCC system prototype. A successful completion of the NCC will require close collaboration between participating institutions, well-defined matrix of responsibilities and contributions in terms of deliverables. These deliverables and planned sources of contributions are outlined below. Within PHENIX, the responsibility for the NCC subsystem will be shared by the subsystem leader, Richard Seto (UCR) and his two deputies, Itaru Nakagava (RIKEN) and Edouard Kistenev (BNL). The subsystem leader reports to PHENIX PM and will represent the NCC in the PHENIX DC.

Simultaneously, E.Kistenev will serve as the DOE contract project manager (CPM), and will have the fiscal and construction responsibility for the DOE funded deliverables as outlined in this proposal. This involves appropriate planning, budgeting, and reporting.

4.2.3 Role of BNL

Because we expect that all DOE funding for this effort will be directed through the BNL Physics Department, BNL line management will have ultimate fiscal and managerial responsibility for the construction of the NCC and for its subsequent operation.

Fig. 4.1 shows a management chart of the NCC project. The subsystem manager has general responsibility for the implementation of the project and is assisted by two deputies, who are responsible respectively for the hardware and software aspects of the project. In addition the manager and his deputies will have fiscal responsibilities. As mentioned Edouard Kistenev will have responsibility for DOE funds. As a separate but related item, Itaru Nakagawa will have the fiscal responsibility for RIKEN funding which may go to the construction of a second NCC. Similar to other upgrade projects in PHENIX, the PHENIX operations manager will assist the project in all integration matters and is responsible for installation of the detector into the PHENIX experiment and for the safety of operations. The institutions that will participate in the implementation of individual tasks are given in the bottom of every task block in Fig. 4.2. When our international collaborators, notably Russia, Czech, Finland, and Korea, are represented by several institutions working together they are indicated by nation, rather than by individual institution. PHENIX safety, DAQ, and infrastructure are common to all subsystems, so they are not listed as an explicit part of NCC management.

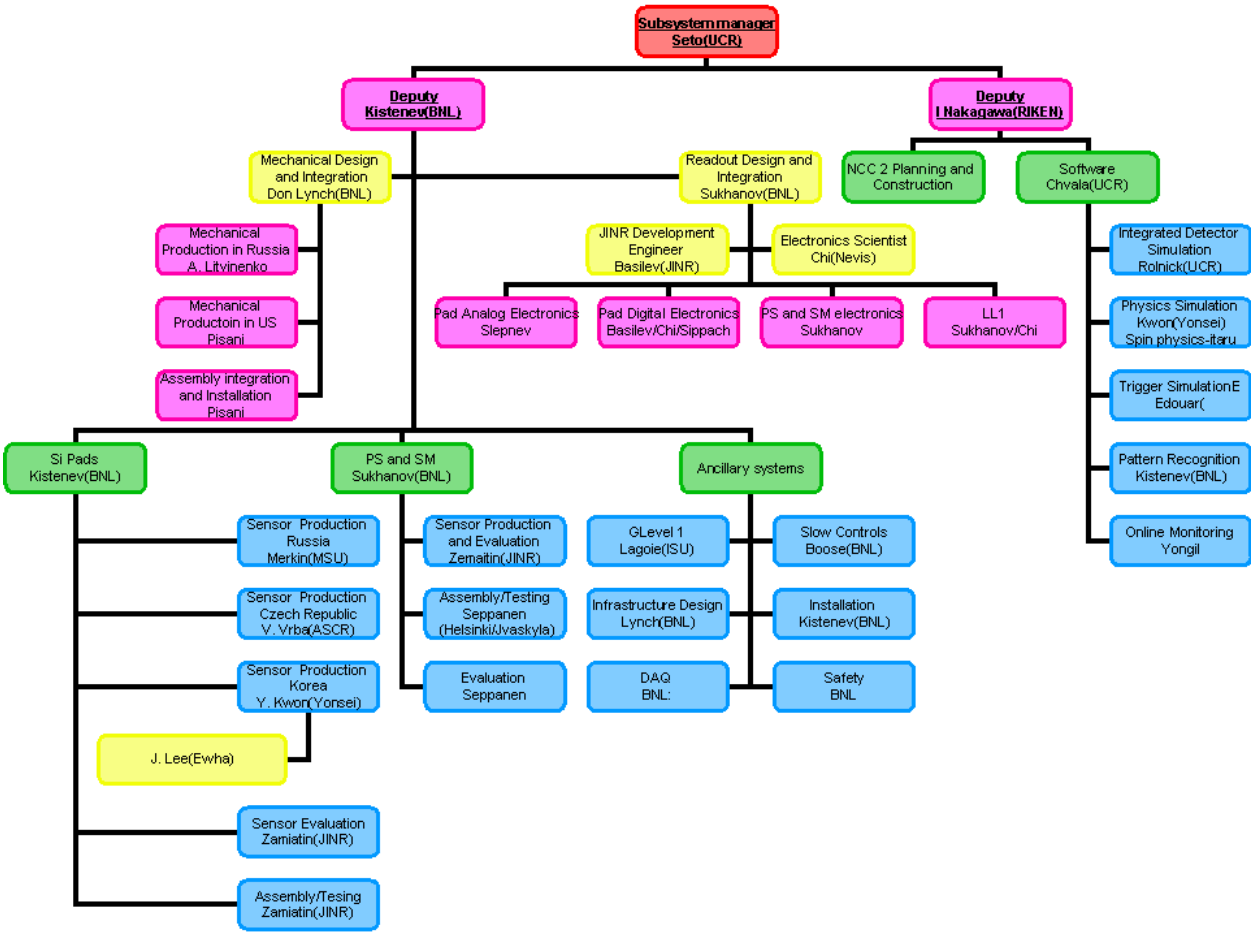

Figure 4.1: Management chart of the NCC project.

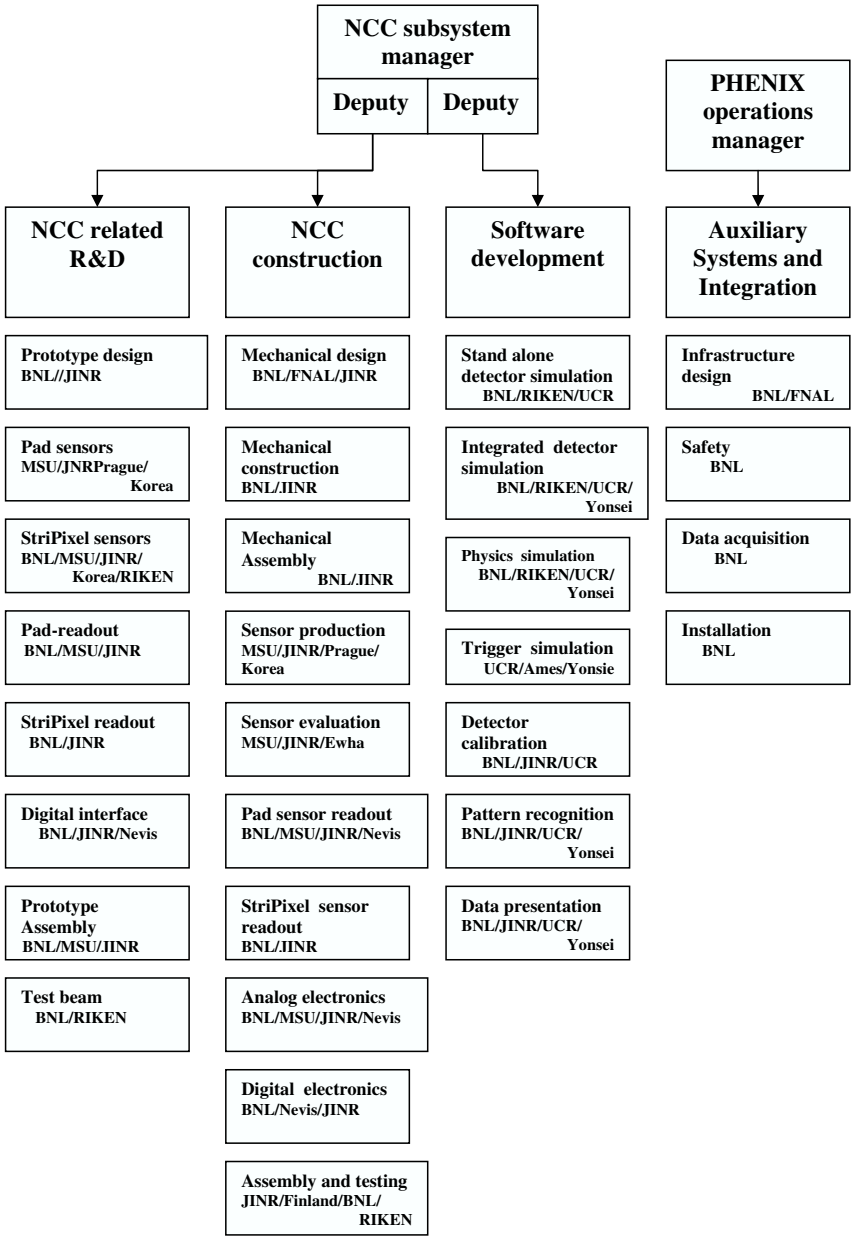

Figure 4.2: Institutional tasks for the NCC project.

4.2.4 Specification of deliverables

The NCC is divided into subprojects, which themselves are divided into tasks detailed in an NCC Microsoft Project File. The main tasks identified as blocks in Fig. 4.2 are closely related to deliverables, which need to be completed before the NCC construction project can be considered complete. Below are the major deliverables and responsible institutions and a brief review of institutional responsibilities. Note that JINR involves three laboratories - the first headed by Anatoly Litvinenko primarily responsible for mechanical design and construction, the second headed by Sergey Basilev, responsible for electronics, and the third headed by Nikolai Zamiatin responsible for silicon detector testing and assembly.

4.2.4.1 Calorimeter

- Silicon pad-structured sensors designed and implemented to the specification: **MSU/JINR/Czech/Korea**
- Silicon strip sensors designed and implemented to the specification: **MSU/JINR/BNL/Korea**
- Readout units for the pad-structured calorimeter layers: **MSU/JINR/Nevis**
- Readout units for PS and SM detectors: BNL/JINR
- Analog data processing electronics for pad-structured layers (EM1/EM2/HAD segments of NCC): **BNL/JINR**
- Detector-end data processing for StriPixel PreShower and ShowerMax layers: **BNL/JINR**
- Digital data processing: **BNL/Nevis/JINR**
- Trigger electronics: **ISU/Ames**
- Support structure and absorber plates: **BNL/UCR/JINR**
- Calorimeter mechanical components: **JINR**
- Assembly and testing of Pad Senor Modules (**JINR**)
- **Assembly and testing of Stripixel Modules (Finland)**
- **Assembly and testing of calorimeter bricks: BNL/UCR/RIKEN**
- **Assembly and testing of calorimeter: BNL/UCR/RIKEN**

4.2.4.2 DAQ system

- Data collection modules for calorimeters and position detectors (PS and SM): **BNL**
- Software development for data collection, monitoring and analysis: **BNL/UCR/RIKEN**

4.2.4.3 Auxiliary Systems and Integration

- System support requirements specified, including heat loads, power distribution, mechanical tolerances and grounding scheme: **BNL/UCR/FNAL**
- Ancillary systems operational, including power distribution and cooling system: **BNL**
- Installation and integration:**BNL**
- Commissioning of full detector system: **BNL/UCR/RIKEN**

4.3 Institutional involvement

4.3.1 US based Institutions

Currently 20 institutions with over 70 individuals are involved in the NCC project. The different institutions bring in diverse research backgrounds, physics interests and expertise, which form a broad base to carry out the proposed project. Each group assumes specific responsibilities and will participate actively in the NCC project. According to their expertise and interests these groups will be involved in construction, installation, commissioning, operation, and data analysis. Formal commitments of the involved institutions will be specified in Memoranda of Understanding (MoU). Many of these groups have been already been actively involved in the R&D effort through institutional contributions, while others have joined the project only recently. Below are brief descriptions of expertise and potential involvement of the institutions.

The BNL Instrumentation Division, Fermi National Laboratory join the NCC project because of their interest in the technological development, but are not members of the PHENIX collaboration.

The PHENIX group at University of California, Riverside has taken primary responsibility for Simulations and Software development, and is heavily involved with ongoing NCC related R&D. As the subsystem manager, UCR group leader Richard Seto has played a leading role in the management of the NCC, and was instrumental in bringing the project to the proposal stage.

The PHENIX Group from the BNL Physics Department provides infrastructure and technical support as part of Systems Engineering and Integration (SE&I) for the entire PHENIX experiment. It has a staff of mechanical and electrical engineers and a group of experienced technicians who are intimately familiar with the detector, and work closely with the BNL Collider-Accelerator Department for operations and any modifications to its present

design. They designed much of the infrastructure for the baseline detector, including racks, cable trays, electrical power, cooling, access, safety systems and numerous other services, and carried out the installation of all of the present subsystem detectors. This group will now be closely involved with the design of the infrastructure and support for the PHENIX Forward Calorimeters, and with its installation into PHENIX.

The BNL physics group is joined by physicists associated with Physics Department and Chemistry Department (former PHOBOS experiment). The two groups bring management and physics experience and broad experience with silicon detector technology. Individual group members bring specific technical skills that will be important for the successful construction, installation, commissioning and operation of a silicon detector in the RHIC environment. Edouard Kistenev of BNL will serve as the DOE contract project manager (CPM). He has taken a leading role in developing the concept and design of the NCC project.

BNL's Instrumentation Division's Silicon Detector Development and Processing Laboratory (SDDPL) will be involved in the development of silicon strip detectors for PHENIX Upgrades. The activity will include detector simulation, design, and processing of prototype detectors. SDDPL will also be involved in laser scan tests of those prototypes, these tests will be carried out in close collaboration with the BNL Physics Department and RIKEN. The BNL Instrumentation Department proposed the solution based upon hybrid amplifiers earlier developed for ATLAS experiment at CERN to serve as a basis for the analog signal processing for NCC. The further activities will involve modification to the schematics for the amplifiers to work with positive polarity signals, compactification of the layout, testing and participation in production. This work is being done in collaboration with engineers at JINR.

The PHENIX group from Iowa State University (group leader John Lajoie) will take responsibility for the design, implementation, construction, and support of the NCC Level-1 trigger system (similar to their earlier work on the design, construction and maintenance of the PHENIX Level-1 trigger system).

The BNL PHENIX group has primary responsibility for a number of major subsystems. These include Electronics Facilities and Infrastructure (EF&I), Online Computing Systems (ONCS) and Offline Computing. These groups will participate in the electronic integration and readout of the NCC detector into the PHENIX data acquisition system, and will be involved with track reconstruction and offline data analysis.

The BNL PHENIX group will also serve a host institution for the project and will provide the lab space for the final detector assembly and testing.

4.3.2 International participation

The Moscow State University group has internationally recognized expertise in silicon detectors and their application in experimental physics. MSU contributed to the ZEUS experiment at DESY (silicon hadron rejector), the D0 experiment at FNAL (central tracker), and a number of smaller projects. Together with JINR, RIKEN, BNL and UCR the MSU group built and tested a "proof-of-principle" NCC prototype, which demonstrated robustness of the technology. MSU will share the major responsibility for production and evaluation of

pad-structured sensors for the calorimeter together with JINR.

The Joint Institute for Nuclear Research in Dubna has a variety of expertise in all aspects of experimentation in Nuclear and particle physics. The JINR PHENIX group can draw on expertise of their local and international collaborators in mechanics, electronics and sensor development. As mentioned previously there are three major groups of physicists at JINR involved with the NCC. The first group, headed by Anatoly Litvinenko has already contributed to the initial design of NCC mechanical structure, will continue this work in collaboration with group from FNAL, and will take major responsibility for production of major mechanical components for NCC. A second group, headed by Sergey Basilev, has taken major responsibilities in the electronics design for the pad modules - both for the pre-amp boards and the FEM. Finally, a group headed by Nikolai Zamiatin will take major responsibility for the assembly and testing of the pad sensor modules.

The Finnish group at Jvaskyla and Helsinki have now taken the responsibility for the testing and assembly of the StriPixel layers. They bring a great deal of experience in this as they have assembled silicon detectors for the ALICE experiment at CERN at their laboratory at the Helsinki Institute of Physics. This work has just come to an end and the facilities will now be used for the NCC. Jyvaskyla has hired a physicist to oversee the operation at the laboratory in Helsinki.

The Korean groups at Yonsei University and Ewha University have become involved in the work on Silicon pad-structured sensors. Ewha has built the Silicon detector for the CREAM balloon project working together with industrial partners SENS Technology - a small company specializing in Silicon detectors. The group is currently working on prototyping the NCC pad detectors on 8” wafers - a major development since this would significantly reduce the cost. The group at Yonsei will also take major responsibilities in software, simulation and data analysis.

The Czech Republic group involves physicists from the Institute of Physics, Charles University and the Czech Technical University, who are primarily interested in the PHENIX spin physics program and silicon detector development. The Czech group has a history of collaboration with groups from JINR, Dubna and an established relationship with the major silicon processing plant in the Czech Republic (ON Semiconductors). As part of their contribution to NCC project, Prague collaborators have already initiated the first round of sensor prototyping at ON Semiconductors, this development will allow to better estimate potential benefits of sensor production in Czech republic and to coordinate the sharing of silicon production efforts between MSU, Korea, and ON Semiconductors.

4.4 Acknowledgements

We thank our PHENIX collaborators for the support and encouragement of the proposed NCC upgrade and for fruitful discussions. We acknowledge R&D and participant funding support from the Department of Energy, Office of Science, Office of Nuclear Physics, the National Science Foundation, and the Research Foundation of SUNY (U.S.), Ministry of Education, Culture, Sports, Science, and Technology and the Japan Society for the Promotion of Science (Japan), Ministry of Education, Youth and Sports (Czech Republic), Korea

Research Foundation, Center for High Energy Physics, and Korea Science and Engineering Foundation (Korea), and Ministry of Education and Science, Rassia Academy of Sciences, Federal Agency of Atomic Energy (Russia).

Chapter 5

Budgets and Schedule

5.1 Overview

The PHENIX Forward Calorimetry Upgrade Project naturally splits into three subprojects namely:

- W-Si Calorimetry R&D to culminate in construction of a W-Si calorimeter system prototype in late 2007 or early 2008;
- Construction and installation of DOE funded NCC staring in 2008 and ready for physics in the fall of 2010;
- Construction and installation of a second NCC starting in 2009 and ready for physics in 2011.

The project is based on a cost sharing between the DOE Office of Nuclear Physics and the PHENIX NCC Group, as introduced in this Proposal. The group is jointly responsible for funding the ongoing W-Si Calorimetry R&D program, which is planned for completion in 2007 with construction and beam testing of the Calorimeter System Prototype. The DOE Construction funding is expected to start in 2008 and continue for three years with peak funding in 2009. It is important to note that in these plans the DOE funding will be for the complete construction of one of the pair of NCC detectors including the R&D.

The PHENIX NCC Group is planning to collect among its members other then US enough funds (R&D and Construction) to cover the cost of the second PHENIX NCC unit.

In what follows we discuss cost and scheduling issues related to the DOE Construction Project to allow implementing the proposed upgrade in the minimal configuration consisting of a single calorimeter unit. The decision to deploy this unit as an upgrade to North or South muon arms will depend on RHIC running schedule and configurations for collisions of different ion species.

The cost and schedule for the NCC Upgrade project has been developed using engineering estimates, vendor quotes and experience from the construction of silicon detectors from participating Institutions. The production schedule of the two subprojects (First and Second

NCC) are not totally independent, and unless extra production capacity is identified the starting date for the Second Calorimeter Project will be constrained by the rate of production of Si sensors at the ELMA (Russia), ON Semiconductors (Czech Republic) and SENS(Korea) facilities. While the estimated base costs of the North and South detectors are identical, the real cost to the PHENIX NCC Group can be different depending on accounting practices specific to collaborating countries. In this section, we outline only those costs which concern the DOE.

5.2 Contingency Analysis

In order to estimate the necessary contingency we have taken the following approach:

- For all tasks that require the production of prototypes, contingency is taken to be 100% of the cost of one extra design plus prototype cycle.
- For all testing, assembly, and installation tasks, we assume that the contingency is 50% of the costs.
- For purchases based on vendor information, 20% of the cost is included as contingency.
- For all other purchases, the contingency is 30% of the costs.

5.3 Overhead Estimate

The overhead applied to funds requested from the DOE we assume an 18% rate which is the current practice for capital construction projects at BNL. This 18% overhead is included into "Cost to Project" in our budget tables. The additional overhead charged by local institutions is not listed separately. However, these costs are included in the budget table via cost estimates for items ordered in foreign countries through collaborating institutions. In particular, all manpower costs are fully burdened costs, including overhead.

5.4 Tungsten-Si Calorimeter R&D

The ongoing collaboration funded R&D efforts is aimed at confirming design ideas developed in he course of earlier 2005/2006 R&D and at constructing and testing a full scale brick-wide prototype of the W-Si calorimeter including the SM and PS layers. When this portion of the project is completed the Collaboration will be in possession of

- the final design and production documentation for DC-coupled pad-structured Si sensors developed to NCC specifications;
- the final design and production documentation for the pixilated strip Si sensors (StriPixels) developed to NCC specifications;

- the final design and production documentation for the pad-structured readout units. The design documentation for readout unit components (carrier and interconnect boards) will be ready for submission to pc-board production houses;

- the final design and production documentation for the pixilated strip readout units including sensor-end hybrids, brick-end receiver boards and front-end modules interfacing the NCC to PHENIX DAQ;

- a full size prototype of W-Si calorimeter brick assembled and tested in a test beam.

The completion of this the R&D program is a major mile stone and is necessary to address the challenges of this Upgrade Project. It is important for the collaboration to accumulate test beam data using detector in all essential aspects identical to one the Collaboration proposes to build. Exposing this detector to high energy particle test beams will confirm performance expectations, and provide the experience and test-data necessary for successful use in the PHENIX experiment.

This R&D program will be supported by the Collaboration with major funding provided by BNL (BNL Generic R&D funds) and other collaborating institutions in US and Japan, and in-kind and man-power contributions from other collaborating Institutions. Most of the funding required to carry this program in 2006 is already committed. Fig. 5.1 below lists the major costs associated with R&D project.

5.5 NCC Construction

The total cost of the Nose Cone Calorimeter Construction Project to DOE including contingencies and overhead is **3.94 million $US**. This number is detailed in the table below where the base cost estimates (including spares), contingency requests and overheads are first quoted separately. We have also separated the costs directly related to construction of a single NCC unit and those for ancillary systems (PHENIX DAQ, infrastructural and installation costs).

The funding from the DOE will cover

-the construction of a single Calorimeter unit comprising two fine electromagnetic and one coarse hadronic pad-structured segments, PreShower and ShowerMax detectors in 2008-2010;

- an upgrade to the PHENIX infrastructure to allow for installation of this detector in 2010;

- installation and commissioning of a single Nose Cone Calorimeter in 2010.

As indicated in Fig. 5.2, the first NCC unit is planed to be ready for physics for the RHIC run that begins in the fall of 2010. Below are the budgetary and scheduling details.

The major cost item and the critical item in the project are silicon sensors. The two kinds of sensors used in the calorimeter are responsible for nearly half of the unit cost. The other half is spread relatively uniformly among mechanics and electronics. The production of sensors drives the schedule. At this time we have identified three suppliers, Russia(ELMA),

R&D 2006-2007: Development	2006(k$)	2007(k$)	Total(k$)
Pxilated strip sensors (StriPixels)	26,300		26,300
Pad-structured readout units	18,565		18,565
Strip-structured readout units	5,000	12,000	20,000
Pad readout analog elecronics		15,200	15,200
Pad readout digital electronics	3,000	5,813	8,813
StriPixel readout electronics	4,000	8,250	12,250
R&D 2006-2007: Design and Prototyping			
Si wafers		39,950	39,950
Pad-structured sensors	70,000	22,531	92,531
Pad-structured ROU's	5,000	19,323	24,323
Electronics for pad-structured layers	10,000	27,500	44,063
Pixilated strip sensors (StriPixels)		10,540	10,540
StriPixel ROU's and electronics		18,185	21,121
Mechanical Structure	5,000	8,850	15,863
Testing (bench and Test beam)		17,038	17,038
2006-2007 request to BNL	**41,565**	**107,247**	**200,273**
2006-2007 request to RIKEN	**105,300**	**57,981**	**166,281**
Others (UCR)	**30,000**	**30,000**	**60,000**

Figure 5.1: Major Costs associated with research and development related to PHENIX NCC Project. Update this table since we got some of the funding

Costs (k$) / Year:	2008	2009	2010	Base Cost	Contin-gency	Over-head	Total
NCC Construction (k$)	900	1800	1007	2331	827	549	3707
Ancillary Systems (k$)			236	160	48	28	236
Total DOE Construction (k$)	900	1800	1243	2491	875	577	3943

Figure 5.2: Profile of DOE cost estimates for first NCC.

Czech Republic (ON Semiconductors) and in Korea (SENS), interested in producing Si sensors following our design. ELMA and ON Semiconductors both have an experience with production of sensors close to NCC specifications, hence cost estimates and schedules presented in this proposal are based upon quotations from ELMA. It will take two years to produce sensors for a single NCC unit if all production is done at ELMA. To shorten this time down to the 18 months reserved for this task in our schedule we will have production running both at ELMA and ON Semiconductors. with the Korean option being seriously investigated. SENS has produced a first pad sensor module which will be tested soon.

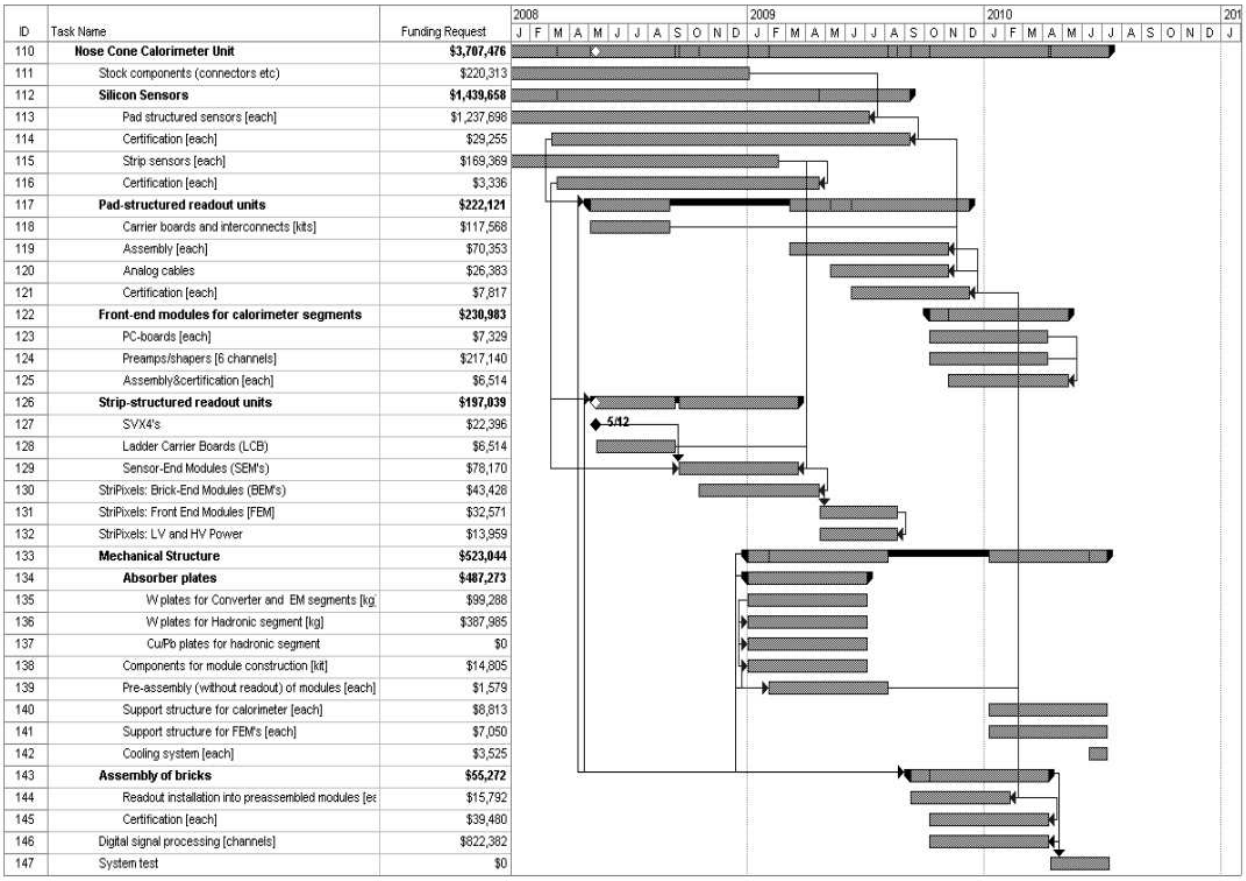

ID	Task Name	Funding Request
110	**Nose Cone Calorimeter Unit**	**$3,707,476**
111	Stock components (connectors etc)	$220,313
112	**Silicon Sensors**	**$1,439,658**
113	Pad structured sensors [each]	$1,237,698
114	Certification [each]	$29,255
115	Strip sensors [each]	$169,369
116	Certification [each]	$3,336
117	**Pad-structured readout units**	**$222,121**
118	Carrier boards and interconnects [kits]	$117,568
119	Assembly [each]	$70,353
120	Analog cables	$26,383
121	Certification [each]	$7,817
122	**Front-end modules for calorimeter segments**	**$230,983**
123	PC-boards [each]	$7,329
124	Preamps/shapers [6 channels]	$217,140
125	Assembly&certification [each]	$6,514
126	**Strip-structured readout units**	**$197,039**
127	SVX4's	$22,396
128	Ladder Carrier Boards (LCB)	$6,514
129	Sensor-End Modules (SEM's)	$78,170
130	StriPixels: Brick-End Modules (BEM's)	$43,428
131	StriPixels: Front End Modules [FEM]	$32,571
132	StriPixels: LV and HV Power	$13,959
133	**Mechanical Structure**	**$523,044**
134	**Absorber plates**	**$487,273**
135	W plates for Converter and EM segments [kg	$99,288
136	W plates for Hadronic segment [kg]	$387,985
137	Cu/Pb plates for hadronic segment	$0
138	Components for module construction [kit]	$14,805
139	Pre-assembly (without readout) of modules [each]	$1,579
140	Support structure for calorimeter [each]	$8,813
141	Support structure for FEM's [each]	$7,050
142	Cooling system [each]	$3,525
143	**Assembly of bricks**	**$55,272**
144	Readout installation into preassembled modules [ea	$15,792
145	Certification [each]	$39,480
146	Digital signal processing [channels]	$822,382
147	System test	$0

Figure 5.3: Budgetary and scheduling details covering major tasks involved in construction of the first NCC unit (extracted from the project file).

In 2008 funding is required to purchase silicon wafers, start sensor production and to set assembly areas at collaborating institutions. Funding in 2009 covers all major purchases including tungsten plates and electronics components (US Industry and Russia), most of the Si (foundries in collaborating countries) and detector assembly (collaborating institutions). We are planning for the last task to be carried mainly in the students laboratories in collaborating Universities.

5.6 Additional NCC to complement DOE Construction project

As stated above, the PHENIX Collaboration is pursuing the design and construction of a complimentary second PHENIX NCC to (a) avoid RHIC running time losses when running asymmetric collision species, (b) to double the yield of rare probes (thereby reducing RHIC running time), and (c) to access the production kinematics resulting in associated production of particles the in forward-backward directions (for example, electrons from Z-decays).

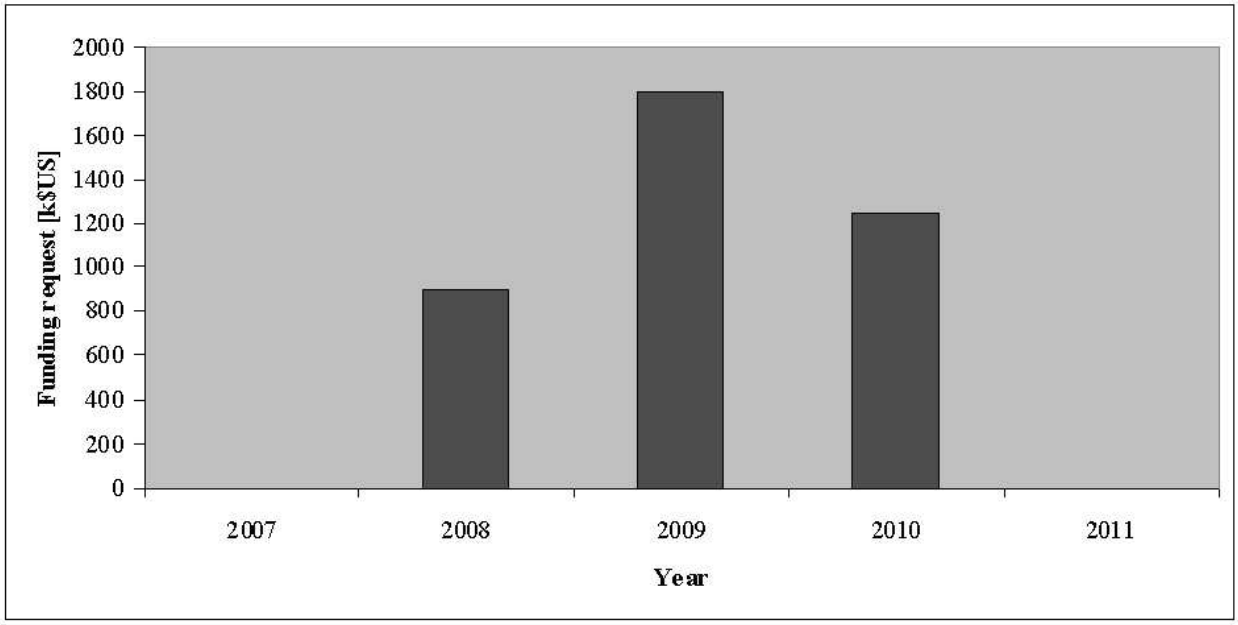

Figure 5.4: Proposed funding profile for DOE Construction project (also see first three columns in Fig. 5.3.

While the details of how to finance the second NCC are not yet clear, its base cost is below 3 million $US and will be limited to production costs. Ancillary system costs are already covered in the first DOE funded stage of the Project. The PHENIX collaboration is actively pursuing now all possible venues for funding this part of the project through international contributions.

Appendix A

Event Rates

In this section we estimate the event rates of selected physics processes corresponding to some of the major goals of the NCC detector. All rates are for a single NCC. We start with expected luminosities for RHIC II from the BNL Collider Accelerator Division (CAD). We then assume a 50% duty factor for the RHIC machine, and a 60% up time for the PHENIX detector during a 12 week run to obtain an integrated luminosity (see table A.1).

There are several typical losses in efficiency from our experience in the first 5 years of data taking. These are listed in table A.2. The first arises from a vertex cut, which we take to be ± 20 cm from the nominal collision point. We assume 55% efficiency from losses due to the spread of the beam. Secondly, the minimum bias trigger uses the Beam-Beam Counters (BBC) located up and downstream of the collision point. In the high multiplicity environment of heavy ion collisions - this trigger is almost 100% efficient. However in low multiplicity p+p and p+A collisions, the efficiency drops since in some cases, no particles actually trigger the BBC. Finally we have taken 80% for the reconstruction efficiency, a reasonable number from our experience in the last several years.

Pythia was used to obtain p+p cross sections for direct photons, π^0's, W's, and the χ_c. To obtain heavy ion yields we assumed a point-like cross section - that is the cross sections were scaled by the product of the atomic weights of the incoming nuclei. For π^0's and the χ_c a suppression factor was assumed consistent with the data from Runs 1-5 or about a factor

Table A.1: Luminosity guidance from CAD for RHIC II. We assume a 50% duty cycle for RHIC to give a weekly integrated luminosity. We then assume a 12 week run and a 60% uptime for PHENIX to give an total integrated luminosity.

Species	p+p 200 GeV	p+p 500 GeV	pAu	CuCu	Au+Au
luminosity ($s^{-1}cm^{-2}$)	1×10^{32}	5×10^{32}	2.5×10^{29}	8×10^{28}	7×10^{27}
luminosity/week ($\mathrm{pb}^{-1}\mathrm{week}^{-1}$)	33	166	0.083	0.025	0.0025
Integrated Luminosity (pb^{-1})	238	1195	0.6	0.18	0.018

Table A.2: Efficiency factors added into the rate calculations. In the analysis we typically require that the vertex be within 20 cm of the nominal collision point, which results in a loss of 0.55. For A+A collisions the minimum bias trigger formed by the Beam-Beam counters are essentially 100% efficient, however in p+p and p+A collisions there is some loss.

Species	p+p 200 GeV	p+p 500 GeV	pAu	CuCu	Au+Au
vertex cut	0.55	0.55	0.55	0.55	0.55
min bias trigger efficiency	0.75	0.75	0.90	1.0	1.0
reconstruction efficiency	0.80	0.80	0.80	0.80	0.80
total efficiency factor	0.33	0.33	0.40	0.44	0.44

of 2 for minimum bias collisions. Tables A.3 and A.4 give the yields for a 12 week run for pp, pA, Cu+Cu and Au+Au collisions for a single NCC.

We are studying the effect of triggering as described in section 3.9.1. A simple 8x8 tile trigger should be sufficient for p+p and p+A collisions given a DAQ bandwidth of 8kHz. However, at present a simple 8x8 trigger will be ineffective in heavy ion collisions giving rejections of less than 2. Using a minimum bias trigger for heavy ion collisions results in substantial loss of a e.g. a factor of 6 in Au+Au collisions and 30 in Cu+Cu collisions. This does not affect the χ_c since this depends on a dimuon trigger and will not come from triggering using the NCC. The work on the trigger is in its very early stages and more sophisticated trigger schemes will be explored. In addition improvements are envisioned to the DAQ to increase its rate by a factor of 2 or more.

Table A.5 gives a summary of the physics program addressed by the Nosecone Calorimeter. Rates for direct photons and π^0's are typically about 5 times that which will be available in the central EMC in A+A collisions. Without the NCC the χ_c would be impossible. The rate into the central EMC is simply too small. The NCC, by contrast utilizes the large acceptance of the muon arms to detect the J/ψ, and is itself a large acceptance detector. For both p+p and p+A collisions, the crucial aspect of the NCC is the forward rapidity coverage which allows one to reach low x.

Table A.3: Yields in p+p collisions of various processes into the acceptance of a single NCC for a 12 week run.

Species	process		Yield
pp 200 GeV	π^0 production	$p_T(\pi^0) > 5$ GeV	62M
		$p_T(\pi^0) > 10$ GeV	260K
		$p_T(\pi^0) > 15$ GeV	8K
		$p_T(\pi^0) > 20$ GeV	450
pp 200 GeV	direct photon production	$p_T(\gamma) > 5$ GeV	1M
		$p_T(\gamma) > 10$ GeV	33K
		$p_T(\gamma) > 15$ GeV	2.6K
		$p_T(\gamma) > 20$ GeV	280
pp 200 GeV	W$\rightarrow e + \nu_e$	$p_T(e) > 5$ GeV	16
		$p_T(e) > 10$ GeV	11
		$p_T(e) > 20$ GeV	5
pp 200 GeV	$\chi_{c1} \rightarrow \gamma J/\psi \rightarrow \gamma\mu\mu$		26K
	$\chi_{c2} \rightarrow \gamma J/\psi \rightarrow \gamma\mu\mu$		42K
pp 500 GeV	π^0 production	$p_T(\pi^0) > 5$ GeV	1300M
		$p_T(\pi^0) > 10$ GeV	17M
		$p_T(\pi^0) > 15$ GeV	1.3M
		$p_T(\pi^0) > 20$ GeV	190K
pp 500 GeV	direct photon production	$p_T(\gamma) > 5$ GeV	24M
		$p_T(\gamma) > 10$ GeV	1.7M
		$p_T(\gamma) > 15$ GeV	270K
		$p_T(\gamma) > 20$ GeV	65K
pp 500 GeV	W$\rightarrow e + \nu_e$	$p_T(e) > 5$ GeV	4.9K
		$p_T(e) > 10$ GeV	4.4K
		$p_T(e) > 20$ GeV	2.8K
pp 500 GeV	$\chi_{c1} \rightarrow \gamma J/\psi \rightarrow \gamma\mu\mu$		790K
	$\chi_{c2} \rightarrow \gamma J/\psi \rightarrow \gamma\mu\mu$		1.1M

Table A.4: Yields in pAu, Cu+Cu and Au+Au collisions of various processes into the acceptance of a single NCC for a 12 week run.

Species	process		Yield
pAu 200 GeV	π^0 production	$p_T(\pi^0) > 5$ GeV	37M
		$p_T(\pi^0) > 10$ GeV	150K
		$p_T(\pi^0) > 15$ GeV	4.7K
		$p_T(\pi^0) > 20$ GeV	270
pAu 200 GeV	direct photon production	$p_T(\gamma) > 5$ GeV	610K
		$p_T(\gamma) > 10$ GeV	20K
		$p_T(\gamma) > 15$ GeV	1.5K
		$p_T(\gamma) > 20$ GeV	170
pAu 200 GeV	$\chi_{c1} \to \gamma J/\psi \to \gamma\mu\mu$		10K
	$\chi_{c2} \to \gamma J/\psi \to \gamma\mu\mu$		16K
CuCu 200 GeV	π^0 production	$p_T(\pi^0) > 5$ GeV	130M
suppressed		$p_T(\pi^0) > 10$ GeV	545K
		$p_T(\pi^0) > 15$ GeV	16K
		$p_T(\pi^0) > 20$ GeV	942
CuCu 200 GeV	direct photon production	$p_T(\gamma) > 5$ GeV	4.1M
		$p_T(\gamma) > 10$ GeV	130K
		$p_T(\gamma) > 15$ GeV	10K
		$p_T(\gamma) > 20$ GeV	1.1K
CuCu 200 GeV	$\chi_{c1} \to \gamma J/\psi \to \gamma\mu\mu$		40K
suppressed	$\chi_{c2} \to \gamma J/\psi \to \gamma\mu\mu$		65K
AuAu 200 GeV	π^0 production	$p_T(\pi^0) > 5$ GeV	100M
suppressed		$p_T(\pi^0) > 10$ GeV	440K
		$p_T(\pi^0) > 15$ GeV	13K
		$p_T(\pi^0) > 20$ GeV	1.1K
AuAu 200 GeV	direct photon production	$p_T(\gamma) > 5$ GeV	4M
		$p_T(\gamma) > 10$ GeV	130K
		$p_T(\gamma) > 15$ GeV	10K
		$p_T(\gamma) > 20$ GeV	1.1K
AuAu 200 GeV	$\chi_{c1} \to \gamma J/\psi \to \gamma\mu\mu$		43K
suppressed	$\chi_{c2} \to \gamma J/\psi \to \gamma\mu\mu$		70K

Table A.5: The coverage by the NCC of some of relevant kinematical variables given the rates mentioned previously.

Process	Species	Physics Goal	
π^0 production	pAu 200 GeV	saturation	$1< y <3$; $p_T \sim 15$ GeV
	p+p 200 GeV	"CGC"	$1< y <3$; $p_T \sim 15$ GeV
direct photon production	pAu 200 GeV	saturation	$1< y <3$; $p_T \sim 15$ GeV
	p+p 200 GeV	"CGC"	$1< y <3$; $p_T \sim 15$ GeV
π^0 production	Au+Au 200 GeV	parton energy loss	$1< y <3$; $p_T \sim 15$ GeV
Heavy Ions	Cu+Cu 200 GeV		$1< y <3$; $p_T \sim 15$ GeV
	pAu 200 GeV		$1< y <3$; $p_T \sim 15$ GeV
	p+p 200 GeV		$1< y <3$; $p_T \sim 15$ GeV
direct photon production	Au+Au 200 GeV	jet tomography	$1< y <3$; $p_T \sim 15$ GeV
"photon-jet"	Cu+Cu 200 GeV		$1< y <3$; $p_T \sim 15$ GeV
Heavy Ions	pAu 200 GeV		$1< y <3$; $p_T \sim 15$ GeV
	p+p 200 GeV		$1< y <3$; $p_T \sim 15$ GeV
$\chi_{c1} \rightarrow \gamma J/\psi \rightarrow \gamma\mu\mu$	Au+Au 200 GeV	confinement	$1< y <2$
Heavy Ions	Cu+Cu 200 GeV		$1< y <2.5$
	pAu 200 GeV		$1< y <3$
	p+p 500 GeV		$1< y <3$
π^0 production	p+p 200 GeV	$A_{LL}(p_T)$	
Spin	p+p 500 GeV		
direct photon production	p+p 200 GeV	$\Delta G(x)$at low x	$x \sim 3 \times 10^{-3}$
Spin	p+p 500 GeV		$x \sim 1 \times 10^{-3}$
W$\rightarrow e + \nu_e$ *Spin*	p+p 500 GeV	$\Delta\overline{q}$	
Spin			

Appendix B

Physics Simulations

This appendix outlines the progress made in understanding the capabilities of the NCC in the study of a variety of physics topics. The physics analysis topics addressed by the NCC require:

- The measurement of π^0 spectrum to 30 GeV (15 GeV $p_\perp$) in AA, pA, and p+p collisions.
- The measurement of the direct photon spectrum in AA, p+A and p+p collisions, and correlations of direct photons and high momentum π^0's.
- the measurement of jets in p+p collisions for extraction of Bjorken x.
- the ability to use isolation cuts to identify direct photons and leptons from W bosons and heavy quarks in p+p and dAu events on an event-by-event basis.

In what follows, all plots assume the luminosities stated in Appendix A.

As mentioned previously, electromagnetic calorimetry in the central region ($-0.35 < y < 0.35$) has been a very powerful tool for the PHENIX detector. The purpose of the NCC is to extend these measurements to higher rapidity, and to increase the statistics for low event processes such as direct photon events. The increase in statistics can be rather large. RHIC II gives us a factor of 10 increase in luminosity while a single NCC will give us an increase in acceptance of about 5. Theoretically this leads to an increase in yield of a factor of 50. Practically however, the increase is somewhat less than this since the p_T spectrum drops off as a function of rapidity. As an example, the NCC will see about 3 times as many direct photons in AuAu collisions above a p_T of 5 GeV than the central EMC.

The increase in statistics is critical for many measurements. For example for correlation measurements in the case of photon-jet events in Au+Au collisions- we wish to divide the event sample into bins of transverse momentum and rapidity in order to be able to reconstruct the energy loss of partons as a function of momentum as well as the energy density of the collision.

For the signals we are interested in for heavy ion collisions, namely the χ_c, high momentum direct photons, and π_0's, we have tools we can use to isolate the signal. For the χ_c the

tool is the invariant mass difference $m_{\gamma\mu\mu} - m_{\mu\mu}$. For the direct photon measurements in Au+Au and dAu we will use the method of looking at the comparison of the γ to π^0 ratio measured vs expected, where we must make a very good measurement of the π^0 spectrum. This method was used to generate the direct photon signal shown in Fig. B.1. In p+p and p+A collisions, for event-by-event measurements of the direct photon to measure x_{BJ}, we will use higher momentum photons and isolation cuts. In what follows we assume RHIC II luminosities as shown in table A.1.

B.1 Direct Photons

The method used in this the PHENIX data analysis to extract the direct photon signal (Fig B.1) makes use of the fact, that we can measure the precise π^0 spectrum. We will use the same method in the NCC - this will be possible because the PS/SM detectors should give us a good identification of showers associated with π^0's as explained in section 3.4.6. Once a π^0 spectrum is measured, the direct photon analysis proceeds as follows: A simulation is used to calculate the expected γ to π^0 ratio using the measured π^0 spectrum, putting in all known sources except direct photons. In the simulation a ratio is made between the photon spectrum and the π^0 spectrum. The same is done in the data and a double ratio is made i.e.

$$R = \frac{(\gamma/\pi^0)_{measured}}{(\gamma/\pi^0)_{expected}} = \frac{(\frac{\gamma_{\pi^0}+\gamma_{direct}}{\pi^0})_{measured}}{(\frac{\gamma_{\pi^0}}{\pi^0})_{expected}} \sim 1 + \frac{\gamma_{direct}}{\gamma_{\pi^0}}$$

This method cancels many systematic errors. In particular overlapping showers will cancel in the ratio if the simulation is done correctly. Fig. B.1 shows the the statistical errors which will be reached in such an analysis in Au+Au collisions.

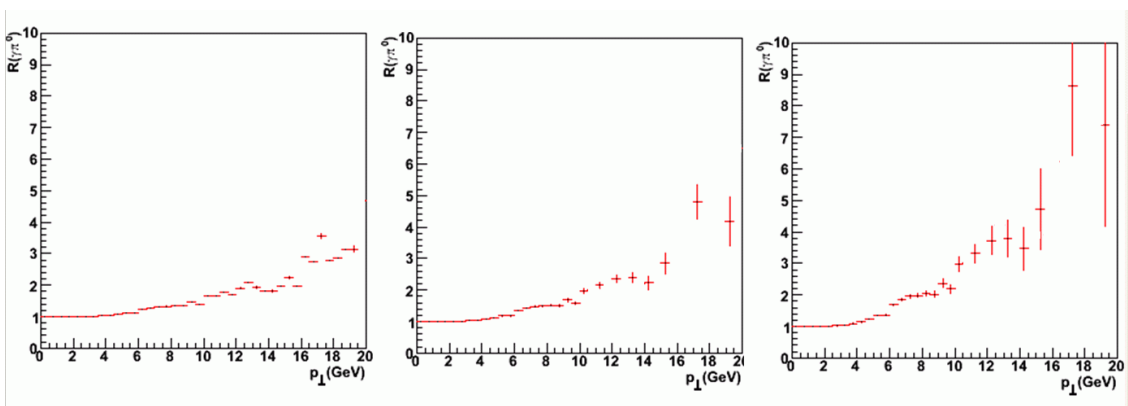

Figure B.1: Simulation of the direct photon signal, i.e. the ratio $R = \frac{(\gamma/\pi^0)_{measured}}{((\gamma/\pi^0)_{expected})}$ as measured by the NCC. R in p+p collisions[left] ; R in p+Au collisions[center]; R in Au+Au collisions [right]. Our final analysis will require a comparison of all three systems. Error bars are from the statistics we expect to get in the experiment. The fluctuations of the points arises from lack of statistics in the simulation.

In a single run at RHIC II luminosities the NCC should be able to make measurements of the direct photon spectrum to 15 in p_T at rapidities between 1 and 3 nicely complementing the results to be obtained at central rapidity.

The study of direct photons opposite a high momentum hadron allows for a study of a calibrated jet since the photon does not undergo any quenching. While the process is most easily visualized on an event by event basis, in practice it is done using correlation functions where the angular correlation between photons and high momentum π^0's are plotted. The combinatorial background is subtracted using a mixed event technique. Using the technique of recognizing showers which actually arise from the decay of π^0 described in section 3.4.6 a background sample of decay photons opposite high momentum π^0's can be constructed and subtracted from the original distribution to yield a correlation function of direct photons and hadrons. As was mentioned in 2.1 such studies can be done as a function of the reaction plane to enable a 3-D tomography of the system.

It is well known that isolation criteria can be used in p+p collisions to identify direct photons. Fig. B.2, left panel shows the yield of photons from decays in QCD events (blue) and direct photons (red) in 500 GeV p+p collisions. After requiring a separation criteria, $E_{cone}/E_{direct-photon} < 0.1$, where E_{cone} is the amount of electromagnetic energy in a cone of size $\Delta\eta\Delta\phi$=0.8, the direct photons dominate over decay photons above a p_T of 7 GeV. See fig. B.2 (right panel).

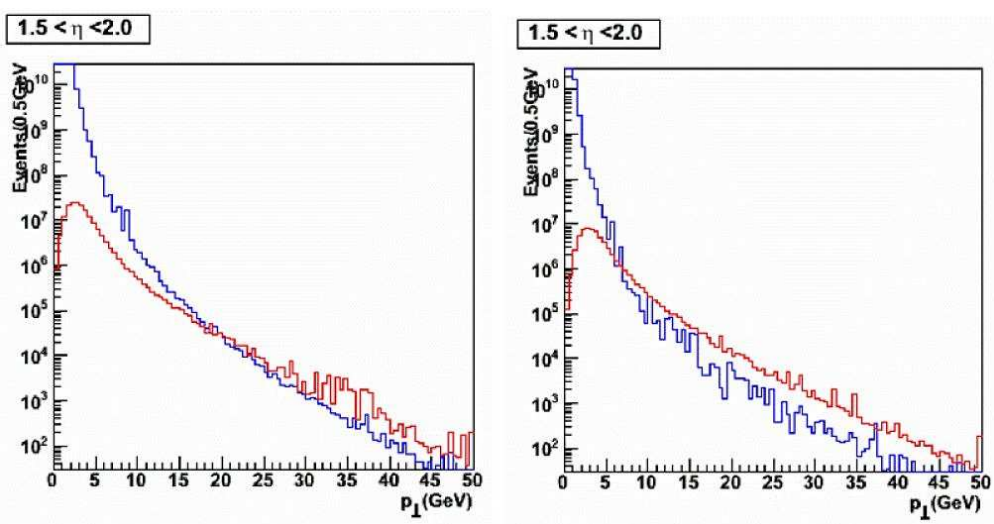

Figure B.2: Yield of photons between $1.5 < \eta < 2$ from decays in QCD events (blue) and direct photons (red) in 500 GeV p+p collisions [left]; Yield of photons between $1.5 < \eta < 2$ from decays in QCD events (blue) and direct photons (red) in 500 GeV p+p collisions after an isolation cut as explained in the text [right].

The method works in p+A collisions as well since the photon is generally separated from the bulk of the produced particles. Fig. B.3 shows the yield of photons from decays in QCD events (blue) and direct photons (red) in pAu collisions. Of course, one can also use a method similar to that used in heavy ion collisions and obtain the direct photon

spectrum on a statistical basis, which would then allow one to go to low p_T. An important point, mentioned previously is that in the case of suppression due to the initial state - i.e. the CGC, direct photons should should experience a similar suppression as the hadrons. Photons, which to first order, do not interact via the strong interaction, should not be sensitive to final state effects - i.e. nuclear matter or any sQGP and should be clean indication of suppression due to initial state effects.

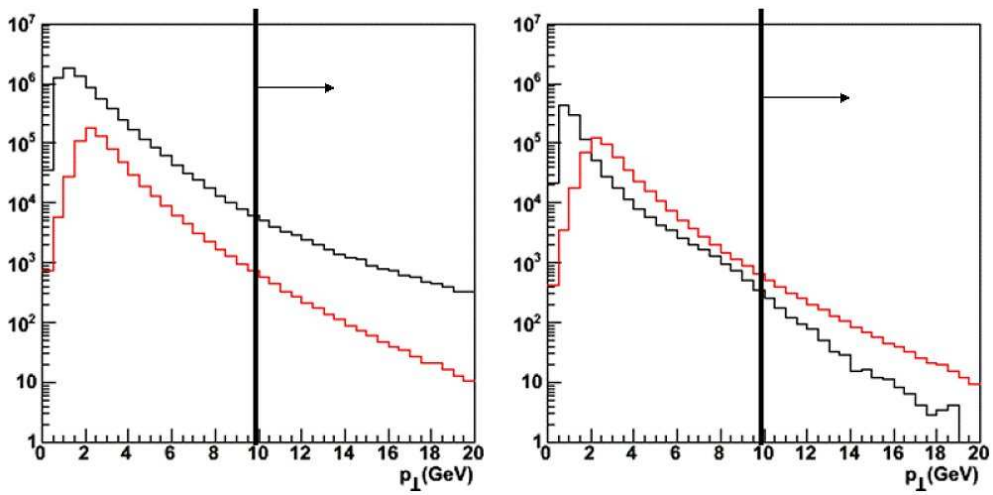

Figure B.3: (left) Photons from decays in QCD events [black] and direct photons [red] in pAu collisions between $1 < \eta < 3$. (right) For the QCD background, only the highest energy photon in each event is plotted. Photons between $1 < \eta < 3$ from decays in QCD events [black] and direct photons [red] in pAu collisions after an isolation cut in which $E_{cone}/E_{direct-photon} < 0.1$, where E_{cone} is the amount of electromagnetic energy in a cone of size $\Delta\eta\Delta\phi$=0.8. Unlike the other figures in this section, the simulation was done using a heavy ion event generator HIJING. For the generation of QCD background events a cut of 10 GeV was made on the hard scattering of partons, hence one should look at the region to the right of the line in these plots.

B.2 The χ_c

The χ_c decays into a J/ψ and a photon. We first identify the J/ψ via its di-muon decay - it may also be possible to use the di-electron channel as well. For χ_c's in which the muons are detected in the muon arms - the photon is accepted in the NCC more than 60% of the time(Fig. B.5). In order to see the χ_c one reconstructs the $\mu^+\mu^-\gamma$ invariant mass and subtracts off the $\mu^+\mu^-$ invariant mass where the dimuon mass is required to be in the J/ψ peak. The χ_c should show up as a peak at the χ_c-J/ψ mass difference of about 400-500 MeV. There are actually 2 χ_c states which decay with large branching ratios to the J/ψ with masses 3511 and 3556 MeV, however our resolution will now allow us to separate these two states. Note that the resolution is now primarily due to the resolution of the photon and

not the resolution of the muon spectrometer. This technique has actually used by PHENIX to identify the χ_c in pp collisions using the central arms, where we have electromagnetic coverage. See Fig. B.4.

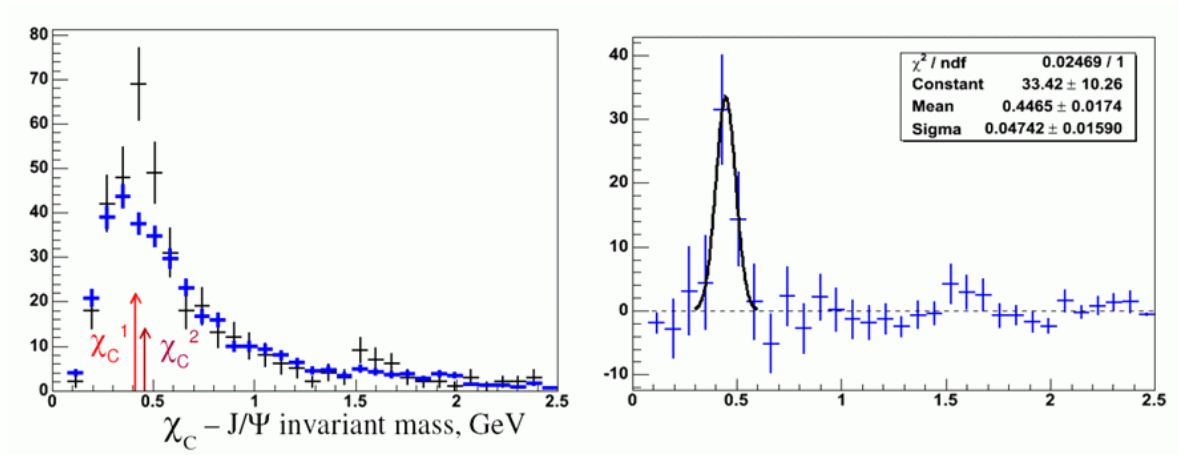

Figure B.4:
$J\psi\gamma J\psi$ invariant mass spectrum showing the χ_c peak in pp collisions as seen by the PHENIx central arm in run-5. We see about 50 χ_c. Background subtracted spectrum is shown on the right. The resolution of the peak is about 50MeV consistent with the resolution of the EMCAL.

A simulation was done in which single χ_c events were generated using PYTHIA which were overlaid on a background of photons corresponding to a variety of cases from p+p collisions to central Au+Au collisions. The S/B on the J/ψ was taken from present data, where we have assumed an improvement in resolution and background rejection of decay muons from the FVTX. In the case of central AuAu collisions this lead to a S/B of about 1/5. The J/ψ was then reconstructed and paired will all photons in the event to form a γJ/ψ invariant mass distribution. We assumed that the background could be subtracted using a mixed background technique.

As an example fig. B.6 shows the invariant mass difference for simulated full events in p+p collisions for rapidity between 2 and 2.5. The background distribution is shown in black with a subtracted spectrum shown on the right. The resolution is about 120 MeV. Note that the typical energy of the photons is about 1 GeV. The energy resolution for showers contained in in EM1 and EM2 is $0.03 + \frac{0.18}{\sqrt{(E)}}$. When higher energy showers greater than 10 GeV enter the HAD compartment however, the resolution becomes $0.03 + \frac{0.27}{\sqrt{(E)}}$. We believe that out estimate of the calorimeter resolution is reasonable. If however, the calorimeter resolution is much worse the χ_c can still be reconstructed, at least in p+p events. Fig. B.7 shows the resolution if the resolution is degraded to $\frac{0.50}{\sqrt{(E)}}$.

In heavy ion collisions, the combinatorial background is considerably larger. Fig. B.8 and B.9 show the χ_c signal for the top 10% ccentrality in Cu+Cu and Au+Au events. Even in central Au+Au events, the signal at rapidities 1-2 should be clear.

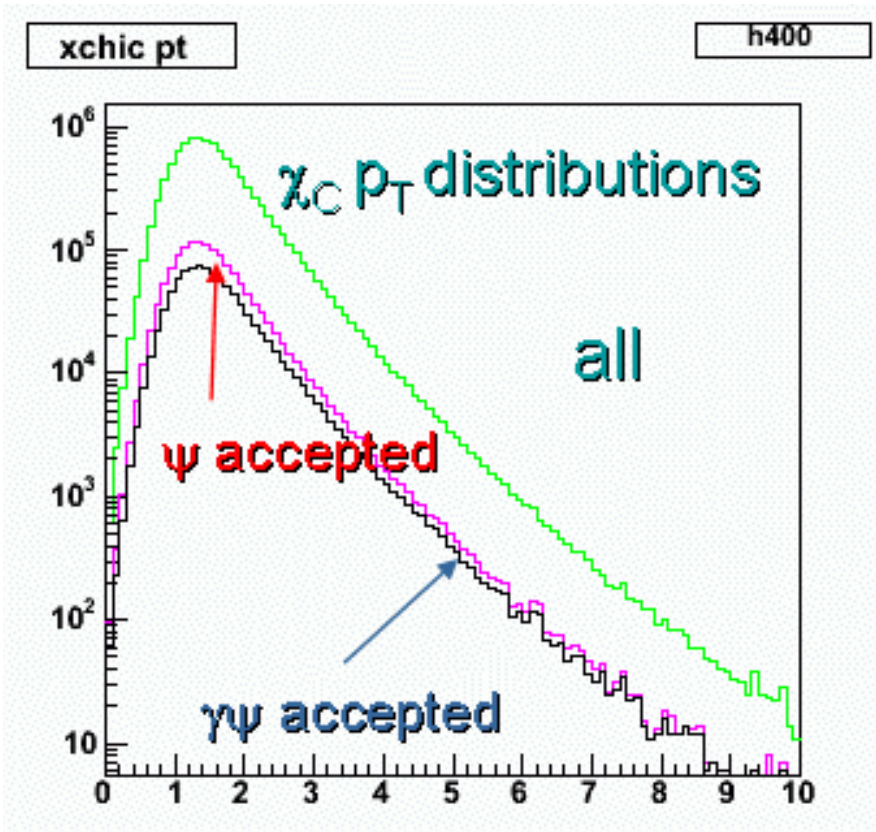

Figure B.5: p_T distributions for the χ_c. Green-all, red-J/ψ accepted in the muon spectrometer, blue-χ_c decay photon accepted in NCC and J/ψ accepted in the muon spectrometer.

We can then form the R_{AA} for the χ_C. This is shown in Fig. B.10 where the J/ψ is detected via its di-muon decay in the muon spectrometer. The photon detected by the NCC is in the rapidity range 1¡—y—¡1.5 (we need to show others later. This is compared to the $R_A A$ of the J/ψ measured by PHENIX in Run-4. Errors for the χ_C are statistical only. It is assumed that the pp measurement of the χ_C adds a negligible error to the ratio. The errors are of the order of 10% which simply comes from the fact that about 10K χ_C's are detected over a background of 600K. Since this is a S/B of less than 2%, systematic errors on the background subtraction must be evaluated carefully. This needs to be pursued. Ultimately we will need test beam data to understand how well we can the multi photon background to the signal photons, and a test where the prototype is put into PHENIX for a short while to measure the level of expected backgrounds.

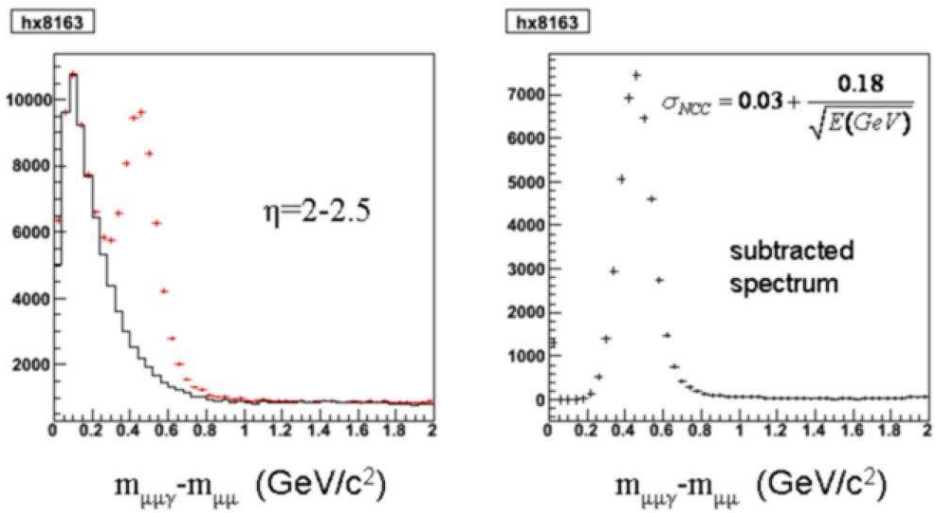

Figure B.6: The $M_{\gamma\mu\mu} - M_{\mu\mu}$ invariant mass distribution in p+p events. The left plot shows the raw mass difference spectrum (red) and background (black). The right shows the subtracted spectrum.

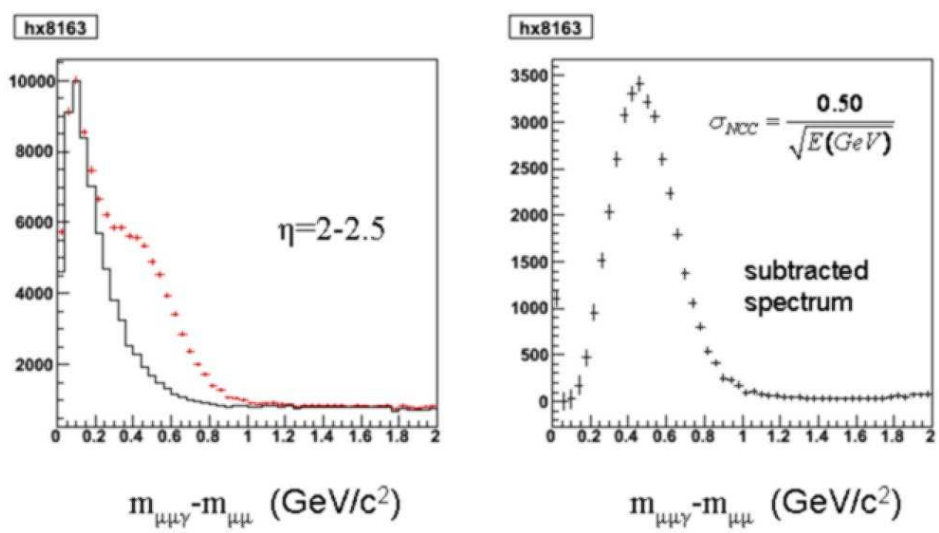

Figure B.7: Same as the previous figure with the resolution of the NCC degraded to $\frac{0.50}{\sqrt{(E(GeV))}}$

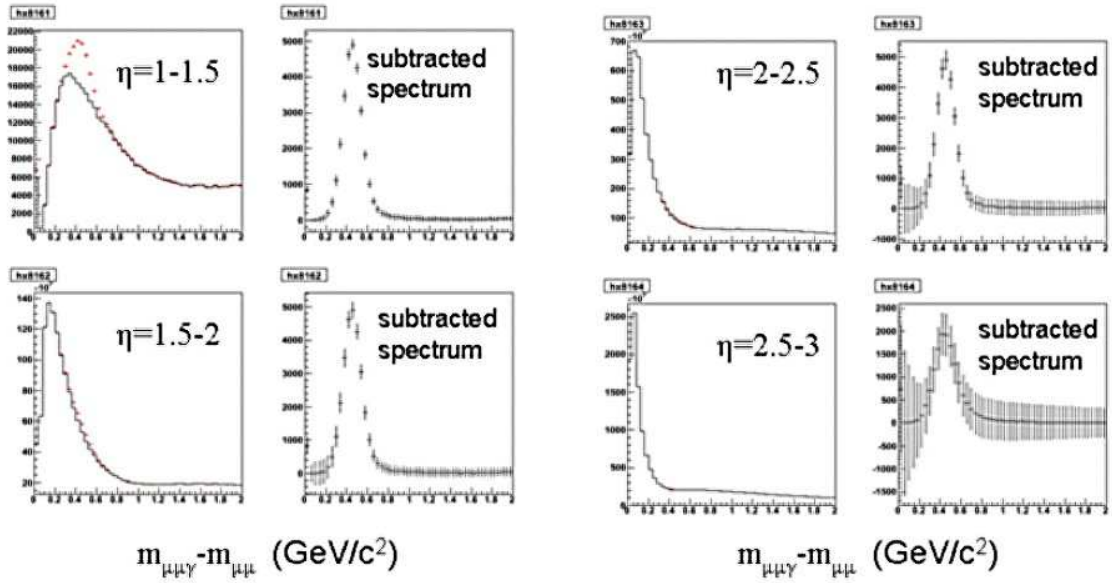

Figure B.8: Central 10% Cu+Cu events at various rapidities. The left plot of each pair show the raw mass difference, the right plot shows a background subtracted distribution.

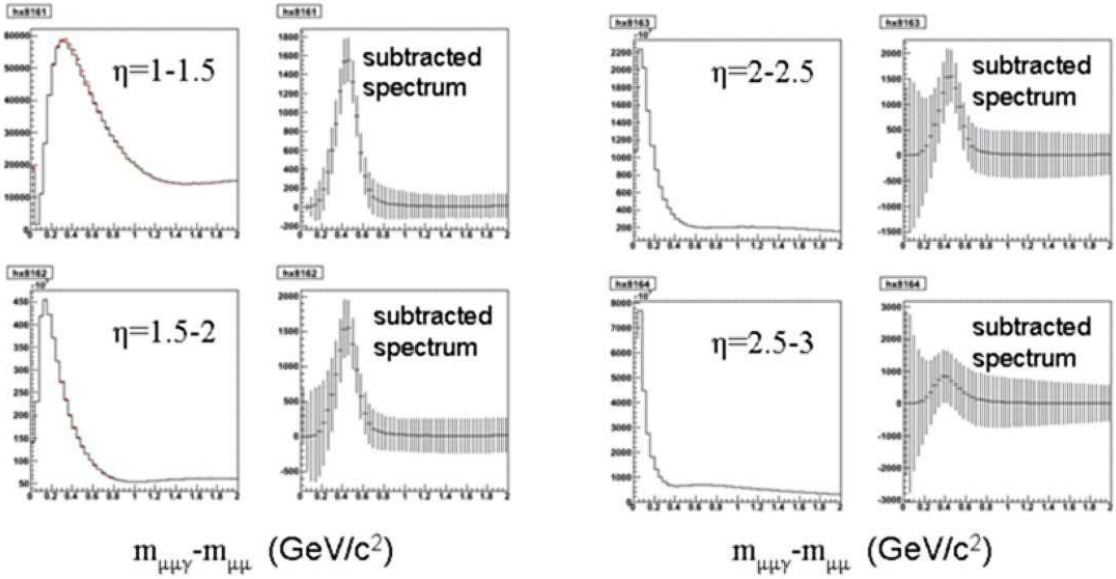

Figure B.9: Same as the previous plot for central Au+Au events.

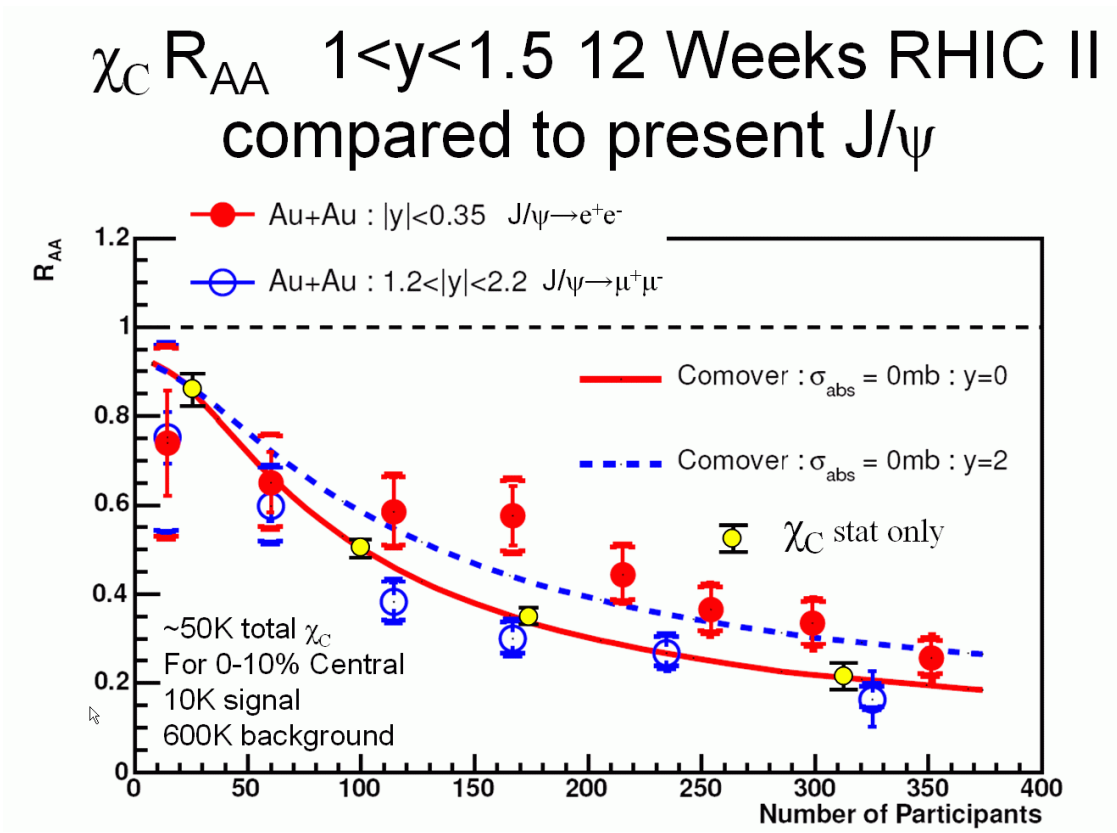

Figure B.10: R_{AA} for the χ_C in where the χ_C decays to a $J/\psi + \gamma$ and the J/ψ is detected via its di-muon decay in the muon spectrometer. The photon detected by the NCC in the rapidity range 1¡—y—¡1.5 (we need to show others later. This is compared to the $R_A A$ of the J/ψ measured by PHENIX in Run-4. Errors for the χ_C are statistical only. It is assumed that the pp measurement of the χ_C adds a negligible error to the ratio.

B.3 Spin Simulations

The double longitudinal spin asymmetry A_{LL} for direct photon events gives the most theoretically clean access to the gluon polarization of the nucleon $\Delta g(x)$ because it is dominated by a single subprocess (Fig 2.x) and because one does not need to include the effects of fragmentation into a leading hadron. Jet events, if they can be reliably isolated, also allow one to avoid fragmentation uncertainties, but at the cost of a larger number of subprocesses which contribute to the asymmetry. Given a limited experimental acceptance, the asymmetry for production of a high p_T particle will typically yield the highest statistical precision, but one loses information about the particular kinematics of each event, in other words, the momentum fractions x_g of the gluon and x_q of the quark.

The present PHENIX spectrometer is only instrumented to detect photons and hadrons in the central rapidity region $\eta < |0.35|$, allowing an excellent measurement of A_{LL} with single photon and π^0 detection, but with limited ability to determine jet kinematics. The central rapidity is most sensitive to the gluon polarization at intermediate x. Given that the unpolarized gluon distribution is larger at somewhat lower x_g, there is strong interest to explore the gluon polarization to as low x_g as possible. The addition of the NCC immediately extends the range x accessible at PHENIX by nearly an order of magnitude lower, just by extending the acceptance for single photons. At the same time, it expands the range in rapidity for "jet" (or at least leading hadron) detection, thus giving a significant range over which the parton event kinematics, and hence x_g, can be determined. This range is further extended if the central (VTX) and end cap (FVTX) silicon vertex detectors are included.

In photon-jet events, assuming the dominance of the leading order graphs, one can measure x_g on an event-by-event basis by assuming that the lower x is that of the gluon and by measuring the angle of the jet, for example, as follows:

$$x_q = \frac{x_T}{2}\left(e^{+\eta_\gamma} + e^{+\eta_{Jet}}\right)$$

$$x_g = \frac{x_T}{2}\left(e^{-\eta_\gamma} + e^{-\eta_{Jet}}\right)$$

where

$$x_T = \frac{2p_{\gamma T}}{\sqrt{s}}$$

using the γ to determine p_T (this assumes intrinsic k_T effects are negligible in the kinematics).

In the following, we present the results of simulations of the accessible kinematics of the PHENIX spectrometer instrumented with the NCC, and assuming hadron detection for $\eta <\sim |2.5|$ (actually, the recoil parton η); this assumes therefore the inclusion of the VTX barrel and FVTX. Studies were performed for collision energies $\sqrt{s}$ of 200 and 500 GeV. The event generation is performed by PYTHIA using GRSV98 parton distribution functions Polarization effects are added by hand using the parton polarizations determined in AAC. The hard scattering asymmetry is calculated from the parton kinematics to leading order only. We have further applied a 10 GeV/c cut in p_T to photons.

The x_g range of the events are shown Fig. B.11, the number of gluon Compton scattering events which are detected as a function of $\log_{10} x_g$. The red points display the events with only

the existing (central) PHENIX photon detection, while the green points show the extension provided by the NCC. The black points provide a reference for the case in which there was full photon acceptance up to an η of 3. There are also clear regions of overlap between the NCC and central detectors which should allow crosschecks of the measurement of the gluon polarization.

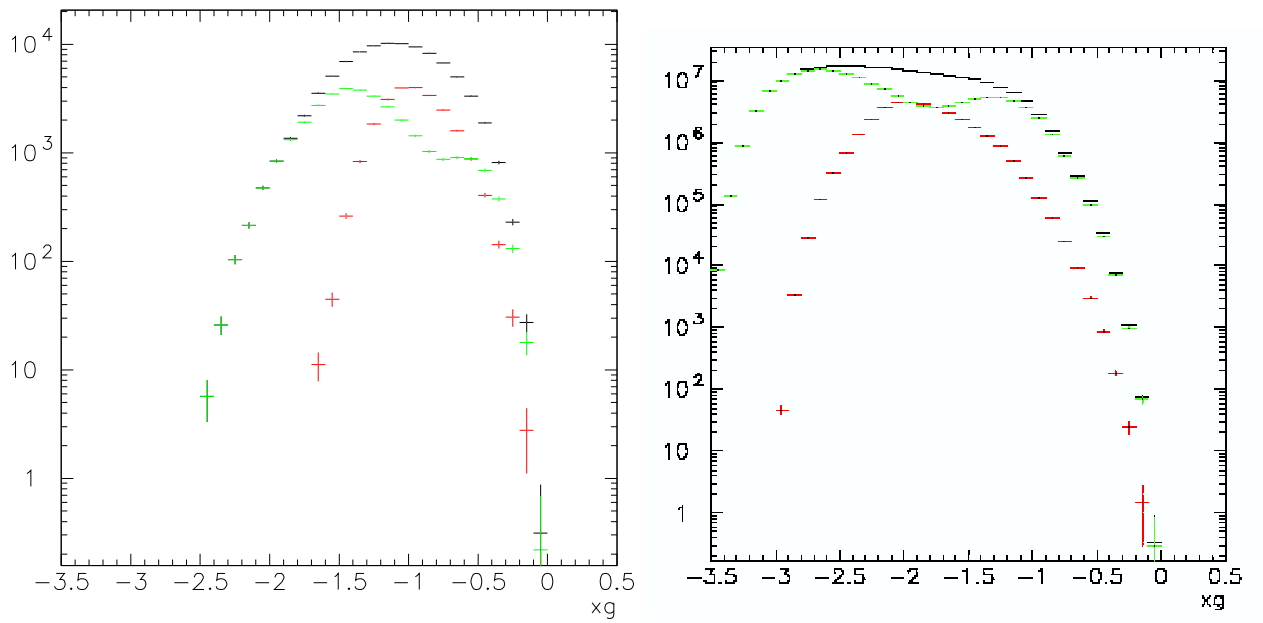

Figure B.11: Distribution of direct photon events at $\sqrt{s}$ of 200 (left) and 500 GeV (right). Red points refer to photons in the central detectors ($\eta < |0.35|$), while green points include the addition of the NCC ($1 < \eta < 3$). Black points show a hypothetical full acceptance ($\eta < |3|$).

This is where the power of the full PHENIX spectrometer will come into play. Using the tracking in the central SVX, the FVTX and the NCC PHENIX should be able to measure the jet angle over a large range. This together with the central EMC and the large acceptance of the NCC will give a measurement of both the photon and the jet over a nearly 5 units of rapidity giving access to $x_g \sim 10^{-3}$. It may be also be possible to disentangle events where the gluons are carrying a large momentum fraction to measure the spin structure functions at large x as well.

The actual double spin asymmetry as a function of photon p_T is shown in Fig. B.12, for $\sqrt{s} = 200$ GeV. The left panel shows the asymmetry measured in the central detectors, while that on the right shows the asymmetry for photons detected in the NCC. The simulation allows us to replot the asymmetry as a function of $\log_{10} x_g$, shown in Fig. B.13, clearly showing the range to which each acceptance is sensitive. One can directly see the range of $\Delta g(x_g)$ accessed (again via the simulation) in Fig. B.14.

Results of the simulation for $\sqrt{s} = 500$ GeV are shown in Figs. B.15. As expected, these measurements are sensitive to even lower x_g.

Further studies are underway to determine the effects of smearing from the actual photon

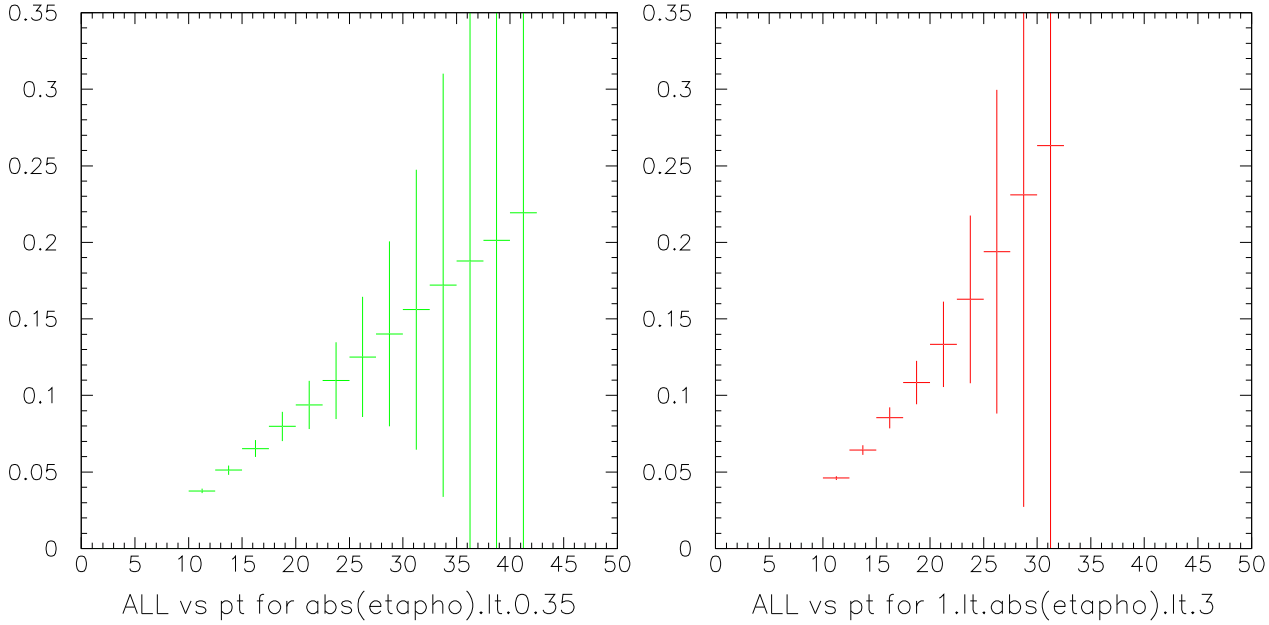

Figure B.12: Double longitudinal spin asymmetry for direct photon events at $\sqrt{s}$ of 200 GeV, as a function of photon p_T. The left panel shows the direct photon asymmetry measured by the central detectors ($\eta < |0.35|$), while the right panel shows the asymmetry measured by the NCC ($1 < \eta < 3$).

detection and jet angle resolutions for different detector configurations.

B.3.1 W isolation cuts: the quark structure of the nucleon.

While a cut on the pt of the muon can select W events, isolation cuts are traditionally used to clean up the signal offline. This is particularly important if there are fake muons coming from hadrons or hadron decays in the muon spectrometer. The isolation cut has been traditionally used to suppress the QCD background. Fig. B.16 shows that the one can get a suppression of the QCD background by a factor of 10, while loosing only 20

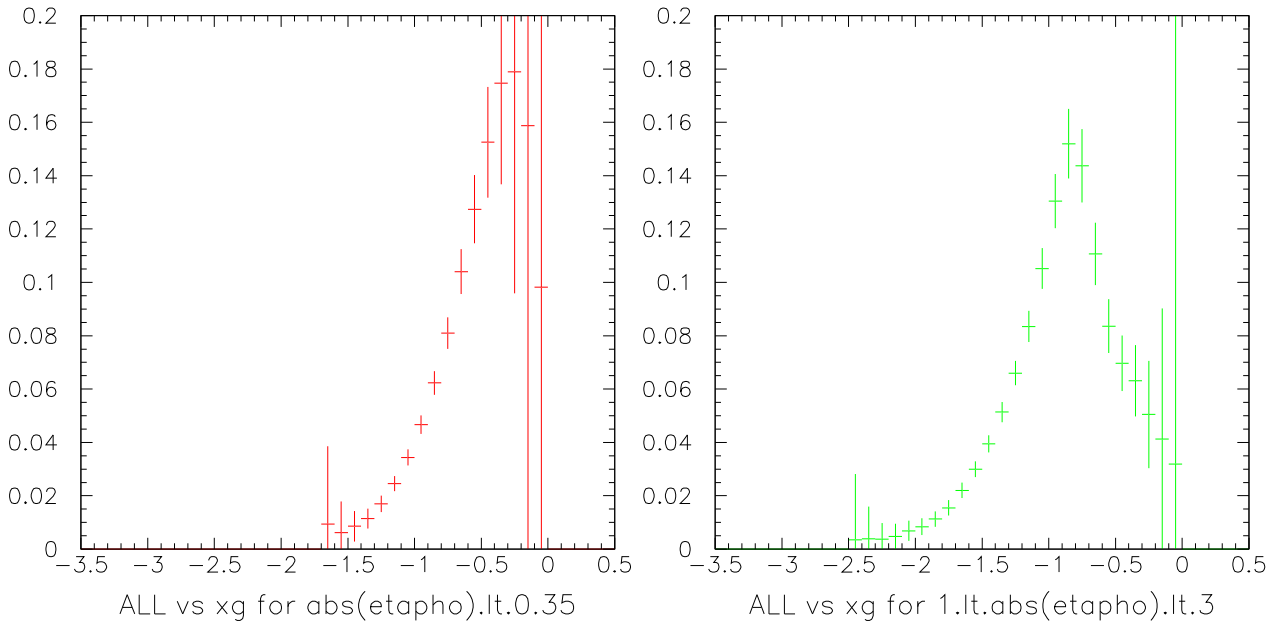

Figure B.13: Double longitudinal spin asymmetry for direct photon events at $\sqrt{s}$ of 200 GeV, as a function of $\log_{10} x_g$, as determined from the simulation. The left panel shows the direct photon asymmetry measured by the central detectors ($\eta < |0.35|$), while the right panel shows the asymmetry measured by the NCC ($1 < \eta < 3$).

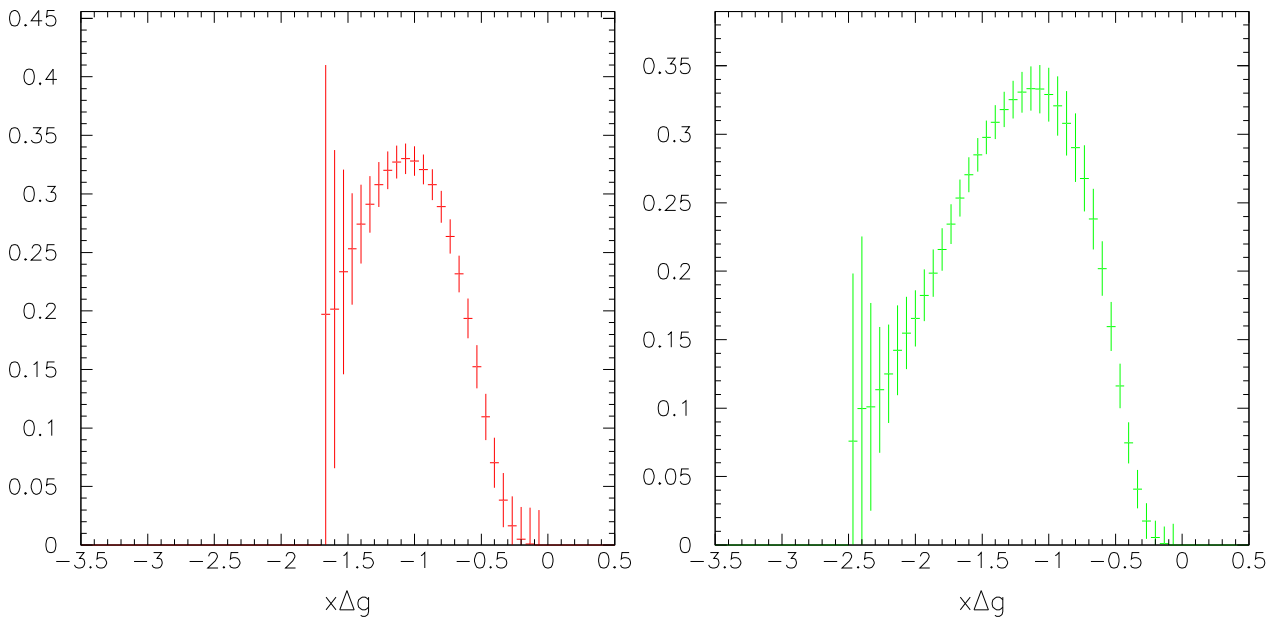

Figure B.14: Polarized gluon distribution function Δg for direct photon events at $\sqrt{s}$ of 200 GeV, as a function of $\log_{10} x_g$, as determined from the simulation. The left panel shows Δg measured by the central detectors ($\eta < |0.35|$), while the right panel shows Δg measured by the NCC ($1 < \eta < 3$).

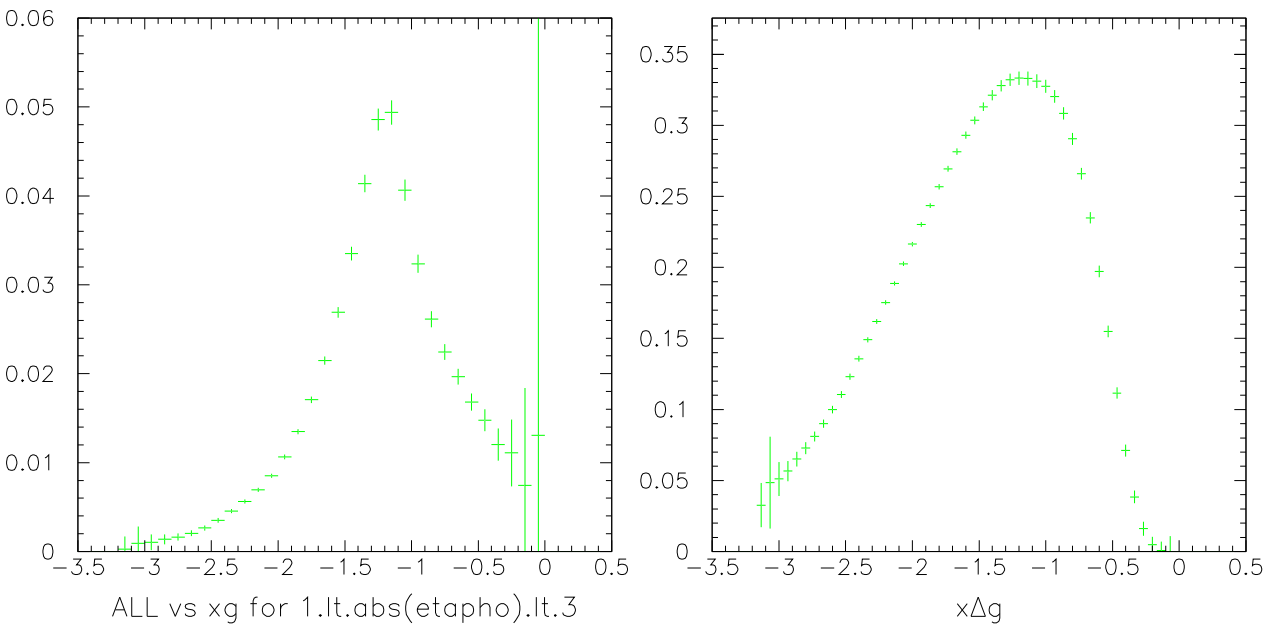

Figure B.15: Distributions for direct photon events at $\sqrt{s}$ of 500 GeV measured by the NCC ($1 < \eta < 3$) showing the reach to $x_g \sim 10^{-3}$. Double longitudinal spin asymmetry as a function of photon x_g (left). Δg (right).

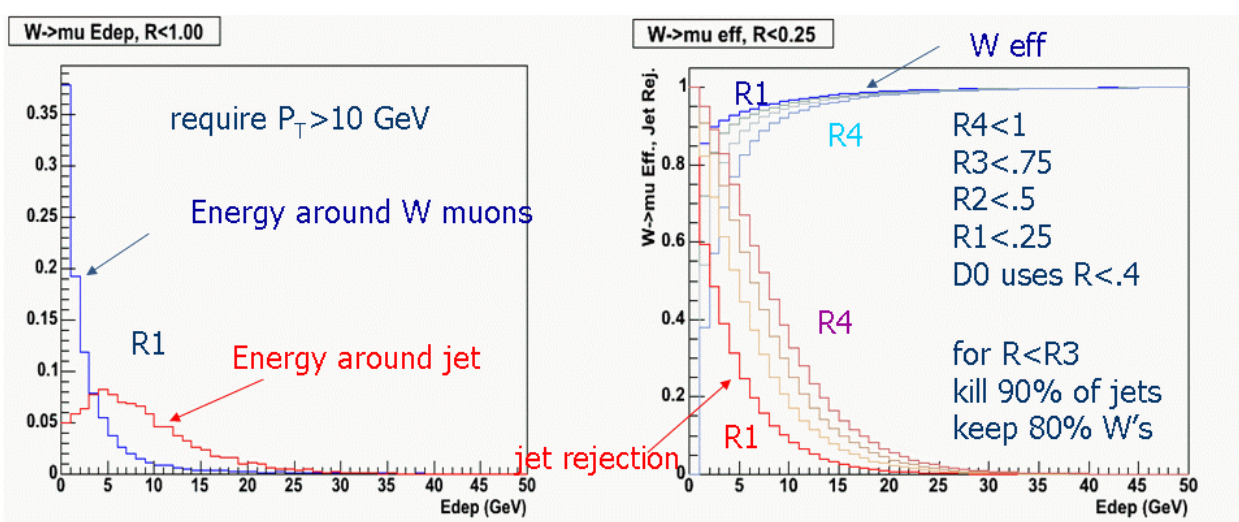

Figure B.16: (left) energy deposited around the muon in W events and jet events. (right) Suppression of background via isolation cuts.

B.4 Looking for a Colored Glass Condensate - a Simple Model

As an exercise, a model of the saturated gluon function [81] was used to understand what one might see in the simplest cases for the direct photon signal in d+Au collisions. Other models are now on the market with parameterizations that can used for such studies. However, the GBW model is simple in that it simply flattened out the Gluon distribution below some value of x, depending on the value of the saturation scale for the particular centrality and rapidity in question. Fig. B.17 shows an example.

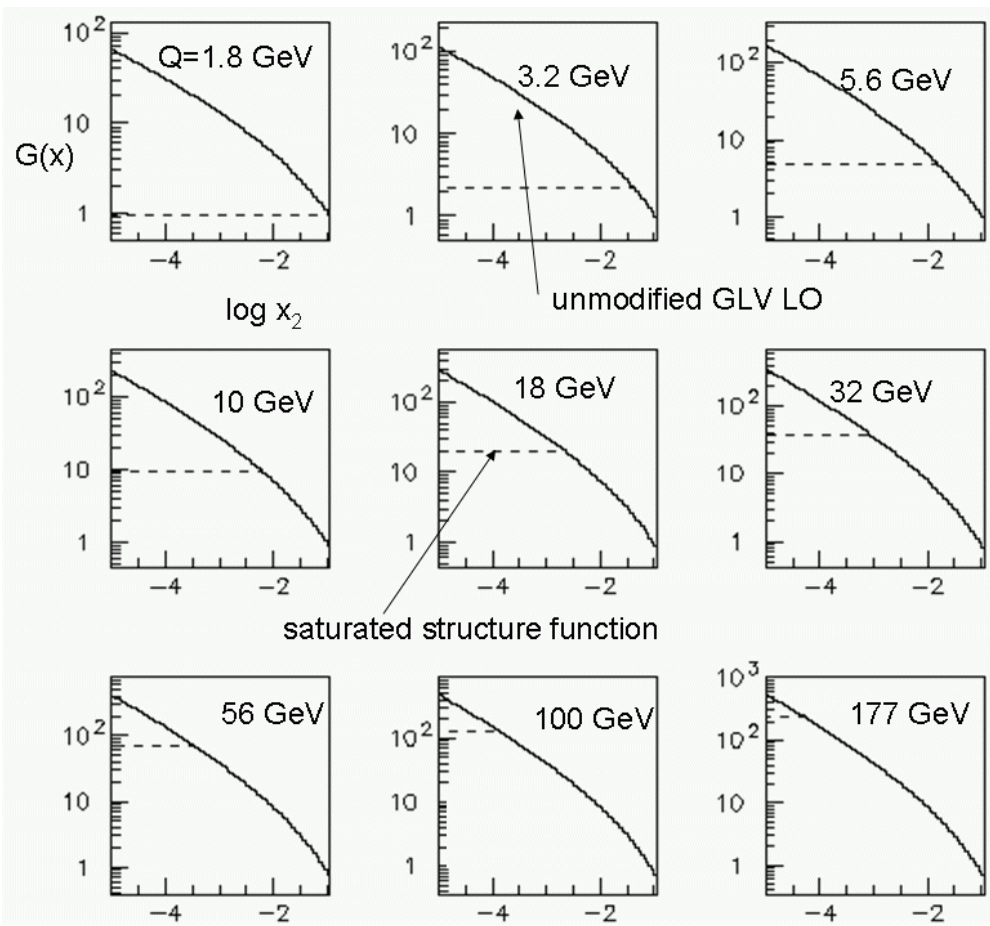

Figure B.17: Modified gluon structure function

R_{dAu} was then generated with these new distributions and checked against the measured values of R_{dAu} as measured by the PHENIX and Brahms collaborations for consistency. R_{pA} is defined similarly to R_{AA}

$$R_{pA} = \frac{dN_{pA}}{< N_{coll} > \times dN_{pp}} \tag{B.1}$$

where dN_{pA} is the differential yield for a point-like process in a p+A collision, and dN_{pp} is the differential yield for the same process in nucleon-nucleon collisions. The new gluon

distributions were then used in Pythia for the production of direct photon events and a ratio R_{pA} was constructed from the simulated data. Note that in Pythia there is no Cronin enhancement. Fig. B.18 shows R_{pA} as a function of η in various bins of p_T.

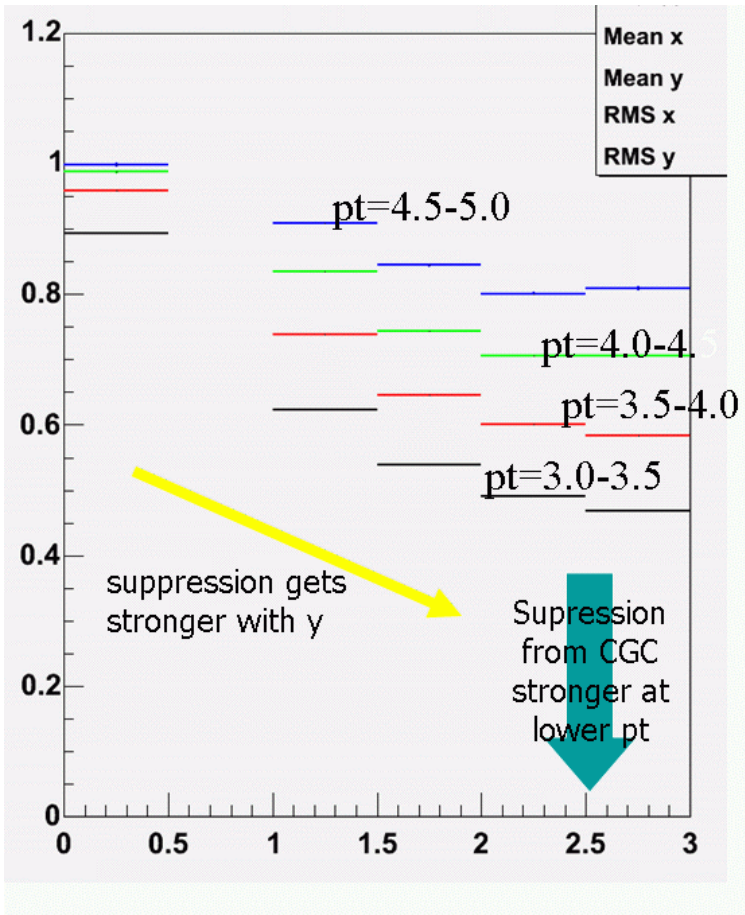

Figure B.18: R_{pA} shown as a function of η for various values of pt using a particular modified gluon structure function [81].

There are two characteristics that one sees: (1) The suppression increases for increasing rapidity, which makes sense because forward rapidity implies lower x. (2) The suppression is stronger at low p_T.

B.5 A Simulation Study of the Reaction Plane by the NCC

When two nuclei collide slightly off-center, the initial high-density volume has the shape of their overlap region during the collision. That region is elongated along an axis perpendicular to the reaction plane–that is, the plane defined by the beam direction and the line between the centers of the two nuclei as they collide. This asymmetry gives a natural way to vary the distance a parton travels in the collision volume before escaping. Using the correlated direct photon-high p_T particle measurements versus the reaction plane will give information on the energy loss as a function of the distance traveled in the medium. A measure of the reaction plane resolution is $< cos\psi >$ where $< cos\psi >$ is the correction factor of the reaction plane resolution and is simply called the "reaction plane resolution". Measurements are as a function of reaction plane are diluted by a factor $(\frac{1}{<cos\psi>})^2$. Hence larger values of $< cos\psi >$ refer to a better reaction plane resolution. Present measurements using the Beam-Beam counters have a reaction plane resolution of $< cos\psi >$=0.4. A reaction plane detector is being proposed to increase this to $< cos\psi >$=0.7. The NCC will have a reaction plane resolution $< cos\psi >$=0.9. The following explains the simulation work to obtain this resolution.

The NCC detector is defined and installed in PISA GEANT simulation to replace the entire nosecone. Using the given geometry, a single particle simulation with charged and neutral pion was performed to prepare a mapping file, which covers full phase space (rapidity, p_T, ϕ) with uniform distribution. The mapping file is then used in the 2nd step of simulation, which include realistic multiplicity (charged pion and π^0) and flow (v_2) depending on the p_T and rapidity. Therefore, the backgrounds from other detector elements as well as NCC itself are included. Fig. B.19 shows an overlay of several single track events.

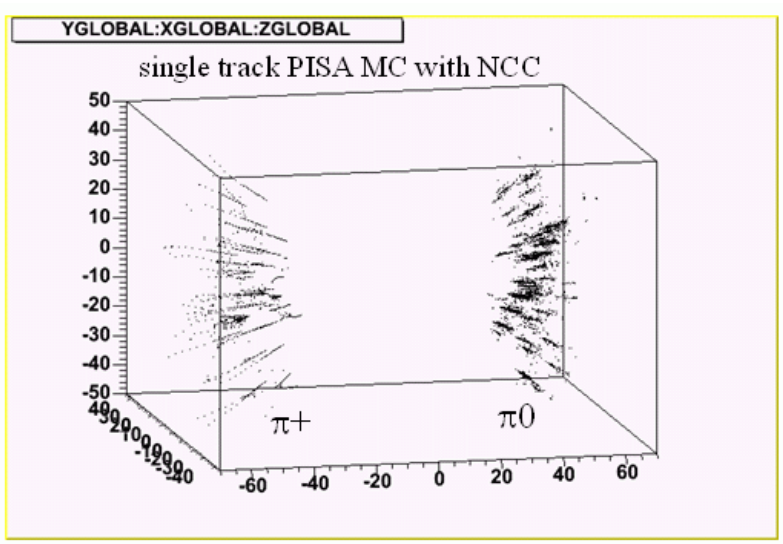

Figure B.19: An overlay of GEANT events in the NCC

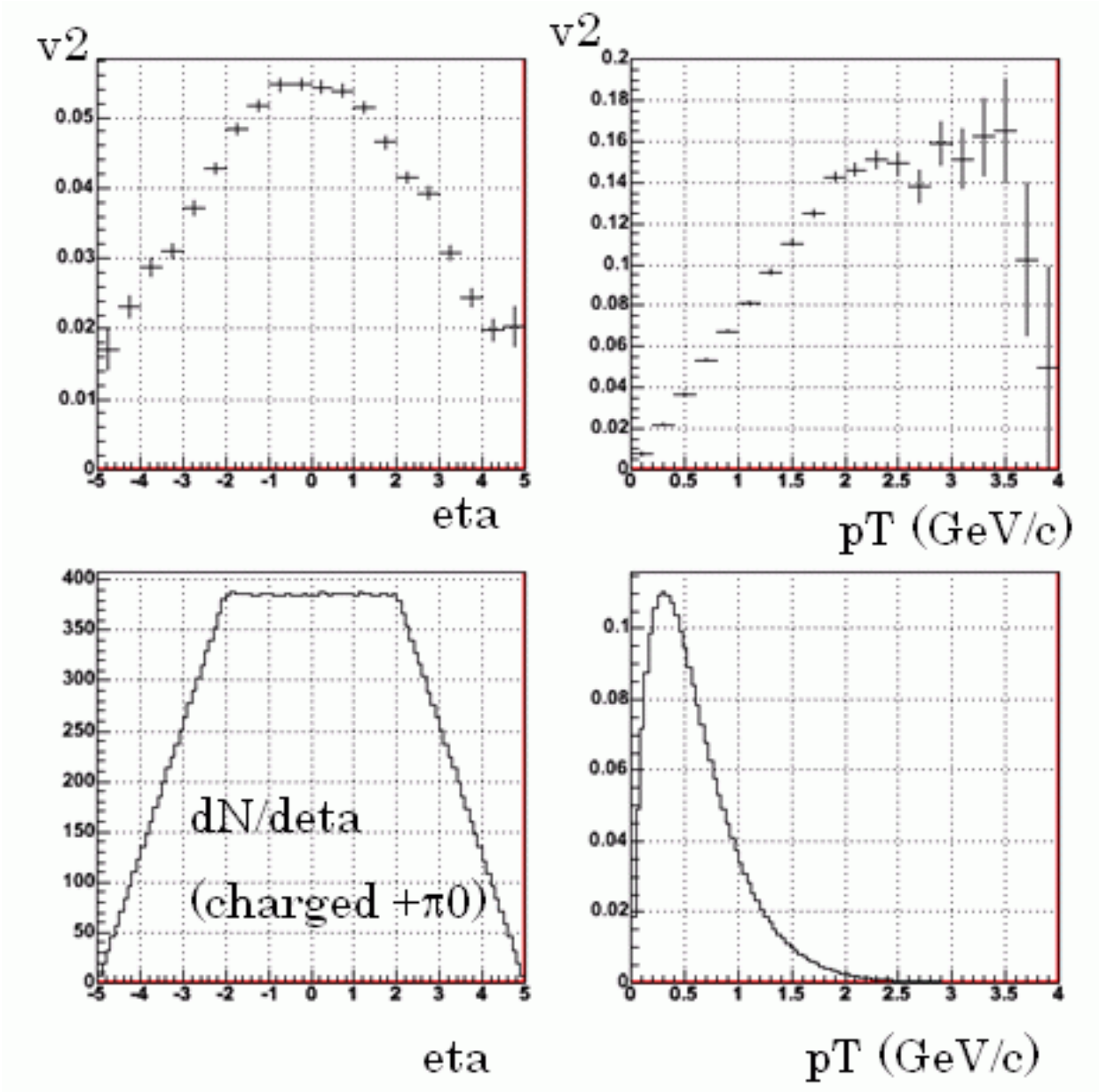

Figure B.20: Input flow (v_2) values as a function of η and p_T used in the simulation [top two panels]. η and $p_T$distributions used in the simulation [bottom two panels].

Input flow values and multiplicity used in the 2nd step of simulation are shown in Fig. B.20. The top 3 panels in Fig. B.21 show the hit position in x-y on the NCC detector for 3 different z sectors, the first electro-magnetic sector (EM1) and the second electro-magnetic sector (EM2) after SM ID strip layer and the third hadronic sector (HAD). The radial hit distribution, azimuthal hit distribution with respect to the generated primary track and azimuthal hit distribution with respect to the simulated reaction plane orientation are shown in the bottom three panels in Fig. B.21.

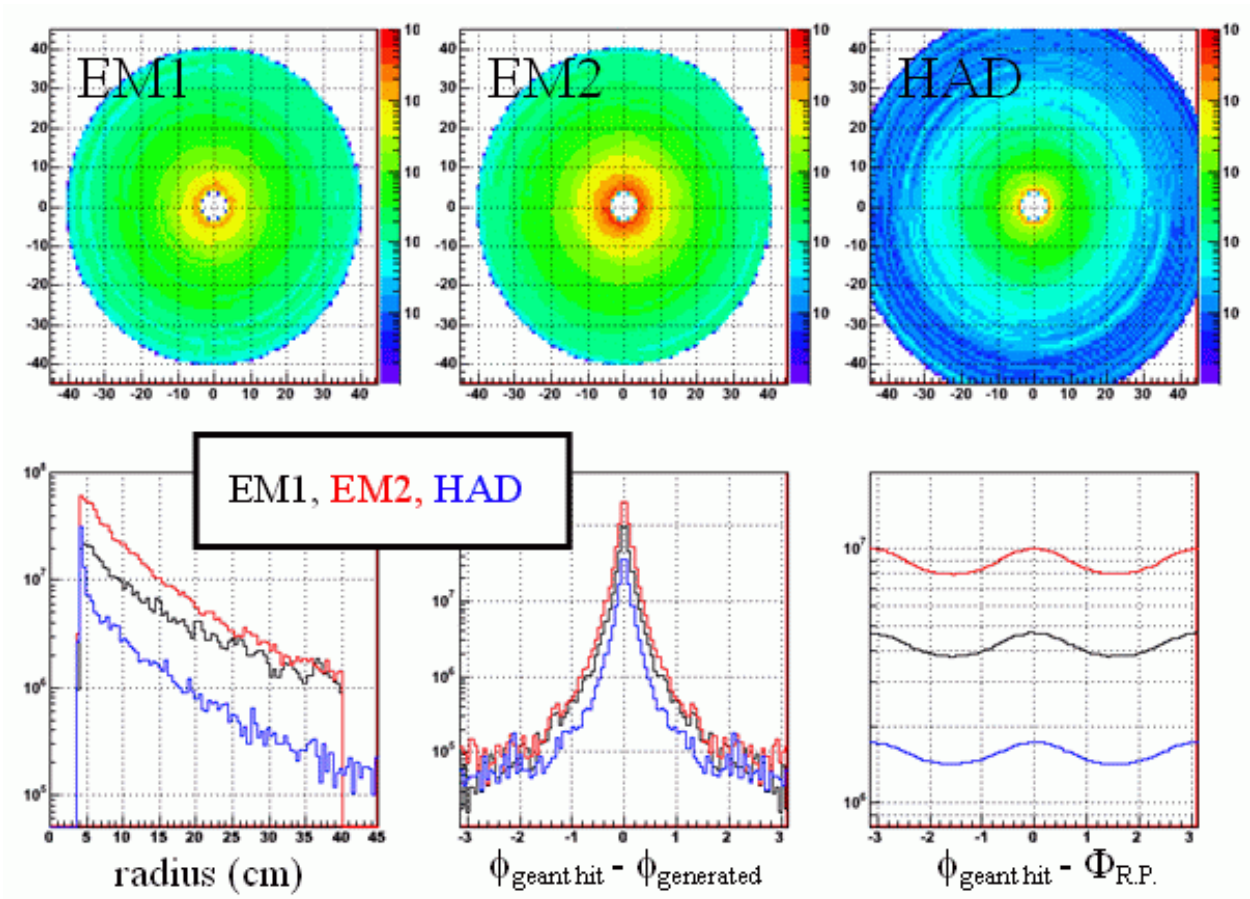

Figure B.21: Hit position in x-y on the NCC detector for in EM1, EM2, and HAD(top 3 panels). Radial hit distribution, azimuthal hit distribution with respect to the generated primary track and azimuthal hit distribution with respect to the simulated reaction plane orientation(bottom 3 panels).

Fig. B.22 shows the reaction plane distribution ($\Phi_{calc} - \Phi_{true}$) with different weighting methods described in the figure caption. The bottom panel shows the reaction plane resolution with different cases as described in the figure caption. The resolution goes up from about 0.8 in the case (2) with charged particle alone to about 0.9 case (7) by including $\pi 0$ conversion, dE/dx weighting and optimizing the weight. The three regions in the bottom panel show the radial dependence of the reaction plane resolution for each z sector, the pink dashed lines show parameterized function of radial dependence of resolution, which is used to weight each reaction plane to get the best resolution in the case (7).

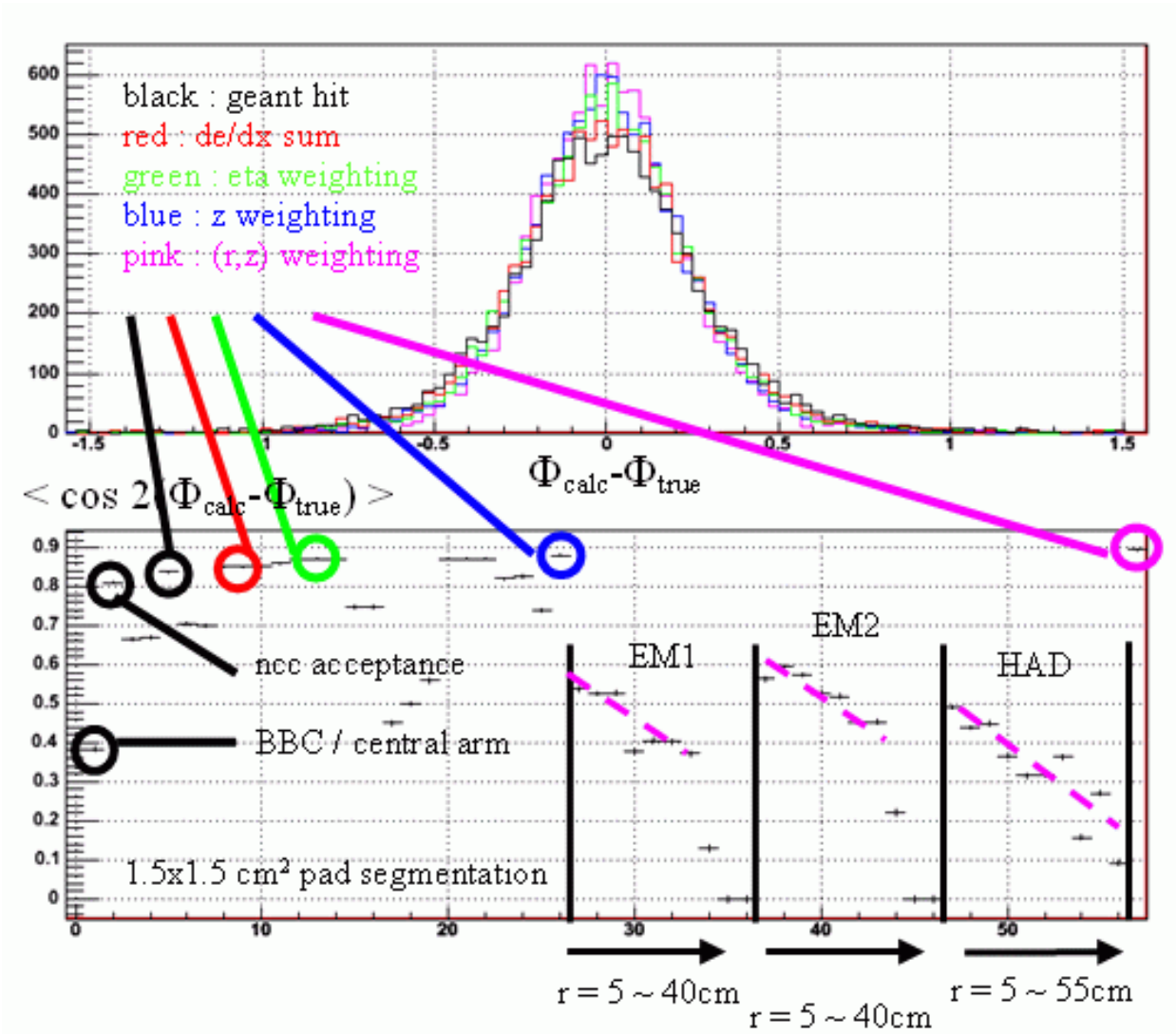

Figure B.22: (top) The reaction plane distribution ($\Phi_{calc} - \Phi_{true}$) with different weighting methods. (Bottom) Reaction plane resolution for different cases, where the conditions marked with circle are described in the following. (1:black) BBC or central arm reaction plane resolution is about 0.4, (2:black) use all charged particles in NCC acceptance, (3:black) use all GEANT hits in NCC, (4:red) weighting all the GEANT hits with dE/dx, (5:green) v2 weighting according to eta dependence of v2 in addition to (4), (6:blue) z sector depending weight in addition to (5), (7:pink) 2 dimensional r, z weight in addition to (5). The resolution goes up from about 0.8 in the case (2) with charged particle alone to about 0.9 case (7) by including π^0 conversion, dE/dx weighting and optimizing the weight.

B.6 Muons and Background

In addition to the topics covered in the main text, the NCC can be used together with other detectors to solve some problems - in this case the identification of muons.

The major sources of hard muons are

1. the semi-leptonic decay of heavy flavored quarks in the intermediate p_T (transverse momentum) range of $2 \sim 15$ (GeV/c),

2. the decays of W bosons above very high p_T of above 20 (GeV/c).

Heavy flavor production and W boson productions at RHIC are of great interest. As an example, the major focus of the ongoing muon trigger upgrade is to understand spin structure of the protons through very high p_T muon measurement. With the luminosity upgrade and the muon trigger upgrade, we will reach very high p_T regime beyond our current statistical limit.

Beyond the statistical limitation, one of the major challenges in achieving high p_T muon measurement is a fake high p_T background. The background originates from a small fraction of the soft light hadrons, $\pi^{\pm}$ and $K^{\pm}$ which penetrate the front absorber composed of the NCC and magnet yoke, and subsequently decay into muons between muon tracking station 1 and station 3 , and are reconstructed by chance. The rigidities of the reconstructed trajectories are determined by the bend angle between tracking station 1 and tracking station 3. Decays can fool this rigidity determination and generate seemingly hard tracks with a rare, but significant occurrences. Fig. B.23 shows the reconstructed p_T distribution from various p_T ranges of the light hadrons generated with realistic multiplicity for p+p collisions at $\sqrt{s} = 500GeV$. For each range, a small fraction (10^{-3} to 10^{-4}) contributes to the fake hard p_T distribution. Due to the large multiplicity, low p_T hadrons dominate the real muon contribution from W decays even at very high p_T.

The NCC is positioned between the collision location and the tracking station 1, and measures crossing locations of the reconstructed trajectories at the accuracy of about 150 μm at two independent planes - PS and SM. While real high p_T tracks travel along a straight line trajectory between the collision location and the tracking station 1, fake high p_T tracks do so with large deflections inversely proportional to the momenta. So, for a chosen momentum or p_T, we can select a narrow window of possible deflection ranges and reject fake high p_T tracks with large deflections my matching hits in the PS or SM of the NCC. Fig. B.24 shows the reconstructed p_T distribution similar to Fig. B.23, but with a window optimized for $p_T \sim 25$ (GeV/c). According to a preliminary study, the finite NCC occupancy in p+p collisions at $\sqrt{s} = 500$ GeV does not degrades the performance, but performance degradation due to the large occupancy in Au+Au collisions must be investigated.

In conclusion, nose cone calorimeter (NCC) can reject fake high p_T tracks effectively, and will help prompt muon measurements.

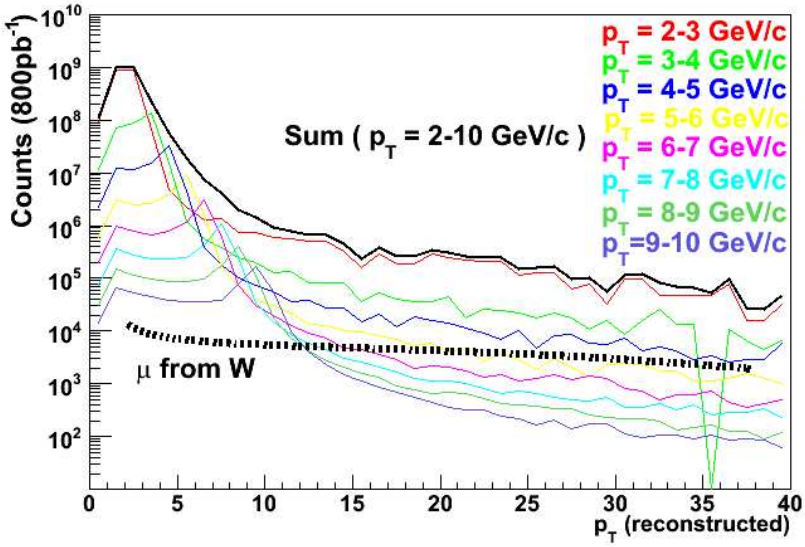

Figure B.23: . Reconstructed p_T distribution from various p_T intervals of produced light hadrons. Muons from W boson decays are also shown.

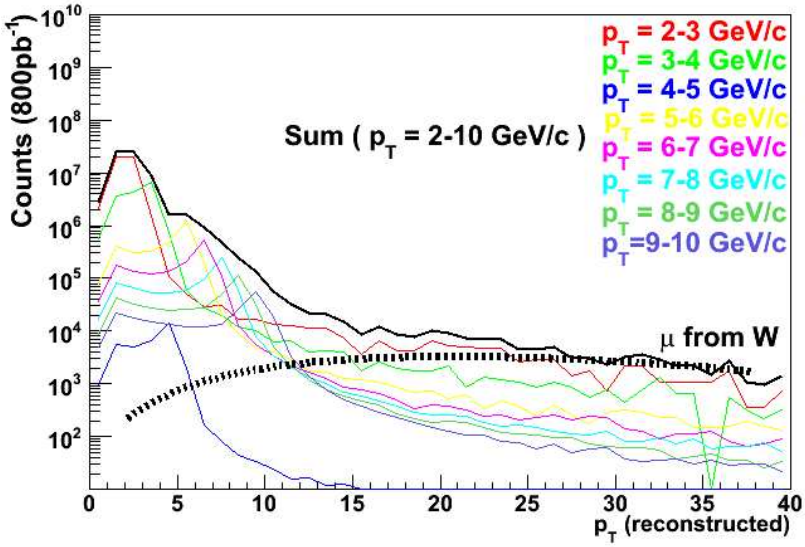

Figure B.24: Distribution similar to Fig. B.23, but with the background suppression by matching tracks from the muon spectrometer to the NCC.

Appendix C

Test Beam Results

The prototype NCC was designed as a proof-of-principle device for the Collaboration to acquire the experience in silicon detector production, and to test at least one possible assembly scheme and the robustness of technology. The prototype calorimeter was designed of 22 sampling layers, with the first 16 cells grouped into 6 cell and 10 cell segments. These were designed as the as electromagnetic segments (2.5 mm W + 2.5 mm readout). The last 6 cells (15 mm W and 2.5 mm readout) serving as a hadronic segment. The calorimeter was built to allow installation up to 4 sensors per layer (12x12 cm^2). We used one position in every layer to install prototype DC coupled sensors. Fig. C.1 is the photograph of a single assembled ROU (readout unit) connected to the preamplifier board.

In actual test beam experiment we used preamplifier boards developed at MSU and equipped with CR1P4 16 channels preamplifier chips provided by A.Vacchi (Trieste, Italy). To make an optimal use of available electronics the number of geometrically matching pads from individual layers ganged together was limited to 4 thus resulting in prototype being segmented into 6 longitudinal segments (4 fine and 2 ccoarse). Ganged and amplified signals were digitized using off-the-shelf multi-channel ADC unit. The assembled prototype is shown in Fig. C.2.

The prototype calorimeter was exposed to the electron and proton beams from IHEP U70 proton synchrotron in Protvino (Russia) in November 2005. In what follows we present data accumulated exposing the calorimeter to 70 GeV/c protons and 10 GeV/c positrons.

C.1 Data analysis

The amplitude distributions recorded in proton runs were used to establish values of the pedestals, the shape of the signal, minimum ionizing peak values and the signal/background ratio. The result is illustrated in Fig. C.3 which shows the pedestal and MIP signal. The signal/noise ratio is 4-5 with (for comparison we expect it to be ∼40 in a real detector) a good MIP resolution.

In the electron analisys the individual pedestals computed using data from proton run were subtracted to get signal amplitudes in every segment. MIP peak varied segment-to-segment but was nearly independent of hit position in the plane. The recorded data are

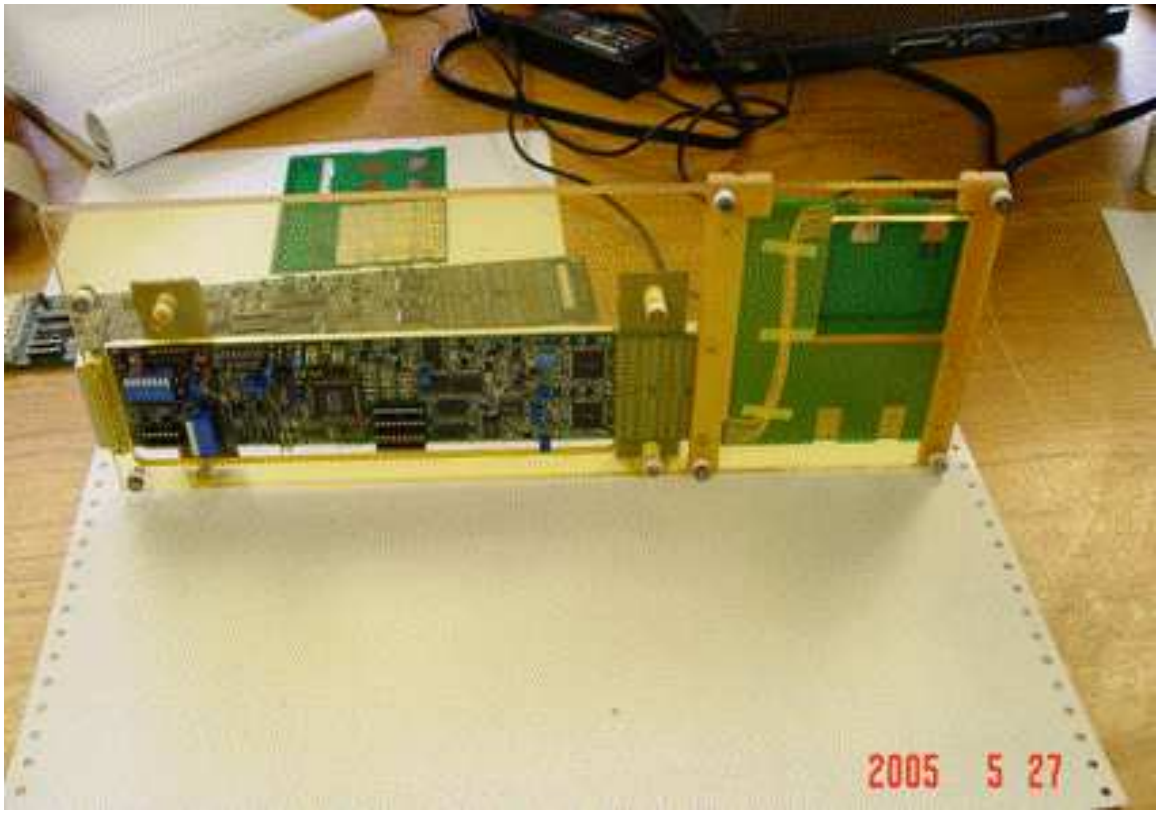

Figure C.1: Single assembled readout layer for the prototype NCC connected to readout electronics.

strongly affected by a common mode noise. Pads outside the base matrix of 3x3 towers centered at the tower with maximum amplitude were used to measure the common mode noise value which was subtracted from all 16 measured amplitudes prior to normalization. In addition the following cuts were applied to clean the data of hadronic contamination present in the electron beam:

- Amplitude sum in segment 1 was required to be smaller then amplitude sum in segment 2 (to exclude tails of showers started upstream of the prototype detector),.
- Amplitude sum in segment 1 was required to be smaller then 600 cnts (to exclude events with multiple hits).

.

A typical event in the prototype calorimeter exposed to positrons of 10 GeV/c momenta cleaned of common mode noise is shown in Fig. C.4.

Average energy in the segment when exposed to positrons is plotted as function of the calorimeter depth at the geometrical center of the segment in Fig. C.5.

The observed behavior is consistent with the expected electromagnetic shower shape. The maximum in the distribution of deposited energy is reached at a depth of $\sim 7\ X_0$ in the calorimeter.

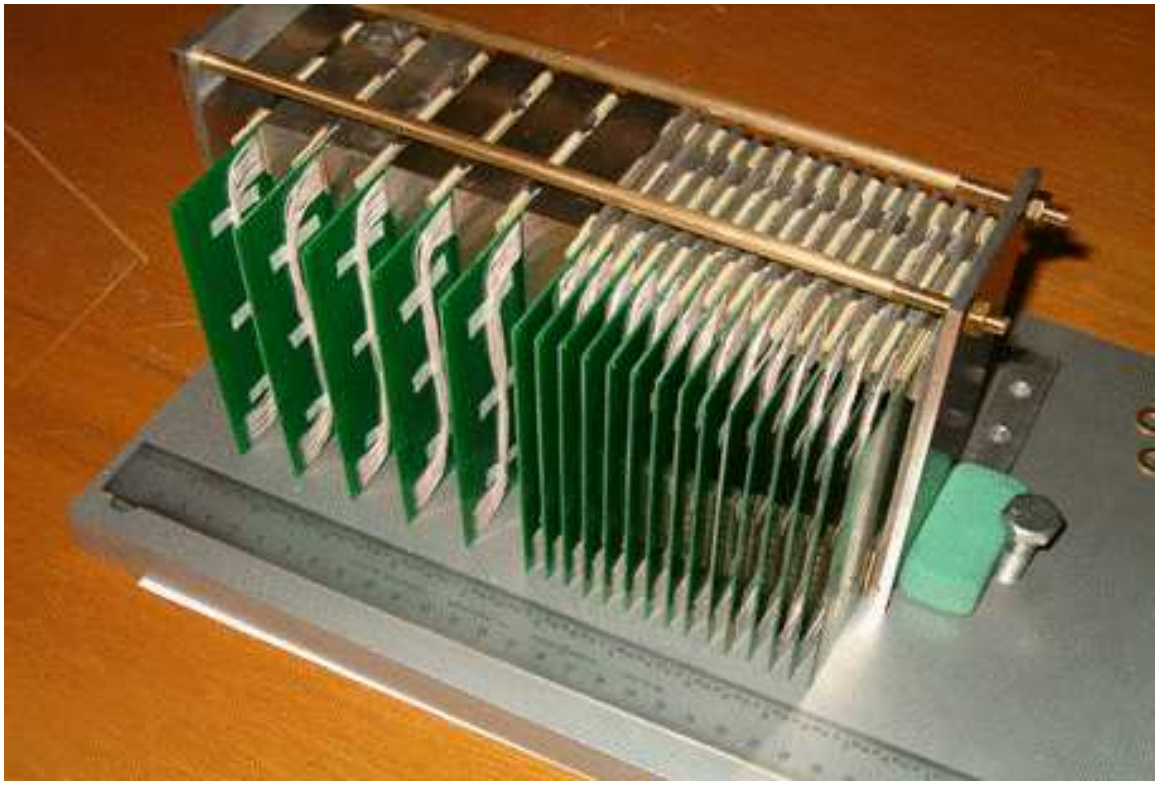

Figure C.2: Assembled prototype calorimeter. Readout electronics not shown.

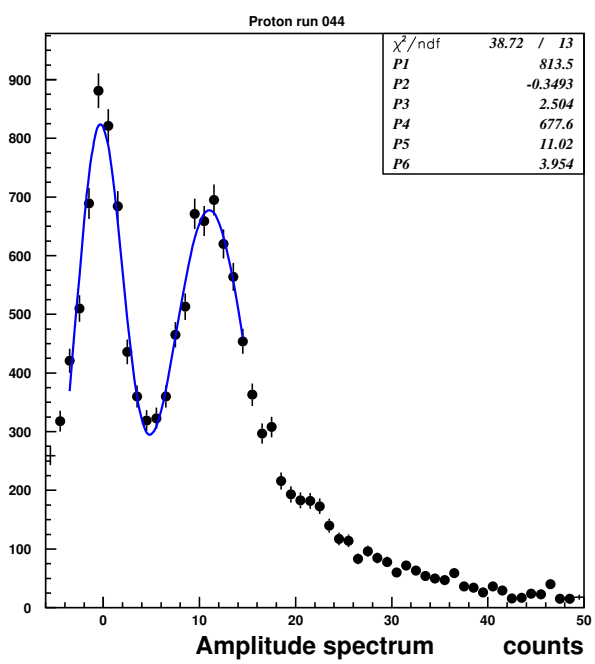

Figure C.3: Amplitude distribution of the signal from the pad near beam impact.

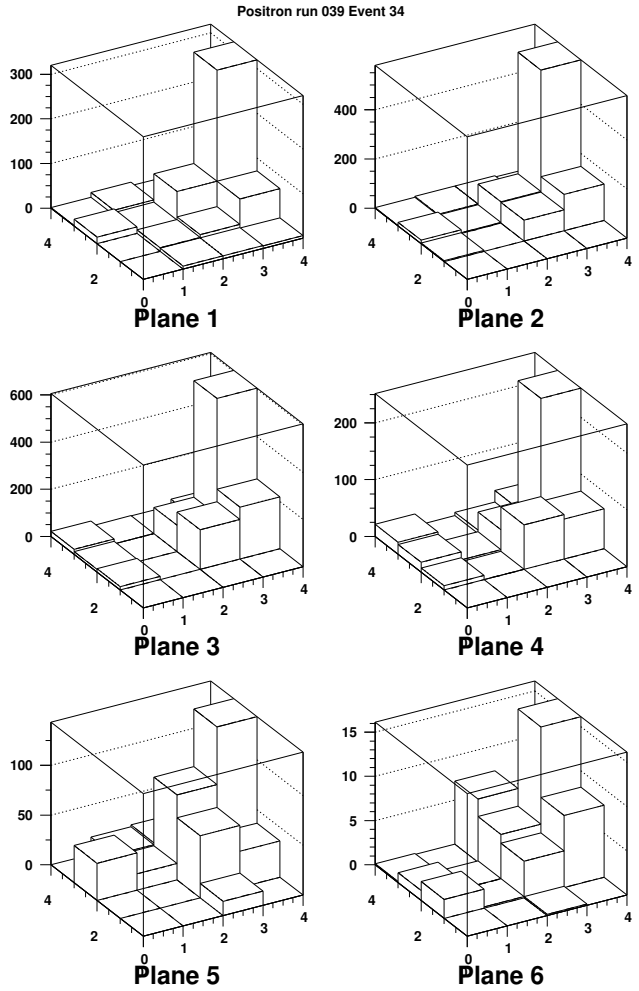

Figure C.4: Example of the electromagnetic shower in prototype W-Si calorimeter

The mean longitudinal profile was fitted with the functional form $k \times X_0^{(a-1)} \times \exp -bt$ which describes the data with good accuracy.

In order to improve the experimental resolution an additional weighting procedure based upon measured longitudinal shower shape was applied to positron data. The final distribution of the weighted amplitude sum is shown in Fig. C.6. The data were fitted by sum of the Gaussian peak and polynomial background resulting in measured resolution of 11% (90% CL) for the 10 GeV/c positron beam consistent with predictions in earlier chapters of this CDR i.e. $\sim \frac{20\%}{\sqrt{(E)}} + 4\%$.

The positron data recorded in every segment of the prototype were further used to study the dependence of position resolution measured in individual segments on the depth position of the segment in calorimeter. In the absence of beam tracking resolution was computed subtracting measured coordinates from those computed using straight line fit to all six measured

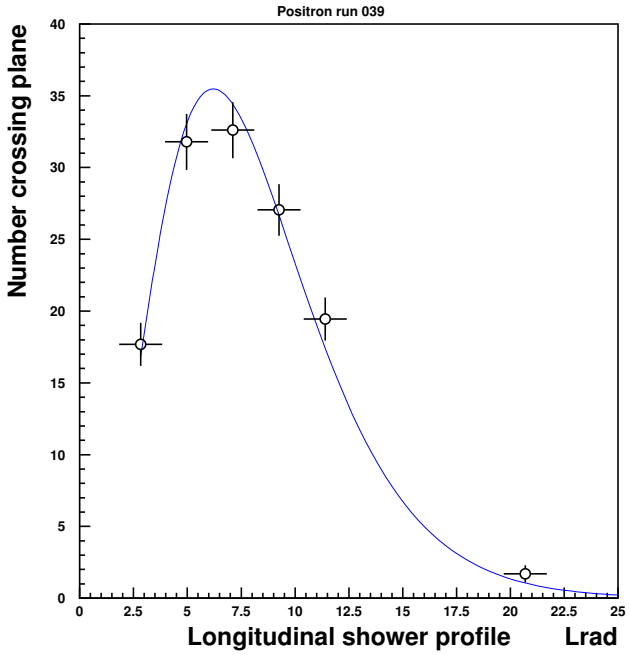

Figure C.5: Longitudinal profile of electromagnetic shower.

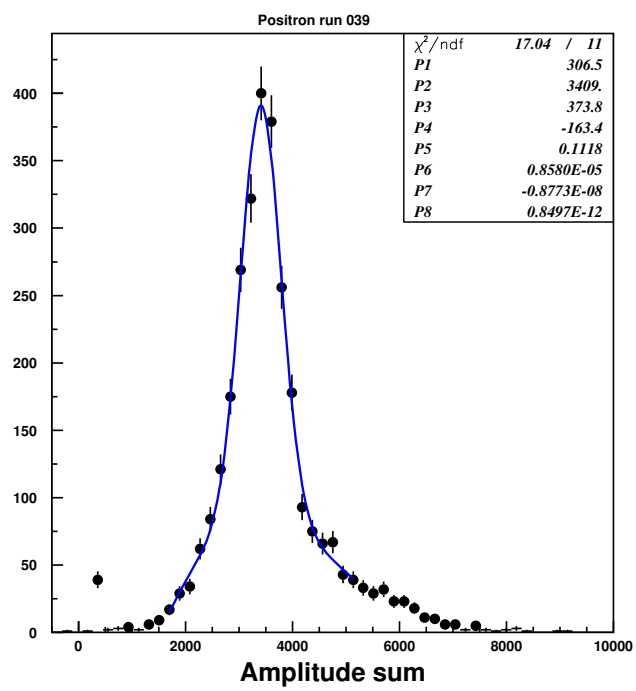

Figure C.6: Energy distribution in the NCC prototype measured exposing detector to 10 GeV/c positron beam.

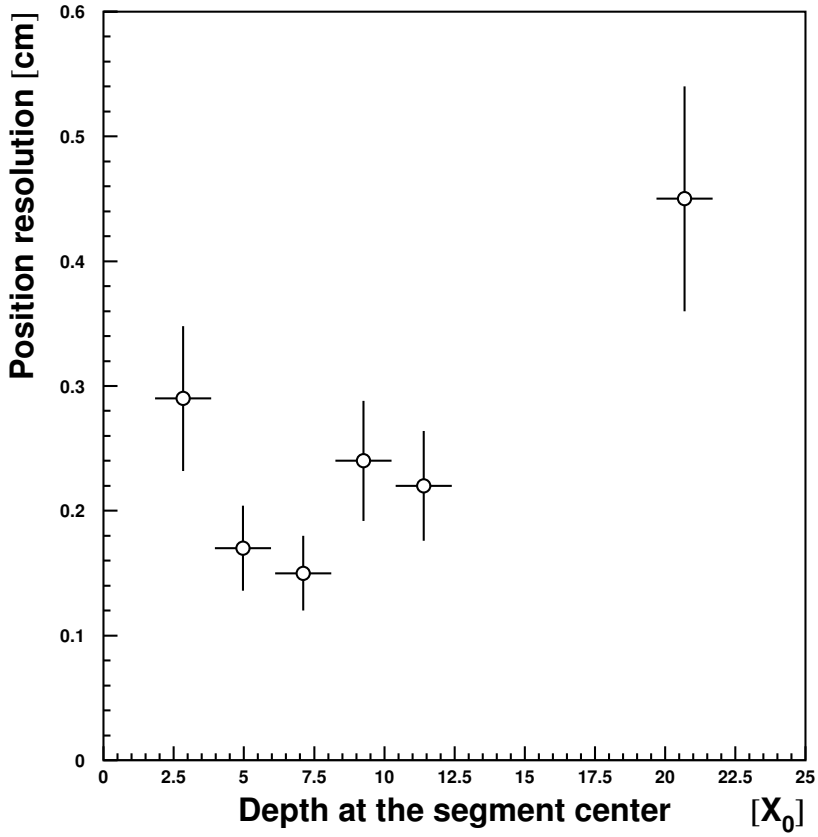

Figure C.7: Precision of the impact point measurements in the segments of prototype detector. Location of the segment geometrical center in the prototype is plotted along X in units of X_0.

points (see Fig. C.7).

As expected the best result ($\sigma = 1.4mm$) at 10 GeV is reached using data from segment next to shower maximum. Combining all 6 points we may estimate the pointing resolution of prototype calorimeter (Fig. C.8)

A value ∼6 mrad was measured in X- and Y- planes what corresponds to pointing resolution $\sim 9mrad$ corresponding to 5mm resolution in impact parameter with respect to collision vertex.

The pointing capability is a byproduct of longitudinal segmentation introduced as an only tool available to forward physics in PHENIX to remove hadronic contamination from the photon sample. While probably non critical, this nice feature may be important in reducing contamination from non-beam sources like cosmic rays which are important background to photons with very high momenta.

Finally in Fig. C.7 we show the 3-d plot illustrating particle identification capabilities of a calorimeter with proposed longitudinal segmentation. Each shower is represented by

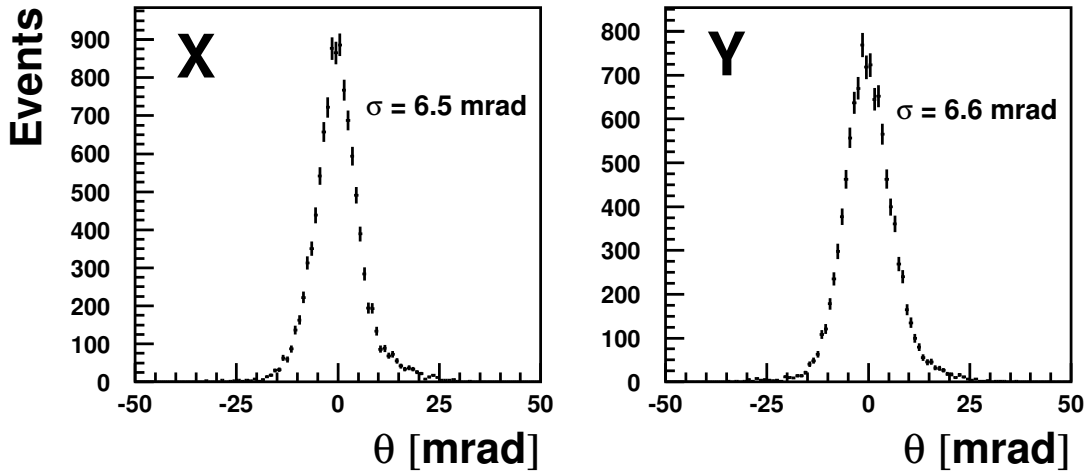

Figure C.8: Pointing resolution measured in the prototype calorimeter exposed to 10 GeV/c positrons. Both X- and Y- planes are shown.

a point in 3d-space: E_1/E_{Tot}, E_2/E_{Tot}, E_3/E_{Tot} where E_1, E_2, E_3 are energies measured in properly combined calorimeter segments. Red points are 10 GeV/c electrons, blue points are 70 GeV/c protons. Two sets of points are well separated.

In conclusion we would like to emphasize the following: the construction of of the prototype and its exposure in the particle beam was probably the most important achievement of our initial R&D efforts. It proved

- the robustness of technology,
- the soundness of the idea to passively sum signals from multiple Si pixels,
- the ability to handle and calibrate data from longitudinally segmented calorimeter,
- the ability of simulation to correctly predict detector performance,
- the ability of a collaboration which has a very brief prehistory and is composed of institutions from all over the world to coordinate its efforts and reach the desired goals.

Very positive results of this project were very encouraging and gave us a great hope that we'll be able to reach similar success with design and prototyping of a real detector and as well as with construction project.

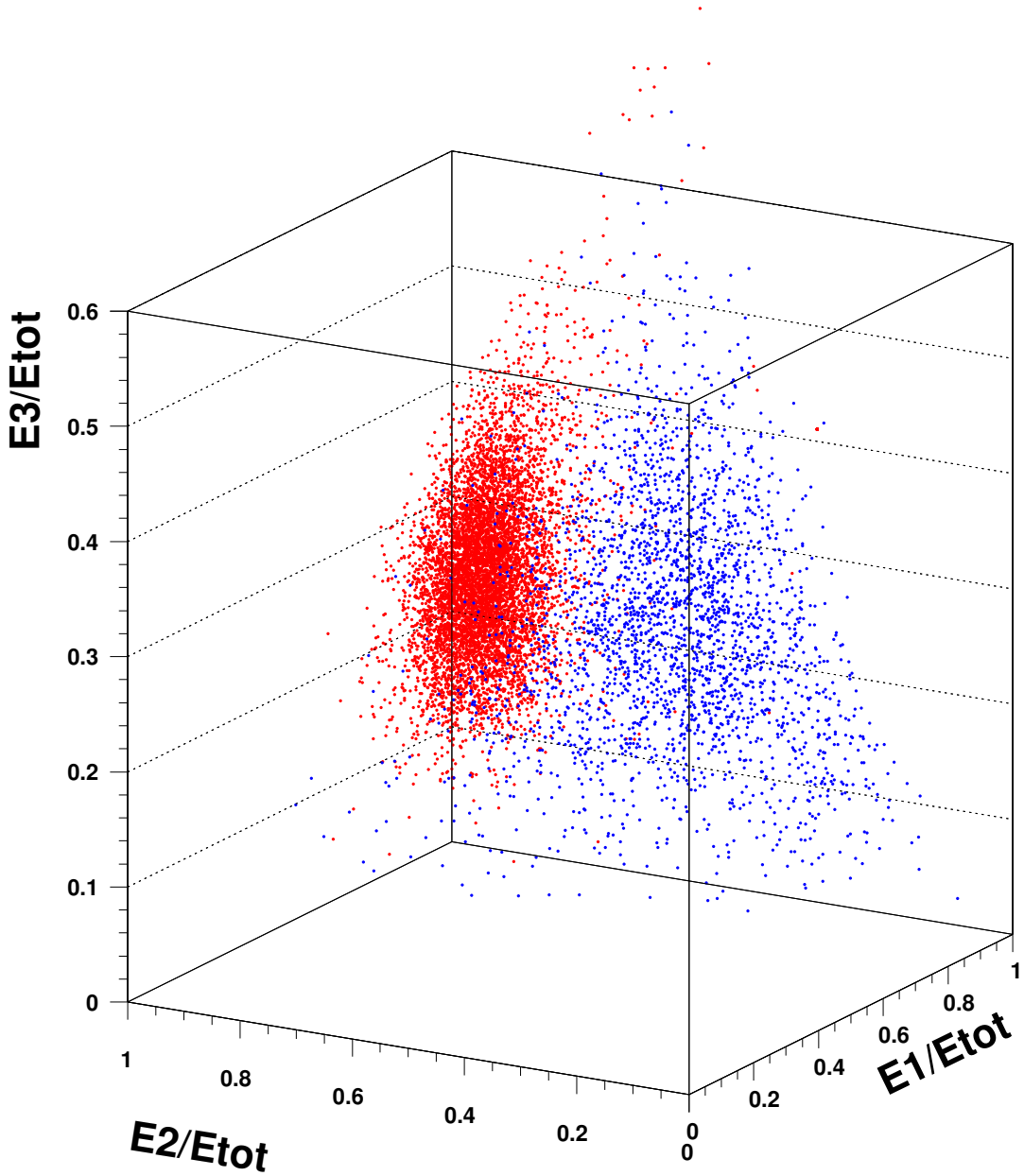

Figure C.9: Shower identification in longitudinally segmented calorimeter. E_1, E_2, E_3 are energies measured in calorimeter segments, E_{Total} is the total energy. Red points are 10 GeV/c electrons, blue points are 70 GeV/c protons.

Appendix D

Sensor Research and Development

Test pad-structured DC coupled silicon sensors were produced at the ELMA subsidery of the Research Institute of Material Science and Technology (RIMST), Moscow, and delivered to our collaborators laboratory at MSU. Following the prescriptions discussed earlier in this document, these test sensors were optimized for radiation hardness. The design was largely influenced by previous experience at MSU (pad-structured sensors for CALICE W-Si calorimeter prototype). The actual sensor picture together with the guard-ring structure are shown in Fig. D.1. The 5kΩ, 300 μm thick FZ- wafers from Wacker (Germany) available at MSU were used for this submission. In total 30 sensors were produced, IV and CV measurements at MSU resulted in 25 sensors accepted and 5 sensors rejected (large leakage currents). Results of the depletion voltage (CV) and leakage current (IV) measurements are shown in Fig. D.2.

Both yield of the good detectors and performance are satisfactory, good sensors were used to build a proof-of-principle NCC prototype later tested in the test beam in Protvino, Russia (IHEP).

As part of the R&D efforts we also tested a number of extreme options illustrated in Fig. D.3 (with decoupling RC networks on and partially on sensors).

The sensors with built-in RC networks are the good option for detectors itended for mass use, they are easy to test and do need a minimal set of external passive components for connection to preamplifiers. Unfortunately this technology routinely results in increased cost and reduced yield associated with extra steps required to grow large capacitances on pad surfaces. In addition it leaves no choice but using detectors with bias voltage applied to the common side. In case of PHENIX NCC where individual pixels are ganged together to allow a single preamplifier to handle analog sum of the pixel currents the advantages of AC coupled design are not obvious at all, in fact it makes biasing sensors and insulating them from detector construction elements quite challenging. Our project was reviewed by the unofficial panel of Si detector experts at SiDet Laboratory at FNAL, the recommendation which we accepted were to either use DC coupled sensors or to limit the upgrades to growing polysilicon resistors on the sensors (keeping external decoupling capacitances). While no firm commitment was made at a time the modified design was proposed for considerations by ELMA, ON Semiconductors (Czech Republic) and SENS (Korea) companies. ON Semiconductors delivered test samples to our Collaborators in Prague for evaluation.

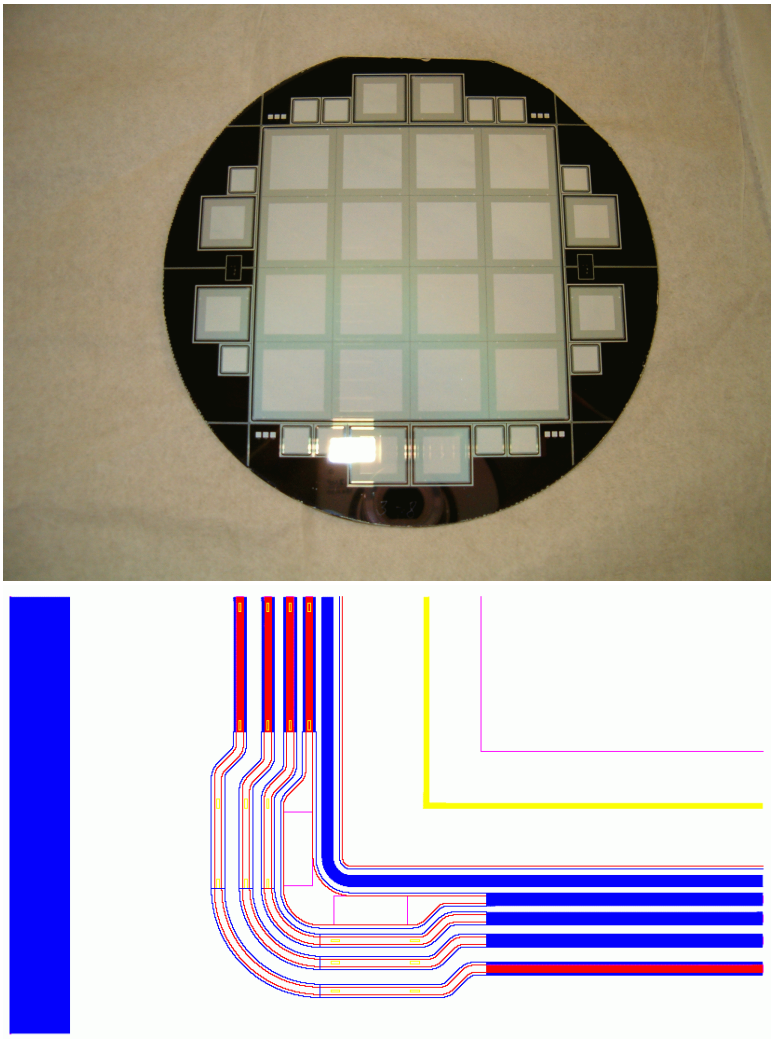

Figure D.1: NCC Silicon sensor. Undiced wafer is shown. Active area is subdivided into 16 readout pads 1.5x1.5 cm2 each. On the right is the structure of the guard rings. The complexity of he design is to prevent voltage breakdowns after radiation exposure.

The uniformity of resistanses was found to be better then 15% all other characteristics were found acceptable. The very first AC coupled sensors manufactured at ELMA were received at MSU and measured. Given a relatively low yield we decided not to pursue this option.

Within the same framework we began development work aimed to optimize the stripixel sensor design to NCC needs. This project has an obvious urgency: critical aspects of charge sharing and crosstalks between crossing strips are very difficult to simulate, final choice can't be made without prototyping variety of structures. The first prototype prototype wafers delivered from ELMA in Russia have shown expected behavior on test structures, the sensors themselves happened to be shortened because of the mismatch between design (made at BNL) and technology used at ELMA. New submission resulted in production of a few good wafers subjected to testing in Silicon Laboratory in JINR (Dubna).

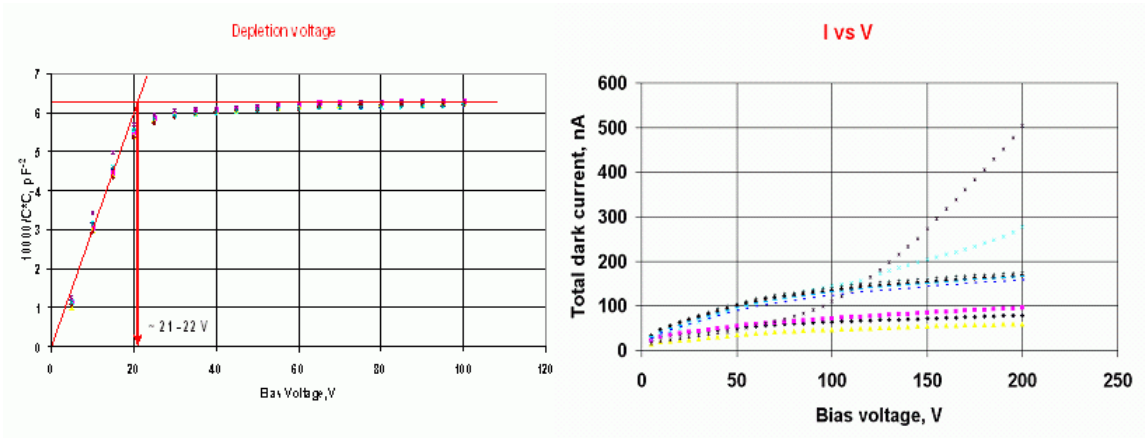

Figure D.2: CV and IV measurement data for the test batch of 30 PHENIX NCC pad-structured sensors produced at ELMA in Russia.

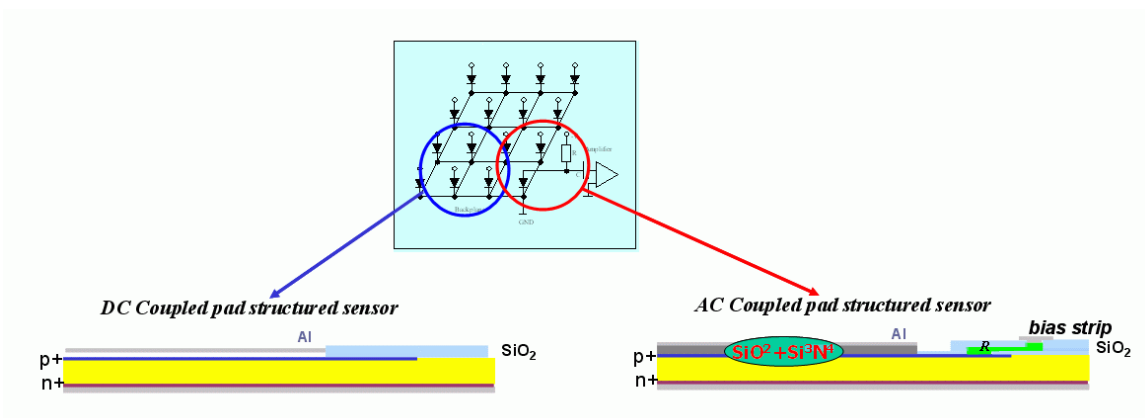

Figure D.3: Two designs for the pad-structured Si sensors. DC on the left and AC (decoupling capacitances and bias resistors are on sensor) on the right

The prototype Sensor were exposed to α-particles from 241Am (E=5.486 MeV) source. Reasonable (but very asymmetric) charge sharing between X and Y pixilated strips was measured.

The charge sharing is improving for the finer structures (min. interstrip separation tested is 15 m). Asymmetry in the charge sharing was traced to effect of implanted bridges. The high resistance of the implanted bridges caused asymmetrical signal degradation and excessive noise what makes them unacceptable. There are also hints of significant crosstalk between neighboring strips(capacitative coupling between p+ "wires" implanted into bulk n- silicon). Further results upcoming.

In many aspects available results from stripixel detector testing are still inconclusive. Observed problems are related to (a) technical difficulties in measuring simultaneously X and Y strips; (b) short path range of alpha particles; (c) multiple scattering of alpha particles in the air. A test with beta source would be crucial for final evaluation of stripixel sensors.

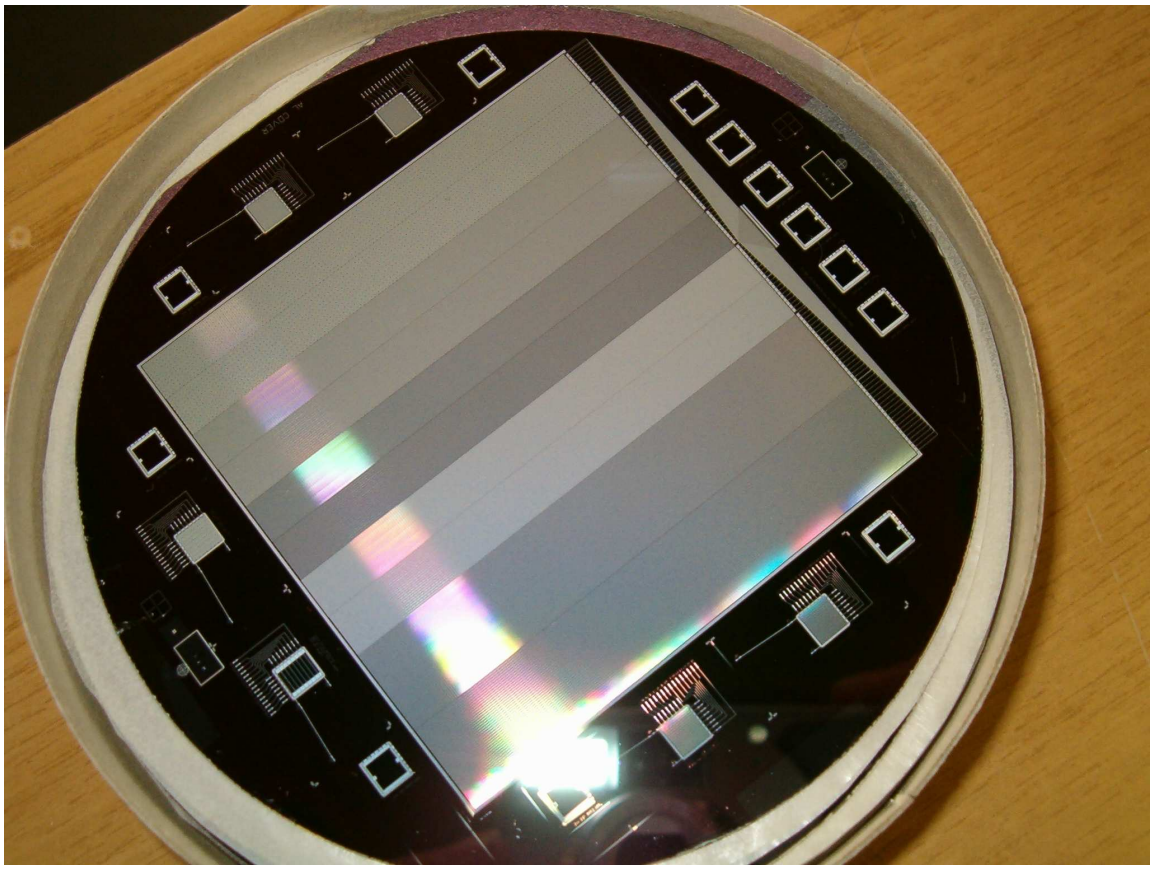

Figure D.4: Prototype wafer with 5 different stripixel structures bot X and Y directions. Technology:single-metal with implanted bridges in orthogonal direction.)

We have built a setup for irradiating stripixel sensors with beta particles. The setup consist of collimated source and two trigger counters in front of precisely movable table where the SRM module will be mounted. The measurements will start as soon as we will have stable stripixel readout functioning.

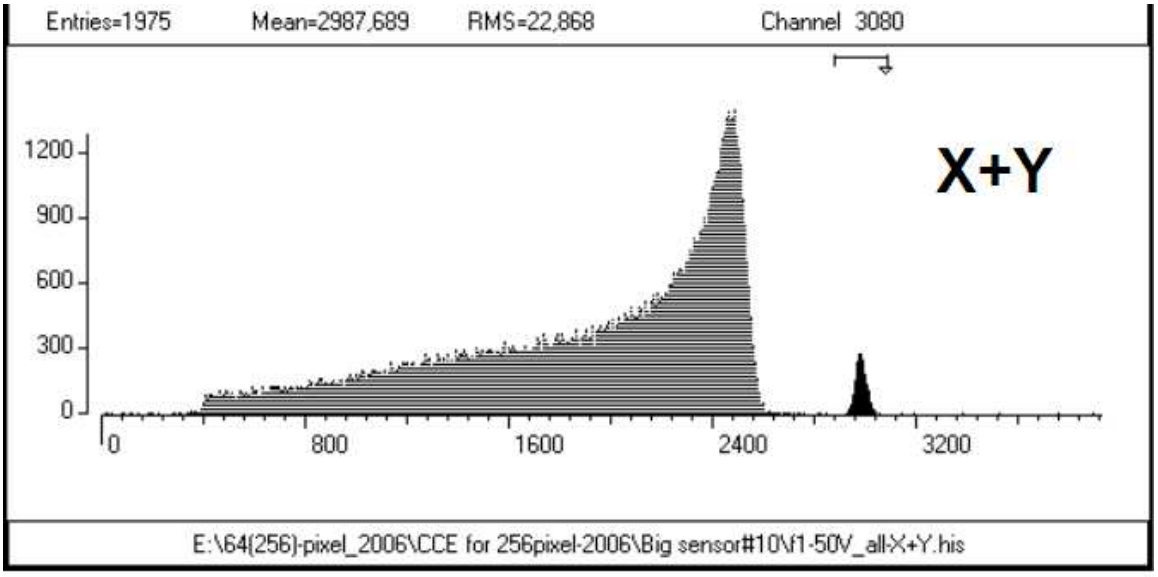
Entries=1975
Mean=2987,689
RMS=22,868
Channel 3080
X+Y
1200
900
600
300
0
0
800
1600
2400
3200
E:\64(256)-pixel_2006\CCE for 256pixel-2006\Big sensor#10\f1-50V_all-X+Y.his

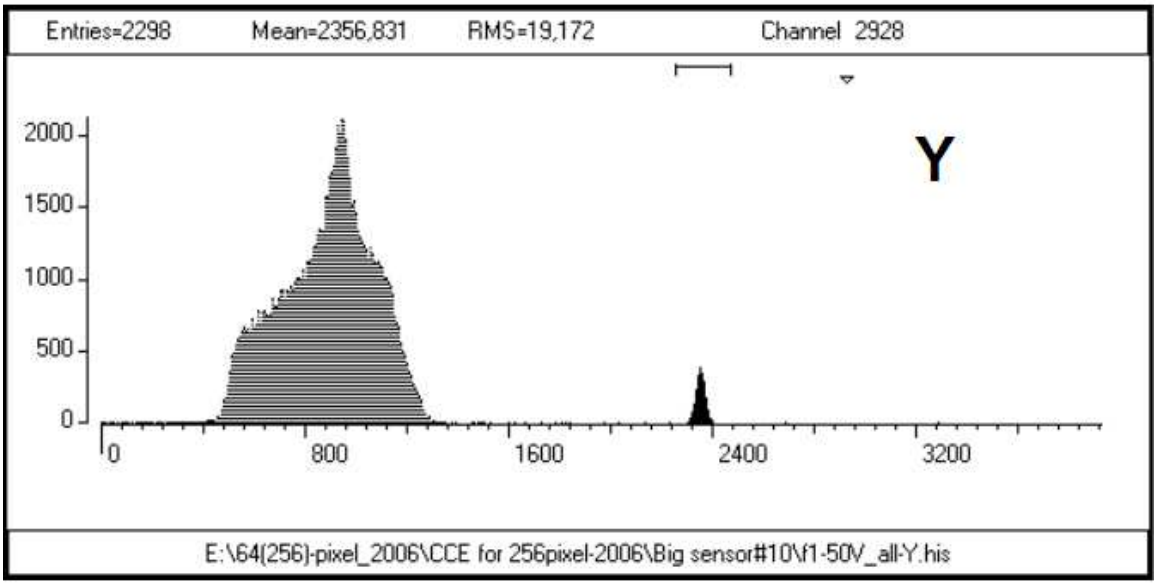
Entries=2298
Mean=2356,831
RMS=19,172
Channel 2928
Y
2000
1500
1000
500
0
0
800
1600
2400
3200
E:\64(256)-pixel_2006\CCE for 256pixel-2006\Big sensor#10\f1-50V_all-Y.his

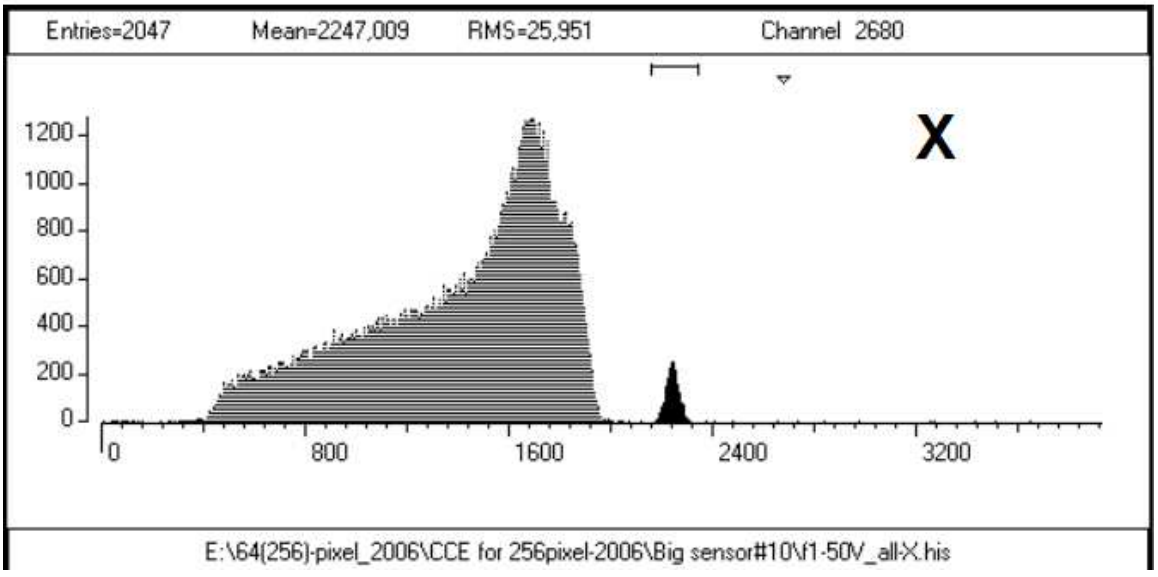
Entries=2047
Mean=2247,009
RMS=25,951
Channel 2680
X
1200
1000
800
600
400
200
0
0
800
1600
2400
3200
E:\64(256)-pixel_2006\CCE for 256pixel-2006\Big sensor#10\f1-50V_all-X.his

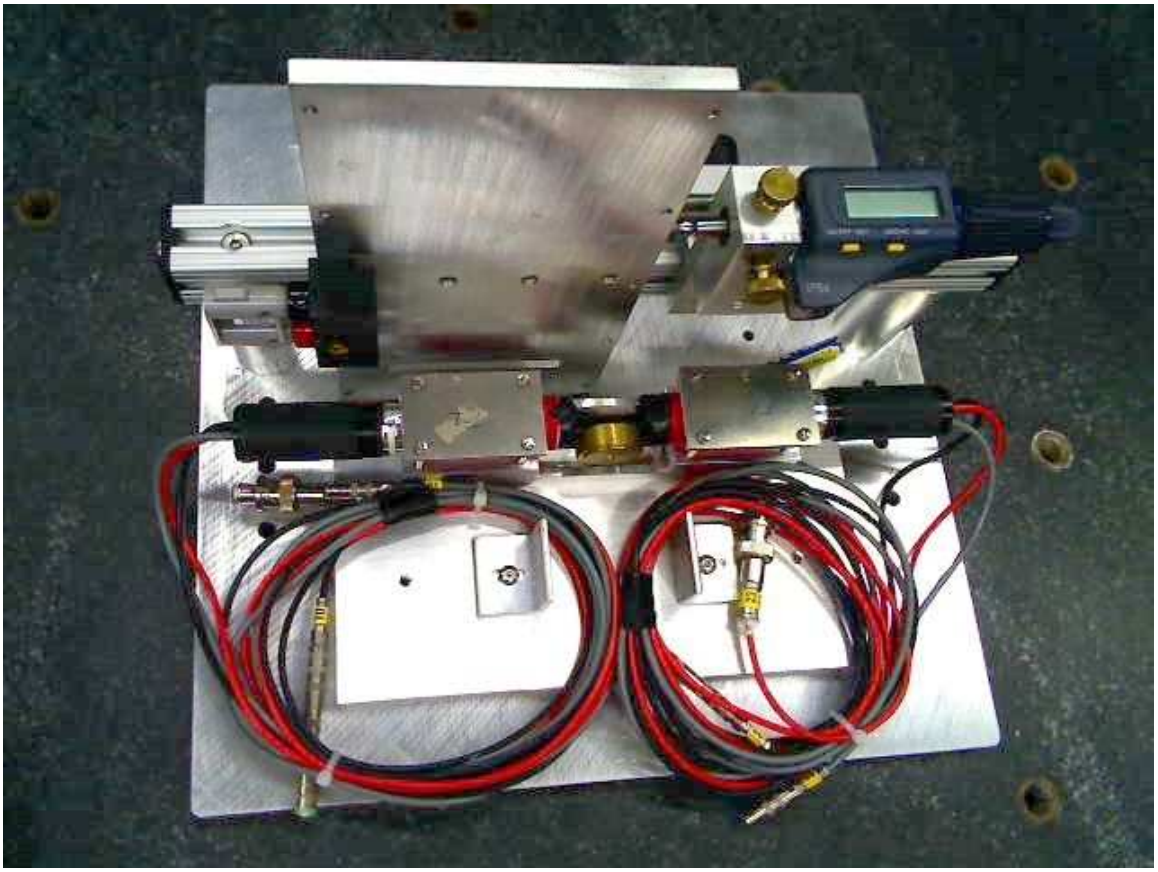

Figure D.6: Test source for stripixel studies with collimated electron source.

Appendix E

Pad Readout Chain

E.1 SPICE Simulation Of The Pad Sensor Readout Chain.

The readout chain for pad sensors was simulated using LTspice[1] program and it is illustrated in Fig. E.1. In this simulation the pad sensors are represented as 50 pF capacitors, seven pads are AC decoupled by capacitors Cd1-Cd7 and connected to the summation point via lossy transmission lines Tcar1-Tcar7. The bias is applied on each pad individually over Rb1-Rb7 resistors. From the summation point the signal goes through a short transmission line Tpa to a preamp E1. The preamp is connected to a differential driver E3, which drives 10 m of differential cable represented by a transmission lines Tpa1 and Tpa2. Other side of the cable is connected to a an integral shaper LT6600-2.5 (low noise differential amplifier and 4th order 2.5 MHz low-pass filter), which acts as an antialiasing filter. From here the differential signal will go directly to an ADC.

The current pulse in pad detector is a result of charge induction due to the drift of electrons and holes originated along the track. The pulse has very sharp front, and a tail which is a sum of two components of equal area: fast component ∼10 ns due to drift of electrons and slow component ∼30ns due to drift of holes[2] . The input signal is simulated as 2mA double-exponential current pulse with rising time constant 2 ns, flat top of 1 ns and falling time constant of 20 ns, the injected charge is 4000 fC which correspond to 1000 MIPs, a half of the maximum signal, expected from the single pad.

The preamp is modeled as an ideal trans-conductance amplifier with gain of 10 KOhm and with input impedance of 50 Ohm, this impedance is divided in two parts: noisy Rin_hot=8 Ohm and noiseless Rin_cold=42 Ohm.

The differential driver (AD8132 or AD8137) is modeled as an ideal voltage regulator.

[1] Available free from http://www.linear.com/company/software.jsp

[2] Helmuth Spieler, '**Semiconductor Detector Systems** ' Oxford University Press, USA (September 27, 2005)
also page 85 of http://www-physics.lbl.gov/∼spieler/Heidelberg_Notes_2005/index.html

E.2 Simulation Model of the Pad Sensors Readout Chain

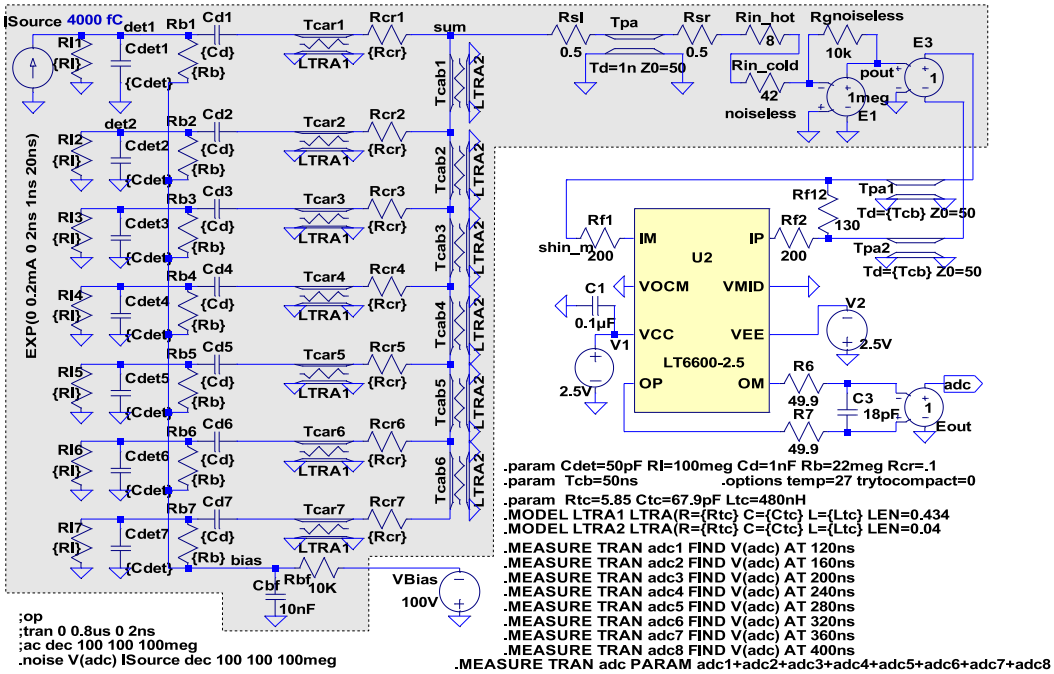

Figure E.1: Simulation model of the pad sensor readout chain.

The lossy transmission line parameters are represented in MODEL and PARAM statements on Fig. E.1 and they are explained in the next section. For this simulation the following parameters were used:

1. Unit resistivity Rtc = 5.85 Ohm/m
2. Unit capacitance Ctc = 67.9 pF/m
3. Unit inductance Ltc = 480 nH/m
4. The line lengths of Tc1-Tc7 varies from 62mm to 434mm

The line impedance of each line is Z=sqrt(Ltc/Ctc) = 84 Ohm.

E.3 Transmission Line Analysis

Source: "High-Speed Digital Design A Handbook of Black Magic". Howard W. Johnson and Martin Graham, Prentice Hall, 1993; ISBN 0-13-395724-1

Mathcad source: http://www.sigcon.com/lib/htm/MSTRIP.htm

local source: http://www.phenix.bnl.gov/s̃uhanov/ncc/electronics/signal_processing/mstrip.mcd

E.4 Selection of Cut-Off Frequency of the Low-Pass Filter

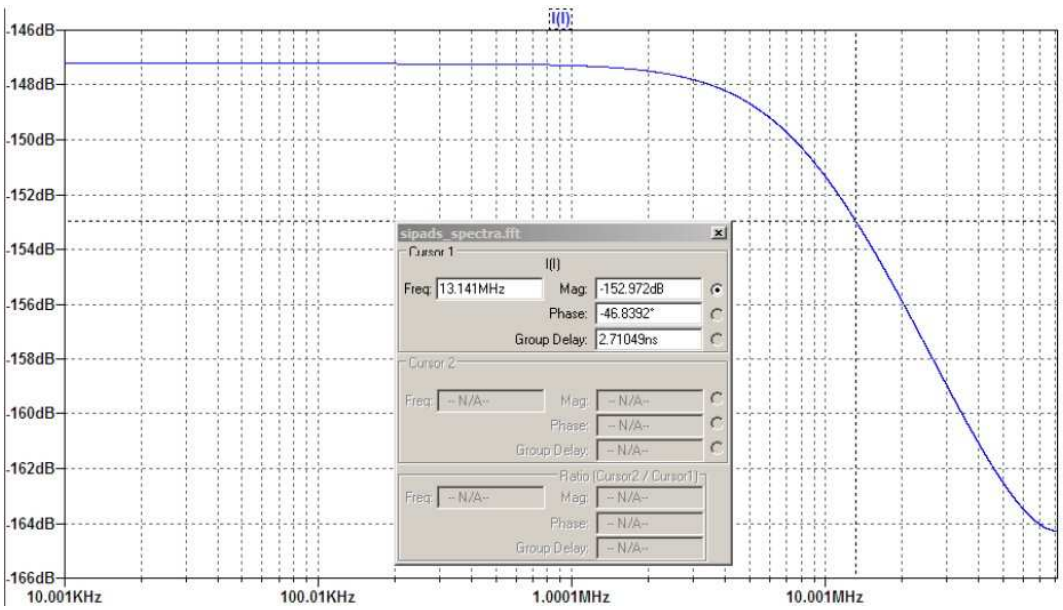

Figure E.2: Spectrum of the source signal. The bandwidth (where amplitude drops by 6 dB) is 13 MHz.

Figure E.2 shows that the bandwidth of the source signal is 13 MHz. Figure E.3 shows the gain of the system from the source to the preamp output, which is determined by combination of detector capacitance, transmission lines, and input impedance of the preamp. Also shown on Fig. E.3 is the noise at the preamp output (red) and the contribution to the noise from noisy part of the impedance Rin_hot (green). We select the cut-off frequency for the low-pass filter based on this figure. At frequencies around 2.5 MHz the gain starts to decline and at the same time the noise is rising. The cut-off frequency of 2.5 MHz ensure optimal signal to noise ratio.

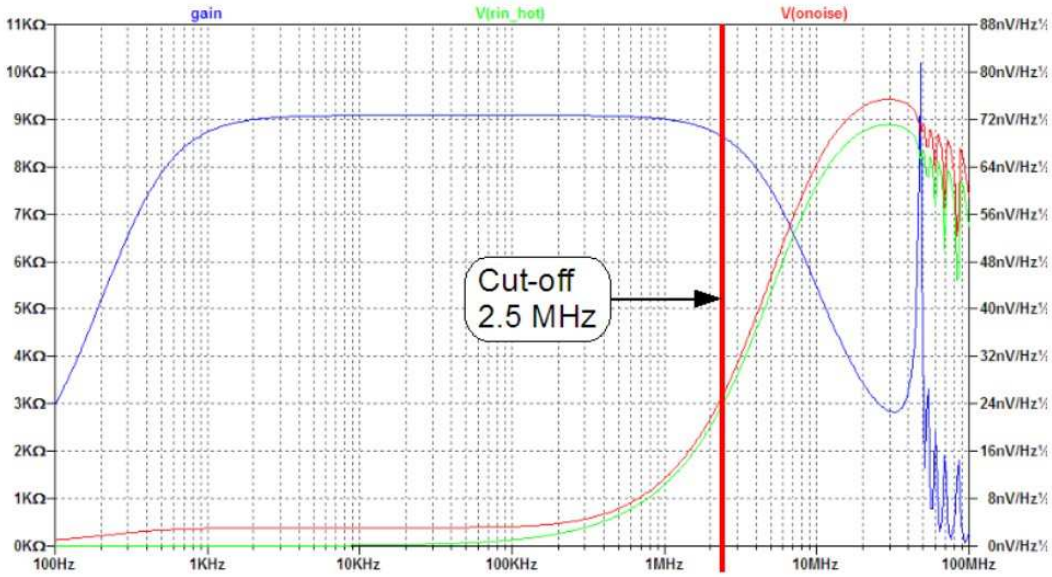

Figure E.3: Gain (blue) and noise (red) at preamp output.

E.5 Transient Analysis

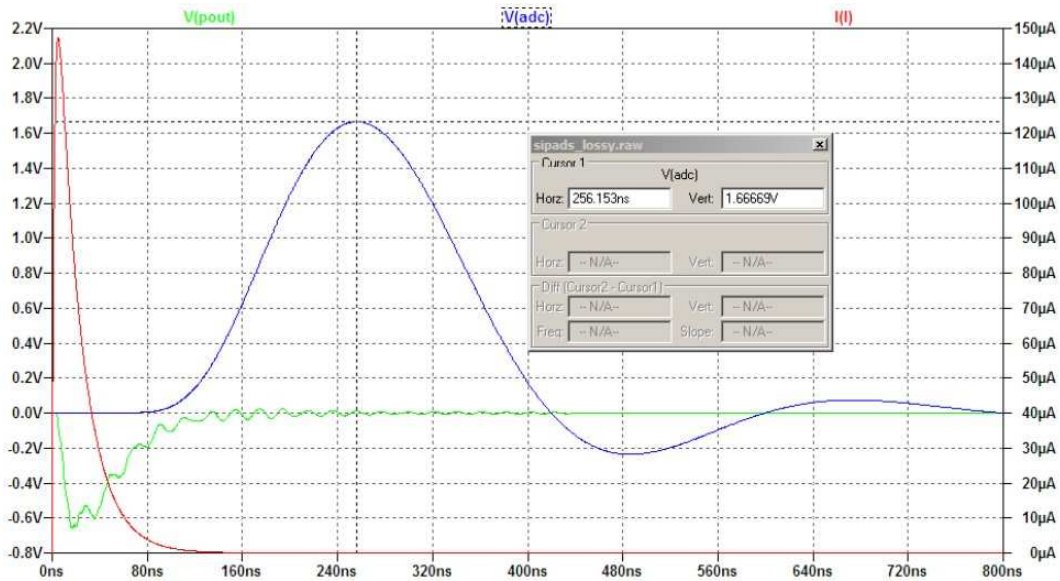

Figure E.4: Transient analysis of the pad readout chain.

Figure E.4 shows the transient analysis of the readout chain. The blue line is the output of the shaper, the green curve is an amplitude at the preamp output, one can see that there are significant reflections caused by mismatched impedances of lines Tcar1-Tcar7 and Tpa. These reflections are fully integrated and do not appear on the output signal.

The reflections could be eliminated by introducing resistors Rcr1-Rcr7 with values in the range of 35-70 Ohm, see Figure E.5. As shown later, these resistors would significantly contribute to the system noise and therefore are not recommended.

E.5.1 Nonlinearity

. The simulation for small signals shows exactly the same shape with no deviation from linearity.

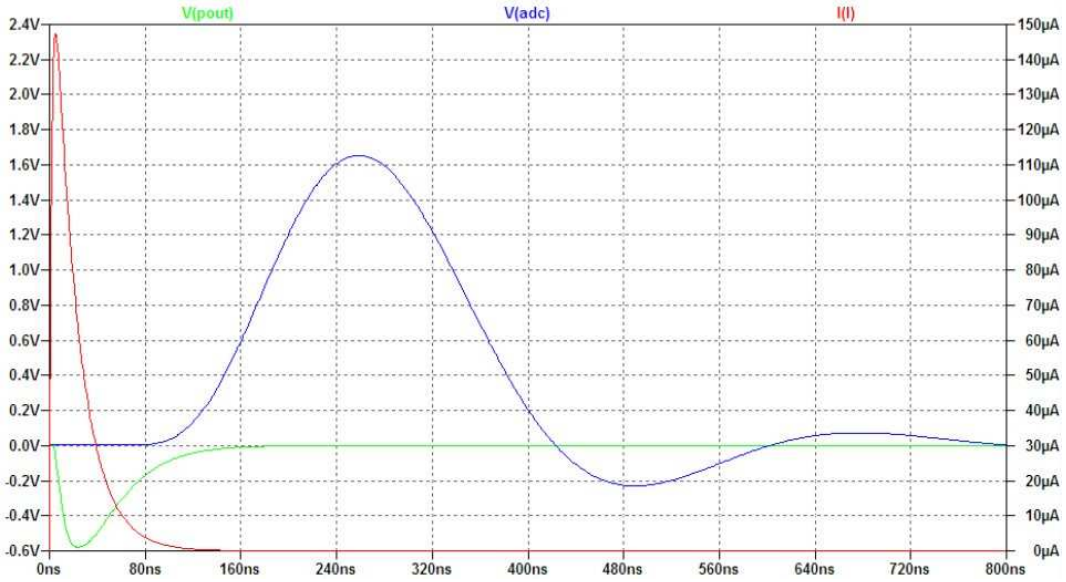

Figure E.5: Transient analysis, Rcr = 35 Ohm.

E.6 Noise Analysis.

The noise analysis at the shaper output is represented on Figure E.6, t shows the system noise (red), noise contribution from serial resistor Rin_{hot} (green), the system gain (blue). The flat area of the system noise below 200KHz comes from the shaper, the increased noise above 5MHz is mainly due to Rin_{hot}. This resistor is main contributor to the total rms noise.

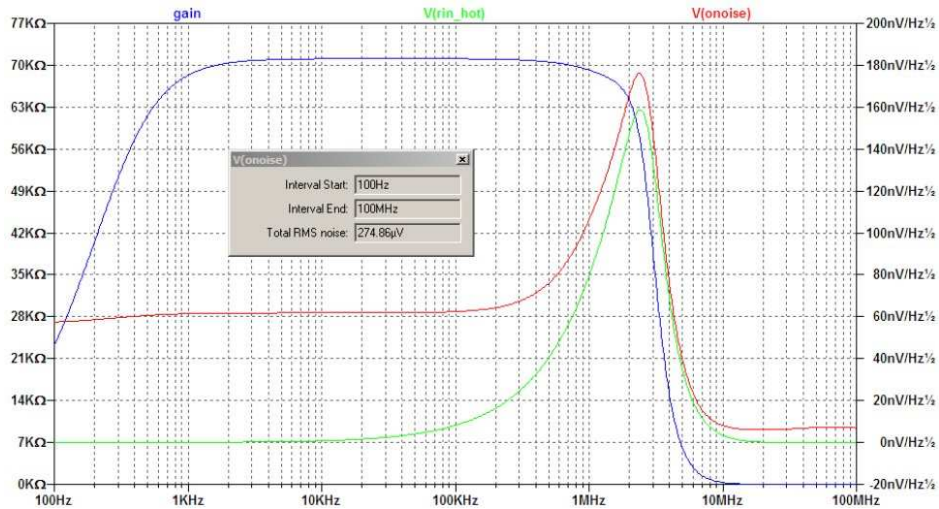

Figure E.6: Gain in kΩ (blue), noise in nV/$\sqrt{\text{Hz}}$ (red), and noise contribution of Rin_{hot} (green) at the output of the filter.

By comparing Fig. E.6 with Fig. E.3 one can see that the gain is high in the region where the noise is low and the gain is sharply cut for the region with high noise.

E.7 Summary Table

Figure E.7 shows the noise at the filter output (RMS1) and the signal-to-noise ratio (S/N), calculated as non-weighted sum of eight ADC samples at different operational parameters.

	RMS of ADC for diff input 2V p-p =					1.25E-004			
	Rcr	SA	PA	PP	ADCsum	RMS1	S/N1	RMS	S/N
	Rcr	Signal Average over 400ns	Peak amplitude	Peak position	ADC sum of 8 samples 50MHz starting at 80ns	RMS Noise 100Hz-100MHz	S/N one sample at a peak	Total RMS noise for 8 samples	S/N including RMS of ADC
	Ohm	V	V	'ns	V	V		V	
1	**Cdet=42pF**, Rin_cold=42, R1=130, R3=R4=200, R2=10K, **LT6600-10** **Cut-off at 10 MHz, 8 samples every 20ns starting at 80 ns**								
1.1	0	0.177	1.240	117.0	3.50	4.37E-004	2.84E+003	1.24E-003	2817
1.2	35	0.177	1.200	118.0	3.50	4.97E-004	2.41E+003	1.41E-003	2480
2	**Cdet=42pF**, Rin_cold=42, R1=130, R3=R4=200, R2=10K, **LT6600-2.5** **Cut-off at 2.5 MHz, 8 samples every 40 ns starting at 120 ns**								
2.1	0	0.347	1.700	251.0	7.39	2.55E-004	6.67E+003	7.32E-004	10096
2.2	35	0.347	1.700	256.0	7.38	2.98E-004	5.70E+003	8.52E-004	8661
	Cdet=50pF, Rin_cold=42								
2.3	0	0.342	1.670	256.0	7.27	2.70E-004	6.19E+003	7.74E-004	**9395**
2.4	35	0.342	1.654	259.0	7.26	3.23E-004	5.13E+003	9.21E-004	7883
	Cdet=60pF, Rin_cold=42								
2.5	0	0.336	1.620	258.0	7.10	2.98E-004	5.44E+003	8.52E-004	8332
2.6	35	0.336	1.605	261.0	7.10	3.51E-004	4.57E+003	1.00E-003	7096

Figure E.7: Noise at the filter output (RMS1) and the signal-to-noise ratio.

The row 1.1 and 1.2 are 10 MHz cut-off and 50 MHz ADC sampling, while all other rows are 2.5 MHz cut-off and 25 MHz sampling. The improvement from using multiple sampling could be derived as ratio of S/N to S/N1 and it is about 50%. The best signal to noise ratio for detector capacitance of 50 pF is 9395 (row 2.3). In row 2.1 is shown the same ratio for smaller detector capacitance of 42 pF, as expected, it is higher: 10096. The RMS noise level at the filter output 270 uV (row 2.3, column RMS), which can be converted to ENC using:

ENC = RMS0/PA x 4000fC/e ENC = 4042 electrons

In this formula RMS1 is the RMS noise level = 270 uV, PA is peak amplitude = 1.67V, 4000fC is the charge applied to the input, e – electron charge. The RMS noise after non-weighted sum of 8 samples is 7740 uV (see column RMS in row 2.3) but effective signal increased to 7.27 V (ADCsum) from 1.67 V. This correspond to ENC of the readout chain = 2665 electrons.

E.8 Dynamic Range of Signal Measurement

The problem of achieving the dynamic range of signal measurement better than 12 bits comes from the fact that the effective number of bits (ENOB) of any off-the-shelf fast ADCs is less than 12 bits no matter what resolution they have. In another words if we take for example 16-bit ADC with ENOB=12 and make a single sample then we cannot achieve resolution better than 12 bit.

The obvious solution is to make several samples and sum them up together. In the simplified case when output shape of the filter is flat and we are taking N samples on plateau then the signal-to-noise ratio will improve sqrt(N) times. In the case of arbitrary signal shape the optimal signal-to-noise ratio will be achieved using weighted sum of the samples when the weights follow the shape of the signal.

Further improvement of better than 20% could be achieved using weighted sum of samples.

Rule:

If dynamic range of a system is D (linear scale) and resolution of ADC is A bits (N<2**A) then dynamic range could be improved K*sqrt(N) times using weighted sum of N samples. The coefficient K<=1 depends on the signal shape (for flat shape K=1). The N should be chosen less than (log2(D) – A). The sampling rate of the ADC should be higher than B*N where the B is the bandwidth of the input signal.

E.9 Summary

- The readout chain of NCC silicon pad sensor pad is simulated using LTspice program.
- The cut-off frequency of the shaper should be 2.5 MHz, above this frequency the system gain is decreasing and the system noise is rising.
- The ADC sampling rate should be 25 MHz or higher.
- The number of samples should be 8 or larger, this will provide at least 50% improvement of S/N relative to single-sample measurement.
- Using weighted sum provides 20% improvement as compared to non-weighted sum.
- The impedance-matching resistors Rcr1-7 should be avoided. They add to the noise.
- Simulations did not show any nonlinearity.
- For 7*50pF pads the dynamic range above 9350 could be achieved when gain of preamp is 10KOhm and its noisy part of the input impedance equivalent to 8 Ohm.
- The Equivalent Noise Charge (ENC) at the input is 2700 electrons, or 0.43 fC.

Appendix F

Silicon Strip Sensors and Readout

F.1 Strip Sensors

We plan to instrument the preshower and shower max layers of the NCC with silicon strip detectors of a novel design, as illustrated in Fig. F.1. The sensors developed by the BNL Instrumentation Division provide two-dimensional position sensitivity. The readout of sensors is based on SVX4 chips, which were developed for silicon strip detectors by FNAL and LBL. In the final readout system the SVX4 chips would be arranged on readout cards SRC's and mounted directly on the sensors.

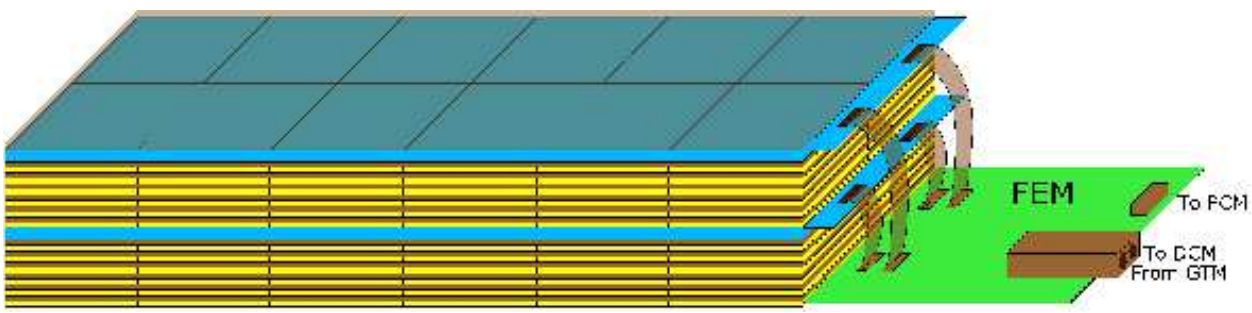

Figure F.1: Conceptual layout of the NCC electromagnetic brick. Blue layers are silicon-strip planes (preshower and shower max); brown layers are tungsten plates, yellow layers – silicon-pad readout planes. Both silicon strip planes are read by FEM board located inside the bricks envelope. The FEM sends data to PHENIX DCM boards over optical fiber. Power and ground are distributed from a PCM board located near the detector.

F.1.1 Design Principle

The concept of the stripixel detector is described in publication of Zheng Li[1]. The sensor is a segmented detector with 0.5mm*0.5mm pixels.

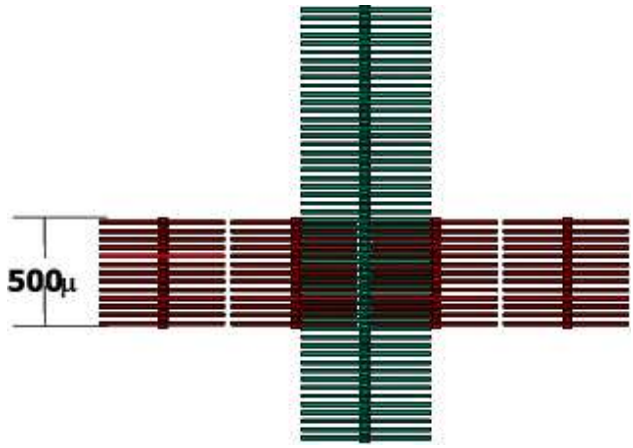

Figure F.2: Comb structure

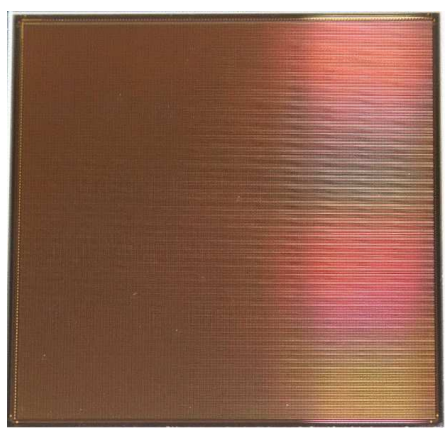

Figure F.3: Prototype of stripixel sensor.

Figure F.2 illustrates that each pixel region has two comb-shaped metal strips to collect charge produced by an ionizing particle that transverses the silicon. A hit by an ionizing particle will deposit charge on two combs. In the original design vertical combs are connected by metal strips, horizontal combs – by implanted bridges. Figure F.3 shows the prototype stripixel produced by SENS Seoul, Korea for Yonsei University.

The decision to use stripixel sensors in **DC-coupled** mode was based on the following considerations:

1. Higher production yield,

2. Higher reliability during operation and

3. 25% lower cost.

The biasing resistors are implemented directly on sensors which will help to greatly simplify the production tests and characterization procedures by allowing simultaneous biasing of all strips. The readout pads are arranged on two orthogonal edges of the sensor.

F.1.2 SVX4 Readout Chip

The strips are read out with the SVX4 chip developed by FNAL/Berkeley collaboration [2]. The SVX4 is implemented in the 0.25 μ TSMC process and is inherently rad-hard. It is a 128-channel chip with a 46-deep pipeline cycled by the beam-crossing clock, thus providing the LVL1-latency required by the PHENIX DAQ. LVL1-accepted events are stored for future pipelined readout. The SVX4 allows up to 8 bits of analog information, although the number of bits are programmable. Several pedestal-subtraction steps offer robust protection against common-mode noise. On-board zero suppression is provided for, but can be turned off (see discussion below). The SVX4 also provides for four-deep multi-event buffering required by the PHENIX DAQ.

F.2 Stripixel Ladder

Figure F.4 shows the stripixel ladder, which comprises 5 to 7 Sensor Readout Modules (SRM). Each SRM reads out signals from two stripixel sensors and hosts four SVX4 chips. The SRMs are mounted on a common ceramic substrate and they are connected to each other by means of short 50-line flat-flex jumpers which form one or two daisy-chains, connected to FEM. The maximum number of SVX4 chips per daisy chain is 16.

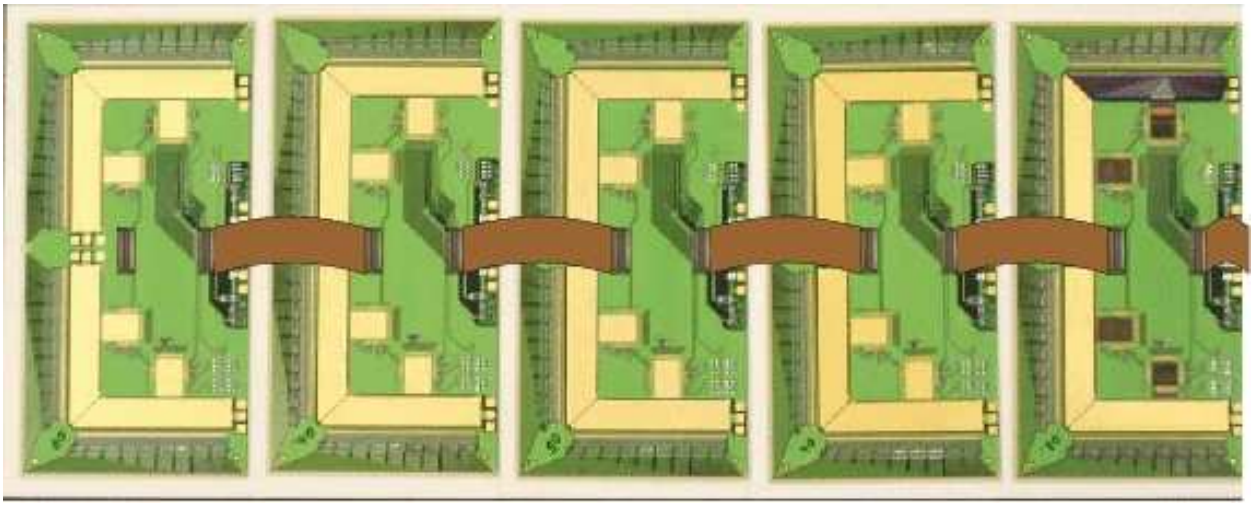

Figure F.4: Stripixel ladder comprising 5 daisy-chained Sensor Readout Modules with two sensor on each. The rightmost SRM is populated with SVX4 and it has one pitch adapter out of four installed.

Figure F.5 shows the arrangement of the stripixel ladder inside the brick. The ladders are inserted between tungsten plates with pad-sensor layers mounted on them.

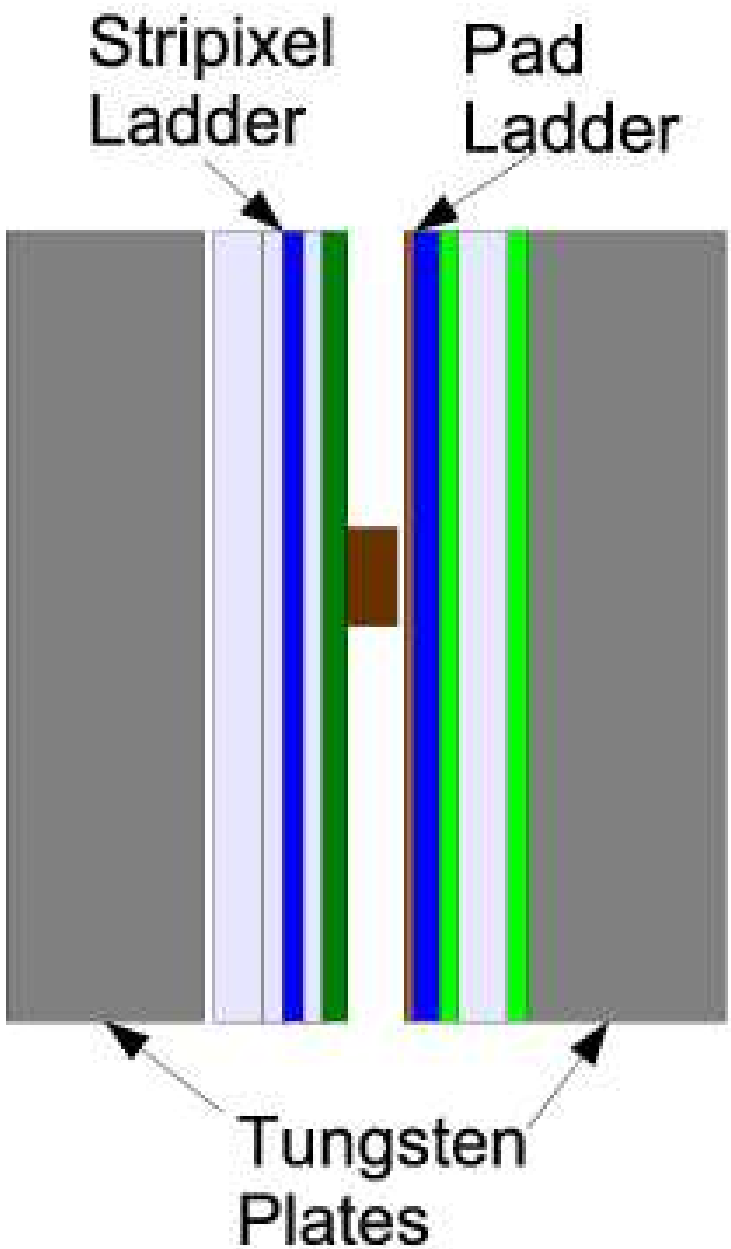

Figure F.5: The arrangement of stripixel ladders between pad sensor assemblies on tungsten plates

F.3 Sensor Readout Module (SRM)

Figures F.6 and F.7 show the sensor readout module comprising two silicon stripixel sensors, which are arranged vertically side-by-side, and a Sensors Readout Card (SRC) mounted on top of them. Sensors are wire-bonded to the edges of the SRC. The SRC is a 0.25 mm thick PCB board manufactured with minimal line width of 75 μ and minimal line space of 75 μ. The board hosts 4 of SVX4 chips.

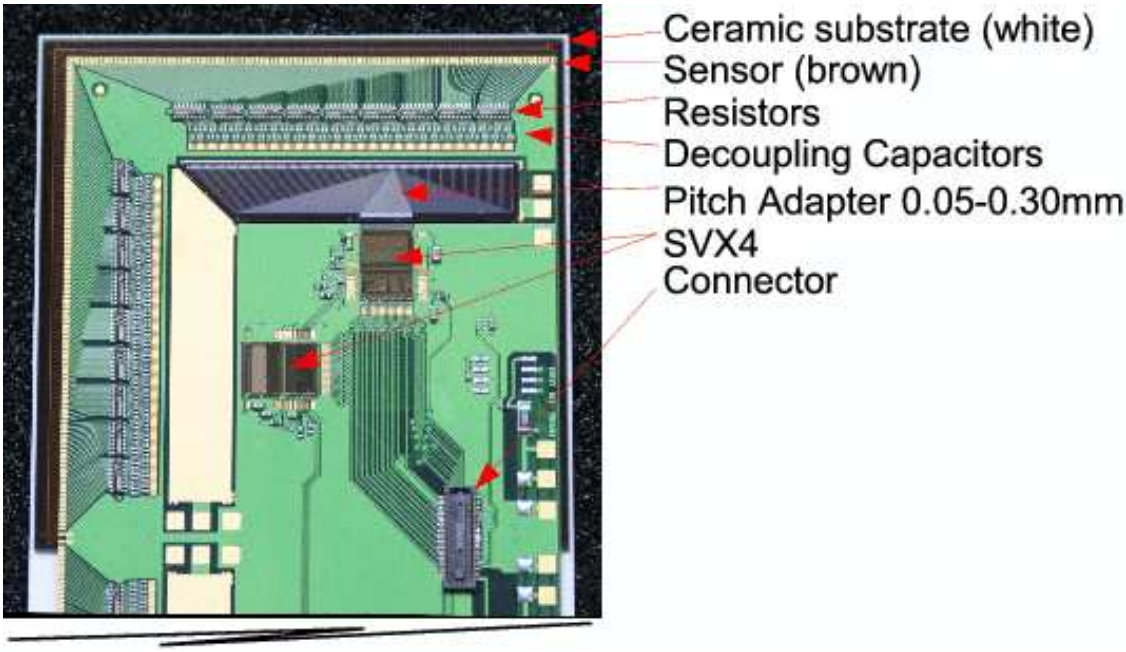

Figure F.6: Sensor Readout Module, the upper half of the module shown. In the final version two connectors will be installed instead of one.

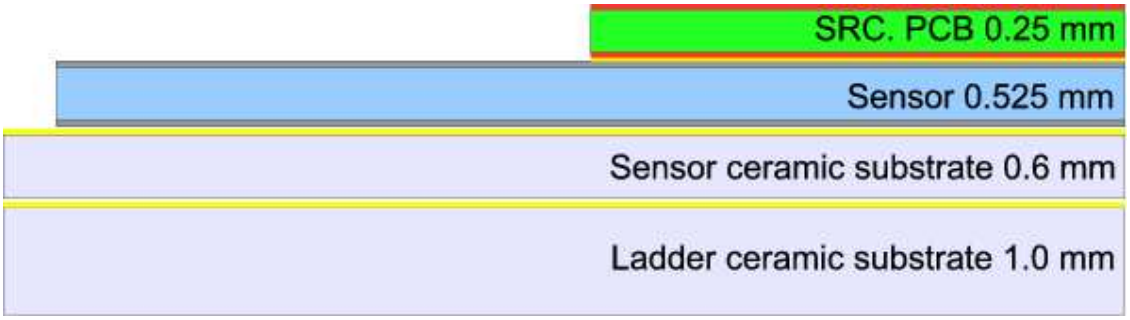

Figure F.7: Stack-up of the Sensor Readout Module.

Connection of DC-coupled sensors to the SVX4 chips requires AC-decoupling network. This network is build using type 0201 capacitors. The pitch adapter is metal-on-silicon bare die, produced from the same wafers as sensors. The sensor ceramic substrate is metalized and it has vias for bias voltage distribution.

A prototype of sensor ceramic substrate has been manufactured and it allows for multiple methods of providing **bias voltage to the sensor**:

1. Wire-bonding from the bottom of the sensor to the bottom of the sensor ceramic substrate and from there soldering to the ladder ceramic substrate.
2. Conductive gluing of sensor ceramic to ladder ceramic.
3. Soldering conductive foil from the bottom of the sensor ceramic to the top of SRC and distributing the bias voltage as a separate line on signal daisy-chain.

The SRM modules are daisy-chained using flat-flex cable jumpers.

Several prototype boards have been manufactured and electrically tested.

The sensor readout modules are mounted on a ladder ceramic substrate which provides the mechanical stability of the ladder and transfer heat from the sensor to the outer skin, it has thin film conductors on top to distribute bias voltage.

The slow control and monitoring of the SRM is done using 1WIRE devices. The following parameters a monitored:

1. Temperature (it is easy to monitor it in several locations) (DS18B20X chip).
2. Leakage current
3. 3 control voltages (DS2450 chip).

The setup voltages for SVX4 like VTH and VCAL are also controlled by 1WIRE devices (DS2890).

F.3.1 Power consumption

The main power consumption sources on the SRM are SVX4 chips. The average load current per chip is 52 mA from AVDD and 13 mA from DVDD, which correspond to 0.22 W. The AVDD load depends on preamp current setting and can reach 90 mA. The average power dissipation per silicon-strip plane is expected to be of the order of 10 W.

F.4 Front-End Module (FEM)

The FEM has 4 readout chains for SVX4. The LVDS data buses are independently fed into FPGA. The FPGA buffers the event, compresses the data stream using Huffman Coding, stores the result in the output buffer and sends it through the optical transceiver to the PHENIX DCM. PHENIX DAQ requires that all subsystem should be able to buffer at least 5 events. The SVX4 chips on SRC have internal buffering for 4 events; the FEM provides at least one additional buffer.

The FEM connects to the PHENIX DAQ over a small-form-factor (SSF) optical transceiver. The receiving part of it is connected to a PHENIX GTM module, while transmitter part – to a PHENIX DCM module.

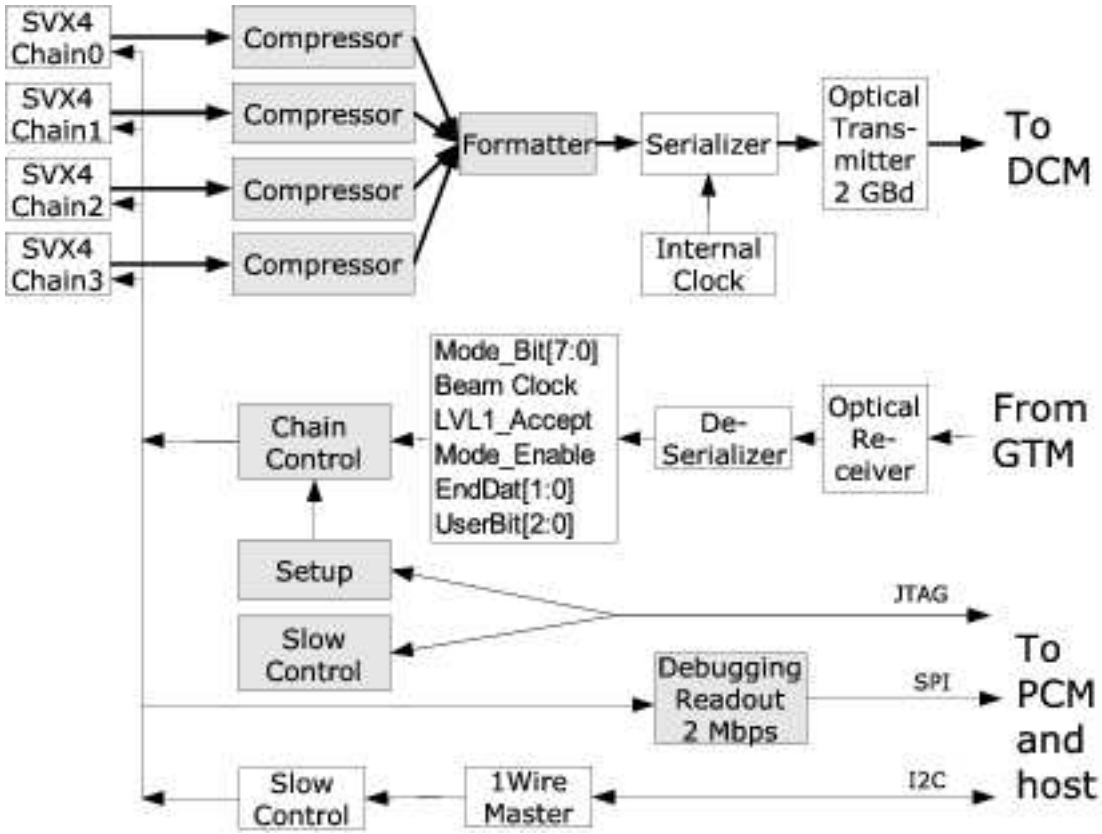

Figure F.8: FEM Block Diagram. Shaded boxes represent the elements implemented in the FPGA.

Figure F.9 shows the signals that the FEM receives from the GTM. These signals are de-serialized using a SerDes chip.

Mode_Bit[7:0]	8
Beam Clock 9.4 Mhz	1
LVL1_Accept	1
Mode_Enable	1
EndDat[1:0]	2
UserBit[2:0]	3
Reserved[3:0]	4
Total	20 Bit

Figure F.9: PHENIX Synchronization Signals.

The clock is defined by the PHENIX GTM; it is four times the Beam Clock, i.e. 40 MHz. This clock is recovered by the SerDes chip; the clock jitter is guaranteed to be less than 40 ps. The transceiver and SerDes are mounted on a small mezzanine board and will be compatible to the optical protocol of the latest DCM.

Raw event size, no pedestal suppression	14448	Bytes
Raw event size with channel ID removed	**7224**	**Bytes**
FEM readout clock, both edges used	40	Mhz
Collection time from 4 SVX4 chains on FEM	22.58	us
Data transfer rate to DCM	2.0	Gbps
Transfer time of raw event	**36.1**	**us**
Hit occupancy	5%	
Output data size, pedestal suppressed	722	Bytes
Transfer time of zero-suppressed event	**3.6**	**us**
Lossless Compression		
Compression factor for raw data	2.5	
Size of compressed event	2890	Bytes
Data transfer time of compressed event	**14.4**	**us**
Lossy compression		
Compression factor for zero suppressed data	3.0	
Event size, zero-suppressed & compressed	241	Bytes
Transfer time, zero-suppressed & compressed	**1.2**	**us**

Figure F.10: Size and Tranfer Time of Stripixel Data from Single Electromagnetic Brick.

The digitization at 40 MHz Front-End clock will be finished in 1.7 us. It is important to keep this time as short as possible because the SVX4 chip cannot do digitization and readout simultaneously.

The longest chain have 16 of SVX4 chips, assuming 5% occupancy the size of the average chain will be 722 bytes and average readout time **3.6** μs. During this time the SVX4s are open to acquire new triggers.

For normal data taking with pedestal suppression and Huffman compression (we expect that Huffman coding of pedestal suppressed data can achieve compression factor of 3:1) the estimated data size from the whole brick is 241 bytes. This data will be transferred to DCM in **1.2** μ**s**. This fits safely into the PHENIX DCM data-taking window (ENDAT) of **40** μ**s.**

The optical transmitter will be clocked by an internal clock generator to eliminate uncontrolled jitter of the beam related clocks, which could result in high probability of data losses.

Note. Even for calibration runs when pedestal suppression is switched off the data size will be reduced from 14.4 Kbytes to 3.0 KB by removing ChannelID bytes from the SVX4 data and applying Huffman compression. The data transfer time in this case will be **14.4** μ**s**, which can be handled by a single DCM by occupying two ENDAT windows of the DCM.

F.4.1 FPGA Selection

F.4.2 Number of LVDS pairs.

Fig F.11 shows that the FEM should process data from four SVX4 chains in parallel. This will require

1. Data transfer bus 4*9 = 36 LVDS pairs.
2. Common clocks BECLK, FECLK. = 2 LVDS pairs
3. PRIOUT[0] 4*1 = 4 LVDS pairs
4. Optional PIOUT[3:1] 4*3 = 12 LVDS pairs

In total it is 42 obligatory and 12 optional pairs.

Number of ladders in brick	2	
Max Number of SEM in a Ladder	7	
Number of SVX4 in SEM	4	
Max Number of SVX4	56	
Number of channels	7168	
Max data size per SVX4	258	Bytes
Max input data size	14448	Bytes
Number of input buffers	1	
Output data size unsuppressed	7284	Bytes
Compression factor for unsuppressed data	2.5	
Output data compressed	2914	Bytes
Hit occupancy	5%	
Output data size, pedestal suppressed	829	Bytes
Compression factor for suppressed data	3	
Output data size, suppressed & compressed	276	Bytes
Size of the pedestal memory	7168	Bytes
Size of the Huffman coding map	512	Bytes
Total memory requred	**29412**	**Bytes**
	235296	**Bits**

Figure F.11: BEM Memory Requirements.

FPGA	Dist RAM [Kbits]	Block RAM [Kbits]	DCM	IO USER	IO DIFF	Price	Source
XC3S500E	73	360	4	190	77	?	
XC3S1200E	136	504	8	190	77	?	
XC3S400	56	288	4	173	76	$27.76	digikey
XC3S1000	120	432	4	173	76	$47.87	Digikey
XC2V1000	160	720	8		324	$200	

Figure F.12: Comparison of FPGA options.

Of the options in Fig. F.12 the XC3S500E is most attractive and it could be less expensive in the near future, but currently the SPARTAN3E FPGA has a very long lead time and is more expensive than SPARTAN3. The FPGA XC3S400 and XC3S1000 both meet all requirements, are not expensive, and are readily available. For prototype boards the XC2V1000 is used.

F.4.3 FEM Ports

SVX4_Chain[3:0] ports These daisy-chains provide all signals, power and ground to the SRCs, in prototype we will test an option of sending bias voltage over daisy-chain . The longest SVX4 chain has 16 SVX4 chips.

JTAG Port JTAG port is vital for the system. It is used for configuration of the SVX4 chips, reconfiguration of FPGA and also to access programmed registers of the FEM module. It also can be used for data transfer for testing and debugging. Essentially all control of the stripixel readout electronics is done through the JTAG port of the FEMs. The JTAG ports of 7 of FEMs are daisy-chained and connected to the PCM module, the signals on this daisy-chain are LVDS levels and they are converted to standard JTAG levels on each FEM. The performance of the JTAG communication link was thoroughly tested on the FEM prototype board and it was achieved reliable communication in both direction using 15m cable at the rate of 400Kbits/s.

MONITOR Port The monitor port has an I2C link to read out 1WIRE devices on SRC boards, and a QSPI link to read data from FEM. The QSPI port will be used for data taking during testing and prototyping when DCM and GTM are not available. The data transfer over QSPI link was tested on the FEM prototype board and reliable data transfer at 2 MByte/s was commissioned.

F.5 Zero Suppression and Data Compression

The SVX4 allows for on-chip zero suppression. However, the PHENIX DAQ is not designed to handle zero-suppression prior to the DCM because the pipelined architecture assumes

a fixed length data packet. However, the use of this feature has significant advantages. Without zero suppression the event size from the brick will be 14448 bytes (Fig. F.11). The compressor will remove the ChannelID bytes reducing size to 7284 bytes. Assuming 40 MHz 16-bit optical data link, this data will be sent in 92 μs, which does not fit to the 40 μs ENDAT window. To handle this amount of data in time we will need triple number of DCM links.

If we allow on-chip zero suppression then assuming 5% occupancy the data size will be reduced to 829 bytes (table 3), which is manageable by a single DCM. We plan to further compress data using Huffman Coding of the zero-suppressed data inside FPGA. Based on our experience at PHOBOS we expect compression factor of 3. This leads to average data size from one brick of the order of 300 bytes.

F.6 Program and Control Module (PCM)

The Program and Control Module provides remote JTAG interface to FPGA over ethernet, it provides fast configuration of FPGA, control and readout of programmable resources of the FEM. It provides 2 modes of slow data readout for testing and monitoring: 1) using JTAG (70 Kbyte/s) and 2) using QSPI (2Mbyte/s). One PCM serves one half-disk of NCC, i.e. 7 bricks; it is located close to the detector. During the initial stage of the project the PCM will also be used for slow control and monitoring of the front-end electronics as well as for remote configuration of the FPGAs. The module is hosting M5235BCC – a credit-card-size CPU board with ColdFire 64-bit 150 MHz CPU, 32 MB of memory, ethernet connection and I2C and QSPI ports. It operates under tiny Quadros OS, the other OS – ucLinux was successfully tested but rejected due to excessive complexity. As a prototype module we are using Evaluation Module for Motorola MCF5235 MCU[3].

F.7 Readout Chain Development

The readout chain was manufactured in February 2007, we tried to be as close as possible to the final design. For final design only minor modifications will be necessary:

- on SRC - change connector type, add second connector, modify solder masking.
- On FEM – changing connector type, implement communication with DCM.

The readout chain consist of the FEM board (big green board on Fig. F.13), PCM board (ColdFire Evaluation board), JTAG LVDS cable connector between FEM and PCM. It has ethernet connection to a host workstation. The setup will be used for testing system integrity and sensor parameters during all stages of assembly.

Figure F.14 shows the data analysis of pedestals and calibration pulses from SVX4 with disconnected inputs.

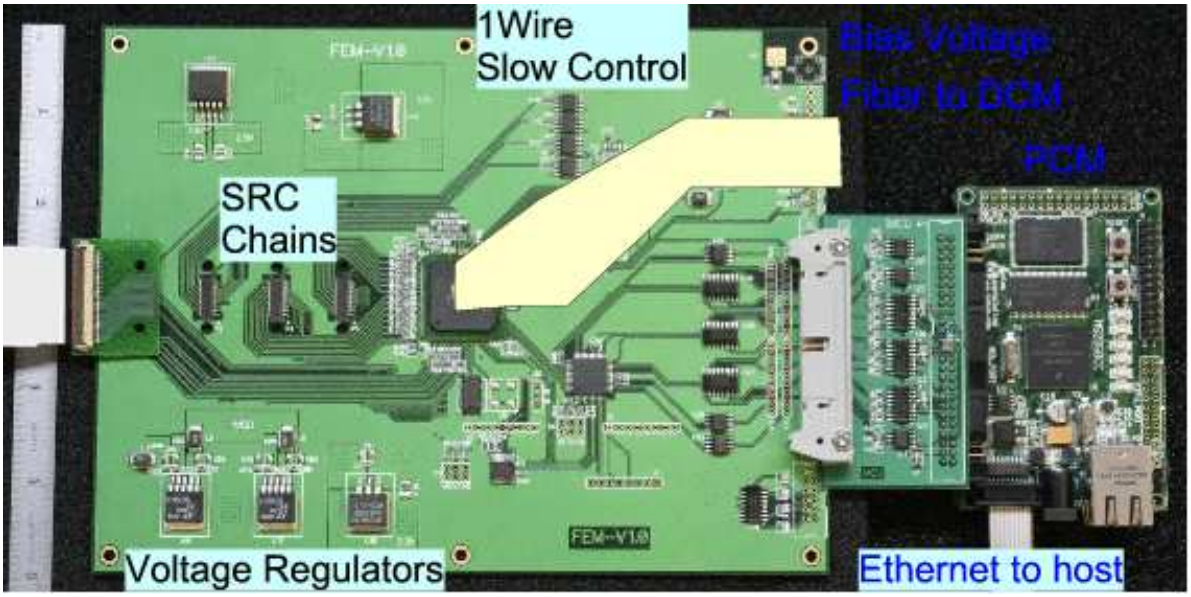

Figure F.13: Photo of the stripixel readout chain.

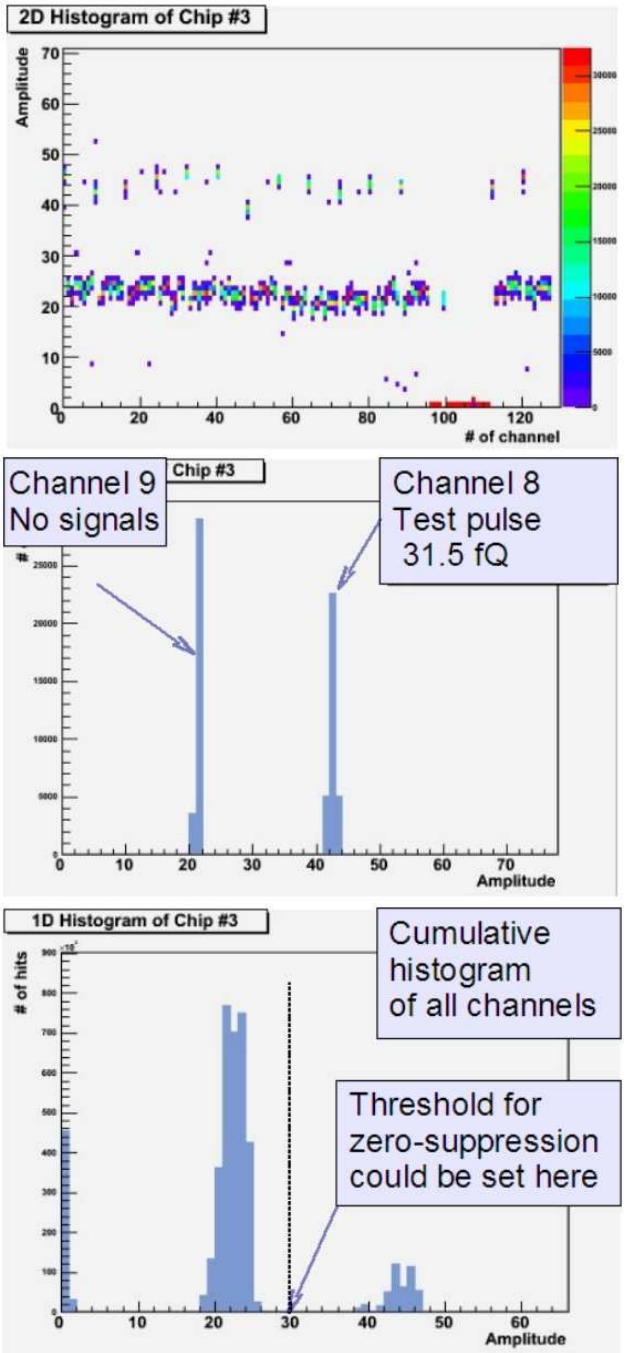

Figure F.14: Data analysis of SVX4 channels when pitch adapter is not connected. Amplitudes from all channels (top), single channels (center) and cumulative histogram of all channels (bottom).

F.8 Production and Assembly of Silicon Readout Layers

The silicon wafers will be manufactured by a commercial vendor; ELMA of Russia. At the vendor the wafers will undergo resistance and doping tests and then be diced into sensors. Further quality assurance (QA) includes IV and CV curves, laser pulse tests of each strip and sensor uniformity response. The QA tests will be carried out at BNL and JINR(LPP) (Nikolai Zamiatin group). The design and layout of all electronics boards is done by JINR(LHE) (Sergey Basilev group).

Figure F.15: Automatic wire-bonding machine in clean room facility at Helsinki Institute of Physics.

The SRC modules with installed SMT components will be shipped to Helsinki Institute of Physics (HIP) where the SVX4 chips and pitch adapters will be mounted and wire-bonded. On each stages the integrity of the SRC readout chain and parameters of the readout channels will be tested and recorded, this will be done without removing the jig from the wire-bonding machine.

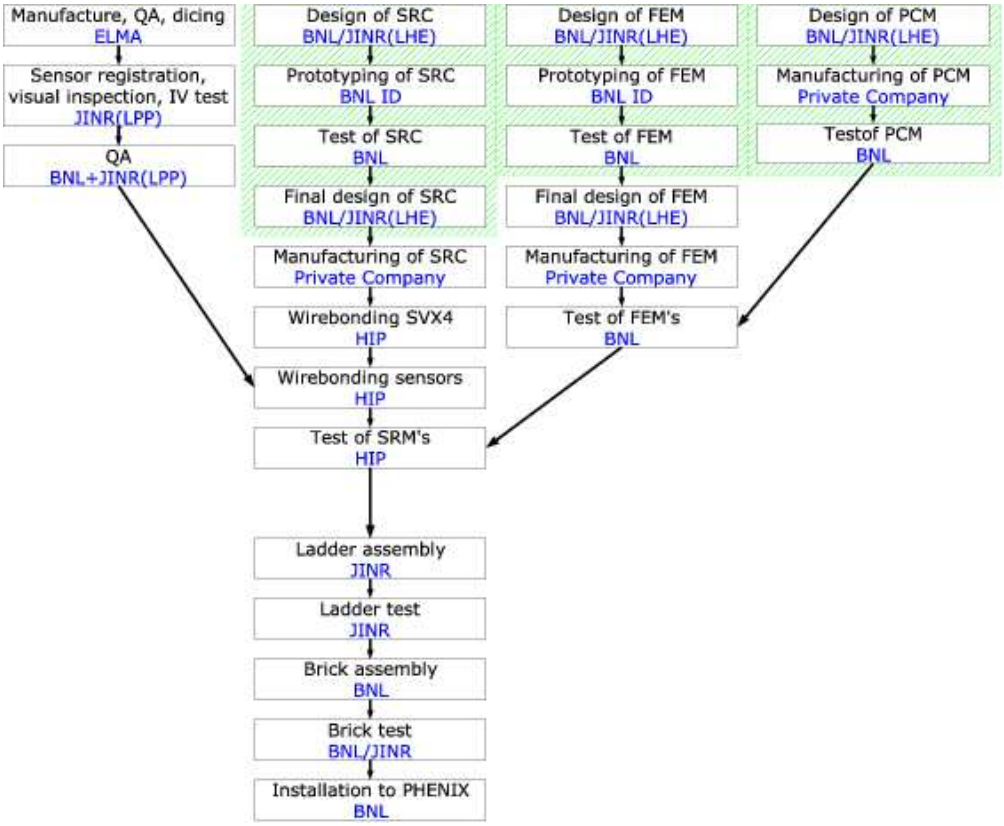

Figure F.16: Strip detector production flow chart. The green area shows accoplished tasks.

F.9 Radiation Tolerance of Front-End Electronics

F.9.1 Inside calorimeter

The components, which are subject to radiation damages inside the calorimeter are the silicon sensors, SVX4 chips and 1Wire sensors (DS18B20X, DS2890, DS2450).

The estimates based on total energy flow simulation predict the Total Ionization Dose (TID) of 100 kRad (in Si) that correspond to the fluence of $3*10^{12}$ equivalent neutrons per cm^2 over the period of 10 years (assuming pp interaction at 200 GeV with luminosity $\sim 2*10^{32}cm^{-2}*s^{-1}$). The leakage current for 300μ sensor after this irradiation will be of the order of 120 μA/sensor. This correspond to 0.5μA per strip. This current poses no problem provided the strip is AC decoupled from the SVX4 chip.

The SVX4 chip is radiation hardened and should sustain the expected TID. Little known about radiation tolerance of the 1Wire devices; it was reported the usage of the 1Wire devices for ionization measurement in space (LAZIO experiment). The radiation tolerance of the 1Wire devices will be tested after completeness of the full prototype of readout chain.

F.9.2 Outside calorimeter

The components, which are subject to radiation damages outside the calorimeter are the components of the FEM boards: FPGA (Xilinx XC3S1000), optical transceiver and SerDes, clock oscillators and voltage regulators.

The TID estimation for this region for AuAu collisions is obtained from PHENIX publication[4]: and is summarized in Fig. F.17.

	RHIC I	RHIC II
R = 53 cm	0.79 rad $2.4*10^7$ cm^{-2}	7.9 rad $2.4*10^8$ cm^{-2}
R = 250 cm	0.17 rad $5.1*10^6$ cm^{-2}	1.5 rad $4.5*10^7$ cm^{-2}

Figure F.17: Mean total ionizing dose (TID) for RHIC I and RHIC II fils, for two positions: 53 and 259 cm from the intereaction region in rads/fill and equivalent neutrons per cm^2 per fill.

Assuming running periods of 30 weeks per year with 3 shifts per day, the expected dose for 10 years of running RHIC II will be of the order of 50 krad or $1.5*10^{12}$ $n*cm^{-2}$(for 53cm).

The ALICE collaboration published the results of the radiation tolerance tests of similar components in ALICE publication[5], which are summarized below.

1. Clock Oscillators and Voltage Regulators
   The clock oscillators PL75108A, SDB0149N, CFPIQXO-71C, PLE5144A where tested.

All the oscillators found to be tolerant to the gamma irradiation up to 100 krad. The voltage regulator of Linear Technology LT1663 family passed the tests.

2. Optical Transceiver and SerDes
   The all Small Form Factor (SFF) optical transceivers which have been tested (HFBR5910E, HFBR5921L, HFBR5920E, V23818-K305-L57, V23818-N305-B57) as well as SerDes (TLK2501, VSC7211) all passed the irradiation test with 10^{12} n*cm^{-2}.

3. FPGA

It was found that the cross section of bit flips in application memory is acceptable, but the cross section for errors in configuration memory is too high. Translated to 50 krad TID it corresponds to 12000 of lost configuration for SRAM-based FPGA (Xilinx Virtex II). The flash-based FPGA (ACTEL ProASIC+) did not show any degradation.

Therefore the only unacceptable tolerance we may expect is in the configuration memory of the SRAM-based FPGA. There are two solutions to that:

1. Use flash-based FPGA (ACTEL ProASIC+), which is little bit slower than Xilinx

2. Monitor the configuration error and reconfigure the FPGA when necessary, the expected rate of such reconfigurations is once per store.

The performance of the stripixel readout electronics in radiation condition will be tested with full-scale prototype of the electromagnetic brick. It will be also established the maximum length of the daisy-chain cable which, according to D0 experience we expect to be about 2 m. If the rate Single Event Upsets will be not acceptable then **we will move the FEM far from the interaction point**.

F.10 References

References

[1] Nuclear Instruments and Methods in Physics Research Section A: Accelerators, Spectrometers, Detectors and Associated Equipment. Volume 518, Issue 3 , 11 February 2004, Pages 738-753

[2] http://www-d0.fnal.gov/d0pub/d0_private/4252/m_svx4_user_guide.pdf

[3] http://www.axman.com/files/CMM5235_man.pdf

[4] S.A. Skutnik, Master's Thesis, "A scalable analytic model for single event upsets in radiation-hardened FPGA in the

PHENIX interaction region"

[5] E.Denes et al. "ALICE DDL Radiation Tolerance Tests fo the FPGA Configuration Loss."

Appendix G

Power Proposal

G.1 PHENIX NCC Bias Voltage Supply

The PHENIX NoseCone Calorimeter Bias Voltage power supply is to be implemented as four, 12 channel cards for each of the North and South arms. Each card contains a single Emco 400 volt 20mA bulk supply which feeds 12 computer controlled push-pull bias output voltage channels. An addressable onboard microcontroller provides control and monitoring of the supply card through an RS485 interface to the PHENIX Rack Monitor and Control (RMC) system. The microcontroller controls and monitors the output voltages via isolated 16 bit DACs and 24 bit ADCs. A controller output port line enables / disables the bulk bias supply by controlling its low voltage regulator source. Serial control commands and responses go through an isolation barrier between the controller and the PHENIX Rack Monitor and Control RS-485 LAN.

Each NCC Power Supply card has its own two digit hex address which is set by the Address High and Address Low rotary switches on the board. There are two indicator LEDs on the front panel. The top green LED flashes at 1Hz indicating computer operation and the bottom amber LED flashes when valid commands are executed. Three grounds are used, chassis ground, bias ground and LAN ground. The control section is referenced to the chassis ground plane. The bias ground plane is isolated from the chassis ground but they are joined at a point near the bulk bias converter by a voltage limiting network. After system reset, the bulk bias supply is disabled and therefore starts in a safe condition with output voltages at zero. The user enables the high voltage by issuing an bias Enable command. This causes the output voltages to begin ramping up to the previously set levels at a predetermined rate. The user sets the individual output voltages by entering the values in the SCADA workstation (Iconics Graphworx32 screen).

The voltage setpoint values are automatically stored in EEPROM and are restored as the default levels on the next reset. All circuitry is enclosed in an aluminum NIM module with steel cover plates and is therefore non-contactable. The output connectors are Tyco 1586037-8, 4.2mm PE series which are UL94V-2, 600VAC and 9 amp rated. The pins are deeply embedded and non-contactable by touching with hands. In addition, the controller is monitored by a watchdog timer and disables the bulk bias supply on either power up,

watchdog or manual reset. Vertical airflow cooling is required mainly for the bulk bias converter and is achieved by using a fan tray.

G.2 PHENIX NCC LV Supply

The proposed NCC LV is the PHENIX standard low voltage supply system based on Vicor second generation DC-DC converters. The 2nd generation PHENIX Low Voltage Power System (LVPS-2) is implemented as a 6U crate with a set of 8 to 12 340mm ("C" size) removable power supply cards (LVLP-2). Each card contains from 6 to 8 Vicor 2nd Generation 300V to 12V converters which provide output of 5V to 14V dc. A Front End crate controller card (LVLPFE-2) provides both backplane power and computer control for 8 to 12 power supply cards. The low voltage outputs then proceed to 160mm noise filter cards installed in the rear of the crate. The filtered low voltage from the filter boards is connected to terminal blocks on the rear panel. Control and monitoring of the LVPS-2 crate is achieved through an RS485 interface to the PHENIX Rack Monitor and Control (RMC) system.

List of Figures

2.1 $R_A A$ for π_0 mesons and inclusive charged particles from as measured by PHENIX. The difference in the observed suppression for charged hadrons and neutral pions between 1-4 GeV/c is due to the changing particle composition of the charged hadrons, highlighting the importance of the π^0 measurement. 2–3

2.2 Data from PHENIX and STAR showing electrons from charm and bottom decay as compared to models theoretical models of Djordjevic et al (left) and Armesto et al (right) where values of dN/dy and $\hat{q}$ far in excess of reasonable values are required to fit the data. (Say this better) [19, 20] 2–4

2.3 Tree level diagrams for the production of direct photons by QCD-Compton processes. The photon produced in the hard scattering only interacts electromagnetically and will escape the surrounding medium produced in nucleus-nucleus collisions without interacting. The jet produced by the partner parton in the interaction will, however, interact and suffer energy loss. Measuring both the photon and jet in the final state allows for a calibration of the energy loss. 2–5

2.4 Measured direct photon invariant multiplicity at mid-rapidity as a function of centrality in AuAu collisions. 2–6

2.5 R_{AA} for direct photons as a function of transverse momentum as compared with that for $\pi^0 s$ showing that the direct photon suppression is consistent with zero. 2–7

2.6 (left) jetcone (right) jetcone 2–7

2.7 The scale r_{med} which gives an estimate for the distance beyond which the force between a static quark anti-quark pair is strongly modified by temperature effects and the Debye screening radius, $R_D = 1/m_D$. Open (closed) symbols correspond to SU(3) (2-flavor QCD) calculations. The horizontal lines give the mean squared charge radii of some charmonium and bottomonium states. 2–9

2.8 PHENIX Preliminary R_{AA} for J/ψ in $Au+Au$ and $Cu+Cu$ 200 GeV reactions. 2–10

2.9 2–11

2.10 R_{AA} for the χ_C in where the χ_C decays to a $J/\psi + \gamma$ and the J/ψ is detected via its di-muon decay in the muon spectrometer. The photon detected by the NCC in the rapidity range 1¡—y—¡1.5 (we need to show others later. This is compared to the $R_A A$ of the J/ψ measured by PHENIX in Run-4. Errors for the χ_C are statistical only. It is assumed that the pp measurement of the χ_C adds a negligible error to the ratio. 2–12
2.11 A schematic showing the saturation of the gluons at low-x. This has the effect of suppressing very low x gluons and pushing them to higher-x 2–14
2.12 Regions of the nucleus showing the CGC region bordered by a line representing Q_S. As one goes forward in rapidity to regions covered by the NCC, one crosses into the CGC region. 2–15
2.13 R_{CP} for charged hadrons as measured in by the PHENIX muon arms for different centralities. 2–16
2.14 Polarized gluon distribution derived from NLO-QCD analysis of existing DIS data. The ranged limited by the dashed curves shows the range of gluon polarizations allowed by the data. The effect of including the direct photon results anticipated from PHENIX data from one year at design luminosity in the same NLO-QCD global analysis are shown in the right panel. 2–21
2.15 Direct photon production in the gluon compton and quark anti-quark annihilation processes. The ratio of the two processes has been studied using PYTHIA and was found to be about 9:1. 2–22
2.16 Kinematic coverage for PHENIX measurements that are sensitive to Δg. x_{Bj} range shown on-top parameterization of ΔG. 2–24
2.17 Range of x and Q^2 accessible by various DIS experiments compared to those accessible at PHENIX. Note that the HERA range denotes the collider experiments H1 and Zeus, which cannot measure the required double spin asymmetries.2–25
2.18 Single spin asymmetry from π^0 mesons at forward rapidity ($\langle\eta\rangle = 3.8$) as a function of Feynman x, measured at the STAR experiment from transversely polarized pp collisions at $\sqrt{s} = 200$ GeV [61]. 2–26
2.19 Forward inclusive π^0 cross sections measured at the STAR experiment from transversely polarized pp collisions at $\sqrt{s} = 200$ GeV [61]; the average pseudorapidity is $\langle\eta\rangle = 3.8$. In the left panel, these results are compared to predictions using PYTHIA [63] as a function of feynman x; in the right panel they are compared to NLO pQCD [62] calculations as a function of the pion energy. 2–27
2.20 Different contributions to A_N, plotted as a function of x_F, for $p^{\uparrow}p \to \pi^+ X$ processes and E704 kinematics. The different lines correspond to solid line: quark Sivers mechanism alone; dashed line: gluon Sivers mechanism alone; dotted line: transversity $\otimes$ Collins. All other contributions are much smaller. Taken from Ref. [75]. 2–28
2.21 Simulation of measurements of light quark polarizations from W boson production at RHIC, compared with preliminary data from the HERMES experiment. 2–1

3.1 A beam view (top) and side view (bottom) of the PHENIX detector in its most recent configuration. BB-Beam-Beam trigger counters, DC-Drift Chambers, RICH - ring imaging Cerenkov counters, aerogel - Aerogel Cherenkov counters, PC-Pad Chambers, TEC - Time Expansion Chambers, PbSc/PbGl – Electromagnetic Calorimeters, MPC- Muon Piston Calorimeters, MuTr/MuId -Muon Tracking and Muon Identification, and ZDC - Zero Degree Calorimeters. Magnetic field is axial in the central region, the muon magnets generate a radial magnetic field. 3–2
3.2 Schematic rendering of the new PHENIX Forward Spectrometer. R1-R3 – new resistive plate chambers built for triggering on muons. All other upgrade components are identified in the figure. 3–3
3.3 NCC assembled on the PHENIX Central Magnet pole. Shadowed is the acceptance of the Cental Arms. 3–4
3.4 Longitudinal structure of a single calorimeter tower showing the locations of the three calorimetric segments, EM1, EM2, and HAD, and the high resolution position detectors- preshower(PS) and shower-max(SM). Bottom panel are electomagnetic and hadronic showers due to 10 GeV/c electron and 40 GeV/c charged pion 3–6
3.5 Radial profile of the electromagnetic showers in different materials(from simulation) 3–8
3.6 Left: Momentum dependence of the sampling faction in NCC segments; Right - energy measured in NCC segments and total energy in NCC vs impact electron momentum. 3–10
3.7 The momentum dependence of the intrinsic NCC electromagnetic energy resolution deduced from simulations. 3–11
3.8 Left: radial distance between electron impact point and measured object; Center: the momentum dependence of the NCC position resolution (based upon energy sharing between towers only); Right: angule between impact vector and track vector measured in calorimeter. 3–12
3.9 The χ^2 distributions for electrons (top) and pions (bottom) in the momentum range 0.5-40 GeV/c in NCC. The corresponding cumulative distributions are in the panels on the right . Currently is based upon energy measurements only.3–13
3.10 Top: Momentum distribution of hadrons impingin on NCC and energy distribution of residual (after χ^2 testing) tracks consistent with electromagnetic pattern. Currently is based upon longitudinally segmented energy measurements only. 3–14
3.11 Energy distribution for all (black and blue) and photon (red and magenta) hits in minimum bias events in NCC. Black - energies from PYTHIA; blue - track energies in NCC; red - photons from PYTHIA; magenta - identified photons. 3–14
3.12 Left: Total enegry of jet fragments hitting NCC vs jet energy (PYTHIA); Center: Measured jet energy vs energy of fragments in NCC; Right: Jet width measured in NCC. 3–16

3.13 The relative RMS of the measured total and electromagnetic jet energies . . 3–16
3.14 Jet angulare resolution (with respect to the vector sum of jet particles). Currently is based upon energy measurements only. 3–17
3.15 Base data used to extract fitting primitives for muons passing through NCC 3–18
3.16 Fake muon rejection in NCC. NCC occupancy per PYTHIA minimum bias. Fake muons were simulated refleting momentum vectors of simulated particles hitting opposing NCC 3–19
3.17 Two-shower effective mass distribution in the events with two distinct maxima found in the pattern of deposited energy in NCC. 3–20
3.18 Probability to find both showers from π^0 decay as two distinct maxima in NCC vs momentum of π^0. 3–21
3.19 Energy patterns in the PreShowr and ShowerMax detectors due to two overlapping photons from 12 GeV/c π^0 decay. (The vertical axis is an energy per strip in GeV). 3–21
3.20 Reconstructed effective mass distribution in the events with a single distinct maximum found in the pattern of deposited energy in NCC. 3–22
3.21 Probability for π^0 in NCC to fail in reconstruction or to end up outside 2σ mass window. 3–23
3.22 Probability for π^0 in NCC to be reconstructed within 2σ mass window. . . . 3–23
3.23 Something about dynamic range 3–24
3.24 PHENIX Nose Cone (left panel). Nose Cone Calorimeter (right panel). Boxes upstream are electromagnetic segments (EM1 and EM2), downstream boxes are HAD.Crates with preamplifiers and cable drivers are also shown 3–25
3.25 NCC building bricks. (left) electromagnetic [preshower and shower max detectors are shown partially extracted], (center) hadronic, (right) Cu skin for the electromagnetic brick. 3–25
3.26 Main components of NCC design: sampling cell, brick, cutofs showing different pats of assembled calorimeter, assemblled calorimeter with analog readout electronics on magnet pole. 3–26
3.27 Pad-sensor stack. Explode view of the sensor stack in the right panel of the picture. 3–29
3.28 Exploded NCC pad-readout unit. Details of the sensor installation scheme are also included. 3–29
3.29 Design of the detector with interleaved pixilated strips with 2-d position sensitivity. Ionization charge produced by charged particles in Si is shared between X and Y oriented strips. 3–31
3.30 Expanded view of stripixel stack 3–32
3.31 Arrangement of strip ladders between pad sensor assemblies on tungsten plates.3–33
3.32 Signal processing block-diagram for NCC towers 3–34
3.33 NCC custom built crate with preamplifiers and differential drivers for analog conditioning of signals from calorimeter towers 3–35
3.34 Digital signal processing in NCC 3–35
3.35 HBD ADC board considered to be a prototype for the NCC pad FEM 3–36

3.36 Block diagram of the combined forward PHENIX Level-1 trigger system showing the nosecone calorimeter, NCC, trigger muon tracker stations and the existing MuID LL1 system for a single PHENIX muon arm. In order to combine the primitives of the various trigger systems a regional trigger processor will combine the trigger information before sending primitives to Global Level-1. 3–38

3.37 Anticipated NCC LL1 rejection factors of minimum bias proton-proton collisions at $\sqrt{s}$ = 500GeV for the 8x8EM and 8x8 trigger tiles, as described in the text. 3–40

3.38 Anticipated NCC LL1 rejection factors of minimum bias heavy ion collisions at $\sqrt{s}$ = 200GeV for the 8x8EM trigger tile, as described in the text. 3–41

3.39 Anticipated NCC LL1 rejection factors of minimum bias heavy ion collisions at $\sqrt{s}$ = 200GeV for the 8x8 trigger tile, as described in the text. 3–41

3.40 Anticipated NCC LL1 rejection factors of minimum bias d+Au collisions at $\sqrt{s}$ = 200GeV for the 8x8EM trigger tile, as described in the text. Note that the trigger rejections depend on whether the NCC arm in in the d-going or Au-going side of PHENIX. 3–43

3.41 Anticipated NCC LL1 rejection factors of minimum bias d+Au collisions at $\sqrt{s}$ = 200GeV for the 8x8 trigger tile, as described in the text.Note that the trigger rejections depend on whether the NCC arm in in the d-going or Au-going side of PHENIX. 3–43

4.1 Management chart of the NCC project. 4–3

4.2 Institutional tasks for the NCC project. 4–4

5.1 Major Costs associated with research and development related to PHENIX NCC Project. Update this table since we got some of the funding 5–4

5.2 Profile of DOE cost estimates for first NCC. 5–4

5.3 Budgetary and scheduling details covering major tasks involved in construction of the first NCC unit (extracted from the project file). 5–5

5.4 Proposed funding profile for DOE Construction project (also see first three columns in Fig. 5.3. . . . . –6

B.1 Simulation of the direct photon signal, i.e. the ratio $R = \frac{(\gamma/\pi^0)_{measured}}{((\gamma/\pi^0)_{expected})}$ as measured by the NCC. R in p+p collisions[left] ; R in p+Au collisions[center]; R in Au+Au collisions [right]. Our final analysis will require a comparison of all three systems. Error bars are from the statistics we expect to get in the experiment. The fluctuations of the points arises from lack of statistics in the simulation. B–2

B.2 Yield of photons between $1.5 < \eta < 2$ from decays in QCD events (blue) and direct photons (red) in 500 GeV p+p collisions [left]; Yield of photons between $1.5 < \eta < 2$ from decays in QCD events (blue) and direct photons (red) in 500 GeV p+p collisions after an isolation cut as explained in the text [right]. B–3

B.3 (left) Photons from decays in QCD events [black] and direct photons [red] in pAu collisions between $1 < \eta < 3$. (right) For the QCD background, only the highest energy photon in each event is plotted. Photons between $1 < \eta < 3$ from decays in QCD events [black] and direct photons [red] in pAu collisions after an isolation cut in which $E_{cone}/E_{direct-photon} < 0.1$, where E_{cone} is the amount of electromagnetic energy in a cone of size $\Delta\eta\Delta\phi$=0.8. Unlike the other figures in this section, the simulation was done using a heavy ion event generator HIJING. For the generation of QCD background events a cut of 10 GeV was made on the hard scattering of partons, hence one should look at the region to the right of the line in these plots. B–4

B.4 . . . . . B–5

B.5 p_T distributions for the χ_c. Green-all, red-J/ψ accepted in the muon spectrometer, blue-χ_c decay photon accepted in NCC and J/ψ accepted in the muon spectrometer. B–6

B.6 The $M_{\gamma\mu\mu} - M_{\mu\mu}$ invariant mass distribution in p+p events. The left plot shows the raw mass difference spectrum (red) and background (black). The right shows the subtracted spectrum. B–7

B.7 Same as the previous figure with the resolution of the NCC degraded to $\frac{0.50}{\sqrt{(E(GeV))}}$ B–7

B.8 Central 10% Cu+Cu events at various rapidities. The left plot of each pair show the raw mass difference, the right plot shows a background subtracted distribution. B–8

B.9 Same as the previous plot for central Au+Au events. B–8

B.10 R_{AA} for the χ_C in where the χ_C decays to a $J/\psi + \gamma$ and the J/ψ is detected via its di-muon decay in the muon spectrometer. The photon detected by the NCC in the rapidity range 1¡—y—¡1.5 (we need to show others later. This is compared to the $R_A A$ of the J/ψ measured by PHENIX in Run-4. Errors for the χ_C are statistical only. It is assumed that the pp measurement of the χ_C adds a negligible error to the ratio. B–9

B.11 Distribution of direct photon events at $\sqrt{s}$ of 200 (left) and 500 GeV (right). Red points refer to photons in the central detectors ($\eta < |0.35|$), while green points include the addition of the NCC ($1 < \eta < 3$). Black points show a hypothetical full acceptance ($\eta < |3|$). B–11

B.12 Double longitudinal spin asymmetry for direct photon events at $\sqrt{s}$ of 200 GeV, as a function of photon p_T. The left panel shows the direct photon asymmetry measured by the central detectors ($\eta < |0.35|$), while the right panel shows the asymmetry measured by the NCC ($1 < \eta < 3$). B–12

B.13 Double longitudinal spin asymmetry for direct photon events at $\sqrt{s}$ of 200 GeV, as a function of $\log_{10} x_g$, as determined from the simulation. The left panel shows the direct photon asymmetry measured by the central detectors ($\eta < |0.35|$), while the right panel shows the asymmetry measured by the NCC ($1 < \eta < 3$). B–13

B.14 Polarized gluon distribution function Δg for direct photon events at $\sqrt{s}$ of 200 GeV, as a function of $\log_{10} x_g$, as determined from the simulation. The left panel shows Δg measured by the central detectors ($\eta < |0.35|$), while the right panel shows Δg measured by the NCC ($1 < \eta < 3$). B–13
B.15 Distributions for direct photon events at $\sqrt{s}$ of 500 GeV measured by the NCC ($1 < \eta < 3$) showing the reach to $x_g \sim 10^{-3}$. Double longitudinal spin asymmetry as a function of photon x_g (left). Δg (right). B–14
B.16 (left) energy deposited around the muon in W events and jet events. (right) Suppression of background via isolation cuts. B–14
B.17 Modified gluon structure function B–15
B.18 R_{pA} shown as a function of η for various values of pt using a particular modified gluon structure function [81]. B–16
B.19 An overlay of GEANT events in the NCC B–17
B.20 Input flow (v_2) values as a function of η and p_T used in the simulation [top two panels]. η and $p_T$distributions used in the simulation [bottom two panels]. B–18
B.21 Hit position in x-y on the NCC detector for in EM1, EM2, and HAD(top 3 panels). Radial hit distribution, azimuthal hit distribution with respect to the generated primary track and azimuthal hit distribution with respect to the simulated reaction plane orientation(bottom 3 panels). B–19
B.22 (top) The reaction plane distribution ($\Phi_{calc} - \Phi_{true}$) with different weighting methods. (Bottom) Reaction plane resolution for different cases, where the conditions marked with circle are described in the following. (1:black) BBC or central arm reaction plane resolution is about 0.4, (2:black) use all charged particles in NCC acceptance, (3:black) use all GEANT hits in NCC, (4:red) weighting all the GEANT hits with dE/dx, (5:green) v2 weighting according to eta dependence of v2 in addition to (4), (6:blue) z sector depending weight in addition to (5), (7:pink) 2 dimensional r, z weight in addition to (5). The resolution goes up from about 0.8 in the case (2) with charged particle alone to about 0.9 case (7) by including π^0 conversion, dE/dx weighting and optimizing the weight. B–20
B.23 . Reconstructed p_T distribution from various p_T intervals of produced light hadrons. Muons from W boson decays are also shown. B–2
B.24 Distribution similar to Fig. B.23, but with the background suppression by matching tracks from the muon spectrometer to the NCC. B–2

C.1 Single assembled readout layer for the prototype NCC connected to readout electronics. C–2
C.2 Assembled prototype calorimeter. Readout electronics not shown. C–3
C.3 Amplitude distribution of the signal from the pad near beam impact. C–3
C.4 Example of the electromagnetic shower in prototype W-Si calorimeter C–4
C.5 Longitudinal profile of electromagnetic shower. C–5
C.6 Energy distribution in the NCC prototype measured exposing detector to 10 GeV/c positron beam. C–5

C.7 Precision of the impact point measurements in the segments of prototype detector. Location of the segment geometrical center in the prototype is plotted along X in units of X_0. . . . . C–6
C.8 Pointing resolution measured in the prototype calorimeter exposed to 10 GeV/c positrons. Both X- and Y- planes are shown. C–1
C.9 Shower identification in longitudinally segmented calorimeter. E_1, E_2, E_3 are energies measured in calorimeter segments, E_{Total} is the total energy. Red points are 10 GeV/c electrons, blue points are 70 GeV/c protons. C–2

D.1 NCC Silicon sensor. Undiced wafer is shown. Active area is subdivided into 16 readout pads 1.5x1.5 cm2 each. On the right is the structure of the guard rings. The complexity of he design is to prevent voltage breakdowns after radiation exposure. D–2
D.2 CV and IV measurement data for the test batch of 30 PHENIX NCC pad-structured sensors produced at ELMA in Russia. D–3
D.3 Two designs for the pad-structured Si sensors. DC on the left and AC (decoupling capacitances and bias resistors are on sensor) on the right D–3
D.4 Prototype wafer with 5 different stripixel structures bot X and Y directions. Technology:single-metal with implanted bridges in orthogonal direction.) . . D–1
D.5 Alpha particles spectra. D–2
D.6 Test source for stripixel studies with collimated electron source. D–3

E.1 Simulation model of the pad sensor readout chain. E–2
E.2 Spectrum of the source signal. The bandwidth (where amplitude drops by 6 dB) is 13 MHz. E–3
E.3 Gain (blue) and noise (red) at preamp output. E–4
E.4 Transient analysis of the pad readout chain. E–5
E.5 Transient analysis, Rcr = 35 Ohm. E–6
E.6 Gain in kΩ (blue), noise in nV/$\sqrt{\text{Hz}}$ (red), and noise contribution of Rin_{hot} (green) at the output of the filter. E–7
E.7 Noise at the filter output (RMS1) and the signal-to-noise ratio. E–8

F.1 Conceptual layout of the NCC electromagnetic brick. Blue layers are silicon-strip planes (preshower and shower max); brown layers are tungsten plates, yellow layers – silicon-pad readout planes. Both silicon strip planes are read by FEM board located inside the bricks envelope. The FEM sends data to PHENIX DCM boards over optical fiber. Power and ground are distributed from a PCM board located near the detector. F–1
F.2 Comb structure F–2
F.3 Prototype of stripixel sensor. F–2
F.4 Stripixel ladder comprising 5 daisy-chained Sensor Readout Modules with two sensor on each. The rightmost SRM is populated with SVX4 and it has one pitch adapter out of four installed. F–3

F.5 The arrangement of stripixel ladders between pad sensor assemblies on tungsten plates F–4
F.6 Sensor Readout Module, the upper half of the module shown. In the final version two connectors will be installed instead of one. F–5
F.7 Stack-up of the Sensor Readout Module. F–5
F.8 FEM Block Diagram. Shaded boxes represent the elements implemented in the FPGA. F–7
F.9 PHENIX Synchronization Signals. F–7
F.10 Size and Tranfer Time of Stripixel Data from Single Electromagnetic Brick. F–8
F.11 BEM Memory Requirements. F–9
F.12 Comparison of FPGA options. F–10
F.13 Photo of the stripixel readout chain. F–12
F.14 Data analysis of SVX4 channels when pitch adapter is not connected. Amplitudes from all channels (top), single channels (center) and cumulative histogram of all channels (bottom). F–13
F.15 Automatic wire-bonding machine in clean room facility at Helsinki Institute of Physics. F–14
F.16 Strip detector production flow chart. The green area shows accoplished tasks. F–15
F.17 Mean total ionizing dose (TID) for RHIC I and RHIC II fils, for two positions: 53 and 259 cm from the intereaction region in rads/fill and equivalent neutrons per cm^2 per fill. F–16

List of Tables

2.1 Dissociation temperatures obtained from different analyses in quenched QCD. 2–9

3.1 Nose Cone Calorimeter design features. All counts are for a single unit . . . 3–9
3.2 NCC Silicon Sensor parameters 3–28
3.3 Anticipated NCC LL1 rejection factors of minimum bias proton-proton collisions at $\sqrt{s} = 500$GeV for the 8x8EM and 8x8 trigger tiles. 3–40
3.4 Anticipated NCC LL1 rejection factors of minimum bias heavy ion collisions at $\sqrt{s} = 200$GeV for the 8x8EM and 8x8 trigger tiles. 3–42
3.5 Anticipated NCC LL1 rejection factors of minimum bias d+Au collisions at $\sqrt{s} = 200$GeV for the 8x8EM and 8x8 trigger tiles. 3–44

A.1 Luminosity guidance from CAD for RHIC II. We assume a 50% duty cycle for RHIC to give a weekly integrated luminosity. We then assume a 12 week run and a 60% uptime for PHENIX to give an total integrated luminosity. . A–1
A.2 Efficiency factors added into the rate calculations. In the analysis we typically require that the vertex be within 20 cm of the nominal collision point, which results in a loss of 0.55. For A+A collisions the minimum bias trigger formed by the Beam-Beam counters are essentially 100% efficient, however in p+p and p+A collisions there is some loss. A–1
A.3 Yields in p+p collisions of various processes into the acceptance of a single NCC for a 12 week run. A–2
A.4 Yields in pAu, Cu+Cu and Au+Au collisions of various processes into the acceptance of a single NCC for a 12 week run. A–3
A.5 The coverage by the NCC of some of relevant kinematical variables given the rates mentioned previously. A–4

References

[1] PHENIX, 1993. PHENIX Conceptual Design Report 1993 (PX20, BNL48922, internal report),.

[2] **PHENIX** Collaboration, K. Adcox *et. al. Nucl. Phys.* **A757** (2005) 184–283 [nucl-ex/0410003].

[3] **PHENIX** Collaboration, K. Adcox *et. al. Phys. Rev. Lett.* **88** (2002) 022301 [nucl-ex/0109003].

[4] **PHENIX** Collaboration, K. Adcox *et. al. Phys. Lett.* **B561** (2003) 82–92 [nucl-ex/0207009].

[5] **PHENIX** Collaboration, S. S. Adler *et. al. Phys. Rev. Lett.* **91** (2003) 072301 [nucl-ex/0304022].

[6] **PHENIX** Collaboration, S. S. Adler *et. al. Phys. Rev.* **C69** (2004) 034910 [nucl-ex/0308006].

[7] **PHENIX** Collaboration, S. S. Adler *et. al. Phys. Rev. Lett.* **91** (2003) 072303 [nucl-ex/0306021].

[8] E. Wang and X.-N. Wang *Phys. Rev. Lett.* **89** (2002) 162301 [hep-ph/0202105].

[9] **PHENIX** Collaboration, S. S. Adler *et. al. Phys. Rev. Lett.* **91** (2003) 172301 [nucl-ex/0305036].

[10] J. D. Bjorken, *Energy loss of energetic partons in quark - gluon plasma: Possible extinction of high p(t) jets in hadron - hadron collisions*, 1982. FERMILAB-PUB-82-059-THY.

[11] M. Gyulassy and M. Plumer *Phys. Lett.* **B243** (1990) 432–438.

[12] X.-N. Wang, M. Gyulassy and M. Plumer *Phys. Rev.* **D51** (1995) 3436–3446 [hep-ph/9408344].

[13] X.-N. Wang and M. Gyulassy *Phys. Rev. Lett.* **68** (1992) 1480–1483.

[14] R. Baier, Y. L. Dokshitzer, S. Peigne and D. Schiff *Phys. Lett.* **B345** (1995) 277–286 [hep-ph/9411409].

[15] R. Baier, Y. L. Dokshitzer, A. H. Mueller and D. Schiff *Phys. Rev.* **C58** (1998) 1706–1713 [hep-ph/9803473].

[16] M. Gyulassy, P. Levai and I. Vitev *Phys. Rev. Lett.* **85** (2000) 5535–5538 [nucl-th/0005032].

[17] M. Gyulassy, P. Levai and I. Vitev *Nucl. Phys.* **B594** (2001) 371–419 [nucl-th/0006010].

[18] **PHENIX** Collaboration, A. Adare *et. al.* nucl-ex/0611018.

[19] M. Djordjevic, M. Gyulassy, R. Vogt and S. Wicks *Phys. Lett.* **B632** (2006) 81–86 [nucl-th/0507019].

[20] N. Armesto, M. Cacciari, A. Dainese, C. A. Salgado and U. A. Wiedemann *Phys. Lett.* **B637** (2006) 362–366 [hep-ph/0511257].

[21] G. Policastro, D. T. Son and A. O. Starinets *Phys. Rev. Lett.* **87** (2001) 081601 [hep-th/0104066].

[22] J. J. Friess, S. S. Gubser, G. Michalogiorgakis and S. S. Pufu hep-th/0607022.

[23] S. S. Gubser *Phys. Rev.* **D74** (2006) 126005 [hep-th/0605182].

[24] F. Antinori and E. V. Shuryak *J. Phys.* **G31** (2005) L19 [nucl-th/0507046].

[25] J. Casalderrey-Solana, E. V. Shuryak and D. Teaney *J. Phys. Conf. Ser.* **27** (2005) 22–31 [hep-ph/0411315].

[26] T. Matsui and H. Satz *Phys. Lett.* **B178** (1986) 416.

[27] O. Kaczmarek, F. Karsch, P. Petreczky and F. Zantow *Phys. Lett.* **B543** (2002) 41–47 [hep-lat/0207002].

[28] M. Asakawa and T. Hatsuda *Phys. Rev. Lett.* **92** (2004) 012001 [hep-lat/0308034].

[29] S. Datta, F. Karsch, P. Petreczky and I. Wetzorke *Phys. Rev.* **D69** (2004) 094507 [hep-lat/0312037].

[30] C.-Y. Wong *Phys. Rev.* **C72** (2005) 034906 [hep-ph/0408020].

[31] F. Karsch *Eur. Phys. J.* **C43** (2005) 35–43 [hep-lat/0502014].

[32] **PHENIX** Collaboration, H. Pereira Da Costa nucl-ex/0510051.

[33] **NA50** Collaboration, M. C. Abreu *et. al. Phys. Lett.* **B521** (2001) 195–203.

[34] **NA60** Collaboration, R. Arnaldi *et. al. Eur. Phys. J.* **C43** (2005) 167–172.

[35] Y. V. Kovchegov, *Isotropization and thermalization in heavy ion collisions*, 2005.

[36] S. Mrowczynski *Acta Phys. Polon.* **B37** (2006) 427–454 [hep-ph/0511052].

[37] R. Venugopalan hep-ph/0511117.

[38] D. Kharzeev, E. Levin and K. Tuchin hep-ph/0602063.

[39] L. D. McLerran and R. Venugopalan *Phys. Rev.* **D49** (1994) 2233–2241 [hep-ph/9309289].

[40] L. D. McLerran and R. Venugopalan *Phys. Rev.* **D49** (1994) 3352–3355 [hep-ph/9311205].

[41] L. D. McLerran and R. Venugopalan *Phys. Rev.* **D50** (1994) 2225–2233 [hep-ph/9402335].

[42] H. Kowalski and D. Teaney *Phys. Rev.* **D68** (2003) 114005 [hep-ph/0304189].

[43] **New Muon** Collaboration, P. Amaudruz *et. al. Nucl. Phys.* **B441** (1995) 3–11 [hep-ph/9503291].

[44] D. F. Geesaman, K. Saito and A. W. Thomas *Ann. Rev. Nucl. Part. Sci.* **45** (1995) 337–390.

[45] D. M. Alde *et. al. Phys. Rev. Lett.* **64** (1990) 2479–2482.

[46] **NuSea** Collaboration, M. A. Vasiliev *et. al. Phys. Rev. Lett.* **83** (1999) 2304–2307.

[47] L. L. Frankfurt, M. I. Strikman and S. Liuti *Phys. Rev. Lett.* **65** (1990) 1725–1728.

[48] B. Z. Kopeliovich, J. Nemchik, I. K. Potashnikova, M. B. Johnson and I. Schmidt *Phys. Rev.* **C72** (2005) 054606 [hep-ph/0501260].

[49] D. Boer and W. Vogelsang *Phys. Rev. D* **69** (2004) 094025.

[50] C. Adloff *et. al. Eur. Phys. J.* **C19** (2001) 289–311.

[51] H. Lai *et. al. Eur. Phys. J.* **C12** (1999) 375–392.

[52] A. Martin, R. Roberts, W. Stirling and R. Thorne *Eur. Phys. J.* **C39** (2005) 155–161.

[53] M. Gluck, E. Reya, M. Stratmann and W. Vogelsang *Phys. Rev.* **D53** (1996) 4775–4786.

[54] Y. Goto *et. al. Phys. Rev. D* **69** (2004) 054021.

[55] E. Laenen, G. Sterman and W. Vogelsang *Phys. Rev. Lett.* **84** (2000) 4296–4299.

[56] E. Laenen, S. G. and W. Vogelsang *Phys. Rev. D* **63** (2001) 114018.

[57] J. Ashman *et. al. Nucl. Phys.* **B328** (1989) 1–35.

[58] G. Baum *et. al. Phys. Rev. Lett.* **51** (1983) 1261–1265.

[59] G. Bunce *et. al. Phys. Rev. Lett.* **36** (1976) 1113–1116.

[60] D. Adams *et. al. Phys. Lett. B* **265** (1991) 462–466.

[61] J. Adams *et. al. Phys. Rev. Lett.* **92** (2004) 171801.

[62] L. Bland `hep-ex/0602012`.

[63] T. Sjostrand *et. al. Comput. Phys. Commun.* **135** (2001) 238–259 [`hep-ph/0010017`].

[64] D. Sivers *Phys. Rev.* **D41** (1990) 83.

[65] J. Collins *Nucl. Phys.* **B396** (1993) 161.

[66] J. P. Ralston and D. E. Soper *Nucl. Phys.* **B152** (1979) 109.

[67] J. Qiu and G. Sterman *Phys. Rev. D* **59** (1998) 014004.

[68] A. Airapetian *et. al. Phys. Rev. Lett.* **84** (2000) 4047–4051.

[69] A. Airapetian *et. al. Phys. Rev. Lett.* **94** (2005) 012002.

[70] K. Abe *et. al.* `hep-ex/0507063`.

[71] J. Collins, S. Heppelmann and G. Ladinsky *Nucl. Phys.* **B420** (1994) 565.

[72] H. Collaboration `hep-ex/0512019`.

[73] P. Mulders and R. Tangerman *Nucl. Phys.* **B461** (1996) 197–237.

[74] A. Bacchetta, C. Bomhof, P. Mulders and F. Pijlman *Phys. Rev. D* **72** (2005) 034030.

[75] M. Anselmino *et. al. Phys. Rev. D* **73** (2006) 014020.

[76] A. Airapetian *et. al. Phys. Rev. D* **71** (2005) 012003.

[77] C. Bourrely and J. Soffer *Phys. Lett.* **B314** (1993) 132–138.

[78] P. Nadolsky and C.-P. Yuan *Nucl. Phys.* **B666** (2003) 35.

[79] M. Harrison, T. Ludlam and S. Ozaki *Nucl. Instrum. Meth.* **A499** (2003) 235–880.

[80] I. Golutvin *et. al.*, 1992. A Silicon Hadron Calorimeter module operated in a strong magnetic field with VLSI read out for LHC, CERN-DRDC-91-54, CERN-DRDC-P-34.

[81] K. Golec-Biernat and M. Wusthoff *Phys. Rev.* **D59** (1999) 014017 [`hep-ph/9807513`].